Application and evaluation of EDAM with assimilated GPS total electron content in the European Sector

By

James Parker

Aberystwyth University (AU)

2018

THESIS

Submitted to Aberystwyth University

by

James Parker

In Candidature for the Degree of

Doctor of Philosophy

Supervised by Prof Eleri Pryse, Prof Manuel Grande and Dr Natasha Jackson-Booth.

Faculty of Business and Physical Sciences – Department of Physics

September 2018

Word Count of thesis: DECLARATION	59051
This work has not previously been accepted in substance for any degree and is not b concurrently submitted in candidature for any degree.	
Candidate name	James Anthony Derek Parker
Signature:	
Date	

STATEMENT 1

This thesis is the result of my own investigations, except where otherwise stated. Where *__correction services__ have been used, the extent and nature of the correction is clearly marked in a footnote(s).

Other sources are acknowledged by footnotes giving explicit references. A bibliography is appended.

Signature:	
Date	

[*this refers to the extent to which the text has been corrected by others]

STATEMENT 2

I hereby give consent for my thesis, if accepted, to be available for photocopying and for inter-library loan, and for the title and summary to be made available to outside organisations.

Signature:	
Date	

NB: *Candidates on whose behalf a bar on access (hard copy) has been approved by the University should use the following version of Statement 2:*

I hereby give consent for my thesis, if accepted, to be available for photocopying and for inter-library loans after expiry of a bar on access approved by Aberystwyth University.

Signature:	
Date	

List of Acronyms and Abbreviations

EDAM – Electron Density Assimilative Model

GPS – Global Satellite Positioning

TEC – Total Electron Content

SuperDARN – Super Dual Auroral Radio Network

NIMS – Navy Ionospheric Monitoring System

TOI – Tongue of Ionisation

SED – Storm Enhanced Density

IMF – Interplanetary Magnetic Field

ACE – Advanced Composition Explorer

Dst – Disturbance storm time

DMSP – Defence Meteorological Satellite Program

IRI – International Reference Ionosphere

ECLAT – European Cluster Assimilation Technology

UKSSDC – UK Solar System Data Centre

HF – High Frequency

MLT – Magnetic Local Time

ISR – Incoherent Scatter Radar

LEO – Low Earth Orbiting

CME – Coronal Mass Ejection

SSC- Sudden Storm Commencement

RO – Radio Occultation

MIDAS – Multi-Instrument Data Analysis System

TOMION – Tomographic Ionospheric Model

NTCM – Neustralitz TEC Models

IONMON, v2 – Ionosphere Monitoring Facility, Version 2

DCB – Differential Code Biases

CODE – Centre for Orbit Determination in Europe

CUTLASS – Co-operative UK Twin Located Auroral Sounding System

POLAN – Polynomial analysis program

MAG – Magnetic Field Experiment

SWEPAM – Solar Wind Electron, Proton and Alpha Monitor

AE – Auroral Electrojet

TECU – Total Electron Content Unit

VTEC – Vertical Total Electron Content

ART – Algebraic Reconstruction Algorithms

EUV – Extreme Ultraviolet

IMAGE – Imager for Magnetospheric-to-Aurora Global Exploration

DE 2 – Dynamic Explorer 2

EISCAT – European Incoherent Scatter

UHF – Ultra-High Frequency

VHF – Very-High Frequency

IGS – International GNNS Service

GNSS – Global Navigation Satellite System

CDDIS – Crystal Dynamics Data Information System

sTEC – slant Total Electron Content

UT – Universal Time

COSMIC – Constellation Observing System for Meteorology, Ionosphere and Climate

OMNI – Operating Missions as Nodes on the Internet

NCAR – National Centre for Atmospheric Research

TIEGCM – Thermosphere-Ionosphere-Electrodynamics General Circulation Model

SAPS – Sub Auroral Polarisation Streams

MTD – Modified Taylor Diagram

Abstract

This thesis presents results from EDAM modelling and observing ionospheric phenomena in the European sector. EDAM used GPS TEC to create 3-D electron density grids that are then used to create vertical Total Electron Content maps. This enabled observations of ionospheric phenomena in the European sector. Alongside EDAM, SuperDARN potential plots and Ionosondes among other data sources are used to help confirm and verify the modelling results.

Statistical results are presented of the main ionospheric trough, obtained from EDAM with assimilated GPS TEC from September to December 2002. The results not only considered the width and depth of the trough but are also used to parameterise the shape of the trough in terms of a set of parameters. The parameters were used in a previous study that used NIMS TEC measurements and tomographic imaging. This study has been published in Annales Geophysicae by Parker et al. (2018) (Reuse of this text is allowed for this Chapter by way of Creative Commons Attribution 4.0 License. There are changes in the text, but the content is the same.)

Observations of the TOI and SED are presented using EDAM assimilated GPS VTEC maps, difference VTEC maps, electron density difference height profiles and SuperDARN electric potential plots. The evolution of the TOI and SED are presented over the Western European sector on 30 September 2002. The results have also considered IMF and solar wind data from ACE, indices such as the Kp index, Dst index and DMSP data plots.

Modified Taylor Diagrams are used to show the performance of EDAM and IRI with respect to a truth receiver between September 2002 and August 2003. The diagrams are categorised into three different parameters to focus on; the time of day, individual satellites, and Kp index. A time period where the EDAM modelled results underperformed compared to the truth data as shown by Modified Taylor Diagrams is discussed, where the cause may have been down to a number of factors including Sporadic E.

Acknowledgments

I would like to thank Prof. S. E. Pryse, Prof M. Grande and Dr. Natasha Jackson-Booth for their supervision of this research project. I would like to extend this thanks to all my colleagues in the Solar System Physics research group and the support of the Institute of Mathematics, Physics and Computer Science at Aberystwyth University and Qinetiq.

I would like to thank the staff at Qinetiq that helped support the research project, particularly Rachel Buckland for their help and support working with the model and data analysis.

The following individuals and organisations are also due thanks: Dr Suzie Imber and staff in the ECLAT group at Leicester University for supplying the data from SuperDARN; the ACE science centre for the provision of ACE data; the UKSSDC for the provision of the geomagnetic indices and ionosonde data and the website run by DK5YA for the amateur radio data.

Financial support for the research project was provided by Aberystwyth University and Qinetiq and this included support for travelling and attending conferences to present the research was provided. Both are gratefully acknowledged for this support.

Contents

Chapter 1

Introduction

1.1 Introduction

The ionosphere, the ionised part of the Earth's atmosphere, holds the footprints of processes between the solar wind and the terrestrial environment. These processes can exert great influence on the properties of the atmosphere and on radio propagation through the ionosphere. The behaviour of the ionosphere is therefore important to study to understand the effects between the two environments and how that effects radio propagation.

The purpose of this thesis is to demonstrate and test the capabilities of the Electron Density Assimilative Model (EDAM), where ionospheric measurements are assimilated to model the ionosphere. This demonstration is done by looking at how ionospheric structures are modelled in EDAM. Understanding and computing the performance of EDAM when modelling a large-scale ionospheric structure, done by comparing parameters of the structure with reference work that was completed using a different method, provides evidence of EDAMs performance. EDAM, with other data sources, is used to produce a case study on ionospheric phenomena where it is compared and discussed with the literature. The study shows the capabilities of EDAM for modelling and analysing these ionospheric phenomena while also offering some insight into the physics involved with these features. To finally show the performance of EDAM, the model is tested against another ionospheric model and data that has not been assimilated to validate EDAM. The model however is not infallible and some of the problems and areas of improvement are also discussed to show there is growth and potential.

The special thing about EDAM, and the results that this thesis provides, is the ability and future potential of real time assimilating and forecasting of the ionosphere. Using data from

multiple sources such as Global Positioning Satellite (GPS), ionosondes etc, EDAM would be able to assimilate these data and create a real-time modelled ionosphere. This potential provides a lot of opportunities and routes of exploitation, such as real time ionospheric and geomagnetic storm effect tracking, showing ionospheric features evolve over time. The thesis provides statistical analyses on the ionospheric phenomena, that are prominent in the ionosphere, to understand if the model would (i) need to include code to create the ionospheric phenomena that could be adapted or (ii) adaptations in the model itself could improve the accuracy of the modelling of the features. While EDAM has been around for over a decade, the work that has been published relates to ionosonde data being assimilated, showing the potential of multiple sources of data used, and a performance testing of the model, compared to other ionospheric models, that have assimilated ionosonde data. This thesis offers something new by using GPS assimilated data to statistically analyse and model ionospheric phenomena, as well as validating EDAM assimilated GPS against GPS data not included in the assimilation. It also shows the potential for development of the model, where improvements can be made for other ionospheric features not described in this thesis and the potential for the study of the physics of the ionosphere rather than just morphology studies.

This is all relevant and needed because being able to correctly account for these ionospheric features in the future provides better accuracy for forecasting and real-time modelling of the ionosphere. This is important because understanding the evolution of the ionosphere will eventually lead to the ability to compute accurate ionospheric corrections when transmitting and receiving radio signals. With the future moving towards technologies that require accurate communication between one another, having a real-time representation of the

ionosphere would enable users and providers to allow for ionospheric impacts on the radio signals to be accounted for accurately.

An introduction to the ionosphere and the near-Earth environment is presented in Chapter 2. While the study focuses on EDAM and its performance, other instrumentation and the data they provide is required verify the model. EDAM and how it works is explained in detail in Chapter 3. The thesis presents a series of studies that have been conducted using a variety of instruments to help compare and analyse the results from EDAM. The Super Dual Auroral Radar Network (SuperDARN) provides high-latitude convection patterns enabling a view of the convection of the plasma. The Advanced Composition Explorer (ACE) spacecraft observes the Interplanetary magnetic field (IMF) and other solar wind parameters such as velocity and temperature. Ground based ionosondes observe the bottom side ionosphere and from them electron density profiles are obtained. These instruments along with the usage of other databases are explained in Chapter 4.

Chapter 5 is the first study using EDAM and it focusses on the main ionospheric trough. The trough is well documented in the literature. A study from the literature used data analysed from the Navy Ionospheric Monitoring Satellite (NIMS) constellation, parameterised the trough from 12 months of data, but this is the first time EDAM assimilating GPS data has done so. The chapter looks at the EDAM results for parametrising the trough and splits the data into differing sets dependent on geomagnetic activity, before comparing the parametrisation to the study using NIMS. This study has been published in Annales Geophysicae by Parker et al. (2018) (Reuse of this text is allowed for this Chapter by way of Creative Commons Attribution 4.0 License. There are changes in the text, but the content is the same.)

Using analysis conducted in Chapter 5, other ionospheric phenomenon known as a Tongue-Of-Ionisation (TOI) and Storm Enhanced Density (SED) were observed and became the focal point of Chapter 6. The study corroborated EDAM with SuperDARN to perform an in-depth study on the TOI/SED observed in the European sector. The feature is well documented in the literature for the North American Sector but that is not the case for European sector.

To understand and analyse the performance EDAM must be verified against 'truth' data to evaluate its true performance. This is done in Chapter 7 primarily using Modified Taylor Diagrams. These diagrams enable the displaying of a number of statistics all on one diagram. This gave the opportunity to show the performance of EDAM compared to another model, the International Reference Ionosphere (IRI), as well as seeing the performance compared to a 'truth' data set.

Chapter 8 focusses on the month where EDAM displayed a poor performance in modelling the ionosphere, briefly discussed in Chapter 7. Understanding the poor performance is crucial to the development of the model. Chapter 8 goes into detail of why this underperformance occurs by using modified Taylor diagrams, geomagnetic indices, solar wind data and ionosonde data.

Chapter 9 concludes the thesis and discusses the potential for future work.

Chapter 2

A Review of the Ionosphere

2.1 Introduction

The atmosphere of Earth is divided into two main regions. The homosphere, where at below 100 km the constituents of gas are fully mixed into a homogenous gas. The heterosphere, above this height range, is where the constituents behave independently, meaning this part of the atmosphere is heterogenous. A typical vertical profile of the temperatures, particle densities and scale heights in the neutral atmosphere is shown in Figure 1. These neutral gases dominate the terrestrial atmosphere. Only 1% of the atmosphere is ionised and it is here that a significant number of free electrons and positive ions are located. The ionised section of the terrestrial atmosphere is known as the ionosphere. The medium itself is electrically neutral, with the charges of the electrons and negative ions being in balance with those of the positive ions. The charged particles exert great influence on the electrical properties in the atmosphere and on radio propagation through the plasma medium. It is therefore important to study the behaviour and effects of the ionosphere.

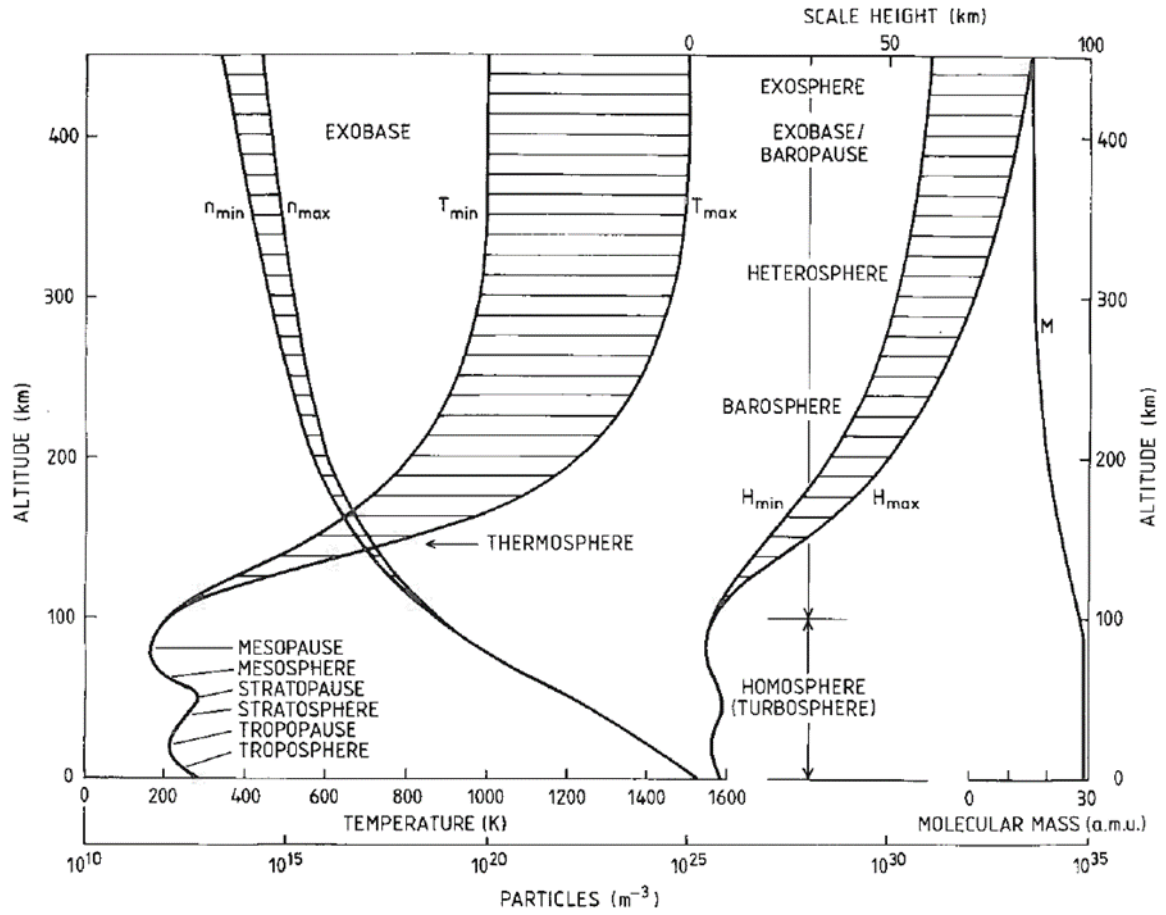

Figure 1 - Typical vertical profile of the neutral atmosphere for profiles showing particle density, temperature and scale height, including both maxima and minima of the profiles. The profile shows the split of homosphere and heterosphere on the right-hand side. (Brekke, 1997)

The exposure of humanity to the ionosphere, albeit without knowledge of what it was, began by experiencing coloured light moving across the night sky, commonly known as visual aurora. The aurora was observed far back in time and then underwent scientific study in the middle ages up to the present day. While early theories were incorrect, the interest and fascination in the aurora led to increased understanding of the features with, for example, British scientist Cavendish, measuring the height of the aurora (Cavendish, 1790) and, Birkeland explaining the nature of the phenomenon. (Birkeland, 1908)

The first suggestion of the ionosphere was made in the 19th century when Carl Gauss and Balfour Stewart thought about the existence of electrical currents in the atmosphere. This was hypothesised to account for the variations in the magnetic field seen at the time (Glassmeier and Tsurutani, 2014). The view was not widely accepted at the time and it wasn't until the experiment conducted by Marconi in 1901 that the existence of the ionosphere was established. His experiment transmitted a radio signal from Cornwall that was received at Newfoundland, and the wave had deflected around the surface of the Earth, greater than what could be attributed to diffraction. Due to this experiment, suggestions by Kennelly and Heaviside put forward the idea that due to the Earth's curvature, the signal must have been reflected by an ionised layer. The layer they proposed was known as the Kennelly-Heaviside layer. In the 1920s work had begun to prove the existence of the Kennelly-Heaviside layer, and the experimental evidence was provided by Appleton and Barnett in 1925. What they also managed to achieve was the discovery of a second layer at a higher altitude (Appleton and Barnett, 1925). This layer, for the time being, was known as the 'Appleton layer' but in the late 1920's after the ionised layers began to be called ionosphere on a regular basis, the Appleton layer and the Kennelly-Heaviside layer were changed to use the labels E and F regions. It was in 1926 that R. Watson-Watt proposed the term ionosphere in a letter to the UK Radio Research Board and three years later, the term was being used in literature.

Currently, a large amount of geophysical data from ground-based instruments and an array of satellites contribute to the advancement of knowledge and understanding of the ionosphere to the point that theoretical models can be used to explain and reproduce the terrestrial ionosphere. This is not to say that a complete understanding of the ionised region

has been achieved, but now further study into the details of the ionosphere can be defined clearly and tackled.

2.2 Vertical Profile of the Mid-Latitude Ionosphere

Historically, the ionosphere was considered to compromise several distinct layers, some of which have been already mentioned. With increased understanding the ionosphere is now considered a continuum with identified regions, including the E region and the F region. The F-region itself is split up into the F1 region and the F2 region, which will be explained shortly. Finally, there is the D region, at altitudes below the E region. A vertical profile showing the different regions, with respect to day and night and solar activity is shown in Figure 2.

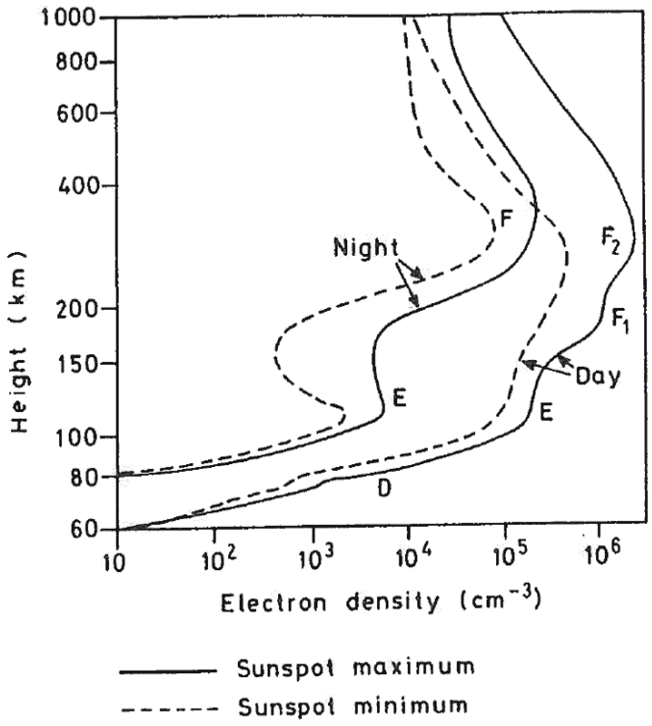

Figure 2 - Typical vertical profiles of the ionosphere with electron density along the x-axis and height on the y-axis. The profiles are shown for day and night regimes, with the dashed traces showing the profiles during sunspot minimum and solid lines for sunspot maximum. (Hargreaves, 1992)

The D region, shown in Figure 2, occurs during the daytime. It is in the altitudinal range of 60 to 90 km. Radiation from the Sun sustains this region and during the night time its thickness reduces significantly when the ionisation decreases rapidly with the source being removed. This region affects radio communications, with it attenuating the signals as they pass through. The level of attenuation, and therefore signal loss, is dependent on a number of factors; the level of ionisation, the frequency of the signal and the number of ionised gas molecules present. (Brekke, 1997)

The E region is dominated by molecular ions such as NO^+ and O_2^+. It is located at an altitude between 100 and 125 km, where the density of the neutral atmosphere is less compared to the D region. In this region radio communication signals are more likely to be refracted instead of attenuated, and in the case of high frequency (HF) signals, ranging between 3-30 MHz, the refraction is great enough for oblique signals to appear as being reflected by the region. As the frequency of the signal increases, the refraction of the wave decreases until a frequency is reached where the radio signal can pass through the E region. The E region occurs predominantly during the daytime, with the solar radiation being the primary source of ionisation. At night, as in the case of the D region, this layer weakens because the primary source of ionisation, is no longer present, like the D region.

The F region is often split into two different layers. The F1 region, typically found between 150-200 km, is the lower part of the F region. It is only present in the daytime and generally only exists in summer. It is dominated by molecular ions NO^+ and O_2^+ like the E region. This region is also governed by photoionisation so when the night arrives, the region vanishes. The F2 region at higher altitudes is also strongly influenced by photoionisation and is the region that exhibits the most ionisation produced by solar UV radiation. However, in this region

transport processes become more important, compared to the other regions, and are present throughout the day. This region varies throughout the day. The maximum frequency that can be reflected from an ionospheric region, known as the critical frequency, would depend on the maximum electron density at the time of reflection. The electron density of the F2 region reaches its maximum value at a peak altitude between 200 – 400 km however, the altitude varies with latitude, solar activity, time and other circumstances such as geomagnetic activity. The primary ion dominating this region is atomic oxygen O^+, rather than the molecular ions dominating the other regions. This region is the main region associated with HF wave propagation as signals in the HF range of the radio spectrum are refracted after reaching the F region back towards the surface, enabling worldwide radio communications to be established.

Above the F2 region is firstly the topside ionosphere, where O^+ is the dominant ion, the same as the F region. It can extend from about 500 km up to a few thousand km, with this upper extreme dependent on the transition from O^+ ions dominating the ionosphere to H^+ ions (Brekke, 1997). The region, once the transition from O^+ to H^+ occurs, is called the protonosphere (Schunk and Nagy, 2000). The transition altitude between the topside ionosphere and the protonosphere can vary due to O^+ to H^+ densities experiencing variability. During the daytime O^+ density is high from photoionisation with atomic oxygen. In the evening the O^+ density decays, leading to H^+ ions to charge exchange with atomic Oxygen to produce more O^+ ions. This helps maintain the F2 region at night.

2.3 Plasma production, loss and transport in the mid-latitude ionosphere

Energy from solar radiation is responsible for the ionisation of neutral atmospheric species, and hence the ionosphere. Once the ionisation is formed, the ions and electrons tend to recombine. The ionisation is also affected by transport processes. The overall rate of electron density increase per unit volume may be expressed by the continuity equation:

$$\frac{\partial N}{\partial t} = q - L - \nabla \cdot (N\boldsymbol{v}). \qquad \textbf{[Equation 1]}$$

In the equation above N is the electron density (that is the number of electrons per unit volume), q is the production rate of the electrons per unit volume, L is the loss rate of the electrons per unit volume, and $\nabla \cdot (N\boldsymbol{v})$ is the loss of electrons per unit volume by transport with $\boldsymbol{v}$ representing the mean drift velocity of the electrons.

2.3.1 Ionisation Production

The production rate of electrons per unit volume, q, in the continuity equation can be expressed as a product of four terms: I, the intensity of the ionising radiation, n the concentration of neutral molecules or atoms, σ the absorption cross-section, which gives a measure of the amount of radiation that is absorbed and η the ionisation efficiency as not all the energy absorbed will go into the process of ionisation. The ionisation production rate, described as the Chapman production function, can thus be written as:

$$q = \eta\sigma n I. \qquad \textbf{[Equation 2]}$$

The formula was developed by S. Chapman in 1931 and the derivation makes some assumptions: the atmosphere is composed of a single species, the atmosphere is plane stratified, meaning there are no horizontal variations, the solar radiation absorbed is in proportion to the concentration of the atoms and molecules and that the absorption coefficient associated with this is constant. The normalised version of the Chapman production function seen in Equation 2 is more commonly used:

$$q = q_{m0} e^{(1-z-\sec(\chi)*e^{-z})}, \qquad \textbf{[Equation 3]}$$

where *z* is the reduced height of a neutral gas atom or molecule, defined as the difference between the height of the level of interest and the height of maximum production divided by the scale height. The scale height is defined here as the distance over which the pressure of the atmosphere decreases by a factor of 1/e (Brekke, 1997). The height of maximum production is determined at the point where the Sun is considered to be overhead, so where the solar zenith angle, χ, is 0°. The term q_{m0} is the production rate at this height of maximum production, when χ = 0°.

The Chapman production function is established as a fundamental parameter for the theory of ionospheric production by absorption of incoming solar radiation and provides a starting point to interpret more complex ionospheric observations.

2.3.2 Ionisation Loss Processes

In the continuity equation, the loss rate for electrons per unit volume is represented by two terms, one for the recombination of electrons and ions, and the other related to transport of

plasma. For the former two types of recombination processes occur. For the first, it is assumed that there are no negative ions present in the ionosphere, meaning electrons recombine directly with positive ions: $X^+ + e^- \rightarrow X + h\nu$, where X is an atom, e^- is the electron and $h\nu$ is the energy of the generated photon. This equation is for Radiative recombination. There is also another process, known as dissociative recombination, where a positive molecular ion recombines with an electron and dissociates into two neutral atoms: $MX^+ + e^- \rightarrow M + X$, where M and X are neutral atoms. The rate of electron loss given by radiative recombination, for example, is:

$$L = \alpha[X^+]N = \alpha N^2, \qquad \textbf{[Equation 4]}$$

where N is the electron density, which is equal to the ion density $[X^+]$ and α is the recombination coefficient.

In this case, at equilibrium, and in the absence of transport, the loss rate, L, equals the production rate, q. Using the Chapman production function given in Equation 2 it can be shown that the peak of the ionisation layer can be found to vary with $cos^{\frac{1}{2}}\chi$. A layer that exhibits these properties is known as the α-Chapman layer.

The second type of electron loss process occurs by the attachment of free electrons to neutral molecules to form negative ions simply given by the chemical reaction: $MX + e \rightarrow MX^-$, where MX is the neutral molecule. This type of recombination process is more dominant type at higher levels of the ionosphere. The rate of electron loss for this process is given by:

$$L = \beta N, \qquad \textbf{[Equation 5]}$$

where β is the attachment coefficient. The loss rate has become linear because the neutral species is assumed to be more numerous compared to the electrons and removing some neutral species has no significant impact on the total remaining.

At equilibrium where the production rate is equal to the loss rate, the peak electron density of the layer now varies with cos χ. This layer is known as the β-Chapman layer. β varies with height as it depends on the concentration of the neutral species. Electron loss in the F-region occurs via a two-stage chemical reaction process:

$$X^+ + M_2 \rightarrow MX^+ + M, \qquad \textbf{[Equation 6a]}$$

$$MX^+ + e^- \rightarrow M + X, \qquad \textbf{[Equation 6b]}$$

where M and M_2 is a neutral atom and molecule respectively and X^+ is an ion. The first step moves the positive charge from the ion to the molecule creating a charged molecule. The second step dissociates the charged molecule through recombination with an electron. The details of the process are given in Hargreaves (1992). At low altitudes the attachment coefficient from equation 5, β, is large, meaning the ions are rapidly converted to charged molecules, as seen in Equation 6a. This leads to the overall loss rate at low altitudes to be governed by an α-type process. At higher altitudes β is small, so the conversion from ions to charged molecules becomes much slower. With this, at higher altitudes the loss rate becomes linear with the electron density, as shown in Equation 5 and 6b, leading to a β-type process.

Below 150 km in the E region, molecular ions are the dominant species, which relate to the α process in Equation 6a. Above this height atomic ions will become more abundant and begin to dominate at F region heights, leading to loss rates governed by the β process in Equation

6b. This shows as you increase in altitude in the ionosphere, the reaction type changes from an α-type process to a β-type process. (Brekke, 1997)

The other term for the loss of electrons in the continuity equation is that describing the loss by transport of the plasma.

Assuming the production and recombination loss functions to be negligible compared to the movement effects, considering the transport term only, the continuity equation simplifies to:

$$\frac{\partial N}{\partial t} = -\nabla \cdot (N\boldsymbol{v}), \qquad \textbf{[Equation 7]}$$

where $\boldsymbol{v}$ is the drift velocity of the plasma.

Taking into account the vertical movement only:

$$\frac{\partial N}{\partial t} = -\frac{\partial (N v_u)}{\partial h}, \qquad \textbf{[Equation 8]}$$

where v_u is the vertical drift speed and *h* is the height. If this drift is related to diffusion the vertical drift speed can be related to the diffusion coefficient (Hargreaves, 1992):

$$v_u = -\frac{D}{N}\frac{\partial N}{\partial h}. \qquad \textbf{[Equation 9]}$$

The diffusion coefficient, D, is derived by equating the pressure gradient in a gas to a drag force due to collisions. In the simplest case of a minority gas diffusing through a stationary majority gas the diffusion coefficient is given as D = kT/mϑ where k is the Boltzmann constant, T is the temperature, m is the mass of the gas molecule and ϑ is the collision frequency.

For this case the situation is the minority gas being a plasma composed of ions and electrons and a majority gas being the neutral air. For the drift in the vertical direction, gravity acts on each of the particles in the plasma. The vertical drift is given by:

$$-\frac{dP}{dh} = Nmg + N\vartheta m v_u. \qquad \textbf{[Equation 10a]}$$

Using, the relation P = NkT, the equation given for the diffusion coefficient and the scale height of the minority gas H_N = kT/mg, equation 10a is rearranged to:

$$Nv_u = -D\left(\frac{dN}{dh} + \frac{N}{H_N}\right). \qquad \textbf{[Equation 10b]}$$

Substituting this equation into the continuity equation gives:

$$\frac{\partial N}{\partial t} = \frac{\partial}{\partial h}\left[D\left(\frac{dN}{dh} + \frac{N}{H_N}\right)\right]. \qquad \textbf{[Equation 11]}$$

This equation is important for the upper F region and protonosphere. As shown earlier this is because the ion production and recombination are small.

A plasma is made up of two minority species, ions and electrons. The ions, being the heavier of the two species, move away from the electrons. This separation of the two oppositely charged species produces an electric field and a restoring force on both the electron and ion. The variables in Equation 10a, including the pressure, mass, collision frequency and temperature, is dependent on whether the species is an electron or ion.

If the density and vertical drift speed of the ions and electrons are the same, the temperature, T, is replaced by the addition of the electron and ion temperatures, $(T_e + T_i)$, and knowing

that the mass of an electron is much smaller than the mass of the ion, equation 10b can be replaced by the following equation:

$$Nv_u = -D_P\left(\frac{dN}{dh} + \frac{N}{H_P}\right), \qquad \textbf{[Equation 12]}$$

where the plasma diffusion coefficient is defined as:

$$D_p = \frac{k(T_e + T_i)}{m_i \vartheta_i}, \qquad \textbf{[Equation 13]}$$

and the plasma scale height:

$$H_p = \frac{k(T_e + T_i)}{m_i g}, \qquad \textbf{[Equation 14]}$$

where *k* is the Boltzmann constant, T_e and T_i are the electron and ion temperatures, m_i is the mass of the ion, ϑ_i is the collision frequency of ions and g is the gravitational acceleration.

Plasma diffusion is more important in the topside F region and protonosphere, which is where the electron temperature is said to usually exceed the ion temperature (Köhnlein, W., 1986). The diffusion coefficient is shown in Equation 13 to increase with altitude, as the collision frequency decreases. With diffusion being of more importance at these higher altitudes, photoionisation becomes less important. During the night when solar ionisation is no longer present, the ionisation diffuses from the topside regions down to populate the lower ionosphere.

2.4 Solar Wind – Magnetosphere – Ionosphere coupling

Space weather is currently a key topic of research in the community due to the impacts it could have on humanity if not accounted for correctly. Many systems use radio signals, which traverse the ionosphere, to communicate with systems such as spacecraft and aircraft. Space weather is a phenomenon that is influenced by the solar wind and the interplanetary magnetic field and has a large impact on the state of the ionosphere. This section describes the coupling between the solar wind, magnetosphere and ionosphere to show the importance of this connection, and the impact of the phenomena associated with space weather can have on the ionosphere.

2.4.1 Solar wind

The solar wind is a continuous stream of matter extended from the Sun. It was proven to exist by E. N. Parker in 1958 who showed that the solar corona is not in hydrostatic equilibrium and expands continuously (Parker, 1958a). The velocities deduced for the solar wind by Parker were between 260 and 1160 kms^{-1} for coronal temperatures between $5x10^5$ K and $4x10^6$ K (Parker, 1961a; Parker, 1961b). It was found, in 1958, that the corona streamed outwards at subsonic speeds to form the solar wind and after a certain point it reached supersonic speeds. The primary ion species of the solar wind are protons with a small minority of alpha particles, with a similar number of electrons for net neutrality. This is the plasma medium by which the effects of the Sun's activity are transported to the Earth's vicinity, making it important for solar-terrestrial relations.

This solar wind carries with it a frozen-in magnetic field, the interplanetary magnetic field, (IMF), where the plasma governs the motion of the field. While the solar wind is extended radially from the Sun, the solar rotation gives the magnetic field a spiral form, known as the Parker spiral (Parker, 1958a). The solar wind experiences variability in plasma density and speed with typical values around 400 kms^{-1} for the velocity and the densities of the protons are typically around 6-8 cm^{-3} in the interplanetary space near Earth (Hundhausen et al., 1970). The IMF experiences variability in magnitude and direction. The IMF is defined as a field vector, **B**, that has three directional components in a Cartesian co-ordinate system defined as B_x, B_y, and B_z, so that $B = \sqrt{B_x^2 + B_y^2 + B_z^2}$ (Brekke, 1997). Two of the vector components, B_x and B_y, are parallel to the ecliptic plane and B_z is perpendicular to the ecliptic. A diagram showing their orientations can be seen in Figure 3. The solar wind and IMF will be discussed later in more detail where attention will be drawn to their effects on the terrestrial ionosphere.

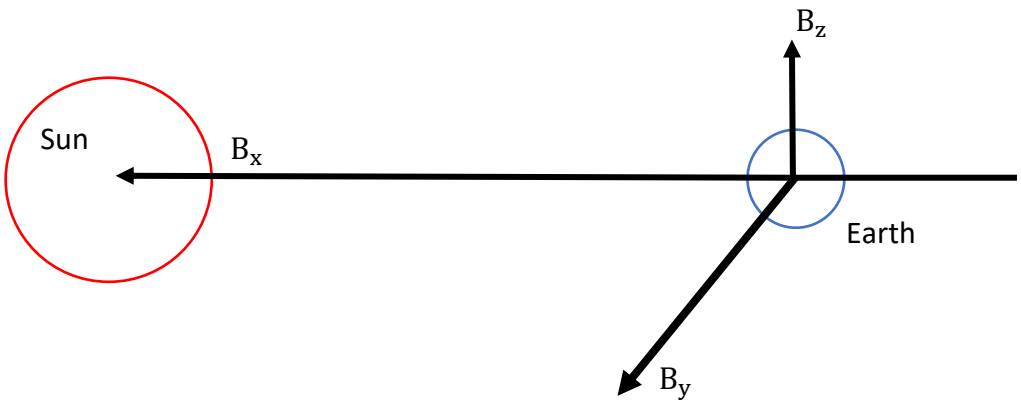

Figure 3 – A diagram showing the configuration of the magnetic field vectors B_x, B_y, and B_z.

2.4.2 Magnetosphere

The Earth has a magnetic field which, within a few earth radii, has a dipolar approximation roughly equivalent to the magnetic field of a powerful bar magnet. The magnetic field is represented as a three-dimensional vector using the geomagnetic co-ordinate system, hence the term geomagnetic field. (Brekke, 1997) The angle of magnetic north relative to geographic (true) north is known as the Declination (D), which varies with location and time. The angle the magnetic field makes with the horizontal plane is known as the Inclination (I) and finally, the intensity of the field in the horizontal plane is given by the H component. At distances of a few earth radii, the geomagnetic field is distorted by the solar wind.

The magnetosphere forms as a result of the solar wind not able to penetrate the geomagnetic field, with the solar wind plasma and the IMF being swept around the Earth's magnetic field. However, the geomagnetic field is not unaffected by the impact of the solar wind, being compressed on the dayside and extended on the nightside to form a feature known as the magnetotail. From the Earth to the "nose" of the magnetosphere is approximately 10 R_E, where 1 R_E is approximately 6400 km. The magnetotail exceeds 100-200 R_E from the Earth but has been detected beyond 1000 R_E (Hargreaves, 1992). A cross-section of the magnetosphere can be seen in Figure 4 with the various boundaries and features labelled.

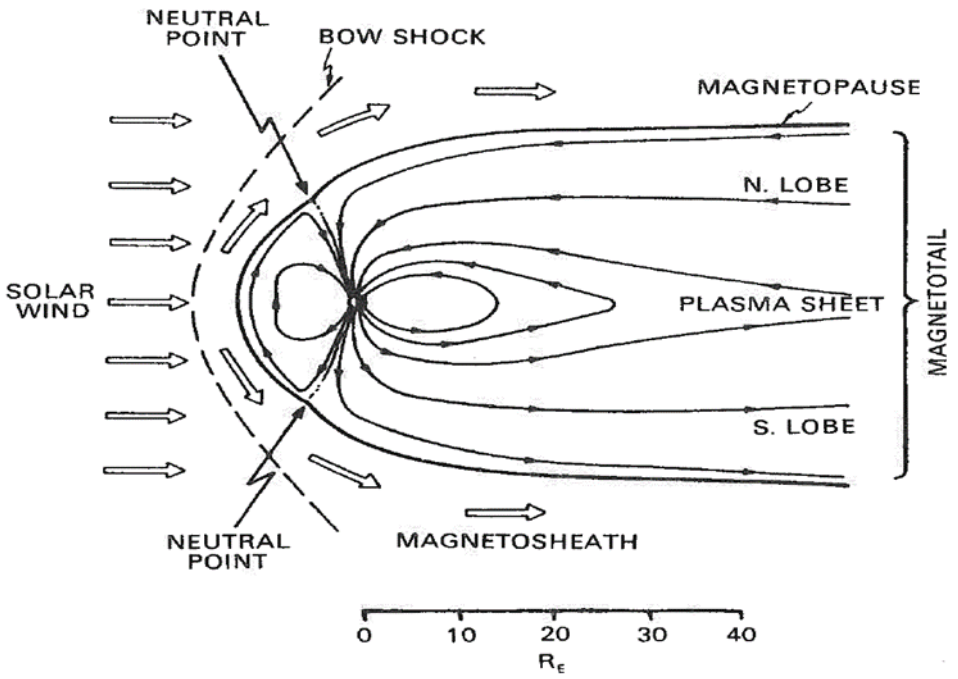

Figure 4 - A cross-section of the magnetosphere. Each region is labelled to correspond to the regions of the magnetosphere. (Hargreaves, 1992)

The magnetopause is a boundary between the solar wind and the geomagnetic field which is deduced from the pressure balance across the boundary. The boundary occurs where the total rate of change of momentum per unit area equals the magnetic pressure from the geomagnetic field. This boundary has a thickness that can range between 400 km and 1000 km, with larger thicknesses occasionally observed. (Berchem and Russell, 1982)

The bow shock of the magnetosphere is the region where the solar wind approaches the Earth's magnetopause, and the bulk velocity of the plasma drops from supersonic speeds to sub-sonic speeds, causing a shockwave. When crossing the shock, the slowed plasma has a corresponding loss of kinetic energy which is then dissipated as thermal energy. This increases the temperature of the plasma in the region called the magnetosheath. Typical densities of the plasma in the magnetosheath are approximately 6 cm^{-3}.

On the nightside, on the far side of the Earth orbit, the magnetosphere contains two lobes, with the field in the northern lobe pointing towards the Earth, and in the southern lobe pointing away. In the central plane of the magnetotail, where the magnetic field reverses in direction, there is the plasma sheet as shown in Figure 4. This sheet lies beyond the plasmasphere (section 2.4.3) where the electron density is lower, and the temperature is higher. The sheet follows the magnetic field lines down latitudes near the auroral zone, which can be seen in Figure 4.

2.4.3 Plasmasphere

The plasmasphere is a torus-shaped region that typically extends to about 4 R_E at mid to equatorial latitudes that contains dense cold plasma (Figure 5) and co-rotates with the Earth. The electron density at 1000 km, in the upper ionosphere, is approximately 10^4 - 10^5 cm^{-3}, and reduces with radial distance (Hargreaves, 1992). Inside the plasmasphere, the electron density is around 10^3 cm^{-3} at between 2 and 4 Earth radii. At approximately 4 R_E, there is a sharp drop in electron density (Chappell, 1974). This defines the boundary of the plasmasphere, the plasmapause. This sharp drop equates to electron density values beyond the plasmapause of approximately 10^0 - 10^1 cm^{-3}.

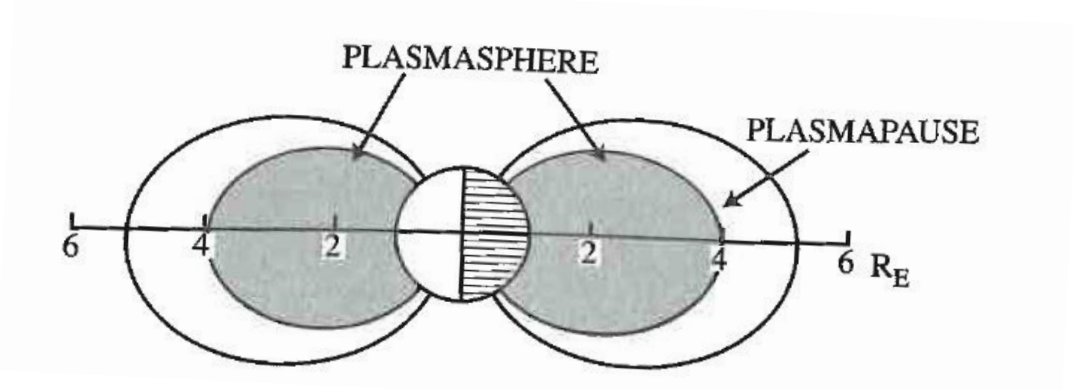

Figure 5 - Schematic illustration of the plasmasphere and the plasmapause. (Chappell, 1974)

The location of the plasmapause varies with geomagnetic activity. The feature has been related to the main ionospheric trough, a feature in the ionosphere that will be described in further detail in Chapter 5.

2.4.4 Magnetic reconnection – Solar wind and Magnetosphere coupling

Although the interplanetary magnetic field in the solar wind sweeps over the geomagnetic field, interaction does occur between the two fields. The principle process associated with this coupling of the solar wind and the magnetosphere is magnetic reconnection. When the IMF that is frozen into the solar wind encounters the geomagnetic field the two may interact. The interaction or reconnection depends on the direction of the IMF and its alignment with the geomagnetic field. If the direction of the IMF has a component that is anti-parallel to the Earth's geomagnetic field, i.e. the z-component of the IMF is negative, dayside reconnection occurs at the equatorial magnetopause. This is illustrated in Figure 6.

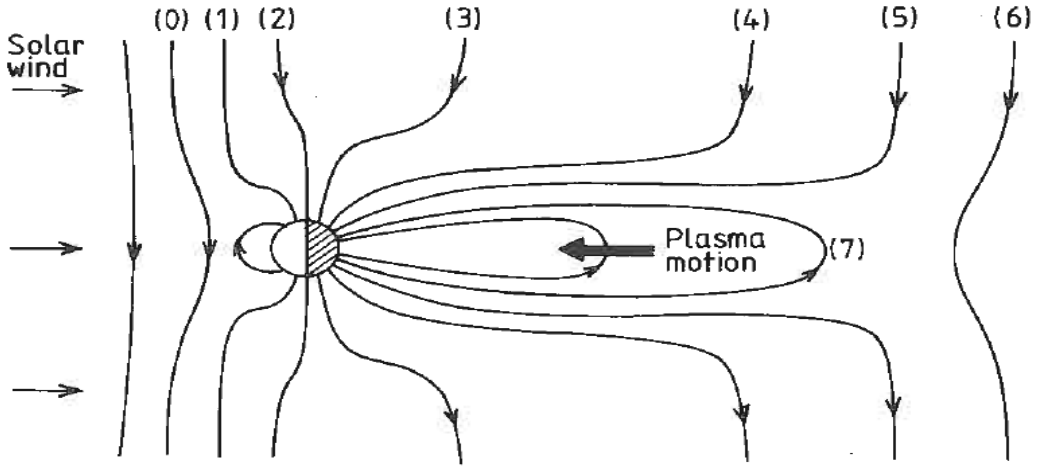

Figure 6 - The process of magnetic reconnection. The solar wind encounters the magnetosphere with the IMF southward, negative Bz component, at (0). The IMF encounters the geomagnetic field, in the opposite direction, and reconnects between (0) and (1). Between (1) and (5) the reconnected field lines are swept over the Earth by the solar wind and form the magneto tail. Between (5) and (6) there is reconnection between the open field lines that have been sweeping between (1) and (5) at (7). This causes the field lines to become closed. (Brekke, 1997)

The geomagnetic field lines that were closed become connected to the IMF field lines of the solar wind and are opened with direct contact between the magnetosphere and the solar wind. The field lines move in the anti-sunward direction and sweep over the Earth. On the night side magnetotail reconnection occurs where the anti-parallel magnetic field lines in the lobes reconnect. The magnetic field is closed and returns earthward (Figure 6).

Under conditions of positive IMF B_z, another type of reconnection can occur, where the northward IMF, positive B_z, reconnects with the magnetic field in the lobes of the magnetotail. (Lester and Cowley, 2000)

2.4.5 Magnetosphere-Ionosphere coupling processes

The details of the underlying theory are still not fully understood, but in essence an effective dawn-to-dusk electric field in the Earth's reference frame causes anti-sunward motion of the solar wind. Under conditions of negative IMF B_z, the solar wind interacts with the geomagnetic field. The associated electric potential difference maps down the geomagnetic field to ionospheric altitudes in the polar region. The resulting dawn-to-dusk electric field in the polar cap ionosphere then drives the plasma anti-sunward over the polar cap by the $\mathbf{E} \times \mathbf{B}$ drift (Schunk and Nagy, 2000). The magnetic field lines mapping from the polar cap ionosphere are open. These must be opened as they are drawn into the polar cap and then closed on the nightside.

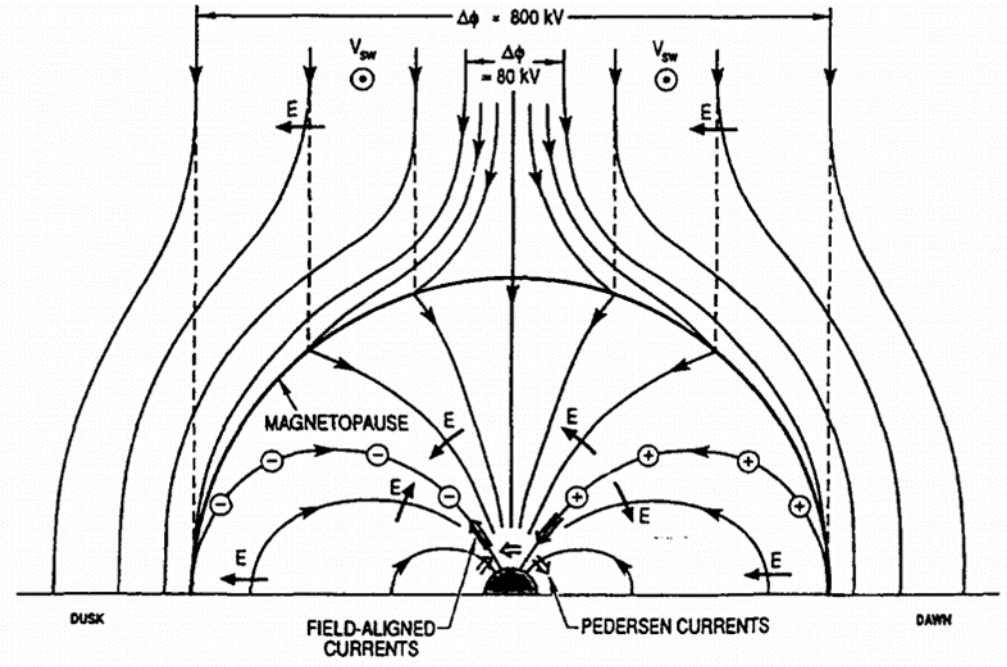

Figure 7 - A diagram showing the electric fields, the magnetic fields and currents in the vicinity of the Earth. The view is from the magnetotail. The solar wind flows toward the observer. (Lyons, 1992)

Figure 7 shows a schematic of the electric and magnetic fields in the coupling process. The view shows the upper hemisphere and upper magnetospheric lobe as observed from the magnetotail. The electric potential difference in Figure 7, $\Delta\phi = 80$ kV, maps down the open field lines to the polar region where the field lines move anti-sunward towards the observer by the $\mathbf{E} \times \mathbf{B}$ drift. Under the assumption that the solar wind flow does not penetrate onto closed magnetic field lines, the electric field maps only onto the region of open polar cap magnetic field, thus the open-closed boundary becomes charged negatively on the duskside, and positive on the dawnside. The + and - show the charges between the open and closed magnetic field lines (Lyons, 1992). Ionospheric plasma on the closed field lines just beyond the open-closed boundary also undergoes an $\mathbf{E} \times \mathbf{B}$ drift, but in a sunward direction, away from the observer in this case. The complete system also encompasses field-aligned currents along the magnetic field known as Birkeland currents. Current closure occurs in the

ionosphere by so-called Pedersen currents. The studies in this thesis do not consider these currents so these will not be discussed in further detail.

2.5 High Latitude Ionospheric Convection

As stated in the previous section, the potential difference mapped down from the magnetosphere to ionospheric altitudes give rise to electric fields that cause **E** × **B** drifts of the plasma. Under conditions of equatorial reconnection, the drift is anti-sunward across the polar cap from the dayside to the nightside. At the lower high-latitudes, the flow on closed magnetic field lines is sunward. This flow of the plasma forms a 2-cell pattern, with anti-sunward flow over the polar cap and sunward flow at latitudes equatorward of the polar cap. A schematic of the flows is shown in Figure 8. This displays a symmetric 2-cell pattern in a magnetic latitude – magnetic local time (MLT) coordinate system.

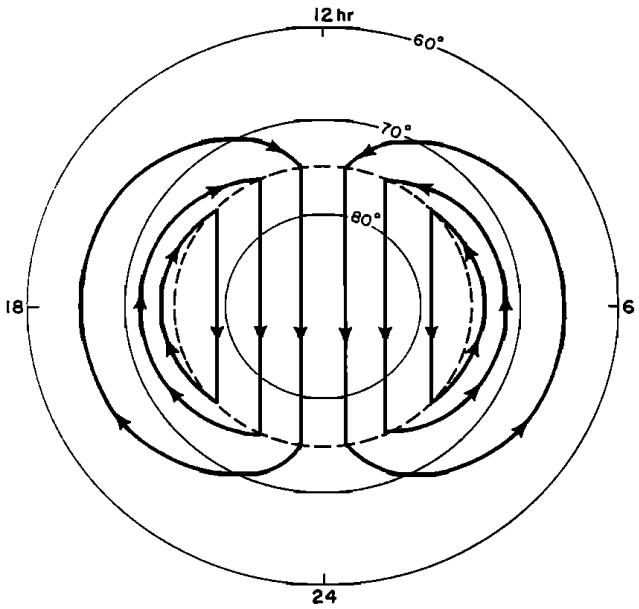

Figure 8 - High-latitude plasma convection pattern, exhibiting the two-cell structure, with the anti-sunward convection across the polar cap and sunward return flow at lower latitudes. The arrows indicate the direction of the plasma flow. (Spiro, 1978)

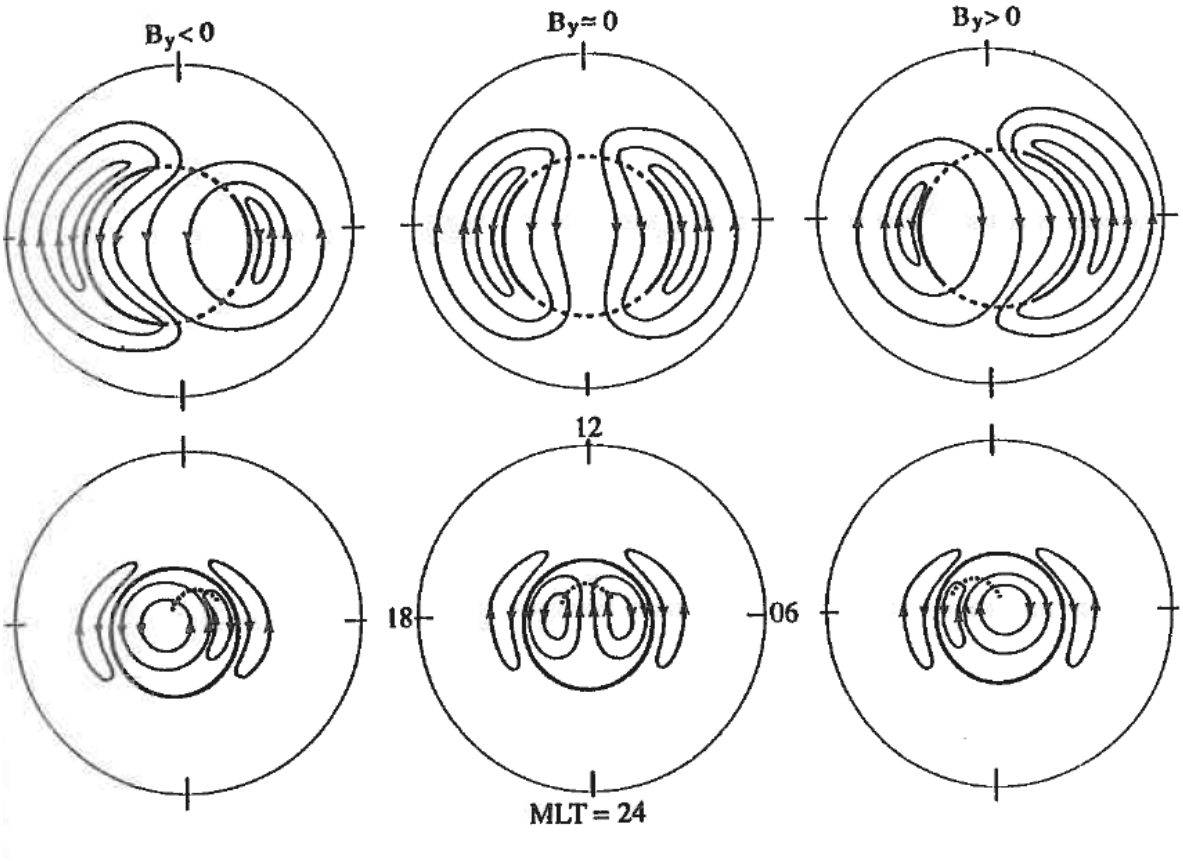

Figure 9 - Diagrams of the polar convection patterns, ordered by the effects of the direction of the IMF. The top row for B_z negative and the bottom row for B_z positive. The top row shows how the two-cell pattern adapts with differing B_Y component, showing which cell becomes dominant in each regime. The bottom row is more complicated as the two cell structure changes. In this case there tends to be a sunward flow in the polar cap. (Lester and Cowley, 2000)

The two-cell symmetric pattern described above is the simplest form for the convection. In reality, the IMF strongly influences the cell structure. The top panels in Figure 9 represent the cell structure when the IMF B_z component is negative with magnetic noon at the top of each panel and magnetic midnight at the bottom. The B_y component is negative for the left-hand panel, is approximately zero for the centre panel and is positive for the right-hand panel. The centre panel is akin to the symmetrical pattern previously described. However, the IMF B_y component alters the structures of the cell quite dramatically depending on the strength of its positivity or negativity. When the B_y component is negative, the dusk cell moves towards the dawn side in the noon sector, with the dayside open-closed field-line region moving to pre-noon hours. The centre circle represents the open-closed boundary and the dashed lines

map to the sites of magnetopause reconnection. The movements of the magnetopause reconnection sites and the open-closed boundary are due to a shifting in the reconnection region at the magnetopause, which is explained in more detail by Heelis (1984) and Lester and Cowley (2000).

The complexities that arise under conditions of B_z positive are shown in the second row in the figure. In this case, the reconnection occurs in the high-latitude magnetopause lobe with the resulting convection pattern showing an initial sunward flow in the polar cap following reconnection. A detailed description of these can be found in Lester and Cowley (2000).

2.6 Ionospheric Interaction with Neutral Wind

2.6.1 Theory of interactions

Pressure gradients in the atmosphere, induced by diurnal heating and cooling, are known to drive and cause the neutral air to produce winds (Brekke, 1997). The interaction then between this neutral wind and the charged particles in the ionosphere would be caused by collisions between the two (Cho and Yeh, 1970). This consideration is for the F region of the ionosphere.

The force on ions and electrons due to a neutral wind is given as:

$$F = m\vartheta U, \qquad \textbf{[Equation 15]}$$

where *U* is the wind velocity in neutral air, ϑ is the collision frequency between neutrals and charged particles and *m* is the mass of the charged particles.

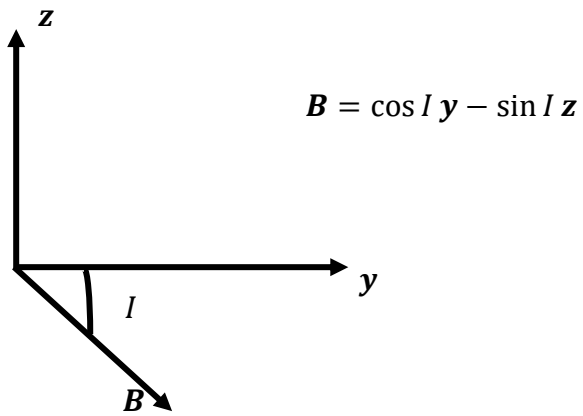

Figure 10 – Lifting effect of the neutral wind in the presence of a magnetic field on the ions and electrons in the ionosphere (Hargreaves, 1992). B shows the direction of the magnetic field.

In a general case, the neutral-air wind blows in the horizontal plane where the ionosphere is relatively uniform. For simplicity is assumed to be in the magnetic meridian. The component of U along the magnetic field is $U_{II} = U \cos I$, where *I* is the magnetic dip angle. The plasma moves in the same way along the magnetic field. The effect of this field aligned neutral wind drift, U_{II}, is to lift or depress the layer. This effect depends on the vertical component of the neutral wind drift, $v_u = U_{II} \sin I = \frac{1}{2} U \sin 2I$. The effect of this drift is greatest where the magnetic dip angle, I, is at 45°.

Under conditions of equilibrium ($\frac{dN}{dt}$ = 0), using equation 9 and 11, the drift, v_u, due to diffusion is approximately $\frac{D}{H_N}$. The addition of the vertical drift due to the wind in the neutral air changes this outlook by adding v_u to the approximation giving $\frac{D}{H_N} + v_u$. The effects of diffusion become more important in the topside ionosphere but to understand where the peak of the F2 region lies, both diffusion and β-type reactions are equally important.

The upper F2 region depends on a β-type process as shown in section (2.3.1). This would lead to an electron density increase with altitude and therefore cannot explain the F2 peak. Diffusion, however, can as the electron density decreases with height. The full process of

equating the characteristic times of the reaction and transport can be seen in Hargreaves, (1992). The outcome of this process gives:

$$\beta \sim \frac{D}{{H_N}^2}, \qquad \textbf{[Equation 16]}$$

where the H is now a typical scale height for the F2 region. Now introducing the vertical drift of the neutral wind:

$$\beta \sim \left(\frac{D}{{H_N}^2} + \frac{v_u}{H_N}\right), \qquad \textbf{[Equation 17]}$$

where v_u is the vertical drift.

With β varying with height as $e^{-\frac{h_m}{H_N}}$, where h_m is the F2 peak, the effect of the neutral wind on the F2 peak is given by:

$$\Delta h_m \sim \frac{v_u}{\beta}. \qquad \textbf{[Equation 18]}$$

This shows how the neutral wind drift acts to change the height of the peak of the F2 region and becomes useful in chapter 6.

2.6.2 Sporadic E

Sporadic E is a region of ionisation enhancements at the altitudes of the E-region in the ionosphere. As the name suggests these layers are sporadic, meaning the feature appears irregularly and are very unpredictable. Sporadic E has been observed from a multitude of differing instrumentation ranging from ground-based remote sensing to satellite sensors.

Sporadic E layers usually occur around 90-110 km in altitude with a very small thickness of up to 5 km (Wu et al., 2005). The extent of the feature in longitude can range from 10 km all the way to 1000 km. The feature may last for minutes or hours causing radio-signal interruption due to the enhanced electron densities.

An example of Sporadic E is shown in Figure 11. The Figure displays data from the Arecibo Incoherent Scatter Radar (ISR) at 18.3°N latitude and 66.75°W longitude. It shows the electron concentration measurements plotted against altitude over the local region of the ISR for 2nd September 1994. The enhanced electron concentration can be seen at 1900 onwards where there is an increased intensity is at an altitude of 100 km.

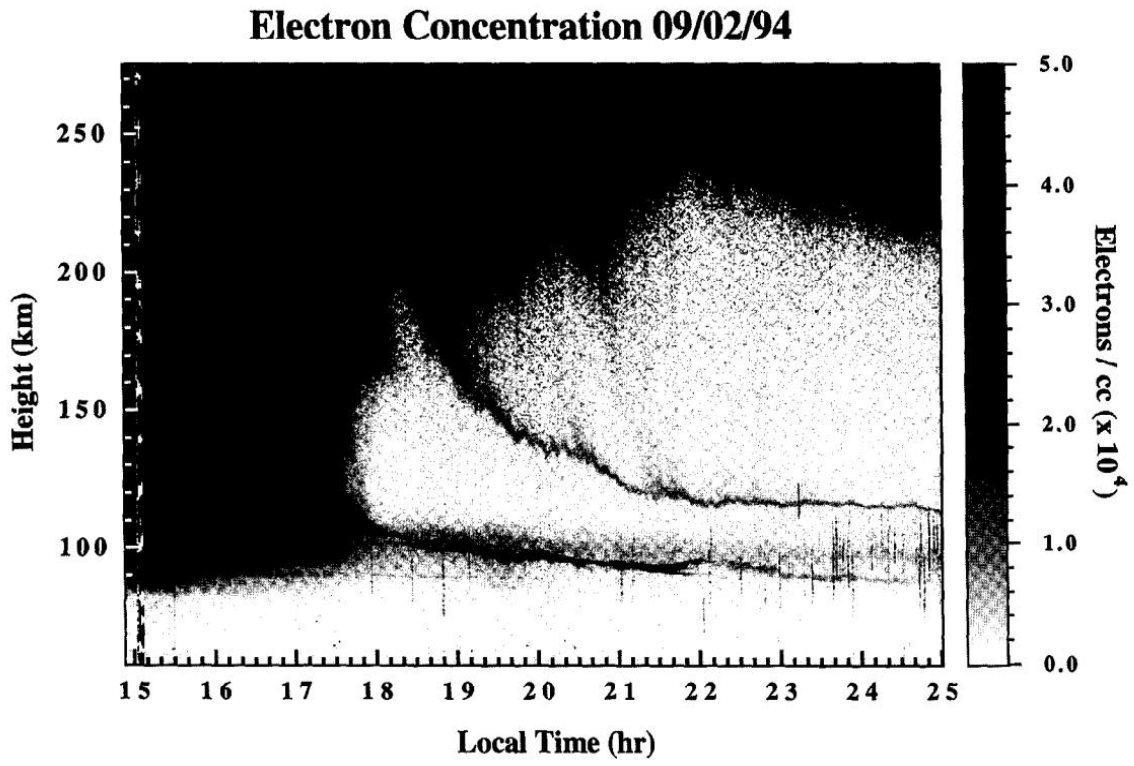

Figure 11 – Arecibo electron concentration measurements from 2nd September 1994. At 1900 an intensification on the layer at 110km is shown, intensifying this region into a Sporadic E event. (Mathews et al., 1997)

Using occultation data from Low Earth Orbiting (LEO) satellites (Wu et al., 2005) enabled the ability to measure the global distribution of Sporadic E, meaning the occurrence locations and rates of Sporadic E throughout a year. A considered complete study of the global distribution

of Sporadic E occurrence (Haldoupis, 2011) was made by Arras et al. (2008) using a large database of radio occultation data obtained with LEO satellites. Figure 12 shows the global distribution of Sporadic E occurrence from Arras et al. (2008) for all 4 seasons for the year between September 2006 to August 2007. The occurrence rate for each season is clearly visible, with low occurrences during the autumn and spring seasons. The largest occurrence rates occur during the Summer season for the northern hemisphere and looking at the winter season, there is a large occurrence for the southern hemisphere. This is due to it being summer for the southern hemisphere. The main conclusion from this is that Sporadic E largely occurs during the summer months of both the northern and southern hemisphere.

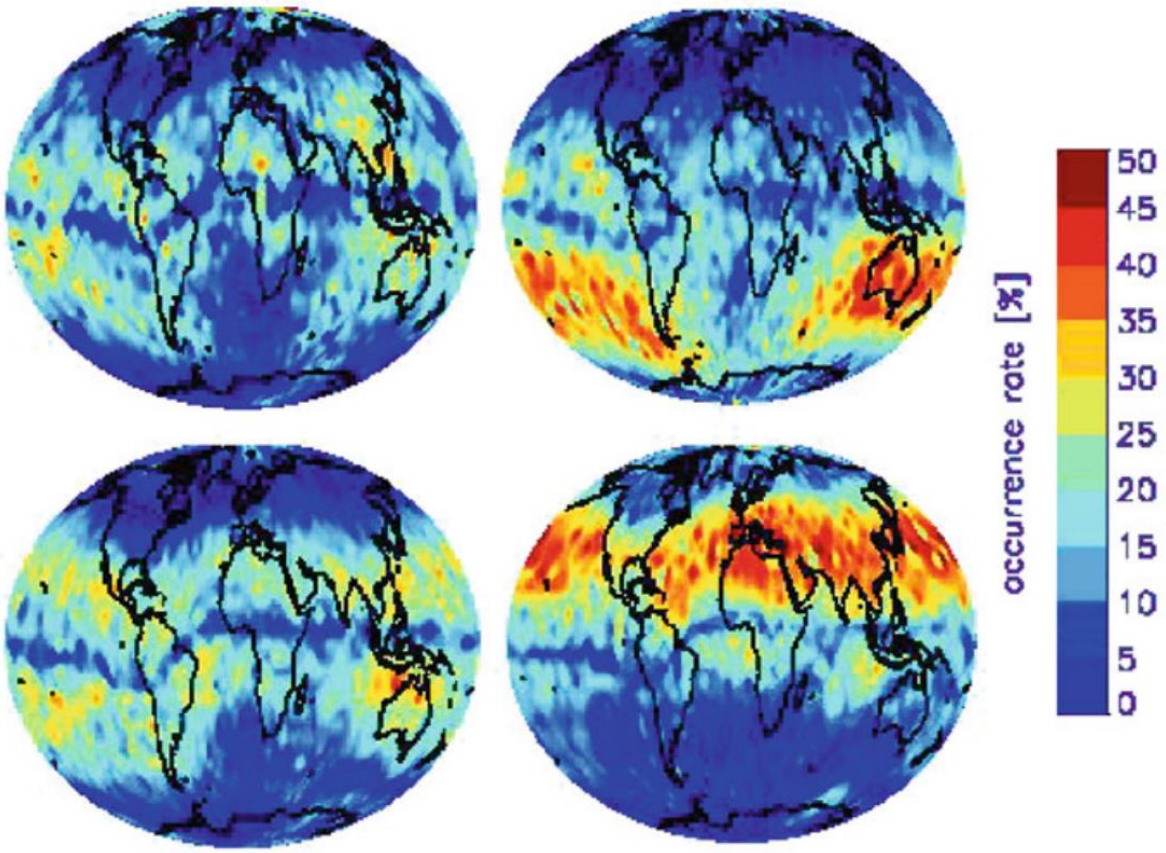

Figure 12 – Global distribution of Sporadic E occurrence during the four seasons of 1 year defined between September 2006 and August 2007. The four seasons, defined for the northern hemisphere, are autumn (top left), winter (top right), spring (bottom left), and summer (bottom right). These distributions are measured using radio occultation methods. (Arras et al., 2008)

The maximum occurrences during the summer are shown to occur at roughly between 10° and 60° geomagnetic latitude.

The cause of sporadic-E is said to be due to wind shears, a variation of the wind speed with height, which in the presence of a geomagnetic field will act to compress the ionisation. A graphical summary of the wind shear mechanism can be seen in Figure 13. Haldoupis (2011) provides an in-depth explanation of the wind shear theory.

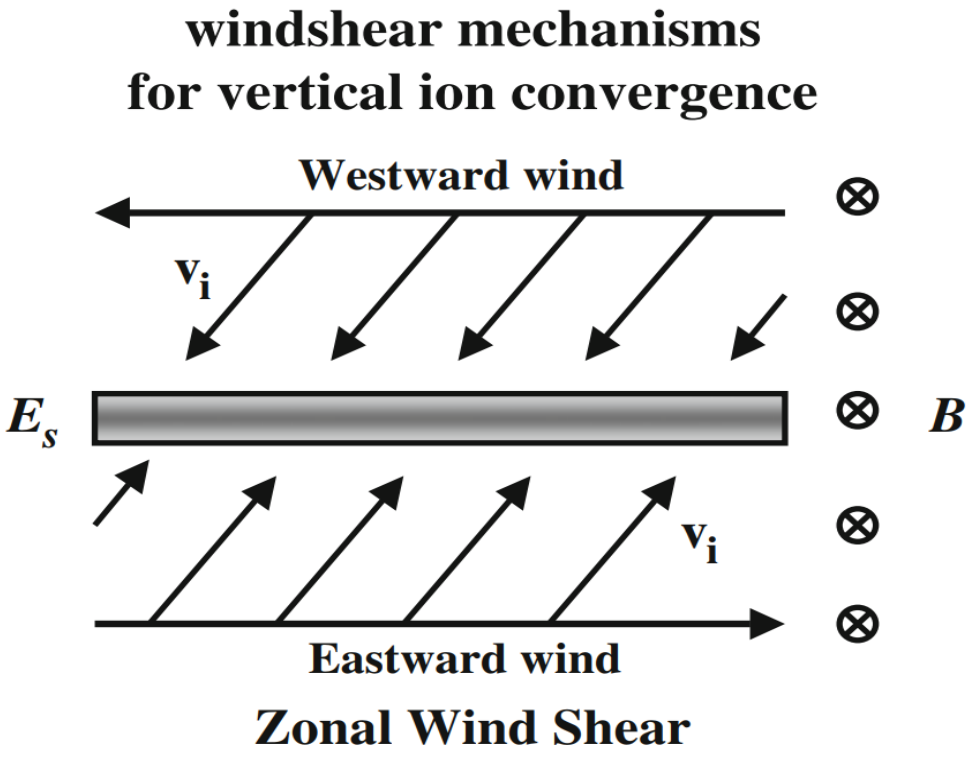

Figure 13 – Graphical representation of the wind shear mechanism for the formation of a Sporadic E layer. (Haldoupis, 2011)

2.7 Storms

2.7.1 Geomagnetic storms

A geomagnetic storm is a disturbance in the terrestrial magnetosphere resulting from processes caused by shock waves from the solar wind and/or interactions between the magnetic field carried by the solar wind and the terrestrial geomagnetic field, where energy

can be transferred into the magnetosphere. These interactions cause an increase in the movement of the plasma throughout the magnetosphere and increases in the electric currents of the magnetosphere and ionosphere. The Disturbance storm time (Dst) index is what is used to define a geomagnetic storm. The Dst index is derived from the effects of currents measured by ground-based magnetometers at low latitudes. The theory of the currents can be found in Hargreaves (1992). More detail will be discussed on the Dst index in section 4.5.3.

During a geomagnetic storm, a large sudden change in the dynamic pressure occurs in the solar wind, sometimes accompanied by a large negative B_z component in the IMF. There are multiple reasons for a large change in solar wind dynamic pressure such as Solar Flares and Coronal Mass Ejections (CMEs). More detailed descriptions on these features are given by Schunk and Nagy (2000).

The four phases of a geomagnetic storm as seen in the Dst index are the sudden storm commencement (SSC), the initial phase, the main phase and the recovery phase. The SSCs are produced by a sudden increase in the dynamic pressure of the solar wind that also have a negative Bz component in the IMF (Tsurutani et al., 1988, Curto et al., 2007). However, these SSCs were defined as an impulse-like disturbance of the magnetic field, and a storm would follow within 24 hours (Joselyn and Tsurutani, 1990). The initial, main and recovery phase of the storm are shown in Figure 14 using the moderate strength geomagnetic storm plot from Loewe and Prölss (1997).

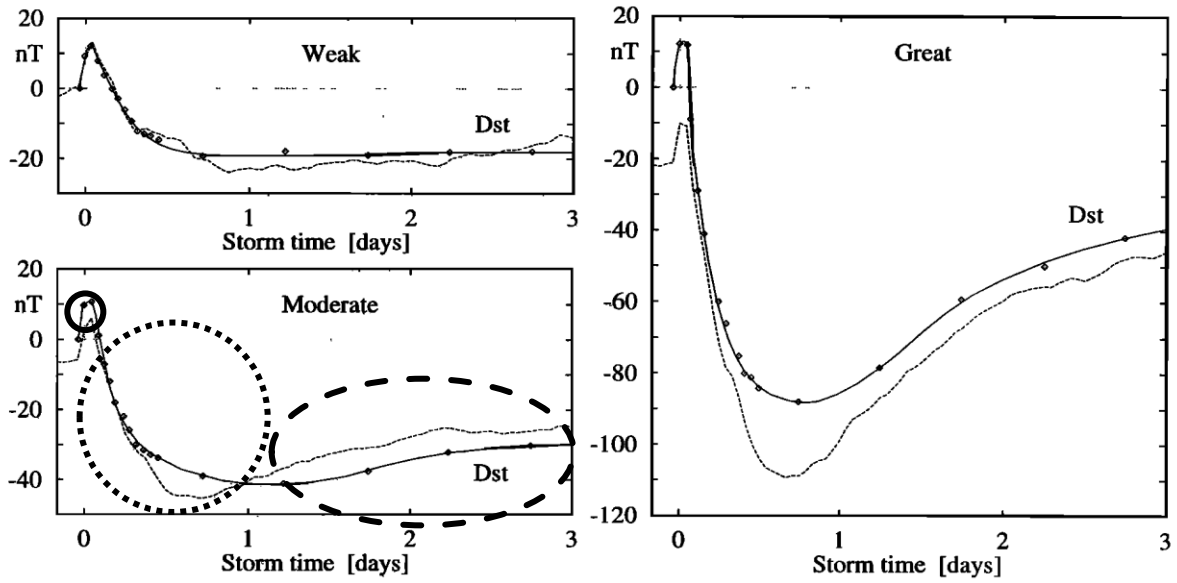

Figure 14 - Adapted Figure from Loewe and Prölss (1997) showing typical Dst index for geomagnetic storms. The three diagrams represent the first three days of weak (≤-30 nT), moderate (≤-50 nT) and great (≤-100 nT) geomagnetic storms. The solid circle represents the initial phase, dotted circle represents the main phase and the dashed oval represents the recovery phase. The Dst drop seen after the small increase, in each case, differs depending on the relative strength of the storm.

The initial phase of the storm is related to the compression of the geomagnetic field that is detectable from ground magnetometers. This compression comes from the arrival of the solar wind plasma impacting with the magnetosphere. The theory of this was originally suggested by Chapman and Ferraro (1931). The effect on the Dst is shown in Figure 14 as the solid black circle, where the increase above 0 nT occurs. This phase generally lasts only up to a few hours.

The main phase of the storm comes after the initial phase. After the increase in the magnetic field, which can be seen in the Dst index, a large decrease occurs that builds up to a maximum negative value for the storm. This is explained by on the arrival of the solar wind that has undergone a sudden increase in dynamic pressure and with a negative B_z component, magnetic reconnection can occur. Resulting from this, the solar wind energy can couple into the terrestrial magnetosphere. Convection resulting from this reconnection strengthens the

electric fields in the magnetotail. This enables particles from the plasma sheet to be transported into the inner magnetosphere, energising the particles. This is the main phase of the storm. More details on this process can be found in Cramer et al. (2013).

The recovery phase of the geomagnetic storm can last up to several days with the Dst index returning to pre-storm onset values. An example of how the index changes under weak, moderate and great storm strength conditions is shown in Figure 14, from Loewe and Prölss (1997). It shows a comparison between the morphology classification of geomagnetic storms originally produced by Sugiura and Chapman (1960).

The effects of the geomagnetic storms can be seen on the Earth in the form of the aurora where the stronger the storm is, the lower in latitude the aurora is visible on Earth. These storms can also have a huge impact on the terrestrial environment, for example disrupting electrical systems, communications and navigation systems.

There is also an effect on the plasmasphere during a geomagnetic storm. Due to the increased activity, plasma is lost or 'detached' in the outer plasmasphere due to the increased electric field and enhanced magnetospheric currents. The plasma is lost into the magnetosphere and eventually the solar wind. When the activity begins to decay, and the effects of the geomagnetic storm are over, the currents and electric field returns to their quiet state. The plasmasphere now begins to slowly refill from the ionosphere. This process takes place over several days.

2.7.2 Ionospheric storm

Ionospheric storms and geomagnetic storms have a resemblance to each other, but only superficially, as the mechanisms of the storms differ (Hargreaves, 1992). Ionospheric storms are characterised by variations in the density of the peak of the F region, the height of peak and variations in electron density in the region. They result from large energy inputs into the upper atmosphere, due to enhancements in electric fields, currents and energetic particle precipitation. A detailed review on the theories of ionospheric storms is given by Bounsanto (1999).

2.7.3 Substorms

A substorm, which in some cases is referred to as a magnetospheric substorm (Rostoker et al., 1980) or an auroral substorm (Brekke, 1997), is a disturbance in the magnetosphere that causes energy to be injected from the magnetosphere into the high-latitude ionosphere. These are different to the geomagnetic storms described in section 2.6.1 in many ways, one of the reasons being the latter take place over several days while substorms take place over a period of a few hours.

From Akasofu (1968) the auroral substorm can be divided into four phases: quiet phase, growth phase, expansion phase and recovery phase. A visual representation of these four phases can be seen in Figure 15.

The aurora has been mentioned in section 2.1 and it is this visual aurora that the effects of the substorm can be viewed through optical means. During the quiet phase, in Figure 15 at T

= 0, auroral activity is generally quiet and weak auroral arcs appear in the midnight region at a geomagnetic latitude of approximately 75°.

The growth phase begins with a substorm onset shown in image B in Figure 15. The arc to the south, below 70° latitude, begins to brighten. After this the expansion phase begins. The arc begins to fold and form a bulge. This bulge expands northward from its original position and begins to move west. Patches begin to form this, as seen in Image C of Figure 15. Image D is where the expansion phase reaches its maximum. The bulge continues its westward and northward expansion.

Once the expansion phase has peaked, the recovery phase beings which can last up to a couple of hours. The contraction northward continues, and the disturbance begins to weaken. The situation retreats to the pre-onset auroral oval seen in Image F of Figure 15.

A full description of the auroral substorm processes is given in Brekke (1997).

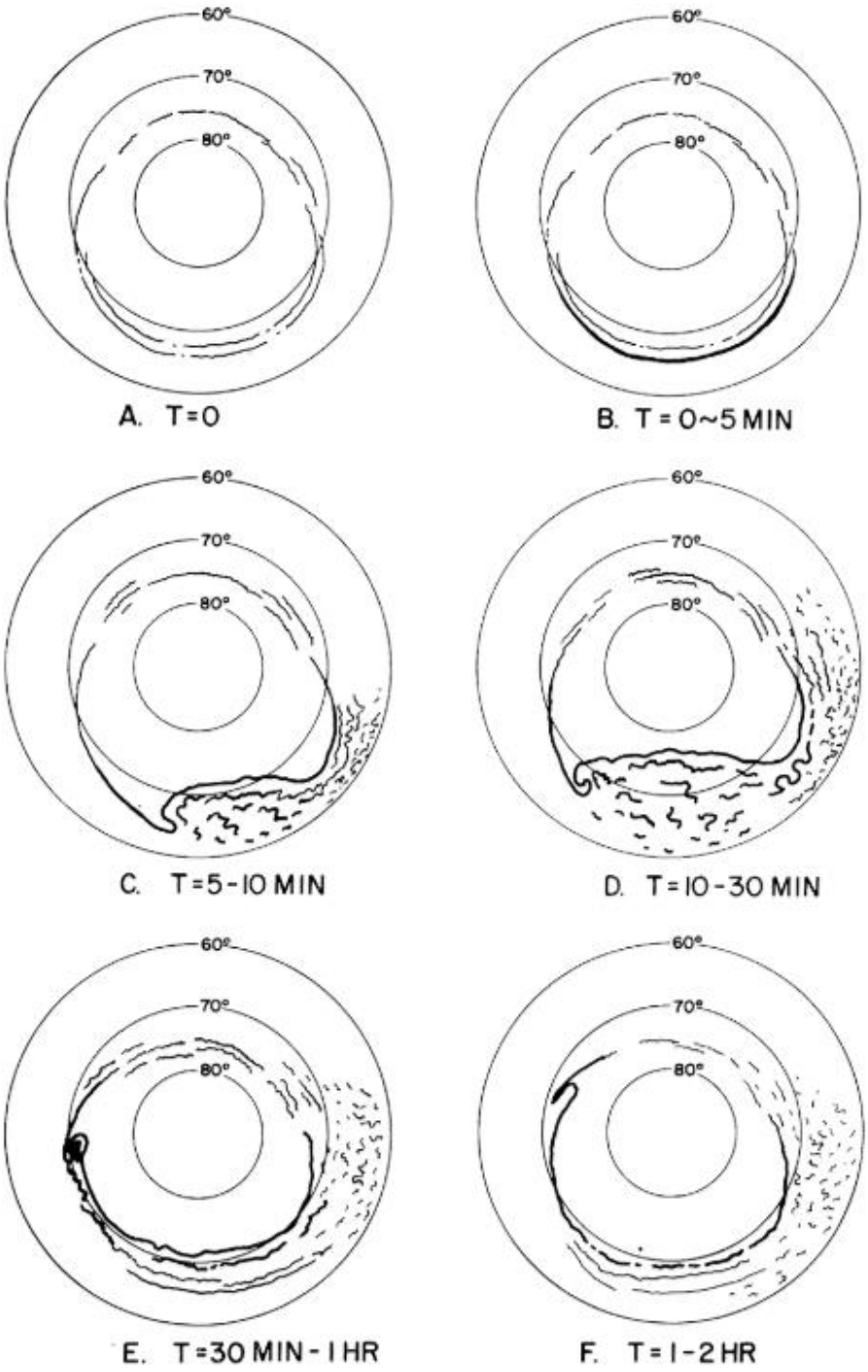

Figure 15 – Schematic representation that shows the development of the four phases of an auroral substorm. (Akasofu, 1968)

Chapter 3

Electron Density Assimilative Model (EDAM)

3.1 Introduction

The Electron Density Assimilative Model (EDAM) (Angling and Canon, 2004) is an ionospheric model that assimilates data sources into a background model, currently provided by International Reference Ionosphere 2007 (IRI2007) (Bilitza et al., 2006). EDAM assimilates ionospheric observations to generate a global (or regional) 3-D representation of ionospheric electron density. The spatial resolution of the voxels in the 3-D grid is 4^{o} latitude by 4^{o} longitude. The altitudinal dimension of the voxels is 10 km. An assimilation time step of 15 minutes is used and the electron density differences between the voxels of the assimilated grid and the background model are propagated from one-time step to the next. Different sources of data can be inputted into the model and assimilated for example ionosonde measurements, Global Positioning System (GPS) measurements and Radio Occultation (RO) data. GPS data are used in this thesis.

EDAM was chosen for this thesis for several reasons. The main reason it was chosen over models such as the Multi-Instrument Data Analysis System (MIDAS) was because QinetiQ sponsored this thesis and the work produced and published from this (Parker et al, 2018) and EDAM was the model developed at QinetiQ. The two models also offer different approaches. MIDAS (Mitchell et al., 2002; Mitchell et al., 2003) is a software package that conducts 4-D spatial and temporal tomography to image the ionosphere. MIDAS does this by using GPS and low earth orbiting (LEO) satellites to use the measurements collected from satellite-to-satellite transmissions, RO data, and satellite-to-receiver measurements. It can provide forecasts, with a slight delay, of the real-time ionosphere. MIDAS can obtain potentially better vertical definition of the ionosphere utilising tomography, which will be highlighted in Chapter

5 comparing EDAM with a different tomographic method, to go with the horizontal definition from the satellite to receiver measurements.

EDAM, however, can show a better spread of the GPS data modelled into a background model such as IRI for the global, regional or local ionosphere utilising a different method. EDAM uses data assimilation techniques to combine theory from a model with observations. From this it obtains the optimal estimate of the electron density of the given region. This method is better than the tomographic method of MIDAS because it uses the GPS measurement made along the satellite-to-receiver path and estimates the electron density in the area that surrounds that satellite-to-receiver path. The model does this accurately when also compared to other ionospheric models as shown in Feltens et al. (2011) and Chapter 7. As shown in Feltens et al. (2011) EDAM performs comparable with two other models, the Tomographic Ionosphere Model (TOMION) and the Neustralitz TEC Models (NTCM). EDAM offers a different approach to TOMION because it uses a background model to assimilate measurements on while TOMION does not. TOMION instead goes through a 3-step process where an initial fit is made at a lower resolution compared to EDAM and then builds on that first estimate to generate a higher resolution TEC map. While TOMION has not been looked at in this thesis in detail, the steps imply multiple runs of the assimilation to get this higher resolution, and therefore increased run-time and processing power is required compared to EDAM. The reason why a background model is beneficial to an assimilative model is shown by the performance of the Ionosphere Monitoring Facility, Version 2 (IONMON, v2) where, in regions of sparsely populated GPS receivers, the performance is poor. At the time of Feltens et al. (2011), IONMON, v2 was looking to introduce a background model.

How EDAM operates will be discussed later and more information on MIDAS can be found in Mitchell et al. (2003).

3.2 Introduction to GPS

The GPS satellites are in approximate 12-hour circular orbits at an inclination of near 55^o to the equatorial plane. Currently, there are 31 active GPS satellites in orbit, although only 24 that are evenly spaced, would be needed to provide full coverage. They were originally desired for, and so configured to, providing the capability of determining the user's position in latitude, longitude and elevation; the configuration of a satellite receiver pair is shown in Figure 16. The GPS transmitted frequency, as it propagates through the ionosphere, will have a positional inaccuracy of 5-15 m for a satellite at the zenith angle. At low elevation, this inaccuracy increases as the propagation length through the ionosphere is longer. (Grewel et al., 2001)

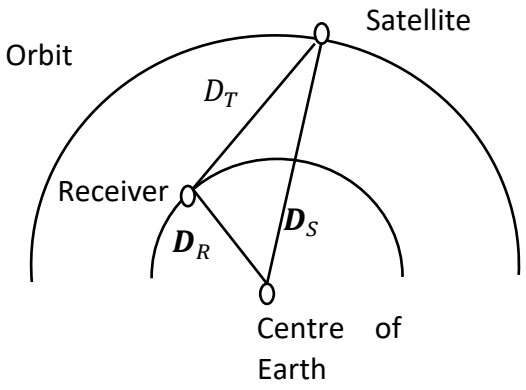

Figure 16 – Configuration of a satellite and receiver pair. The position vector from the centre of the Earth to the receiver is $\mathbf{D_R}$. The position vector from the centre of the Earth to the satellite is $\mathbf{D_S}$The diagram shows how to calculate the receiver position, true distance ($\mathbf{D_T}$) relative to the satellite and the centre of the Earth. More than one satellite is needed to determine the position of the receiver.

The principle is that the absolute magnitude of the position vector from the centre of the Earth to the Satellite ($\boldsymbol{D}_S$) minus the position vector of the GPS receiver from the centre of the Earth ($\boldsymbol{D}_R$) would provide a true distance between the receiver and satellite (D_T). Each

calculated true distance is said to define a sphere with the centre of the sphere being the satellite (Hofmann-Wellenhof et al., 2001). To obtain the latitude, longitude and altitude of the receiver, true distances (D_T) to three satellites would be required. The intersection of the three spheres defined above provides the latitude, longitude and altitude. The fundamental equation for this technique to calculate the true distance is given in Equation 19.

GPS receivers use a slightly different technique to the one described above, employing an oscillator that uses the resonance of a vibrating crystal to create an electric signal with precise frequency (Marrison, 1948). This is an inexpensive crystal clock. The clock is set to approximate GPS time rather than precise GPS time. GPS time is explained in more detail in Hofmann-Wellenhof et al. (2001).

Due to this offset, the distance measured to the satellite differs from the true distance. These distances are defined as pseudoranges because they are defined as a true distance plus a correction (ΔD_T) due to receiver clock bias as shown in Equation 20:

$$D_T = |\boldsymbol{D}_S - \boldsymbol{D}_R|, \qquad \textbf{[Equation 19]}$$

$$P = D_T + \Delta D_T. \qquad \textbf{[Equation 20]}$$

Four different pseudoranges are therefore required to solve the four different variables to obtain the position of the receiver. Three for the positional components and the fourth for the clock bias. GPS however can be used for much more than positional information. A fundamental frequency is generated from oscillators onboard the GPS satellites that is used to then generate the signals that carry satellite clock readings and orbital parameter information. (Spiker, 1996a)

3.3 Total Electron Content calculation

3.3.1 Theory

As previously stated, the ionosphere is a significant source of error in radio propagation. To quantify the effects of propagation of a radio wave travelling through the ionosphere, the refractive index of the medium must be specified. The ionospheric refractive index was derived by Appleton and Hartree (Hunsucker, 1991) and the refractive index of the ionosphere at GPS frequencies reduces to (Brunner and Gu, 1991):

$$n = 1 - \frac{X}{2}, \qquad \textbf{[Equation 21]}$$

for a simple dual frequency ionosphere correction of the refractive index (Deines, 2006). This dual frequency ionospheric correction is used to correct for ionospheric range error due to ionospheric horizontal gradients. From the Appleton-Hartree equation, $X = \frac{N_e e^2}{\epsilon_0 m f^2}$, where f is the frequency of the propagating wave, N_e is the electron density, e is the electron charge, ϵ_0 is the permittivity of free space and m is the mass of an electron. $\frac{e^2}{\epsilon_0 m}$ is a constant calculated to equal 40.3 Nm.

The ionosphere would act to slow down the velocity of the wave packet, group velocity, carrying the transmission between the satellite and the receiver to a velocity below the speed of light, c, in free space. The inverse would occur for the phase measurements travelling along the radio wave, where the phase velocity would be advanced by the same magnitude of the former, above the speed of light (Klobuchar, 1996). The relationship between the delay of the group velocity and the carrier phase is:

$$\Delta\phi = -f\Delta t, \qquad \textbf{[Equation 22]}$$

where $\Delta\phi$ is the carrier phase, Δt is the group delay and f is the frequency of the transmitted radio wave. This shows that for every phase advance there is a 1/f seconds of time delay. (Horvath and Crozier, 2007)

The pseudorange, defined in section 3.2, is an absolute measurement of this group delay between the time the radio wave is transmitted from the satellite and received at the receiver. Equation 20 is the sum of the true distance between the satellite and receiver and the clock offsets and receiver, atmosphere and ionospheric delays. (Hajj et al., 2000)

The group delay caused by the ionosphere on radio propagation, expressed as a time delay, can be calculated from:

$$\Delta t = \frac{1}{c}\int (1 - n) dl. \qquad \textbf{[Equation 23]}$$

Equation 23 gives a measure of the delay caused by the ionosphere on measuring the distance between receiver and satellite. (Deines, 2006)

Using equation 21 for the refractive index of the ionosphere, the ionospheric group delay becomes:

$$\Delta t = \frac{40.3}{cf^2}\int N_e dl. \qquad \textbf{[Equation 24]}$$

The integral of the electron density along the path of propagation, between the receiver and the satellite, gives a value of the total number of electrons in a column, with a cross-sectional area 1 m^2, between the receiver and satellite. This is the Total Electron Content (TEC). Multiplying the time delay by the speed of light then expresses the ionospheric delay in terms of a distance.

Rearranging Equation 24 to make the TEC the subject of the equation and multiplying by c to give the group delay in metres gives:

$$TEC = -\frac{f^2}{40.3}\Delta t. \qquad \textbf{[Equation 25]}$$

The GPS receivers used in this study are dual frequency, meaning they operate using two different frequencies, L1 at 1575.42 MHz and L2 at 1227.60 MHz. In this scenario, a differential time delay and a differential carrier phase can be calculated from the measurements from both frequencies.

The TEC from the dual frequency receivers may be calculated from either the L1 or L2 frequencies that are transmitted from the satellite. Both frequencies however propagate over slightly different paths, therefore, the TEC calculated on each frequency would be slightly different from each other.

3.3.2 EDAM TEC Calculation

The separation between the transmitted L1 and L2 signals is usually small. An assumption in EDAM is made where both frequencies travel along the same path. This allows the TEC to be calculated from the phase difference between the two carrier frequency signals, L1 and L2 (Schreiner et al, 1999):

$$TEC_{Phase} = -\frac{f_1^2}{40.3}\Delta\phi = -\frac{f_2^2}{40.3}\Delta\phi = \frac{f_1^2 f_2^2 (\Delta\phi_1 - \Delta\phi_2)}{40.3 (f_1^2 - f_2^2)} + B + \nu, \qquad \textbf{[Equation 26]}$$

where f_1, f_2 are the carrier frequencies, corresponding to the L1 and L2 frequencies, and $\Delta\phi_1$, $\Delta\phi_2$ are the phase measurements corresponding to those frequencies. B and ν are biases in the TEC. B is a bias associated with the difficulty of counting the number of cycles of the

carrier frequency between the satellite and receiver because of the uniformity in the carrier frequency. This is known as phase ambiguity. ν is a bias associated with noise in the TEC value. Calculating the TEC from the difference of the phases, $\phi_1$and ϕ_2, cancels out satellite position, transmitter and receiver clock errors from the pseudorange and phase measurements as modelled from Hajj et al. (2000).

The phase ambiguity bias must be removed. This can be achieved by calculating a TEC value using the pseudorange (group delay), using the differences of the mean of the TECs calculated from the carrier phase and pseudorange and taking that difference from the carrier phase calculated TEC values. This uses a similar approach to the TEC calculation from the carrier phase, except a different bias is considered:

$$TEC_{Pseudorange} = \frac{f_1^2 f_2^2 (\Delta t_1 - \Delta t_2)}{40.3 (f_1^2 - f_2^2)} + C + \zeta, \qquad \textbf{[Equation 27]}$$

with C being related to the receiver differential code biases (DCB), which will be discussed later, and ζ is another bias relating to the noise in the TEC.

In EDAM the phase ambiguity is removed by first calculating the mean of the differences between of the carrier phase measurements and the differences of the pseudoranges. This difference is then subtracted or added to the $\Delta\phi_1 - \Delta\phi_2$ term from Equation 26 depending on If $\Delta\phi_1 - \Delta\phi_2$ is lesser or greater than $\Delta t_1 - \Delta t_2$ from Equation 27. This gives a corrected form of $\Delta\phi_1 - \Delta\phi_2$ that is used to calculate the TEC values assimilated into EDAM and removing the phase ambiguity. This leaves only the DCBs left to account for.

Generally, there are two categories of DCB, intra-frequency and inter-frequency biases. Intra-frequency bias is between two code observations seen at the same frequency, inter-frequency bias between code observations at two frequencies. More information on DCBs

can be found in Wang et al. (2016a). Monthly DCBs are downloaded and read into EDAM from the centre for Orbit Determination in Europe (CODE).

The raw satellite navigation system data, the carrier frequency measurements, the pseudoranges and the received times are held in a Receiver Independent Exchange Format (RINEX) file (Gurtner and Estey, 2006) for use in this thesis.

The RINEX files used contain one day of data with intervals of 30 seconds. There were files for each receiver used in the assimilation. These files were used as the primary source of data for assimilation into EDAM, where they went through pre-processing, which means a data store was created for the pseudoranges and phases.

In the 15-minute assimilation period, a TEC value is calculated for 5 min intervals in the 15-minute period. The values are validated before assimilation takes place.

3.4 EDAM Assimilation

3.4.1 Introduction

Before the assimilation starts, the grid on which the GPS TEC will be assimilated on, is initialised. For this thesis, the EDAM grid is set to Europe with boundary conditions of 20°W to 40°E in longitude and 45°N to 70°N in latitude. They are spaced out by 1° in both latitude and longitude. The starting altitude for the altitudinal dimension of the grid is 100 km which reaches a defined limit of 1000 km, in 10 km increments. This gives a dimension of each assimilated TEC value to be a point of 1° x 1° x 10 km which is part of the larger voxel described in Section 3.1.

The TEC values are passed to a routine which assimilates the calculated TEC value into the background electron density grid, generated from the International Reference Ionosphere (IRI) 2007 model. This is done for the first-time step in the assimilation. EDAM also requires a parameter, maximum variance in the background electron density, that it used to generate the variances, which measures the spread of the numbers from the mean, associated with IRI. This maximum variance has been coded into the program at 1×10^{-19}.

With everything defined and a background model from IRI set up, the process of assimilating the TEC value, obtained by the description in Section 3.3.2, from the receiver into the model begins.

3.4.2 Assimilation theory in EDAM

The number of TEC values to be assimilated is determined as this defines the dimension of the observation vector, the vector that holds the values to be assimilated, which will be discussed later in further detail. For the purpose of this thesis, three TEC values are assimilated which represent the 5-minute intervals in the 15-minute assimilation period, but only one TEC goes through the assimilation process at any time. The grid in the assimilation assumes electron density remains constant throughout each voxel.

New axes for the grid that holds the electron densities from IRI must be generated which would bisect the axes defined before the assimilation step began. This allows the TEC value to be assimilated into the centre of each defined voxel rather than the edge of the voxel. This means the new points on the axis would lie halfway between the two points of the old axis. An example of this is if the altitude axis starts at 100 km and the next point in altitude is 110 km, the first altitude point on the newly generated axis will be 105 km. The

background model returns electron densities at the co-ordinates inputted in the original latitude, longitude and altitude grid. This bisection is done for the assimilation as it is necessary to have a grid where it is assumed the electron density remains constant throughout the voxel.

With the new axis generated, each voxel in the grid is given a number, called an index. An array is generated which is split into 3 dimensions. The first dimension holds the voxel indices, which is defined in the model as a limit of 400 voxels, where the rays from the satellite to receiver pass through. The second holds the latitude, longitude and altitude of the new grid and holds the lengths of the ray that has passed through the corresponding voxel. The final dimension is defined by the number of measurements, which is one for this thesis. The array is then trimmed in size, so only the number of voxels on which the TEC value is assimilated into is retained.

A vector is generated that includes all the voxels that have been traversed by a ray path between the receiver and the satellite, and the near neighbours to these voxels, which allows the assimilated data to be spread from the traversed voxels to the surrounding area. The vector is the background model vector (x_b), which is a subset of the full background grid from IRI. To find the size of this vector a dilation operator, a spreading kernel, is used to expand on the voxels traversed by the satellite-to-receiver ray path. A default kernel is used in EDAM, so the assimilation spreads 4 voxels away.

A vector which holds the background model variances for each element in the background model vector, and an index vector, which relate each element of the background model vector to the latitude, longitude and altitude axes, are generated. These vectors are sorted

so that the elements are ordered in terms of distance from the GPS transmitter. An array is generated which holds the lengths of the ray path in the voxels of the model (H).

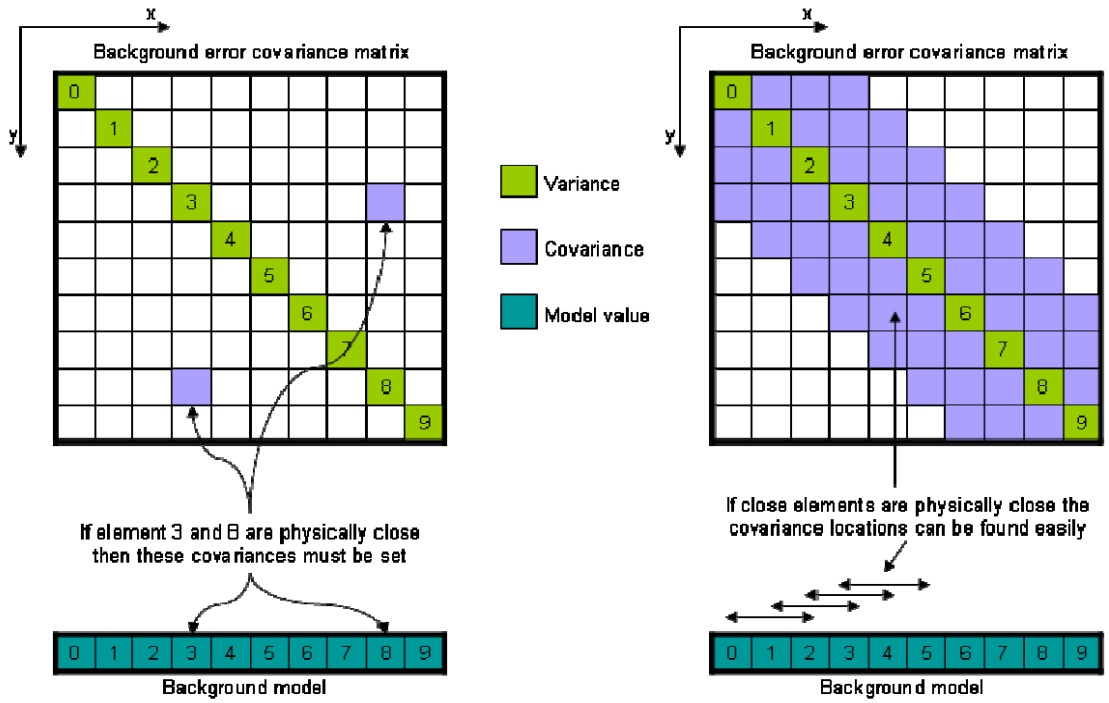

Figure 17 - A example diagram of how error covariance matrices are obtained from the model variances. If 2 of the model values (voxels) are physically close, then the covariance value of these two are set in the covariance matrix with the variances of the model values being in the diagonal of the matrix. On the right-hand side of the diagram, it shows how the covariances are set if close elements in the model are physically close, the locations of the covariance are found easily.

The error matrices are generated, for both the background model (B) and the observation operator (O). The error matrices are defined as covariance error matrices. Covariance (Rice, 2007) is the mean of the sum of the deviation of two variances. For both the background and observation errors, this means that the matrix specifies the deviation in the observation errors between two variances in both the observation operator and the background model. The covariance matrix is a diagonal matrix where the diagonals are the variances of the observations and the procedure of how the matrix is obtained is shown in Figure 17. The variable known as x_{bvar} is the variance vector associated with the trimmed background model.

The DCBs that were collected earlier are appended to the background model error covariance matrix. Arrays that hold the bias additions to the background model (x_{bBias}) and the observation operator (H_{bias}) are also set up which will be used in the final process of calculating the final assimilated grid, known as the analysis grid (x_a). The DCB additions to the observation operator (H_{bias}) are set as -1, 1 or 0 as the biases are already provided in terms of TEC. The biases for this operator are calculated during the TEC calculation process in Section 3.3.

With all the arrays set up, the next step is generating an analysis grid. It begins by taking a partial differential of the observation operator, with respect to the background model. This is known as a Jacobian (Ja), shown in Equation 28. In EDAM, the Jacobian has two dimensions, the first is related to the background model and the array that holds the lengths of the ray paths. The second dimension holds the H_{bias} parameter, which can be directly appended into the Jacobian as H_{bias} is a linear operator.

The generation of an operator, K, known as the Kalman gain is next. Kalman gain tells the model how much to change the estimate, the background grid, by given a measurement (Kalman, 1960), in this case a TEC value. The Jacobian is used to calculate this along with the observation error covariance matrix and the background error covariance matrix seen in Equation 29.

Using the trimmed background model grid (x_b), the observation operator (TEC) is added to this grid by subtracting the background grid from the observation operator (Hx_b) and adding the multiplication of the two biases ($H_{bias} * x_{bBias}$). This is then multiplied by the Kalman (K) gain which is finally used to update the background grid and produce the analysis grid (x_a) (Angling and Khattatov, 2006) in Equation 30:

$$Ja = [H * (10^{x_b}) * alog(10), H_{bias}], \quad \textbf{[Equation 28]}$$

$$K = BJa^T[Ja * B * Ja^T + O]^{-1}, \quad \textbf{[Equation 29]}$$

$$x_a = x_b + K\big(TEC - Hx_b + (H_{bias} * x_{bBias})\big). \quad \textbf{[Equation 30]}$$

An error covariance matrix is generated for the analysis grid (Rodgers, 2000). This is done in a similar way to Equation 30 but this time instead of the background grid, it is the covariance matrices that are used. The Kalman gain is multiplied by the lengths of each ray passing through the voxels (H) and the background error covariance matrix. This is then subtracted from the background error covariance matrix giving the error covariance matrix for the analysis (A). The covariances are not propagated with each time step by EDAM, so only the variances are required.

The analysis grid is checked for extreme values following the assimilation step. If accepted, the background model, the variances and the DCBs are updated. This process is looped for all receivers that are assimilated into the background grid.

With all the receivers having gone through the assimilation process and an assimilated electron density grid finalised for this time step, the difference between the background grid and the newly updated analysis grid is calculated. This is called the fractional electron density difference and is done for the variances too. The electron density differences are written to a file along with other parameters such as the grid axis and time epoch for storage management purposes. This keeps the file sizes down as well as being able to use the data later to recreate the electron density grid, which is utilised for Chapters 5-8.

From one assimilation time step to the next, the fractional differences between the background grid and the analysis grid are propagated. These differences are also decayed

using the scale time, which is set to 4 hours in the model, so that if the data switches off or is lost, the difference fields will drop to 0. This enables EDAM to return to being equal to the background model. In this thesis with regional grids being used, the difference electron density grids are shifted in longitude to match the time shift between the difference electron density grid and the next time step of the assimilation. Three sets of arrays are generated, one holding the background model, one holding the assimilated electron density grid from the previous time step and the one which holds the new assimilated grid for this time step. The whole process, from the start of the section to the updating of the electron density grid, is looped over the period defined at the beginning of the model.

Chapter 4

Experimental Instrumentation

4.1 Introduction

The terrestrial ionosphere is a dynamic medium with structures present on a wide range of temporal and spatial scales. Chapter 2 has given an outline of some of the main ionospheric structures, the operative processes in the ionosphere and focussed on the features important to this thesis. To justify the results of EDAM, multiple instruments and other analysis methods are used to validate these results and interpret the behaviour of the structures observed in the ionosphere.

The Super Dual Auroral Radar Network (SuperDARN) is the first instrument focussed on in this chapter. Sections on ionosondes and on the Advanced Composition Explorer (ACE) spacecraft follow this. The different geomagnetic indices used in the thesis round out the chapter.

4.2 SuperDARN

SuperDARN is a network of HF radars operating with common viewing areas so Doppler information contained in backscattered signals can be combined to produce maps of the plasma convection in the high-latitude ionosphere, of interest for the study presented in this thesis. The original research objectives of the radar network included providing a global scale view of the convection of the plasma in the high latitude ionosphere, as well as the region's dynamics. It also tested various theories of the polar cap expansion and contraction under storm-time conditions.

The first SuperDARN radar was built in Canada in 1983 (Greenwald et al., 1985). It was a steerable, narrow beam, phased-array HF radar. The radar transmits and receives HF signals from 8 MHz to 20 MHz, employing a 16-beam scan creating a field of view that extends

approximately 52° in azimuth, and from 200 km to more than 3000 km in range. Subsequently, several radars have been built in both the northern and southern hemispheres. Most radars, in the northern hemisphere, are located in North America but there is a pair that operates in Iceland and Finland, the Co-operative UK Twin Located Auroral Sounding System (CUTLASS), that observe at auroral latitudes in the European longitudinal sector (Lester et al., 2004). The radars are at Pykkvibaer (63.86° N 19.20° W) and Hankasalmi (62.32° N 26.61° E). These radars collect data in the region of the interest to the study presented in this thesis. The data from other radars are included to provide the full electric potential map.

The radars transmit pulse sequences, at HF radio signal, into the ionosphere. The large range of frequencies used is necessary due to variability of the plasma electron density and how it influences the refraction of the radio signal in the ionosphere (Greenwald et al., 1995). These signals are coherently scattered back from decametre-scale field-aligned plasma density irregularities in the ionosphere (Chisham et al., 2007). The backscattered signals undergo changes in frequency, called Doppler shifting. The Doppler shifts are analysed and corrected before the line of sight component of the ionospheric drift can be determined. The radars are primarily arranged in pairs to enable the observation of a common area of the ionosphere from different angles.

SuperDARN goes through three levels of processing from the retrieved backscatter, but data is available for SuperDARN at all three levels. Raw backscatter autocorrelation functions comprise the first level of the data, and echo spectra can be calculated from these (Danskin et al., 2004). A fitting technique is then applied to calculate the backscatter power, Doppler shift and echo widths, comprising the second level of the data (Villain et al., 1987). The fitted echoes from all the radars are then combined to provide a global convection pattern of the

ionospheric plasma in the high-latitude ionosphere, with the convection described in section 2.5. This final level of data has been provided by European Cluster Assimilation Technology (ECLAT) at the University of Leicester for use in this thesis.

To obtain the convection pattern, an assimilation process is used that combines the fitted echoes from the second level of processing. This process is called the map potential technique. The convection of ionospheric plasma at high latitudes is driven by solar wind-magnetosphere coupling imposed electric fields, discussed earlier on in Section 2.5 and convects according to Equation 31. The global convection electric field, also known as the distribution of the electric potential, is shown in Equation 32:

$$\boldsymbol{v} = \frac{\boldsymbol{E} \times \boldsymbol{B}}{B^2}, \qquad \textbf{[Equation 31]}$$

$$\boldsymbol{E} = -\nabla \Phi. \qquad \textbf{[Equation 32]}$$

Equation 32 is useful for specifying the current state of the high-latitude ionosphere (Ruohoniemi and Baker, 1998). Equations 31 and 32 relate the electrostatic potential, convection electric field and velocity together which is needed for mapping the large scale high-latitude ionospheric convection maps. This is what the map potential technique performs. The map potential technique represents the electrostatic potential as an expansion of spherical harmonic functions and converts the line-of-sight velocities to the mapped grid used in this thesis. A full description of this technique is described in Ruohoniemi and Baker (1998).

The expansion does not extend over all latitudes as electric potential is assumed to be zero at the lower latitudes, below the approximate boundary of the auroral oval. This boundary, known as the Heppner-Maynard boundary, was determined empirically using Dynamics

Explorer 2 satellite data by Heppner and Maynard (1987) and shows the extent of the ionospheric convection pattern. More recently it has been used as a proxy for the location of the auroral oval. (Imber et al., 2013)

4.3 Ionosonde

An ionosonde is a type of radar that measures the plasma density in the ionosphere. The radar consists of a high frequency transmitter (an antenna), which broadcasts over a wide range of frequencies ranging typically from 0.1 to 30 MHz, a tracking receiver which tracks the frequency of the transmitter and digital control and data analysis circuits. There are two types of ionosonde, vertical sounding ionosondes and oblique sounding ionosondes. Vertical ionosondes are the types used in this thesis.

Vertical ionosondes work by broadcasting a sweep of frequencies in the range mentioned above where the transmitted signal is broadcasted vertically into the ionosphere until it is reflected and returned to the receiver. The transmitter and receiver are collocated. As the frequency of the transmission increases, the radio signal penetrates further into the ionosphere. Measuring how long it takes for a radio signal for each transmitted frequency to be reflected and returned to the receiver, it is possible to estimate the electron concentration and the height of each layer of ionisation.

As the wave approaches the point of reflection, the group velocity of the wave is zero. As the frequency continues to increase, the radio signal will eventually reach a frequency that enables the wave to penetrate the layer without being reflected. This occurs when the frequency transmitted by the ionosonde exceeds the frequency at which the plasma particles

are oscillating, that is the plasma frequency. The frequency of penetration for a given ionospheric layer is known as the critical frequency of that layer.

The critical frequency of the layer is related to the electron density by;

$$f_c = 8.98 * \sqrt{N_e}, \qquad \textbf{[Equation 33]}$$

where f_c is the critical frequency in Hz and N_e is the electron density in m^{-3}.

All transmitted frequencies above the critical frequency will penetrate the layer without being reflected, until a higher layer with a larger plasma frequency reflects the signal. The wave will then be reflected, and the returned signal will have to pass back through the underlying ionisation, causing a longer delay for the returned signal.

There are two different modes of waves, ordinary and extraordinary modes. The reflection for the case of ordinary modes has been described. For extraordinary waves, the magnetic field has an additional effect and the reflection occurs at a frequency that is higher than for the ordinary mode by half the electron gyrofrequency. This however will not be focussed on here.

The measured delay between the transmission and reception of the signal can give a height for the point of reflection. This height is known as the virtual height of the reflected signal. This delay return signal is due to the underlying ionisation in the ionosphere. A procedure known as true-height analysis (Titheridge, 1985) recreates a true-height profiles of the electron concentration. The virtual height of each layer and the frequency of the signal are recorded in an ionogram.

An ionogram is a graph of the range at which the frequency has travelled, in km, against the transmitted frequency in MHz. The ionospheric layers picked up by the transmitted frequency

show as approximately smooth curves separated by each other by an asymptote at the critical frequencies of each layer. An example of an ionogram can be seen in Figure 18 from the UK Solar System Data Centre (UKSSDC) database. The virtual height of the each of the layers are scaled from the lowest point on each curve.

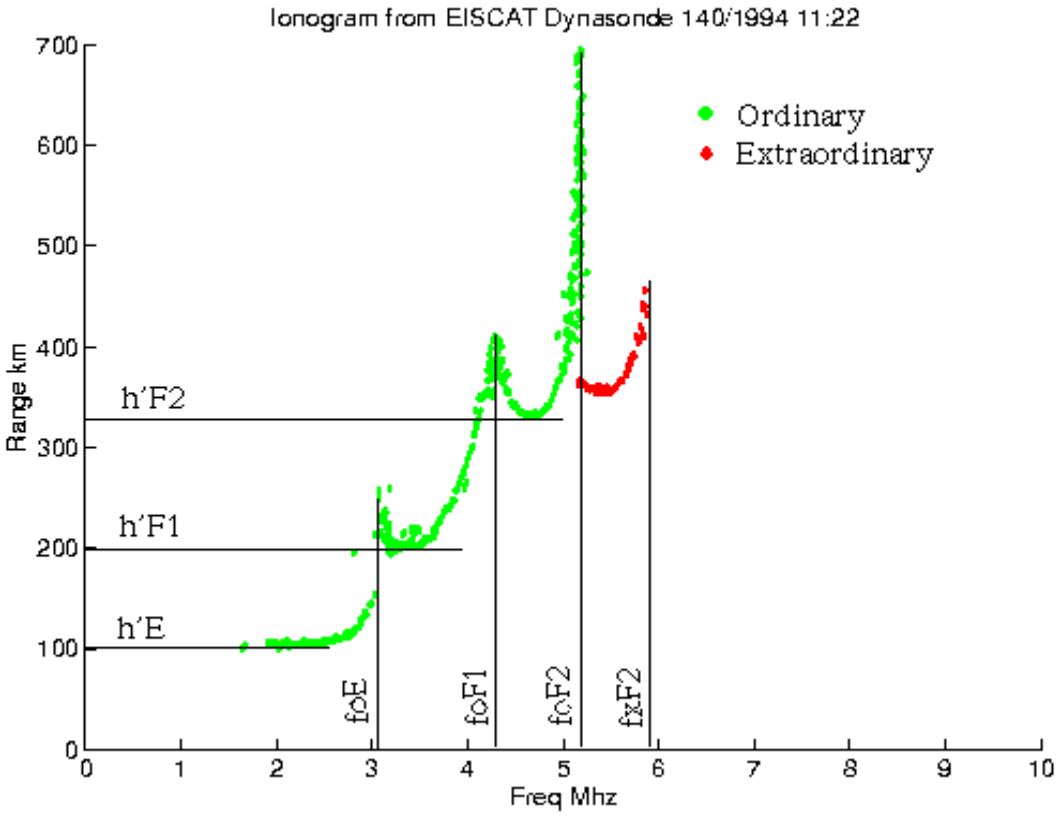

Figure 18 - Ionogram example from the UKSSDC. The critical frequencies (f_o) and virtual heights (h') of each layer is highlighted on the diagram for the ordinary and extraordinary waves. The lowest point on the curves signal the virtual height of the layers with the asymptote between the layers equalling the critical frequency of the layer.

The true height analysis, mentioned previously, is an attempt to recreate the actual plasma density profile from the ionogram data. The analysis is computed by using the polynomial analysis program or POLAN (Titheridge, 1985). POLAN is used to obtain the true height values of each layer, which means the whole ray path must be reconstructed and assumptions about the electron concentration along the ray path are made. The true-height profile is also sensitive to two approximations. The first is the start position, which is at the altitude where

the virtual height of the lowest frequency echoes on an ionogram. The second is a way of estimating the amount of unseen ionisation in the valley between two layers, known as the valley approximation. More details on this analysis can be found in Titheridge (1985).

4.4 ACE

The Advanced Composition Explorer (ACE) is a spacecraft mission in orbit at the L1 Lagrangian point which was launched in 1997. From that location it is able to provide near-real-time continuous coverage of solar wind parameters upstream of the Earth.

The spacecraft carries six high-resolution sensors and three monitoring instruments. It was designed to study low-energy solar particles and high-energy galactic particles in the solar wind and interplanetary medium (Chiu et al., 1998). The data collected by ACE for use in this thesis are the B_y and B_z components of the interplanetary magnetic field of the solar wind, the velocity, temperature and density of the H^+ ions measured by the Magnetic Field Experiment (MAG) and Solar Wind Electron, Proton, and Alpha Monitor (SWEPAM) instruments on the spacecraft.

The MAG consists of two vector magnetometers, which measure the vector components of the magnetic field. The sensors are mounted on poles on the spacecraft. These are extended 4.19 metres from the centre of the spacecraft, on opposite sides.

SWEPAM measures the solar wind plasma densities and rates of particle flow as functions of energy and direction. Electron and ion measurements are made with different sensors. The ion sensor measures the energies of the particles between 0.26 and 36 keV while the electron sensor measures the particle of energies between 1 and 1350 eV. Both sensors use what is

known as electrostatic analysers that have fan-shaped fields of view. The analysers measure the energy per charge of each particle and the field of view is swept across all directions of the solar wind by the rotation of the spacecraft. (McComas et al., 1997)

4.5 Geomagnetic Indices

The Geomagnetic Auroral Electrojet (AE) Index provides a global measure of the magnetic activity in the auroral region. This is produced by enhanced ionospheric currents around the auroral boundary and is measured as the total deviation from quiet day values of the horizontal magnetic field at the auroral region (Davis and Sugiura, 1966). The AE index is used in Chapter 6 and data are obtained for the days 29 and 30 September 2002.

The Kp index depicts the magnitude of geomagnetic storms by measuring the deviations in the disturbed horizontal component of the magnetic field at 13 selected stations located below the auroral boundary. The stations at these locations record their own local index and a global average is determined. The values of Kp are between 0 and 9 with 0 showing very little geomagnetic activity and 9 being the strongest level of activity and are based on 3 hourly measurements. Kp indices are used in Chapters 5 – 8 of this thesis and are obtained for September 2002 to August 2003.

The Dst index is used to measure the severity of magnetic storms, based on the average value of the horizontal component of the Earth's magnetic field. The magnetic field is measured at near-equatorial stations every hour and measures the strength of the changes in the magnetic field at these low latitudes. An average of each value computed at the near-equatorial

stations give the Dst index (Nose et al., 2015). The Dst index is used in Chapter 6 of this thesis and was obtained for 29 and 30 September.

Chapter 5

Modelling the main ionospheric trough using EDAM with assimilated GPS TEC

5.1 Introduction

The purpose of this Chapter is to present a comparison between the main ionospheric trough parameterised using EDAM assimilated GPS data and the parameterisation conducted in Pryse et al. (2006). The investigation presented was the first study to model and analyse the main ionospheric trough by assimilating GPS TECs into EDAM. This study has been published in Annales Geophysicae by Parker et al. (2018) and parts of this publication has been quoted verbatim (Reuse of this text is allowed for this Chapter by way of Creative Commons Attribution 4.0 License. There are changes in the text, but the content is the same).

5.1.1 Background

The main ionospheric trough is a depletion in the ionosphere that resides between the high-latitude region on its poleward side and the mid-latitude region on its equatorward side. Observations in Europe, for example those conducted by Krankowski et al. (2009), showed the feature is normally first observed in the late afternoon, at around 17:00 UT, at geographic latitudes poleward of 60°. The trough then moves equatorward through the night reaching its most equatorward latitude before dawn. With the increasing sunlight at dawn, increased photoionisation results in the trough filling in with increased density, which leads to the apparent rapid retreat to higher latitudes.

The smaller electron density values in the trough are normally bounded by a sharp ionisation density gradient on the poleward wall and a shallower gradient on the equatorward side. These characteristics are extended in longitude. An example of the trough shape with respect to latitude is given in Figure 19.

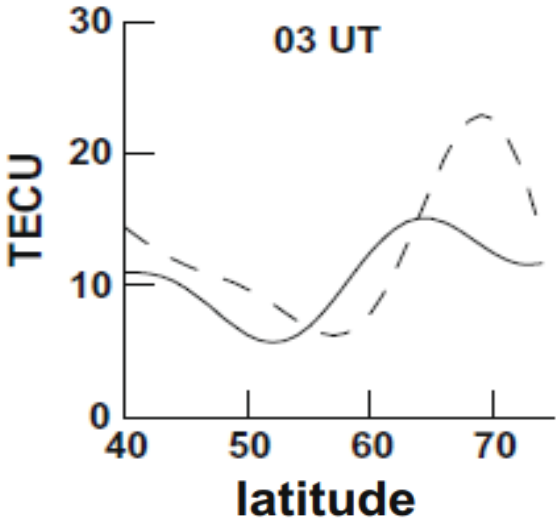

Figure 19 - Latitudinal TEC profiles in geographic coordinates on November 1, 2000 shown by the dashed line and a solid line on November 10, 2000 taken from Krankowski et al. (2009). The dashed line is for a quiet geomagnetic day and the solid line is a more active geomagnetic day. A TECU is defined as $1x10^{16}$ electrons m^{-2}.

The trough observed in the late afternoon at UK latitudes may be a continuation of a high-latitude trough occurring at higher latitudes, such as those observed at Scandinavian latitudes in the earlier post-noon sector. (Kersley et al., 1997)

5.1.2 History of Research

The feature, which can also be referred to as the mid-latitude trough, has been extensively studied over several decades. Muldrew (1965) was the first to study the trough using topside sounder data. The critical frequency of the F2 region (foF2) was measured from Alouette 1 and contour maps of these observations along with ionograms from the Ottawa telemetry station were used by Muldrew (1965) to characterise the mid and high latitude ionosphere, which include a minimum in the observed data relating to the main ionospheric trough. Alouette 1 ionograms were also used to identify the main ionospheric trough and its relationship with geomagnetic activity and position of the plasmapause (Rycroft and Burnell, 1970). Bates et al. (1973) focussed on the poleward edge of the trough under quiet

geomagnetic activity. Their study found that the maximum electron density at the wall of the trough, in the F region, was some 1° latitude equatorward of the visible aurora. Reviews of these early studies were conducted by Moffet and Quegan (1983) and Rodger et al. (1992). In later years, the trough was investigated for its dependence on other parameters. Examples of the other parameters included season and solar activity (Ishida et al., 2014), geomagnetic conditions (Werner and Prölss, 1997) and longitude. (He et al., 2011; Whalen, 1989)

Many studies aimed to characterise the production and properties of the main ionospheric trough. Spiro et al. (1978) related the trough, in the nighttime sector, at subauroral latitudes to flow stagnation due to the interaction between the co-rotation and the magnetospheric electric fields which effects the high latitude convection pattern. Zou et al. (2011) used GPS Vertical TEC (VTEC) and complimentary instruments, such as observations from an incoherent scatter radar, to investigate the dynamics of the main ionospheric trough under magnetic substorm activity in the Alaskan sector. It was found that the trough moved rapidly equatorward at the onset of a substorm because of enhanced electron precipitation. This caused the trough to become narrower or even disappear but during the recovery phase of the storm, as the activity retreats poleward, the trough can make a reappearance. Yizengaw and Moldwin (2005) used tomographic reconstructions of TEC, derived from measurements by a network of GPS receivers and use of an inversion technique known as the algebraic reconstruction algorithms (ART), and Extreme Ultraviolet (EUV) images from the Imager for Magnetospheric-to-Aurora Global Exploration (IMAGE) Earth satellite, to show agreement between the plasmapause and the global positions of the main ionospheric trough.

Werner and Prölss (1997) used electron density measurements from the Dynamics Explorer 2 (DE 2) satellite, at altitudes between 300 km to 1000 km, to develop two empirical models

for the trough minimum magnetic latitude as a function of Magnetic Local Time (MLT), for the mid- and the high-latitude troughs. The same DE 2 data was used by Feichter and Leitinger (2002) to model other properties of the trough including parameters of trough depth, width and steepness of trough walls. For this they also used the COSTprof electron density model (Hochegger et al., 2000) to map the DE 2 measured electron densities to values at the F region peak altitude.

5.1.3 Observation Techniques

The main ionospheric trough has been studied using many different observing techniques. Methods of observation include: ionospheric sounders such as the networks considered by Whalen (1987 and 1989); incoherent scatter radar (Voiculescu et al., 2010); satellite TEC observations, for example by the Navy Ionospheric Monitoring System (NIMS) (Kersley et al., 2004); and ionospheric tomography reconstruction using NIMS TEC observations (Pryse et al., 1993). In more recent years TEC measurements using GPS radio transmissions have been used to observe and study the trough. Krankowski et al. (2009) used GPS observations from a network of receiving stations in Europe. The system was also used in the statistical study of Yang et al. (2015) to investigate the dependency of the trough on the season, geomagnetic activity and solar conditions. Each of the techniques has its strengths and limitations. Incoherent scatter radars provide information on the electron density structure, electron and ion temperatures and ion drift velocity. Observations from multiple radars can be combined for enhanced studies of the structure and time evolution of the trough. Hedin et al. (2000) used observations from the EISCAT Svalbard radar and the Ultra-High Frequency (UHF) and Very-High Frequency (VHF) mainland EISCAT radars in northern Scandinavia in a comparison

with models of the trough minimum. The limitation of these systems is that they are expensive and are located at specific locations leading to limits with the observing geometry. Radio tomography has also been used to image the trough's latitudinal structure. The method in this case suffers from limited ray-path geometry from the configuration of the satellites and receivers (Yeh and Raymund, 1991). It also requires a priori information to support the tomographic reconstruction process (Raymund et al., 1993). In another application Mitchell and Spencer (2003) presented an algorithm using GPS observations that yielded the time-evolving, three-dimensional ionospheric electron concentration. Their Multi-Instrument Data Analysis System (MIDAS) has proven successful for ionospheric imaging, however, there are still limitations, where lower ionosphere dynamics mask some of the topside features in the ionosphere. (Jayawardena et al., 2016)

Interest in the trough also occurs in applications of ionospheric radio propagation. This is largely driven by the influence of the feature on the propagation of High Frequency (HF) radio signals as shown along the oblique subauroral paths considered by Andreev et al. (2006).

5.1.4 EDAM

The modelled trough in EDAM is described in terms of a few defined parameters which include the trough minimum. Statistical analysis of these parameters allowed the evaluation of EDAM in modelling the main ionospheric trough. The trough parameters modelled by EDAM are compared with observations of an earlier study (Pryse et al., 2006), which used multi-station measurements of the phase coherent radio signals from the satellites of NIMS.

In this earlier study TEC observations at three ground receivers in the UK, at similar longitudes but separated in latitude, were used to image the trough by use of tomographic reconstruction. The current EDAM study was aimed at providing a fair comparison with the previous study, where enough data points were analysed to allow for the evaluation of the ability of EDAM. The data for the current study was taken from broadly the same period as the earlier study, so conditions of solar activity could be kept similar (10.7 cm solar flux).

The earlier study had only considered cases where the trough was prominent as relatively few troughs had been identified in the summer. No seasonal variations in trough behaviour could be established from these findings. Summertime troughs were also not considered for this study to keep it as similar as possible to the previous study. The trough profiles were confined to the equinox and winter period with the data set covering September to December 2002, inclusive. This period provided approximately 1950 latitudinal profiles of the trough, which was significantly larger than the 618 troughs of the earlier NIMS study. The period which included autumn, a season where the trough is prominent (Lee et al., 2011), also provided data that represented the general behaviour of the prominent troughs in the earlier study.

The use of the four months gave a fair representation of the prominent trough and was reinforced by Figure 6 of Le at al. (2017), where the data at 04 MLT for months 9 to 12 was representative of the prominent trough, in particular under low Kp. TEC characteristics of the summertime trough modelled by EDAM in June 2002 are presented in Section 5.6, which are different to those considered in the main study.

5.2 Data collection

The GPS data for September 2002 through to December 2002 was downloaded from the International GNNS Service (IGS) archive from the Crystal Dynamics Data Information System (CDDIS). Each downloaded data file holds the GPS measurements recorded at 43 receivers located across Western Europe shown in Figure 20. Across this period some receivers were unavailable, so GPS measurements from approximately 43 receivers were assimilated into EDAM each time interval. EDAM is used to convert the measurements into TEC via the process in Chapter 3, and then to assimilate the vales of TEC into a background model (IRI2007). The grid was restricted to 45.0°N to 70.0°N latitude and 20.0°W to 40.0°E longitude. The assimilated TEC was contained within the altitudes of 100 km to 1000 km and having a separation of 10 km between each point. The TEC was considered negligible at lower altitudes.

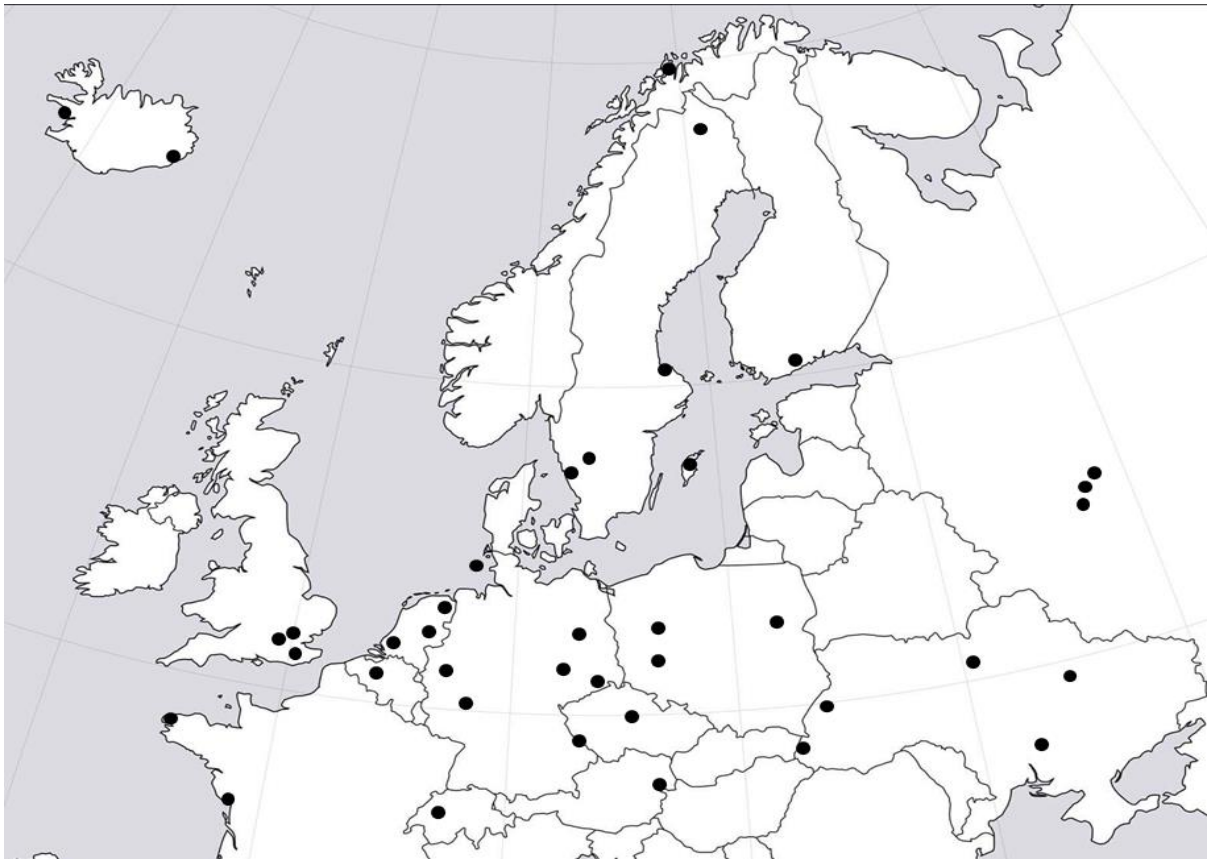

Figure 20 - A map showing the locations of the receivers used in the assimilation.

Once the assimilation was completed, the electron density differences between the starting background grid and the newly updated grid, the difference files, were used to recreate the grid after assimilation for every 15-minute interval. This made it easier for analysing the data by calling in the file and specifying the area we were going to focus on. Data files were produced from this re-creation that held the key information needed to define the trough. These were the electron density values, given as log electron densities, the latitude, longitude and altitude axis of the grid and the time epoch.

Another product of the grids re-creation was image plots of the final Vertical TEC (VTEC). The VTECs were obtained by integrating the electron density values, in the vertical dimension. The difference between the VTEC here and TEC mentioned in Chapter 3, otherwise known as

slant TEC (sTEC), is that sTEC is calculated directly along the ray path from satellite to receiver. However, VTEC is the summation from the receiver vertically up to the edge of the ionosphere, in this case up to 1000 km. Figure 21 shows the difference between the two. VTEC was used in this study.

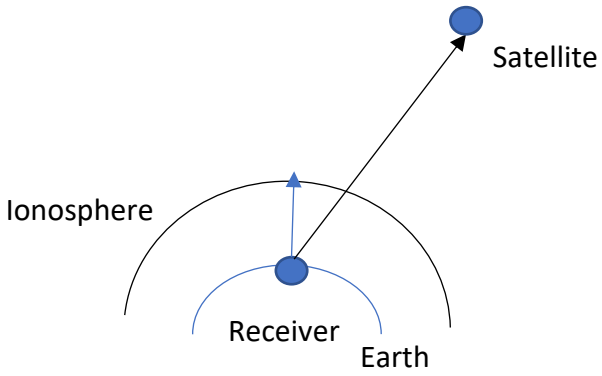

Figure 21 – A diagram showing the difference between Vertical and slant TEC. The Blue arrow depicts the Vertical TEC, from the receiver directly up to the edge of the ionosphere. The black arrow depicts the slant TEC, from the receiver directly to the satellite.

5.3 Parameterisation

The modelled troughs in the EDAM grid, an example of this is shown in Figure 22, have been characterised in terms of parameters that can be used to represent the trough position, depth and wall gradients. For this the latitudinal profile of the VTEC at 0.0°E has been considered, which is representative of UK longitudes. The time epochs are located on the hour between 16:00 and 07:00 UT for this study as this is the time for the prominent appearance of the main ionospheric trough and provides enough samples for a statistical study.

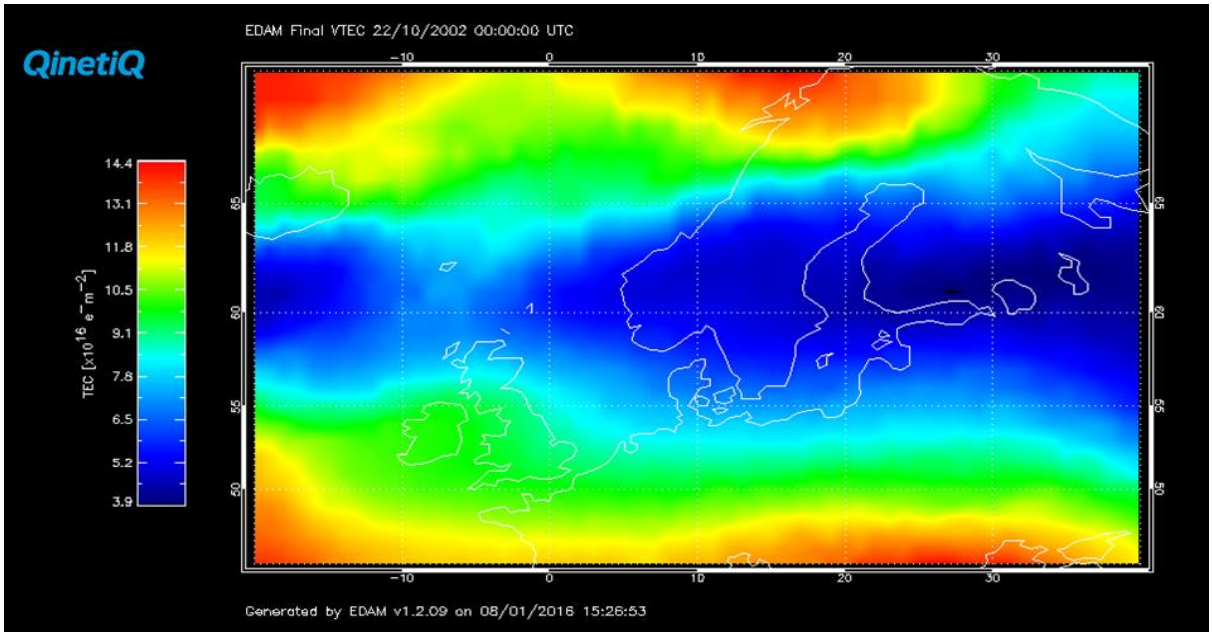

Figure 22: Vertical TEC through the EDAM grid at 00:00 UT on 22 October 2002. The spatial coverage of the figure extends from 20.0°W to 40.0°E and from 45.0°N to 70.0°N. The trough extends across the field-of-view with its minimum TEC of approximately 4.0 TECU near 60.0° N.

The parameters characterising each trough are illustrated in Figure 23, which shows a typical latitudinal profile of the vertical TEC through a trough. The set of parameters includes the latitude and TEC of the trough minimum (T_M) and the latitude and TEC of the extreme points at 50.0°N on the equatorward extreme (D_E) and at 70.0°N on the poleward extreme (D_P). Intermediate points are also identified. For these the average TEC over the latitudinal profile is determined, shown by the horizontal line in the Figure 23, and breakpoints are identified where this average level intersects the profile. The latitude and TEC at the equatorward breakpoint (B_E) and the latitude and TEC at the poleward breakpoint (B_P) are determined. Additional points are also identified at a latitude halfway between the trough minimum and the equatorward breakpoint, the equatorward half point (H_E), and at the latitude halfway between the trough minimum and the poleward breakpoint, the poleward half point (H_P). The set of parameters enables the gradients on the trough walls to be determined, on either side of the minimum. One additional point is identified where the TEC reaches its maximum value on the poleward side of the trough minimum (P_{max}), if it exists, with the latitude and

TEC at this point being recorded. This maximum TEC is likely to be the effect of the boundary blob (Crowley, 1996) at the poleward extreme of the trough and at the equatorward side of the auroral oval.

The set of parameters match those used in the earlier study of Pryse et al. (2006) but there are differences that arise due to the different observing techniques.

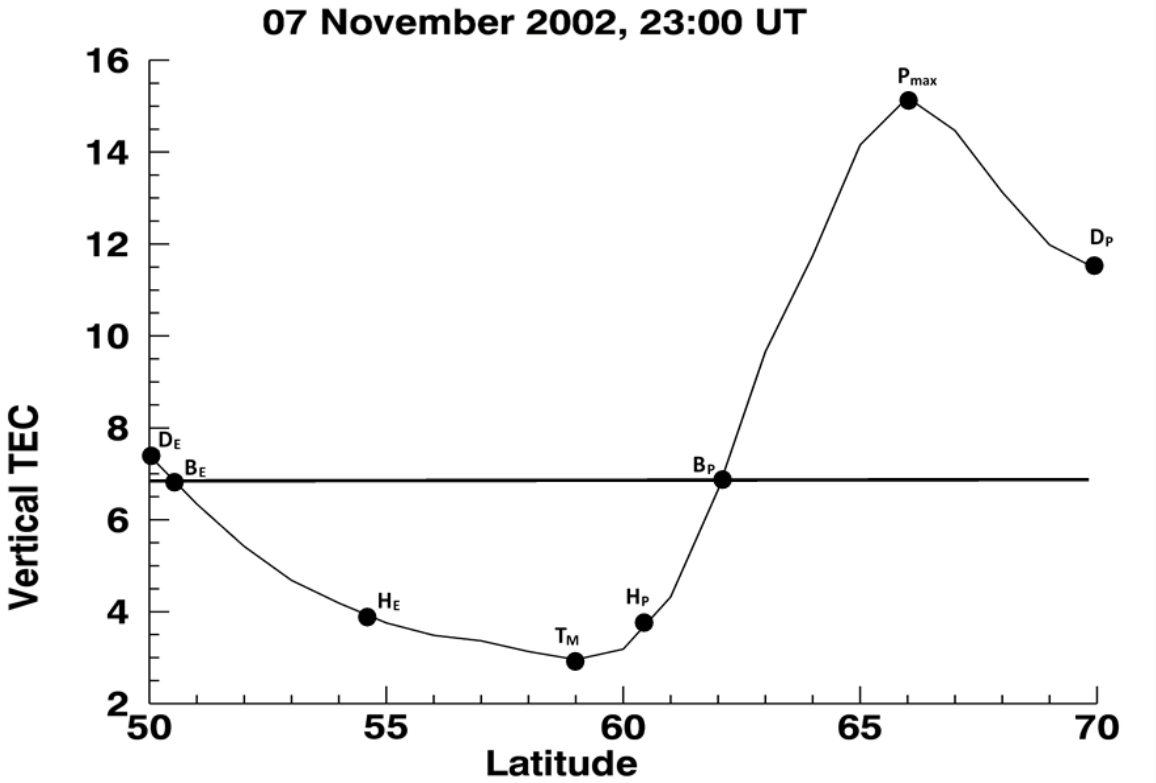

Figure 23: Example plot, for 2300 UT on 7 November 2002, of VTEC (in TECU) at a longitude of 0.0°E for the EDAM electron density grid as a function of latitude (in degrees). It illustrates the set of parameters used to characterise the location and shape of the main ionisation trough. The horizontal line shows the average TEC over the latitudinal profile, and breakpoints are identified where this average level intersects the profile. The trough is characterised by the parameters: the trough minimum (T_M), equatorward extreme (D_E), poleward extreme (D_P), equatorward breakpoint (B_E), poleward breakpoint (B_P), equatorward half point (H_E), the poleward half point (H_P) and the poleward maximum (P_{max}). The half points are used to characterise the shape of the trough in the vicinity of the trough minimum.

5.4 Database

The data are sorted with respect to time epoch, starting at the beginning of each month and ending at the end of the month, using Microsoft Excel. A 3-hourly Kp index was obtained via the UK Solar System Data Centre (UKSSDC) and is added to the database. The next step in the process was to sort all the hourly sets of parameters into three categories, low, mid and high. Low Kp index is defined as equalling 0 to 2+, Mid Kp index is defined as equalling 3– to 4 and high Kp is defined as being equal to or greater than 4+. This process is repeated for each month and brought together in one large database.

Using the parameters defined in Section 5.3, statistics that included standard deviation, medians and means were calculated on each of them.

5.5 Results

Figure 24a shows the median latitude of the trough minimum (T_M) for each 1-hour interval and each of the three geomagnetic levels between 16:00 UT and 07:00 UT. Upper and lower quartile ranges were determined for each point on the graph. The medians of the quartile ranges were used to provide a representative interquartile range for the data points. The interquartile range is approximately 4.0° latitude and it is shown on two points only on Figure 24a. This is to avoid clutter on the plot. They are not shown on figures after this. There is overlap of the interquartile range on the three data sets for the different geomagnetic levels, but the trends in the data are clearly revealed. The black diamonds, corresponding to high Kp, show the trough minimum under disturbed geomagnetic conditions to be near 65°N at 16:00 UT and then moving equatorward to reach its lowest latitudes of about 52°-53°N between

02:00 UT and 05:00 UT. A retreat polewards is seen by 07:00 UT as the trough is filled by the ionisation production at dawn. The corresponding grey and white diamonds are for moderate and quiet geomagnetic activity and show similar trends but at increasingly higher latitudes as the activity is lower for each data series.

Figure 24b shows the corresponding plot for the mean latitudes of the trough minimum. In this case the bars show the standard error in the mean. The sequences of points show the same trends as for the median values, although with slight difference with the minimum values at high geomagnetic activity reaching 54°N-56°N between 02:00 UT and 05:00 UT, which is a higher latitude than that for the median values.

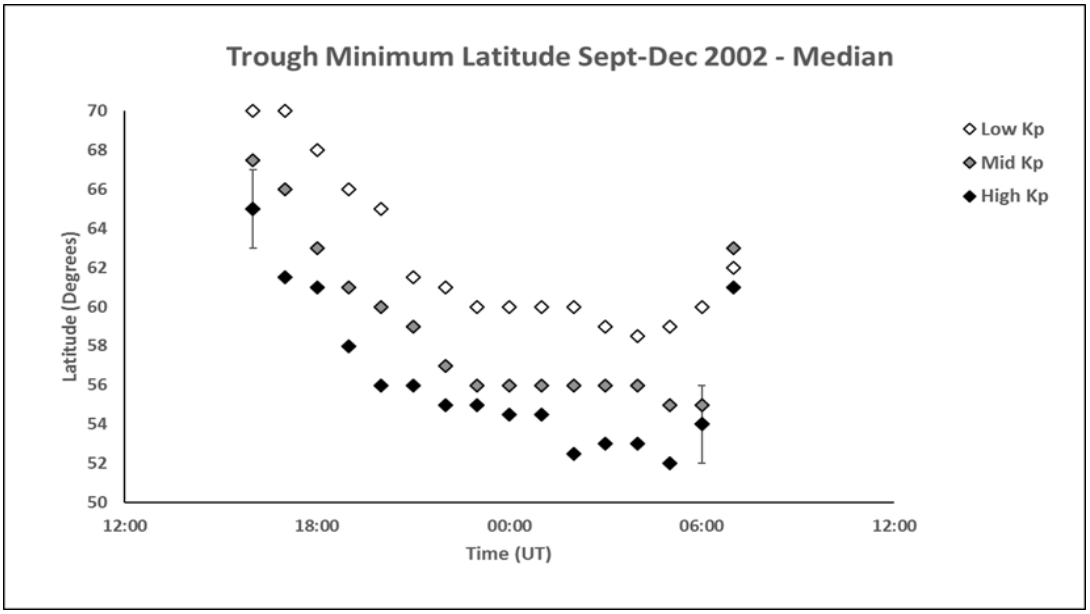

Figure 24a: Median latitudes for the trough minimum from 16:00 UT to 07:00 UT for low Kp (0 to 2+), mid Kp (3– to 4) and high Kp (≥ 4+). The representative interquartile range, shown on two points, is approximately 4.0° latitude. The trough minimum occurs at the highest latitudes in early evening and moves progressively equatorward with increasing UT before retreating rapidly poleward near 07:00 UT.

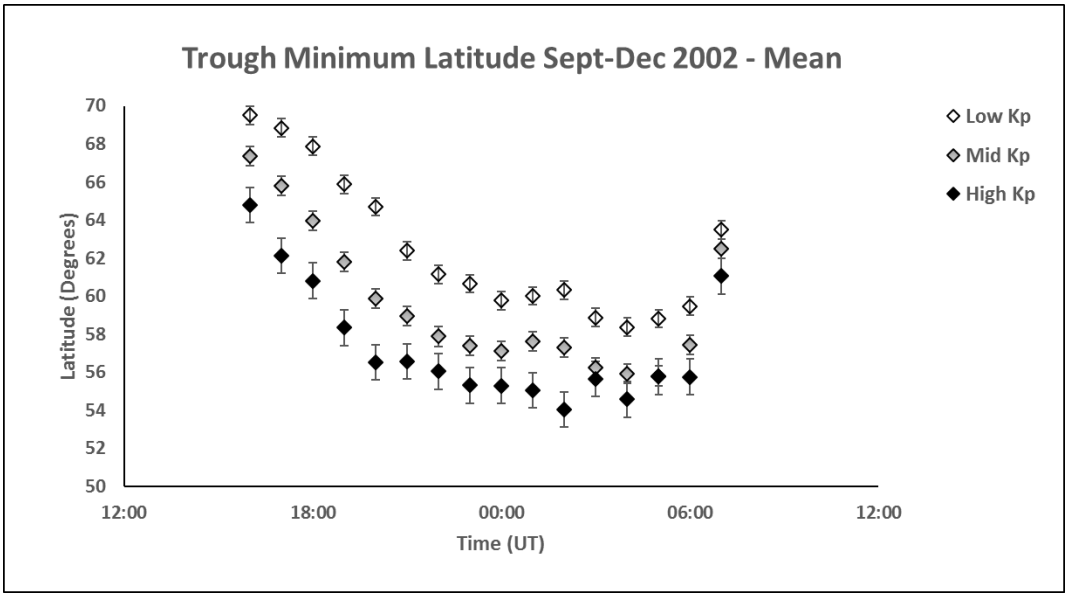

Figure 24b: Mean latitudes for the trough minimum from 16:00 UT to 07:00 UT for low Kp (0 to 2+), mid Kp (3– to 4) and high Kp (≥ 4+). The bars show the standard error in the mean for each point. The trends in the plot are the same as for the median values in Figure 24a.

The median and mean VTEC values at the trough minimum are shown in Figures 25a and 25b. The representative interquartile range for the median plot was approximately 2.5 TECU and the standard error in the mean for each mean value are indicated by the bars on Figure 25b. Figure 25a shows that the earlier VTEC are larger for the high Kp range, being more than 12 TECU at 16:00 UT. At times, beyond 21:00 UT and until 05:00 UT, the median values for the low Kp range tend to be less than 4 TECU, although there is no clear difference between the values for the three ranges of geomagnetic activity in this region given the overlap of the interquartile ranges. A similar trend is seen in the mean values. The effect of increased ionisation production at dawn again starts to be evident at 06:00 UT in these figures and is clear by 07:00 UT.

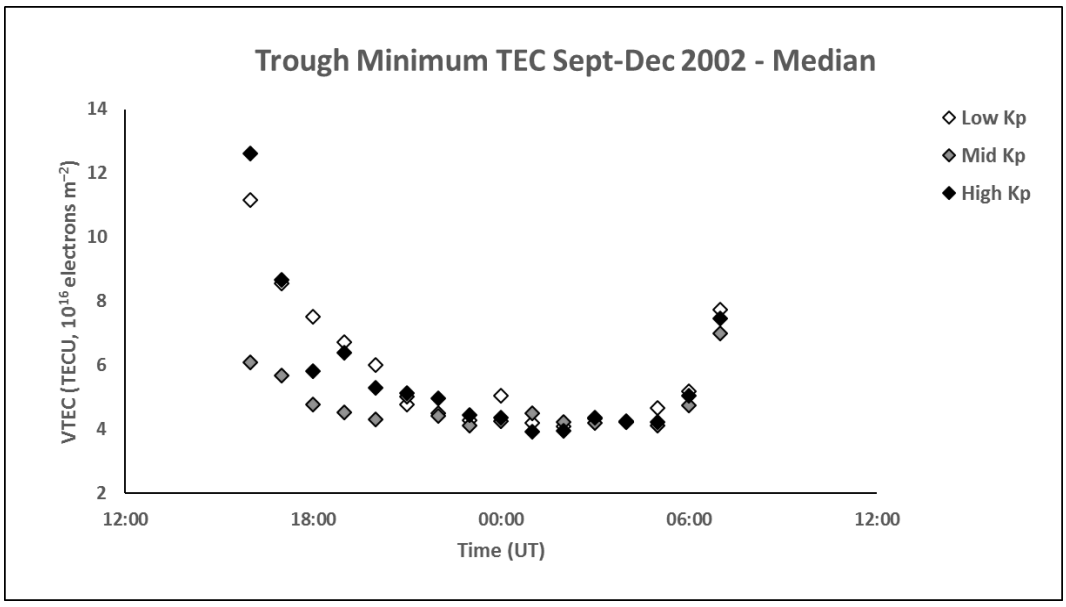

Figure 25a: Median VTEC for the trough minimum from 16 UT to 07 UT for low Kp (0 to 2+), mid Kp (3– to 4) and high Kp (≥ 4+). The representative interquartile range is approximately 2.5 TECU. Between 21:00 and 07:00 UT there is no clear difference between the values for the three ranges of geomagnetic activity.

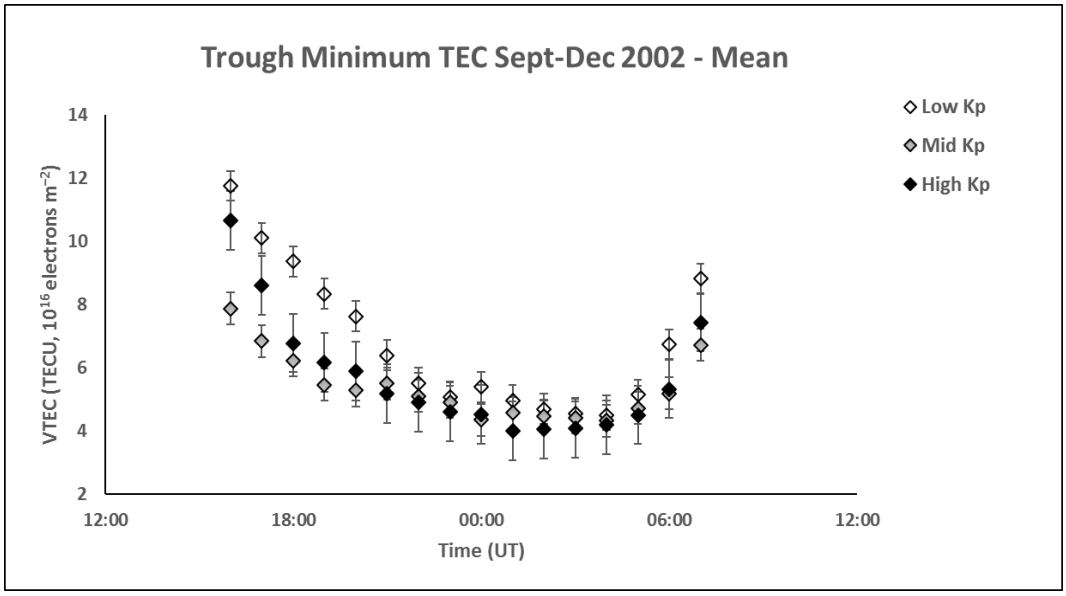

Figure 25b: Mean VTEC for the trough minimum from 16:00 UT to 07:00 UT for low Kp (0 to 2+), mid Kp (3– to 4) and high Kp (≥ 4+). The bars show the standard error in the mean for each point. Similarly, to Figure 25a, there is no clear difference in the VTEC between the three levels of geomagnetic activity at 21 to 07 UT.

Median and mean values were also considered for other parameters, but given the similar trends observed in the two parameters only the median values are shown for these. Consideration of the median values reduces potential effects of outliers in the presented data.

Figure 26 shows median trough widths, defined as the latitudinal range between the two break points (B_P and B_E). For most of the night the width is largest for the lowest Kp range, being between 11° and 13° after 21:00 UT. Distinguishing between the other two Kp ranges is not so clear, with both tending to show variable widths of between 9° and 11° latitude with lowest values occurring between 23:00 UT and 04:00 UT.

Figure 27 shows the median trough depth, defined as the difference between the average VTEC of the profile (VTEC at the breakpoint) and its value at the trough minimum. There is

no clear dependency on Kp, with each activity range showing values below 4 TECU from 18:00 UT and reaching consistently lower values of 2 TECU or less from about 03:00 UT.

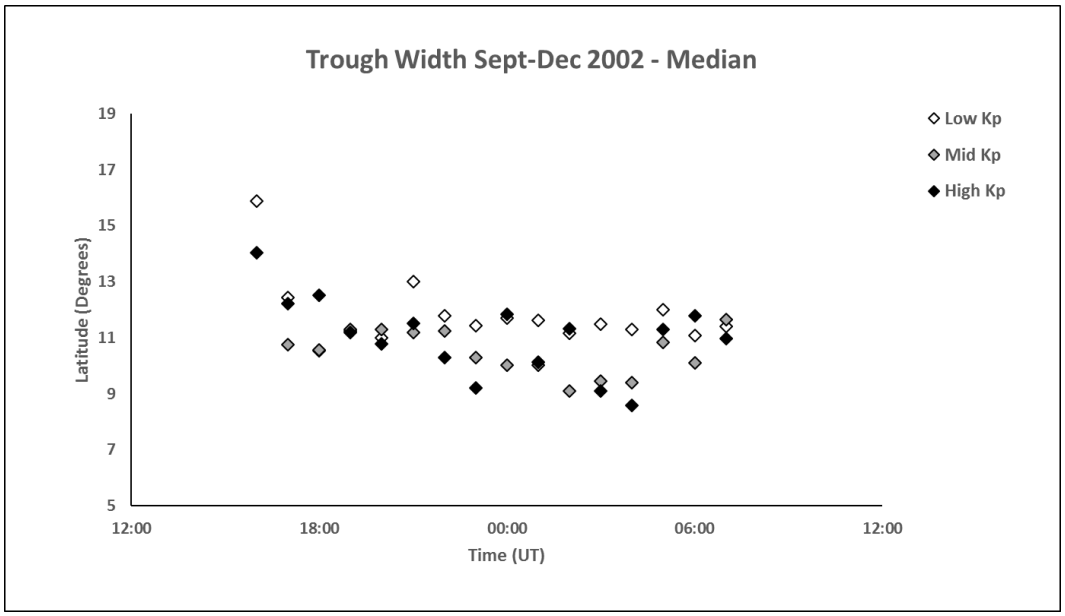

Figure 26: Median trough widths from 16:00 UT to 07:00 UT for low Kp (0 to 2+), mid Kp (3– to 4) and high Kp (≥ 4+). The representative interquartile range is approximately 2.5° latitude. Between 21 and 04 UT, the trough width, of 11°-13° latitude, for the low Kp is generally larger than the widths for the other geomagnetic activity levels.

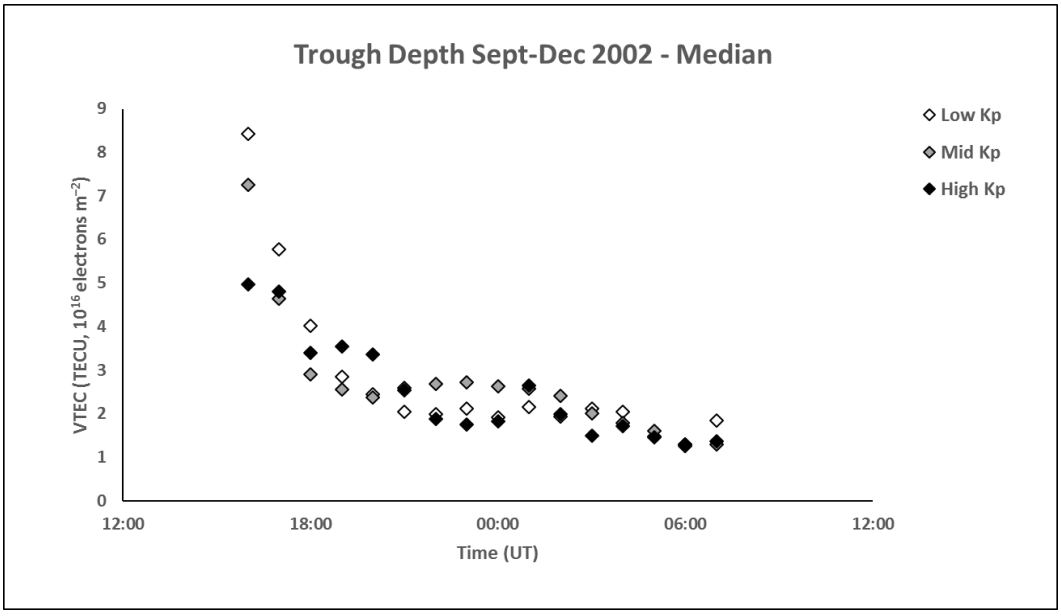

Figure 27: Median trough depth from 16:00 UT to 07:00 UT for low Kp (0 to 2+), mid Kp (3– to 4) and high Kp (≥ 4+). The representative interquartile range is approximately 1.5 TECU. There is no clear dependency of the trough depth on geomagnetic activity.

Evidence of asymmetry in the trough shape is seen in the equatorward and poleward half width of the trough (Figures 28a and 28b respectively). These are the widths from the equatorward breakpoint to the trough minimum and from the minimum to the poleward breakpoint. Median values for the equatorward half width are generally between 4° and 8° in latitude with those for the lowest geomagnetic activity tending to be largest until about 02:00 UT. Values for the poleward half width are generally between about 4° and 6° latitude. The width tends to be largest for the highest Kp range. The suggestion here is that geomagnetic activity affects both the equatorward and poleward sides of the trough.

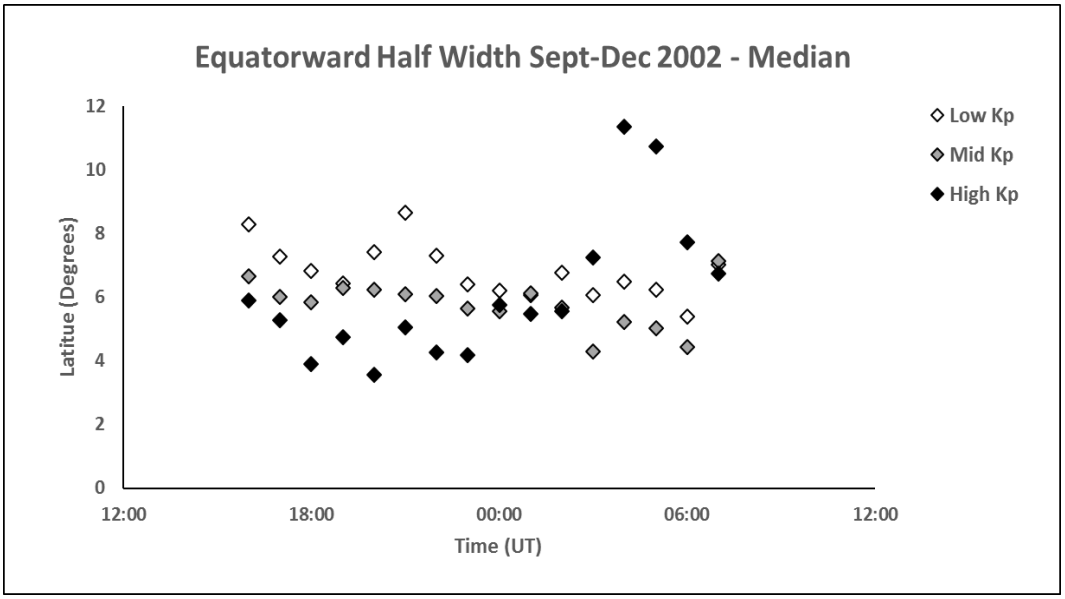

Figure 28a: Median equatorward half width of the trough from 16:00 UT to 07:00 UT for low Kp (0 to 2+), mid Kp (3– to 4) and high Kp (≥ 4+). The representative interquartile range is approximately 3.0° latitude. The equatorward half width prior to 04 UT is generally largest for low Kp level and smallest for the high Kp level.

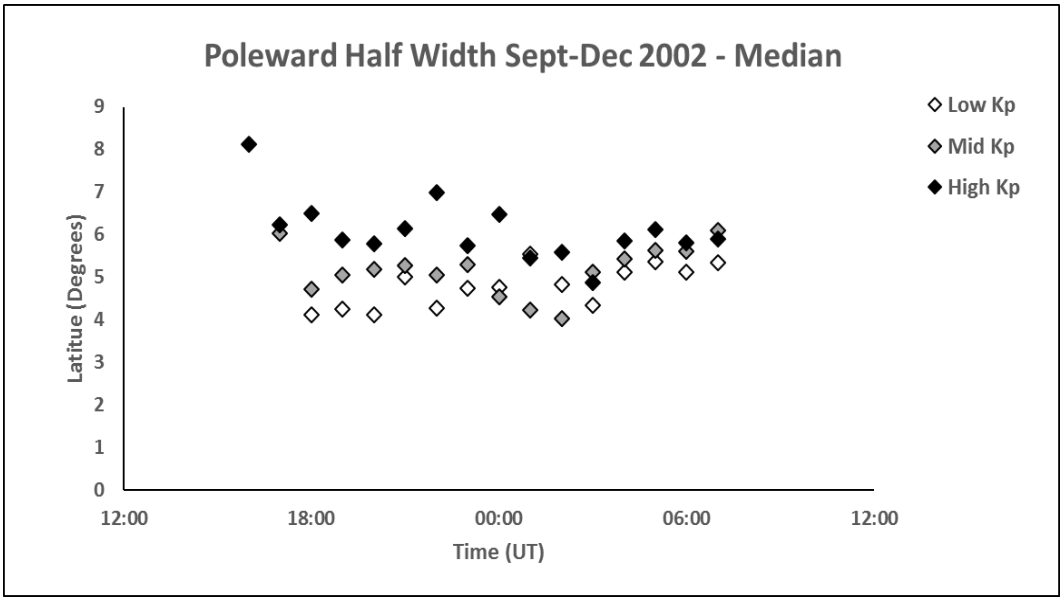

Figure 28b: Median poleward half width of trough from 16:00 UT to 07:00 UT for low Kp (0 to 2+), mid Kp (3– to 4) and high Kp (≥ 4+). The representative interquartile range is approximately 2.5° latitude. In contrast to Figure 7a, the poleward widths tend to be largest for the high Kp levels and smallest for the low Kp.

The median gradient of the equatorward trough wall taken from the trough minimum to the break point is at its steepest at earlier times with the initial values being more than 1 TECU per degree latitude (Figure 29a). It reduces to about 0.2-0.4 TECU per degree latitude from about 22:00 UT and then decreases further before dawn. Except for before 22:00 UT, the gradient of the poleward wall (Figure 29b) tends to be slightly larger than that of the equatorward wall, with values generally between 0.3 and 0.6 TECU per degree latitude but reducing in the pre-dawn hours. It is interesting that both gradients show a hint of increased values near midnight, for the mid geomagnetic range.

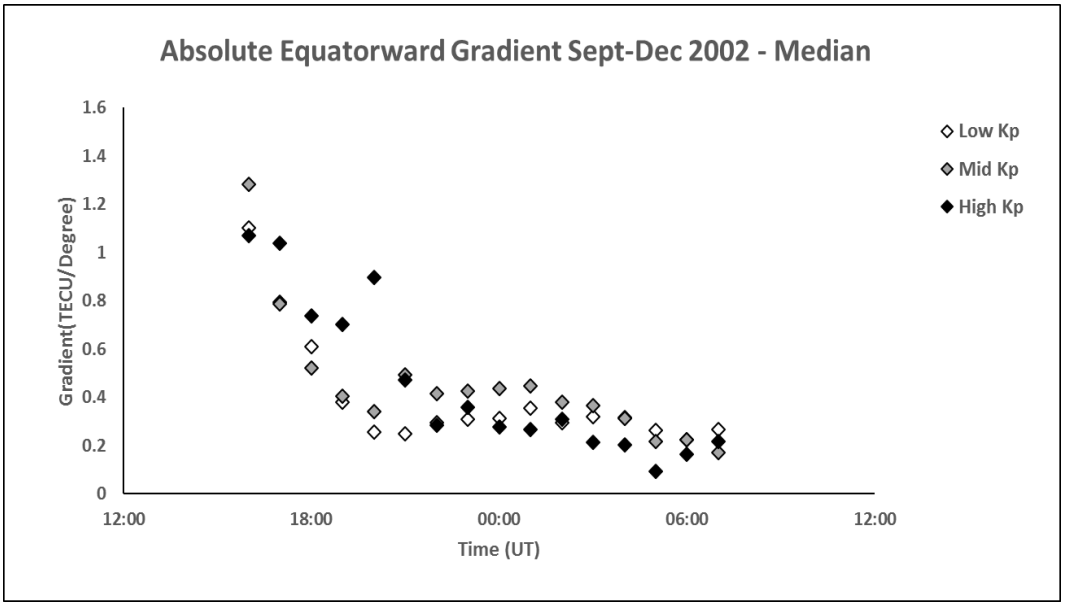

Figure 29a: Median gradient of the equatorward wall of the trough from 16:00 UT to 07:00 UT for low Kp (0 to 2+), mid Kp (3– to 4) and high Kp (≥ 4+). The representative interquartile range is approximately 0.25 TECU deg^{-1}. The gradient declines as the night progresses from in excess of 1.0 TECU deg^{-1} in early evening to less than 0.4 TECU deg^{-1} after about 21:00 UT.

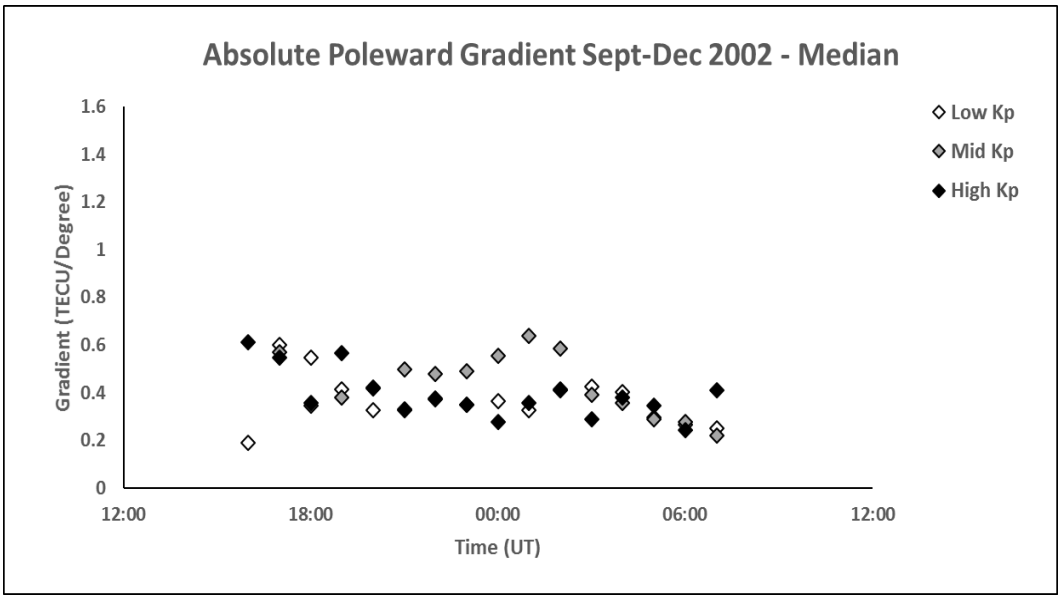

Figure 29b: Median gradient of the poleward wall of the trough from 16:00 UT to 07:00 UT for low Kp (0 to 2+), mid Kp (3– to 4) and high Kp (≥ 4+). The representative interquartile range is approximately 0.3 TECU deg^{-1}. The gradient is generally between 0.3 and 0.6 TECU deg^{-1} throughout the night.

Figures 30a and b show the median latitude of the maximum VTEC on the poleward side of the trough and the maximum VTEC of the feature, respectively. Caution is needed up to about 18:00 UT owing to a small number of data values, with the feature likely to have been poleward of the field of view. The median latitude is generally at higher latitudes for the lowest Kp range between 21:00 UT and 05:00 UT, being at about 68°N in the pre-midnight sector and moving to about 66°N in the post-midnight sector (Figure 30a). The latitude tends to be at about 64°N for the high Kp range in the post-midnight sector but increase near dawn. The maximum VTEC shows a general decrease over the course of the night, but there is no clear dependency on geomagnetic activity (Figure 30b).

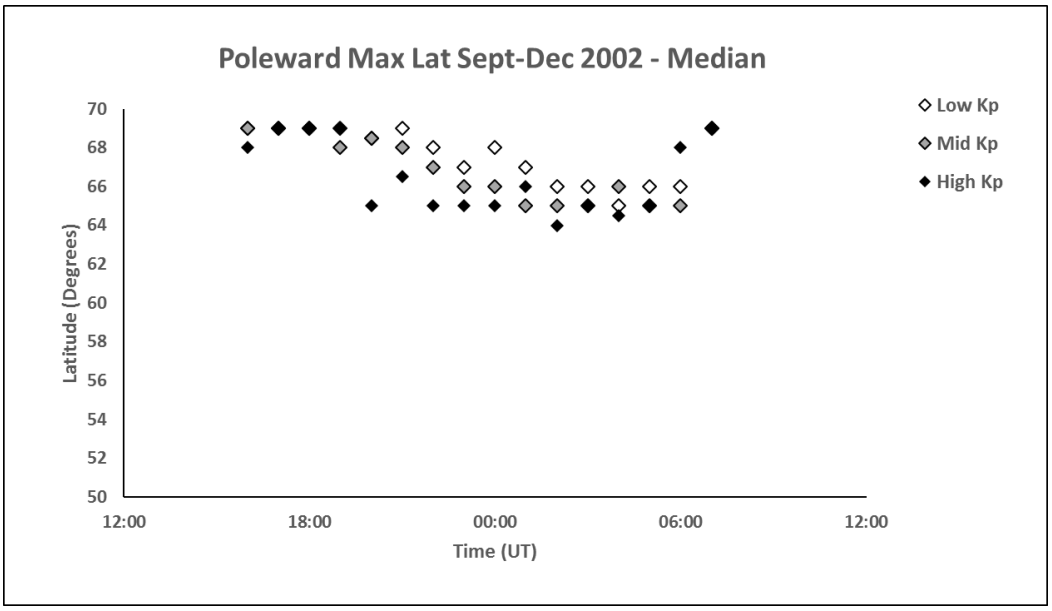

Figure 30a: Median latitude of the maximum VTEC on the poleward side of the trough from 16:00 UT to 07:00 UT for low Kp (0 to 2+), mid Kp (3– to 4) and high Kp (≥ 4+). The representative interquartile range is approximately 2.0°. The poleward maximum moves equatorward during the course of the night, with the location for the high geomagnetic activity being at the lowest latitudes but increasing near dawn.

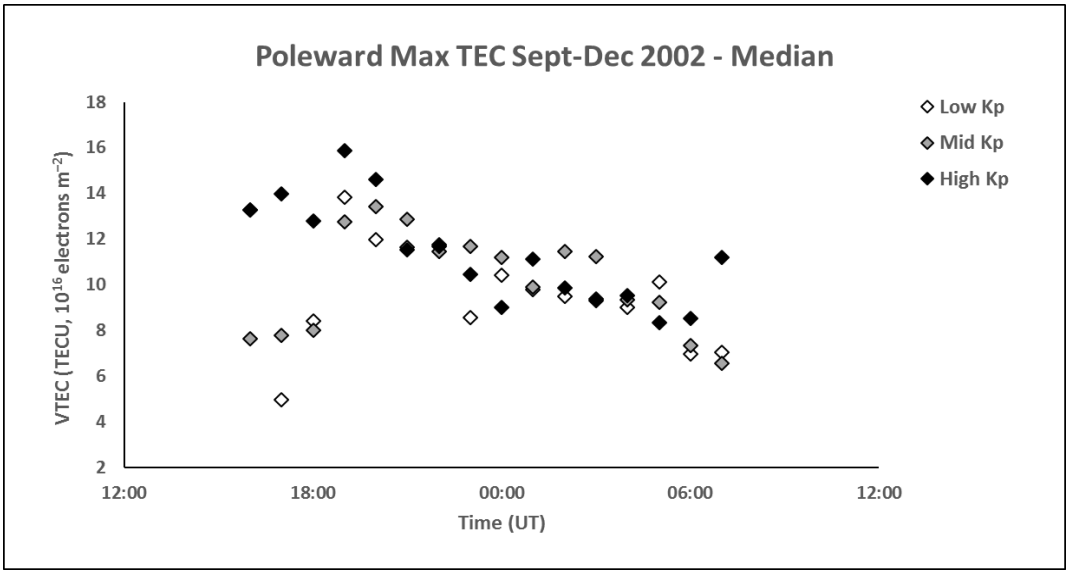

Figure 30b: Median of the maximum VTEC on the poleward side of the trough from 16:00 UT to 07:00 UT for low Kp (0 to 2+), mid Kp (3– to 4) and high Kp (≥ 4+). The representative interquartile range is approximately 5.0 TECU. The VTEC decreases from more than 12 TECU at 19 UT to about 8 TECU at 06 UT.

A comparison of the main trough in terms of the defined parameters from the NIMS tomography observations and the current EDAM/GPS modelling is presented in Figure 31. The trough is represented by the median values of the trough parameters for D_E (equatorward extreme), B_E (equatorward breakpoint), H_E (equatorward half point), T_M (trough minimum) H_P (poleward half point), B_P (poleward break point), P_{max} (maximum VTEC on the poleward side of the trough) and D_P (poleward extreme). The parameters are shown for three-time intervals. For the EDAM data, these intervals were for the confined hourly bins: 21 and 22 UT, 23 and 00 UT, 01 and 02 UT. For the NIMS data the corresponding time bins were for: 21:00 to almost 23;00 UT, 23:00 to almost 01:00 UT, 01:00 to almost 03:00 UT. The three levels of geomagnetic activity were considered. For the EDAM data, these levels were low Kp (0 to 2+), mid Kp (3– to 4) and high Kp (≥ 4+). The boundaries of mid and high Kp were slightly different for the NIMS data with mid Kp (3– to 4–) and high Kp (4 to 7+).

Comparison for low Kp shows good agreement, with the GPS VTEC values being marginally larger than the NIMS values. In both cases the curves show an asymmetry in a wide trough under low geomagnetic conditions with an equatorward wall of smaller gradient than that of the poleward wall. The NIMS results show clear indication of the boundary blob. It is likely that the EDAM model is not so able to resolve the signatures of this latitudinal confined ionisation blob with sharp gradients on either side. In general, the EDAM trough values are consistently higher than those of NIMS with a difference of up to 2 TECU, although it is markedly larger at the equatorward latitudes under quiet geomagnetic conditions. This difference is likely to be the consequence of the altitude of the satellites, with the long path lengths from satellite to receiver in the EDAM cases traversing topside ionisation, while the paths from the lower NIMS satellites do not. There is also some evidence of the equatorward wall becoming steeper as the geomagnetic activity increases in the pre-midnight sector.

The values of the parameters describing the shape of the trough obtained from the EDAM modelling are given in Appendix A for low, mid and high geomagnetic activity levels respectively.

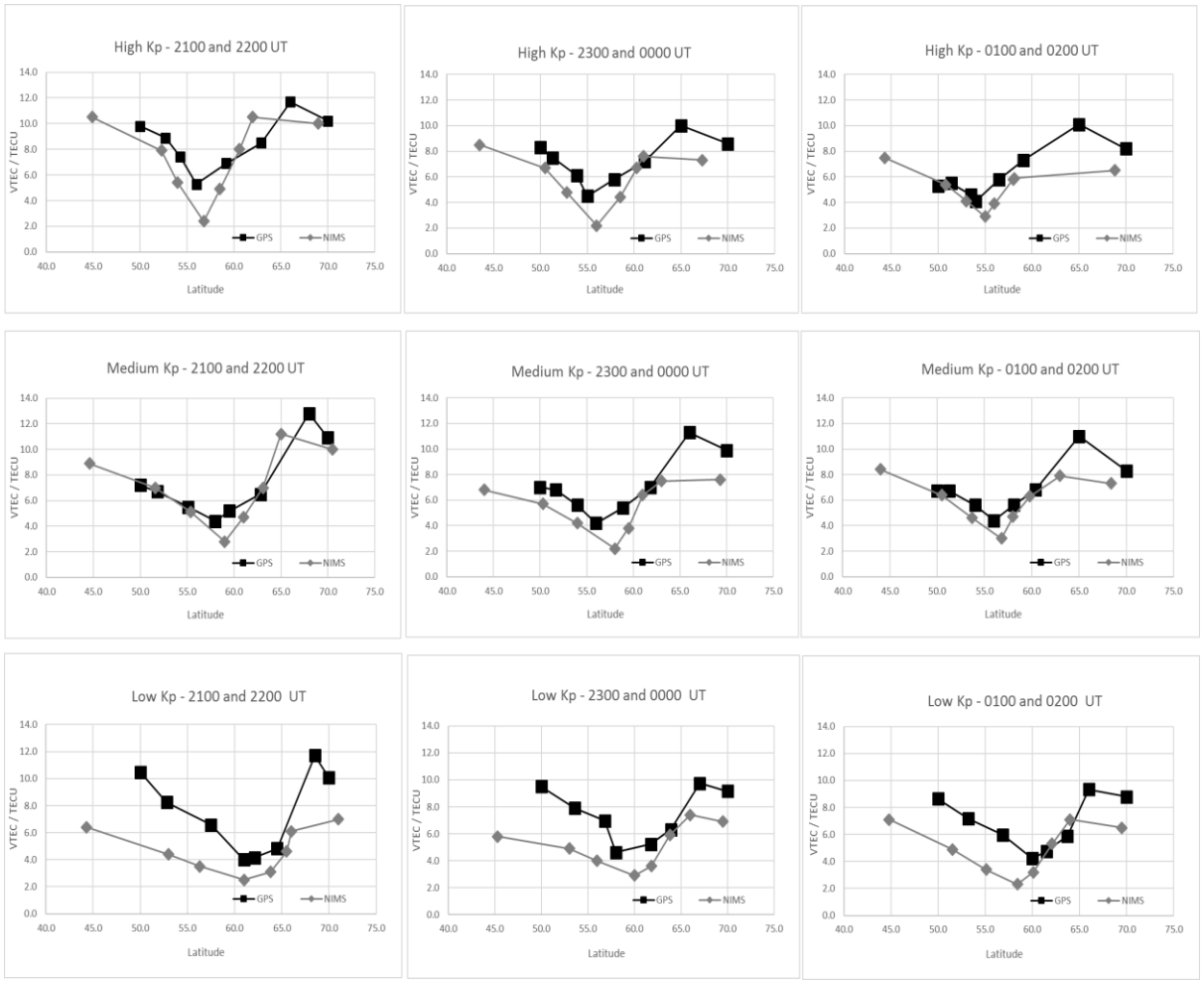

Figure 31: Parameterisation profiles from the EDAM model with GPS assimilated data (black) for low Kp (0 to 2+), mid Kp (3– to 4) and high Kp (≥ 4+) and for the NIMS tomography observations (grey) from Pryse et al. (2006) for low Kp (0 to 2+), mid Kp (3– to 4–) and high Kp (4 to 7+). The points show the median values for D_E (equatorward extreme), B_E (equatorward breakpoint), H_E (equatorward half point), T_M (trough minimum), H_P (poleward half point), B_P (poleward break point), P_{max} (maximum on poleward side of the trough), D_P (poleward extreme) for three time bins. The times on the Figure are for the confined GPS bins: 21 and 22 UT, 23 and 00 UT, 01 and 02 UT.

5.6 Discussion

The trends in the trough behaviour modelled by EDAM show general agreement with the earlier study of Pryse et al. (2006). Both studies made TEC observations using differential carrier phase observations. There were however significant differences between the two studies. The earlier study used the VHF and UHF signals from the low Earth orbiting (LEO) NIMS satellites received at four ground stations. The measured TEC was reconstructed using Tomography and the technique provided a latitude-versus-longitude image of the ionosphere during the 20-min duration of each satellite pass. VTEC was calculated through these images. The current study obtained TEC by using transmissions from GPS satellites at the much higher altitudes of about 20,200 km. These signals were monitored at a network of approximately 43 ground-based receivers across Europe and assimilated into EDAM to give the temporally evolving 3-D electron density grid. The VTEC was calculated as a function of latitude at the grid covering 0.0°E.

During the night, the equatorward motion of the trough minimum at each of the three geomagnetic activity levels (Figure 24a) was as expected from the study of Pryse et al. (2006). Figure 2a from Pryse et al. (2006) corresponds to Figure 24a in this current study. Both figures show the trend of the latitude of the trough minimum, with it moving equatorward from 18:00 UT until 06:00 UT. Both figures also display the effect of geomagnetic activity on the latitude, with the trough minimum, under high levels of Kp, at the lowest latitudes. In the current study the lowest latitude reached by the trough before dawn was approximately 52° N, 55° N and 58° N for the low, medium and high Kp ranges. The difference of about 6° latitude between the high and low Kp ranges is comparable with differences found in other studies. Lee et al. (2011) reported an equatorward shift of about 3°-5° latitude for the trough

minimum with the increased geomagnetic activity in their study. Figure 3 of the statistical study of Yang et al. (2015) showed a consistent decrease in magnetic latitude from low to high Kp values. It is important to identify that different observing techniques have been used and observations have taken place during different times in the solar cycle. An example of this is that Lee et al. (2011) used a GPS RO experiment on board the FORMOSAT-3/COSMIC satellites to infer the maximum electron density for the F2 region, NmF2, while the current study uses the assimilation of slant TEC from GPS measurements into EDAM that was then used to calculate VTEC.

The VTEC values of the trough minimum did not show a dependence on geomagnetic activity (Figure 25a), which is in keeping with the earlier study of Pryse et al. (2006). However, the minimum value in the current study was 4 TECU compared to the 2 to 3 TECU in the previous study. It is likely that the difference is attributed to the techniques used in obtaining the TEC observations. GPS observations were from the ground to satellite altitudes of about 20,200 km, whilst those for the NIMS satellites were to an altitude of about 1100 km. Electron densities at altitudes from 750km to 2000 km at 250 km altitude increments given by IRI2007 at 21:00, 00:00 and 03:00 UT on 20 October 2002 at 60°N were considered. For each time, and assuming an exponential decrease in electron density with height in this altitude range, a decay constant was determined. The decay applied to altitudes from 1000 km to the altitude of GPS at approximately 20,200 km gave TEC values, between 1000 km and the GPS altitude, of 0.6, 0.6 and 0.4 TECU for 21:00, 00:00 and 03:00 UT. While the decrease in electron density may not necessarily strictly follow the exponential decay, it suggests that TEC in the topside ionosphere, altitudes above 1000 km, contributes some 10% to the EDAM VTEC values of the trough minimum. Yang at al. (2015) also reported an essentially constant TEC at the trough minimum of about 4-5 TECU irrespective of geomagnetic activity. They state that high

geomagnetic activity causes the temperature associated with disturbed electric fields in the trough region to increase with a corresponding decrease in density at the trough minimum. It is indicated that investigation into a relationship is needed between the TEC at the trough minimum and the increases in temperature to help with understanding physical processes responsible for formation of the main ionospheric trough. Another factor in the formation of the trough minimum could be the role of the neutral wind which, as shown in Section 2.6, does influence the ionosphere. When they categorised the data by season, a small decrease in TEC was observed at the trough minimum in summer and equinox. This decrease was attributed to a loss mechanism such as chemical recombination. Lee et al. (2011) considered NmF2 observations and found that the values at the trough minimum were slightly larger under active geomagnetic conditions than under quiet geomagnetic conditions.

The scatter in the latitudinal width of the trough, defined as the range in latitude between the two break points (B_E and B_P), was large, ranging from about 9° to 13° latitude (Figure 26), but was smaller than the earlier study of Pryse et al. (2006). The largest width of some 11°-13° latitude tended to occur under low geomagnetic conditions after about 21:00 UT, with the width for the medium and higher Kp ranges at these times being between about 9° and 12°. The large scatter of width may arise due to variability in auroral activity. Zou et al. (2011) investigated the effect of substorms on the trough width in the Alaskan sector. They reported a rapid equatorward movement of the poleward trough wall at substorm onset with a narrowing of the trough and sometimes its disappearance. During the recovery phase the trough expanded back to higher latitudes.

The current study showed that the trough depth, from the level of the breakpoints to the trough minimum, for all Kp ranges tended to group together from about 18:00 UT with

median values of about 2-3 TECU (Figure 27) and with the scatter in the values reducing with increasing UT. At earlier times the values were larger with the largest tending to be at low geomagnetic activity. Values decreased below 2 TECU after about 03:00 UT with further reduction in scatter. The trough depths are suggested to be of a larger spread before midnight than at post-midnight. In the earlier paper of Pryse et al. (2006) reference was made to the different physical processes responsible for the formation of the trough in the pre- and post-midnight sectors. It may be that the different characteristic observed in the current study are also attributed to this. The pre-midnight trough often occurs near slow plasma drift at the interface between the westward flow at the poleward side of the dusk convection cell and the counter eastward co-rotating motion on the equatorward side (Spiro et al., 1978). After the Harang discontinuity near local magnetic midnight the trough may be a fossil from the earlier time in the eastward flow in the dawn sector as mentioned by Pryse et al. (2006), although the continuing decrease evident after 03:00 UT may be attributed to continuing chemical loss (Lee et al., 2011). The statistical study of He et al. (2011) considered NmF2 for magnetic activity Kp of less than 3 and categorised the data by season and hemisphere. They concluded that the depth of the midnight trough showed longitudinal dependency in the equinox seasons and summer and related this to the neutral winds and the configuration of the geomagnetic field. The main ionospheric trough was also shown to respond to solar wind velocities, where the position of the trough minimum varied with a periodic appearance of high-speed solar wind velocities.

The larger equatorward half width, measured from the trough minimum to the equatorward breakpoint, near midnight for the lowest Kp range (Figure 28a), was in keeping with the narrower equatorward half width at highest Kp levels in the earlier study, although there is substantial scatter in this equatorward parameter. As in the earlier study, it was rather

unexpected that processes on the equatorward side of the trough may be affected by geomagnetic activity.

The current study showed a poleward half width with some larger values near midnight under disturbed geomagnetic activity (Figure 28b), but as in the previous study the scatter was smaller than that for the equatorward half width. The results suggest an asymmetry in the trough width. Low geomagnetic activity has the larger equatorward half widths and smaller poleward half widths and higher geomagnetic activity have the larger poleward half widths and smaller equatorward half widths. Further study of the physical processes operative in the trough are needed to reconcile these observations with those of Zou et al. (2011) where the substorm activity rapidly moves the poleward trough wall equatorward.

As in Pryse et al. (2006) there was evidence of a decreasing gradient for the equatorward wall with respect to UT, during pre-midnight hours (Figure 29a). The general decrease continues to later times but at a smaller rate of 0.2 TECU per degree. There was evidence that the moderate geomagnetic data had the steeper gradient near midnight. The reason for this was not clear, but interestingly there was a similar observation for the poleward wall gradient shortly after midnight in the EDAM VTEC (Figure 34b) and likewise in the NIMS poleward gradient values.

Under quiet geomagnetic conditions the boundary blob on the poleward side of the trough moves equatorward in the hours near midnight (Figure 30a). There was also evidence of this at the more active geomagnetic levels, but the blob maximum is generally at lower latitudes under these conditions. The maximum VTEC decreases during the night for each level of geomagnetic activity (Figure 30b).

In summary, there is general agreement and consistency between the observations of the trough in the current study and those of the earlier reported observations, despite differences in the techniques. This broad agreement gives support for the application of EDAM with assimilated GPS TEC to model the main ionospheric trough. It reinforces the use of EDAM for monitoring the trough, and indeed to model other features in the ionosphere with latitudinal gradients on similar scales. Given the coverage of GPS satellites and the network of ground receivers, it opens the possibility of global monitoring of such features and for the use of the technique in scientific studies.

The current study has considered periods when troughs were prominent, so that they were in keeping with the earlier study. Summertime troughs were therefore not considered. Figure 32 shows the median TEC at the trough minimum for June 2003 for the three categories of geomagnetic activity. Apart from 00:00–05:00 UT under conditions of high Kp, all TEC values are larger than those obtained in the main study for September to December 2002, in keeping with increased solar illumination in June. They also show substantially more variability than for the autumn months. Some caution is needed in the interpretation of the high Kp values as the performance of the EDAM was reduced under these conditions for this month, which will be discussed further in Chapters 7 and 8. The differences in the summertime troughs in comparison with those at the equinox and winter provides evidence for seasonal variability in the trough modelled by EDAM. This is not the focus of this study and was not considered further.

This Chapter has considered data from 2002, specifically for comparison with the earlier results. However, for future studies, a larger database of GPS data is available from more recent years. Comparisons of the results from such studies of seasonal variation in the

European sector with studies such as that reported by Le et al. (2017) in the North American sector (60.0 to 90.0W) have the potential of addressing physical processes operating in the trough region, in particular because of the differences in the geographic/geomagnetic latitudes relation in the two sectors, and may give indication of the interplay between the roles of solar illumination and geomagnetic influences on the trough behaviour.

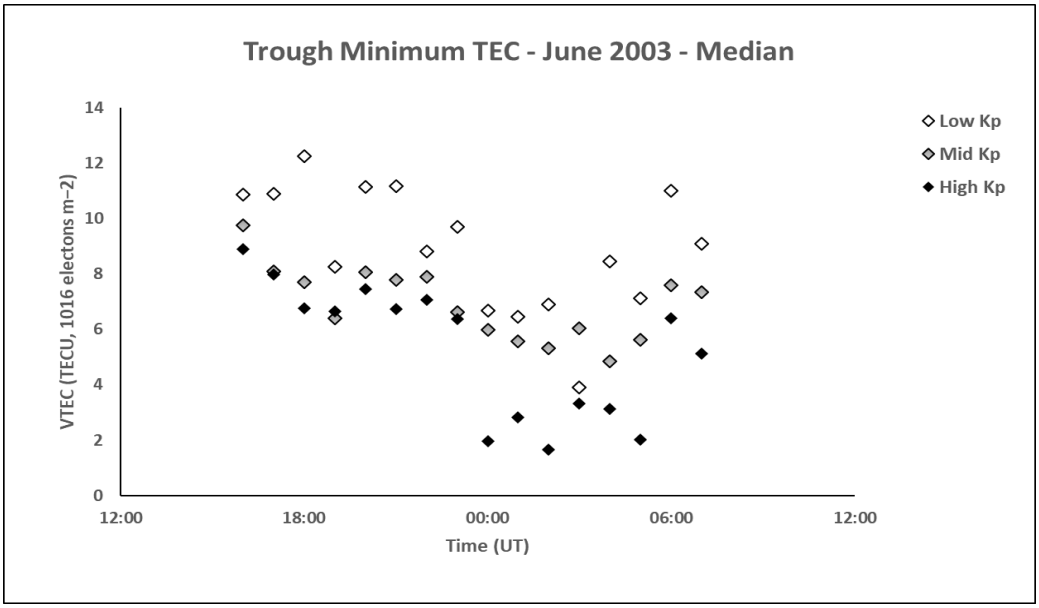

Figure 32 - Median VTEC for the trough minimum in June 2003 from 16 UT to 07 UT for low Kp (0 to 2+), mid Kp (3– to 4) and high Kp (≥ 4+). The representative interquartile range is approximately 2.5 TECU. The VTEC values are clearly larger than for the prominent trough considered for the main study, apart from between 00 and 05 UT for high Kp.

5.7 Conclusion

Statistical results have been presented of the main ionospheric trough, obtained from EDAM with assimilated GPS TEC. Approximately 1950 samples of the trough have been included in the study. The results have not only considered the width and depth of the trough but have also been used to parameterise the trough shape in terms of a set of well-defined parameters. These parameters were used in a previous study that used NIMS TEC measurements and tomographic imaging.

The results showed the expected behaviour of trough latitude, width, depth, and gradients of the trough-walls. The median values of the defined trough parameters showed broad agreement with the values obtained in the earlier studies, despite being obtained using a different technique. Trough minimum VTECs modelled by EDAM were generally some 1-2 TECU larger than that at the minimum observed by the NIMS tomography observations. This is in line with the higher altitude of the GPS satellites compared to the lower orbiting NIMS satellites, with the satellite-to-ground paths of the GPS observations traversing paths through the topside ionosphere. Whilst the electron density in the topside is expected to be low, considering the long path lengths it gives a measurable increase in the TEC.

This is the first time that EDAM has been used in a comparison of the trough with independent observations. Whilst there are differences between the EDAM results and the earlier observations, including the observing geometry, technique, time period of observations, and categorisation of the Kp levels, the similarities in the observed trough behaviour and its parameterisation are encouraging. This provides support for the use of EDAM for modelling the main ionospheric trough. It also provides evidence for the ability of EDAM to model large-scale structures in the ionosphere. Whilst the technique is unlikely, in its present form, to reveal latitudinally narrow structures on scales of typically 1°-2°, such as the boundary blob, the study provides convincing evidence of the ability of the technique to model features on the scale-size of the main ionospheric trough and its poleward and equatorward walls covering approximately 10° latitude.

Given the global coverage of EDAM and the GPS observations, the study shows the potential of the technique to image large-scale latitudinal features on a global basis, provided there are enough ground receivers available. It opens the possibility for using EDAM for statistical

studies of such features and their dependencies on, for example, season, geomagnetic and solar conditions.

Chapter 6

A SED/TOI Modelled and Observed in Western Europe using EDAM.

6.1 Introduction

The purpose of this Chapter is to present the observations of a TOI/SED using EDAM and SuperDARN in the Western European sector. Other data sources were used to corroborate the findings from EDAM and SuperDARN. The investigation presented, in this Chapter, is the first study to model and analyse a TOI/SED using EDAM assimilated GPS data. There are also not many observations of this feature in the European sector and this chapter shows the potential of EDAM to be used to conduct more studies in this area.

6.1.1 Storm Enhanced Densities

Early observations of a SED were conducted using incoherent scatter radar measurements from millstone hill where Evans (1970) originally described this feature. At the beginning of a magnetic storm, the TEC at sub-auroral latitudes starts to increase in the late afternoon, especially in the F-region, and exhibits an observed maximum around sunset, specifically in the North American sector (Evans, 1970). This was originally called the dusk effect by Evans (1970) and was related to an uplifting of the F region to altitudes where the recombination process occurs more slowly. The electron density persists longer leading to an apparent overall increase. For the F-region to be uplifted, Evans (1970) proposed two possible mechanisms. The first suggested that large neutral winds are set up in the F region by a storm that are in the direction away from the poles and act to drive the ionisation up the magnetic field lines. The winds were thought to be of the order of 100 ms^{-1}. The second suggested an east-west electric field is needed to drive a layer vertically upwards. The vertical velocity of the plasma would be equal to $\frac{\mathbf{E} \times \mathbf{B}}{B^2} \cos I$ where **E** is the electric field strength, **B** is the

magnetic field with B the magnitude of that field and I is the dip angle of the magnetic field. The vertical velocity would be opposed by the downward diffusion of the ionisation under the influence of gravity. This results in a net increase in the peak height of the F-region, but a rate considerably less than the vertical velocity driven by the east-west electric field. This net increase would depend on the production, loss and transport terms that Rishbeth (1967) discussed. Evans (1970) put forward, without too much calculation, that the east-west electric field, from the second suggested mechanism, would have to have a strength of approximately 5 mV m^{-1} to establish the vertical drift velocities of the plasma. This velocity would be equal to or greater than the neutral wind, mentioned previously at about 100 ms^{-1} as that velocity was established to be able to alter the height of the F-Region.

Other work around this time suggested that heating in the auroral region causes equatorward neutral wind enhancements. This would be able to drive the ionisation up the magnetic field lines, producing the uplifting of the F region. (Jones and Rishbeth, 1971)

It was Foster (1993) that first used the term Storm Enhanced Density (SED) to describe this dusk effect where it was mentioned that this SED often appears as a latitudinally distinct region of F region plasma, offset from the mid-latitude F-region. The SED location of occurrence, in latitude, is said by the author to decrease with increasing storm time activity, measured by use of the Kp Index, and by local time. Along with the dependency on geomagnetic activity, the SED is characterised by a low electron temperature within the region, an increase to the F region peak altitude and an enhanced topside electron density.

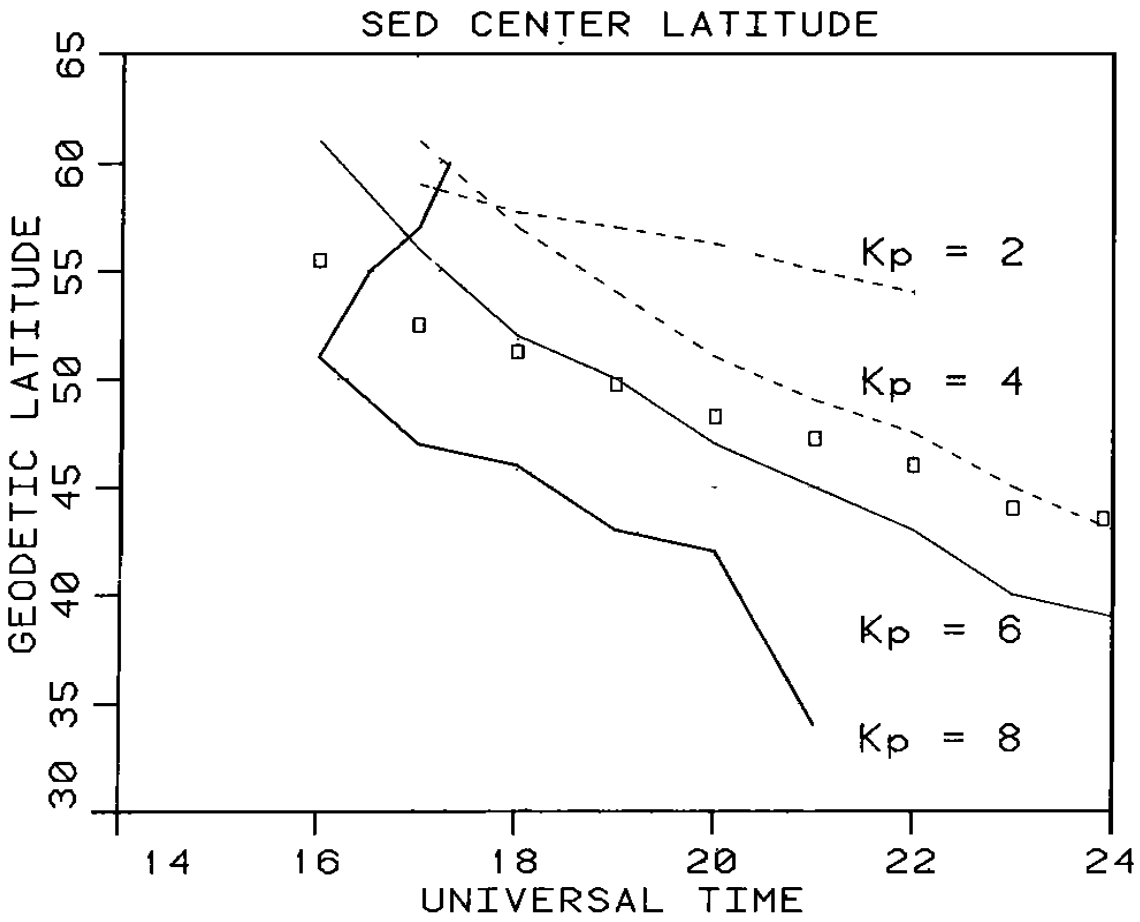

Figure 33 - Average latitude of the SED observed from Milestone Hill for different Kp indices. The squares on the diagram indicate the low latitude extent of the convection electric field, as observed by Millstone Hill, for Kp ≥ 6. (Figure produced by Foster, 1993)

While the SED is studied more during highly active days, it can be identified at as low as a Kp index of 2 (Foster, 1993). Figure 33 shows the average latitude occurrence of the SED, as observed by Millstone Hill Incoherent Scatter Radar, for differing levels of Kp. The figure, produced by Foster (1993), shows how the SED location reacts to increases in geomagnetic activity. It was also observed by the author that the latitudes of the SED decrease with local time at a rate of 2.5^{o} per hour.

There are many uncertainties regarding the production mechanism of the SED. As mentioned in the previous section two possibilities were discussed by Evans (1970), one relating to neutral winds the other relating to electric fields. Another possibility, involving auroral

enhancements, caused the neutral winds to drive the uplifting of the F region. (Jones and Rishbeth, 1971)

It was recently suggested that there are two leading contenders for the formation of the SED (Liu et al., 2016), one for the topside ionosphere enhancements, and the other for the bottom side ionosphere. Figure 9 in the Liu et al. (2016) paper shows the modelled absolute differences in electron density between storm time and quiet time as well as the electron density change rate caused by various other terms including neutral winds and $\mathbf{E} \times \mathbf{B}$ drifts. The topside enhancements were much stronger and were considered as the major contributor to the SED enhancements seen in GPS TEC data. These were generated mainly by the local upward $\mathbf{E} \times \mathbf{B}$ drift, between 50^{o} and 60^{o} geographic latitude, driving the plasma upward and changing the altitudinal distribution of the electron density. At the higher altitude the recombination rate of the charged particles is much lower where it is effectively raising the level of the peak density of the F-region, up to altitudes around 400 km. The vertical transport of the $\mathbf{E} \times \mathbf{B}$ drift would, according to the modelled results, exhibit a change of approximately 400 cm^{-3} in electron density.

This process also occurs in the bottomside ionosphere with the plasma being driven to higher altitudes, thus leaving an electron density decrease in the bottomside ionosphere. Liu et al. (2016) proceeded to explain the effect that neutral winds have in the bottom side ionosphere. Electric fields, imposed by magnetosphere-ionosphere coupling, cause plasma to flow in the anti-sunward direction in the dayside throat region towards the polar cap. This is the dayside region of the high-latitude two-cell convection flow pattern (Heelis et al., 1976). This flow would cause the neutral winds to flow in the same direction, poleward, due to frequent neutral-plasma collisions taking place (Deng and Ridley, 2006). These poleward neutral winds

act to move plasma downward, reducing the plasma density in the topside ionosphere. Therefore, neutral winds are stated to have the decisive role in SED generation in the bottomside ionosphere. In Figure 9 of Liu et al. (2016), the neutral winds are shown to increase the electron density, by approximately 400 cm^{-3}, at altitudes between 200 and 350 km and at geographic latitudes extending between 40° to 70°.

6.1.2 SED and Tongue of Ionisation

One phenomenon that can be attributed to the SED is the tongue of ionisation (TOI) (Sato, 1959; Knudsen, 1974). The feature is tongue-like in appearance and is an enhanced electron density structure that carries plasma from the dayside midlatitude ionosphere, from closed field lines, into the polar cap via the throat region where the field lines are opened. The difference between the two is that the SED is known as a latitudinally narrow feature compared to the TOI that extends from the mid-latitudes to polar latitudes, displayed in Figure 34.

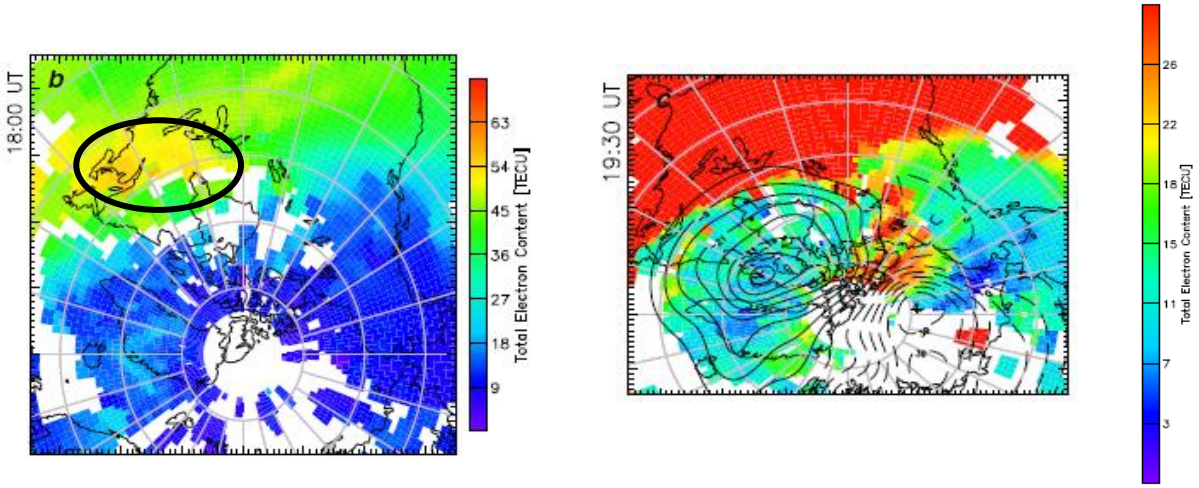

Figure 34 – The first TEC map (left) shows the SED base enhancements, marked by a black oval, compared to the bulk TEC seen at approximately 60° latitude at 18:00 UT. The TOI in the second TEC map (right) extends from the larger TEC region at 19:30 UT and with a TEC scale change is much more visible as the ionisation is picked up and flows over the polar cap. (Thomas et al., 2013)

In a study of a geomagnetic storm Thomas et al. (2013) used Super Dual Auroral Radar Network (SuperDARN) electric potential plots and GPS TEC maps generated by researchers at MIT Haystack Observatory using the Madrigal database to examine the formation of the TOI from a mid-latitude SED during a CME-driven storm on the 26 and 27 September 2011. Using geomagnetic and solar wind OMNI parameters (Figure 35), an online database for near-Earth solar wind magnetic field and plasma data among others, they showed that the locations of the SED occurrence were related to the interplanetary magnetic field (IMF) components and the dynamic pressure.

Figure 5 in the Thomas et al. (2013) paper, shown as Figure 35 here, showed, during a strong negative IMF B_z component of <-20 nT and a sustained positive IMF B_y component, a TOI formed over the North American sector at 18:30 UT. The TOI persisted for 1h 10 mins before the IMF B_z and B_y components are shown to steady out to around 0nT as shown in Figure 35, defined by the grey shaded region labelled SED/TOI. With this change in IMF, the convection electric fields retreated to higher latitudes, and caused a change in the two-cell convection pattern. The SED plume was still observed but could not enter the dayside cusp region. The SED persisted at a near-constant latitude for several hours, as defined the by shaded grey area in Figure 35 labelled SED/NO TOI. No ionospheric scatter from SuperDARN was observed within this 'fossil' and the source mechanism, that drew plasma from the midlatitudes into the polar cap, was no longer locally active. This fossil feature is similar to features observed

by Coster et al. (2006) where the SED plume in GPS TEC during storm days that did not convect over the pole region, indicating the lack of a TOI to connect the SED to the polar cap.

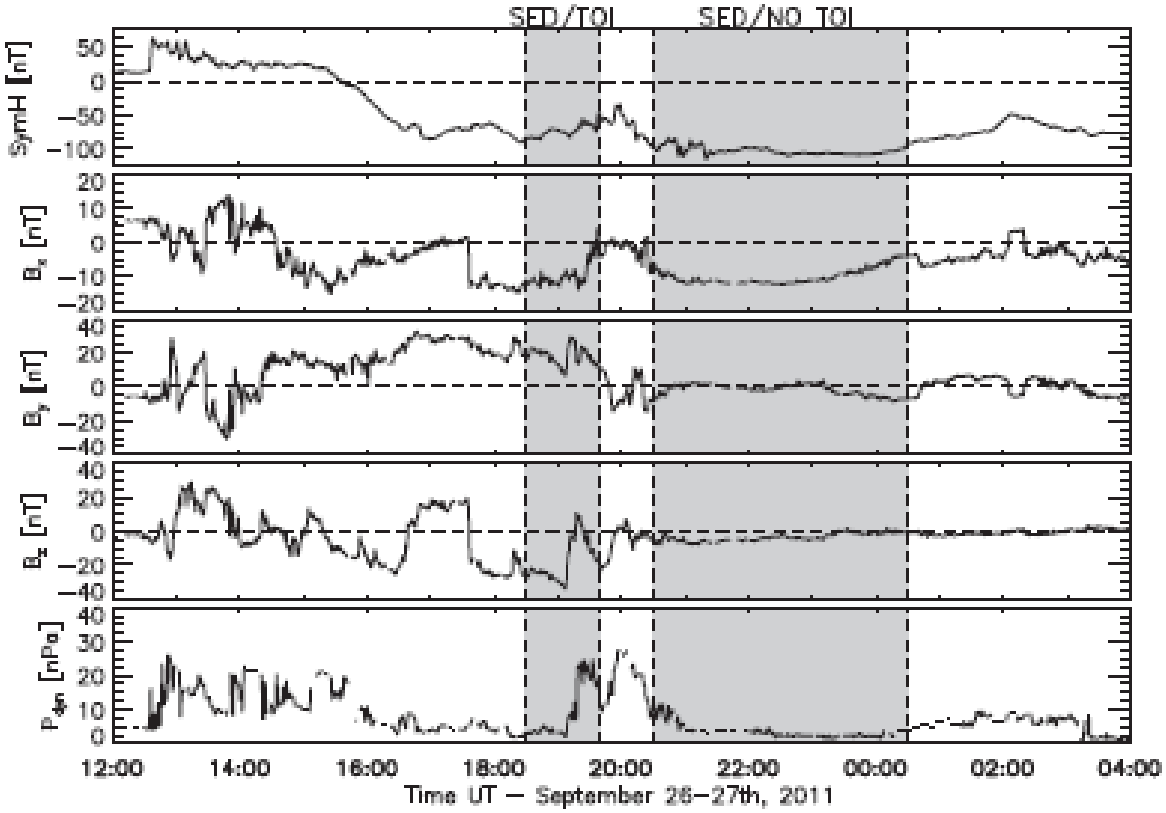

Figure 35 - Geomagnetic and solar wind OMNI parameters on 26–27 September 2011. The first shaded region is the interval from 18:30 to 19:40 UT to show when a TOI formed from the midlatitude SED. The second shaded region indicates a later period from 20:30 to 00:30 UT to show when no TOI was observed forming from midlatitude SED. Taken from Thomas et al. (2013).

Studies have primarily observed SEDs and TOIs in the North American sector as they appear more frequently over this region. The reason behind this is attributed to the offset between the magnetic co-ordinate system and the geographic co-ordinate system (VanZandt et al., 1972). The subauroral geomagnetic latitude and geographic latitude over Europe have a difference of about 4^{o} latitude, while over North America it is about 10^{o}. This enables the use of a multitude of receivers located at geographic mid-latitudes to study geomagnetic high-latitude phenomena. In addition, more of the high geomagnetic latitude region is in sunlight and so in a region of more photoproduction. The study by Coster et al. (2007) considered the European Sector, focussing on the SED and showing the differences between the SED location

in the North American and European sector. Across four different days, where the geomagnetic activity had Kp values of 6, the SED feature was extracted from hourly maps of averaged GPS vertical TEC data. The parameters for the SED plume base, including geographic latitude and longitude, were determined. The authors defined the location of the base of the SED, as where the enhancement of the SED separated from the region of higher TEC in the lower latitudes of the ionosphere. The VTEC values at the location of the SED plume base are shown to range from 25 to 60 TECU, but it is not indicated why there were differences in the maximum TEC observed during 3 consecutive days that was under the same geomagnetic activity, at the same longitude in the European sector. The smallest value on 25 April 2002 was 25 TECU at 40^{o}E while on 1 October 2001, the maximum was approximately around 55 TECU at the same longitude.

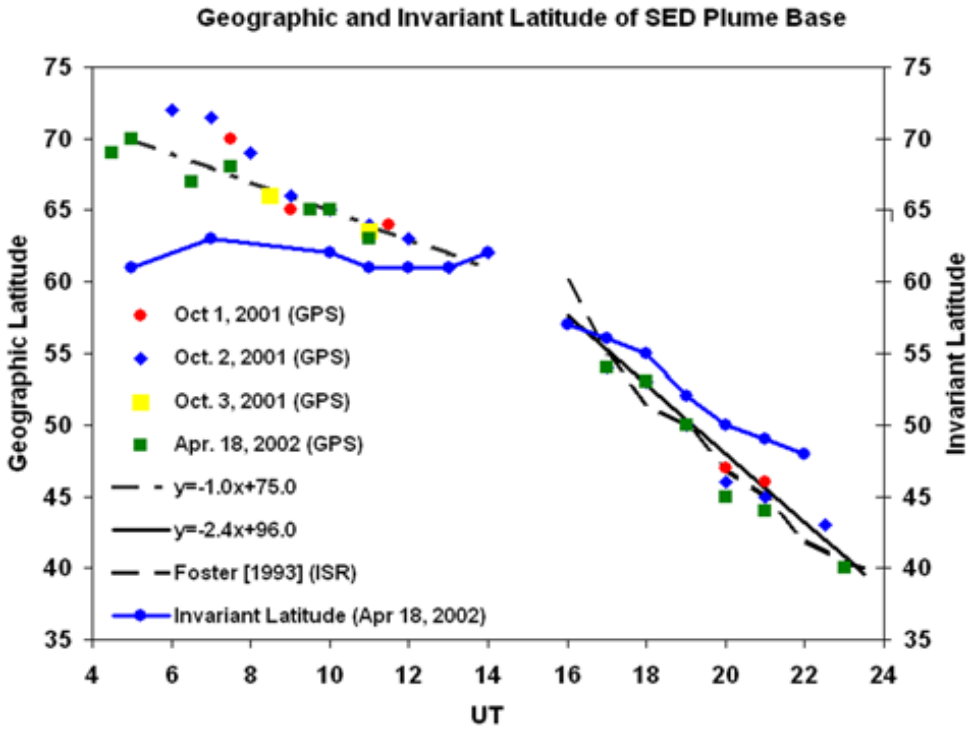

Figure 36 - Comparison of the latitude locations of the SED plume for the four events under conditions of Kp = 6. Each event, in general, form over the Russian sector between 4-6 UT. It would then pass over Europe between 6-15 UT and then move to the American sector between 18-24 UT. (Coster et al., 2007)

The latitude of the plume base shows a decrease from approximately 65°N at 09:00 UT to approximately 60°N latitude at 14:00 UT under conditions of Kp = 6. The results conclude that the latitudinal location of the plume base with respect to UT shows a consistent and repeatable pattern, shown in Figure 36.

TOIs are shown to potentially not depend on geomagnetic activity (Figure 37). A lot of observations take place during levels of high geomagnetic activity (Foster et al., 2005; Thomas et al., 2013) but there are studies that show, even under levels of high geomagnetic activity, a TOI is not formed (Coster et al., 2006). A survey of the Madrigal GPS TEC maps from 2009 to 2015 showed that TOIs are possibly not directly related to high geomagnetic activity (David et al., 2016). Figure 37 displays a histogram from that survey. The histogram shows the occurrences of the TOI to be high during times of low activity, defined by Kp index. Coster et al. (2006) also discuss instances of SEDs forming during levels of high geomagnetic activity but there are no TOIs formed from these.

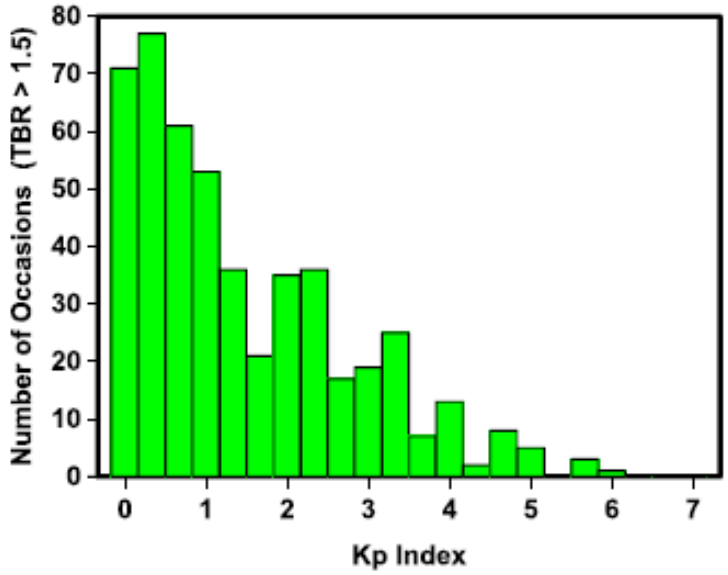

Figure 37 - A Histogram showing the occurrence of a TOI related to the Kp index for the year 2013, based on tongue-to-background ratios (TBR). (David et al., 2016)

6.1.3 Current Study

A SED and TOI event observed in the Western European sector took place on 30 September 2002 a day before a large geomagnetic storm. GPS VTEC maps were produced by EDAM and compared with data from SuperDARN. VTEC Difference maps between a quiet day on the 29 September 2002 and the 30 September 2002 were produced along with electron density height profiles to provide evidence of the SED and TOI. Other sources of measurements, including DMSP, geomagnetic indices and magnetic field data, were taken into account and used as evidence in supporting the observation of a SED/TOI.

6.2 Observations

GPS TEC maps from EDAM and the electric potential plots from SuperDARN comprise the main part of the study. Supplementary data sources were considered to complement and set the scene for the study of the SED and TOI. These included the IMF and the solar wind velocities and densities from ACE, the Kp index, the DST index, the Auroral Electrojet (AE) index and data from Defense Meteorological Satellite Program (DMSP).

6.2.1 IMF

Data from the ACE spacecraft were considered and are presented in Figure 38 for 29 and 30 September 2002. The effects would take time to arrive at the Earth as these measurements are taken at the location of ACE, L1 Libration point. This point is approximately 1,500,000 km away from the Earth and using a speed of the solar wind of about 300 kms^{-1} it would take

approximately 1h for the Earth to be affected. The data considered were the B_y, and B_z components of the interplanetary magnetic field in the incoming solar wind, and the velocity of the H^+ ions. On 29 September, day number 272, the magnetic field components were Bz positive, between 0 and 10 nT and B_y positive at approximately 10 nT. The velocity of the ions was stable at approximately 300 kms^{-1}. On 30 September 2002, day number 273, and just after 273.30 marked on the x-axis, there is a sudden increase in solar wind velocity to approximately 350 kms^{-1}. The B_z component of the interplanetary magnetic field starts to turn negative just as the velocity exhibits this sudden increase, going from 0 nT to approximately -20 nT over a short period of time. There is variability in the B_z component exhibited on 30 September, fluctuating between 10 and -20 nT for the time of interest, 09:00 UT to 14:30 UT. The B_y component in the early hours of the day decreases at the same time the Bz component decreases, from 20 nT to approximately 0 nT, shortly after this increase in solar wind is exhibited. The B_y component returns shortly after to 20 nT. After this return to a strongly positive B_y component, there is variability exhibited in the B_y component between positive and negative for a few hours before remaining positive until much later in the day. The data provided for these plots was obtained from the ACE science centre.

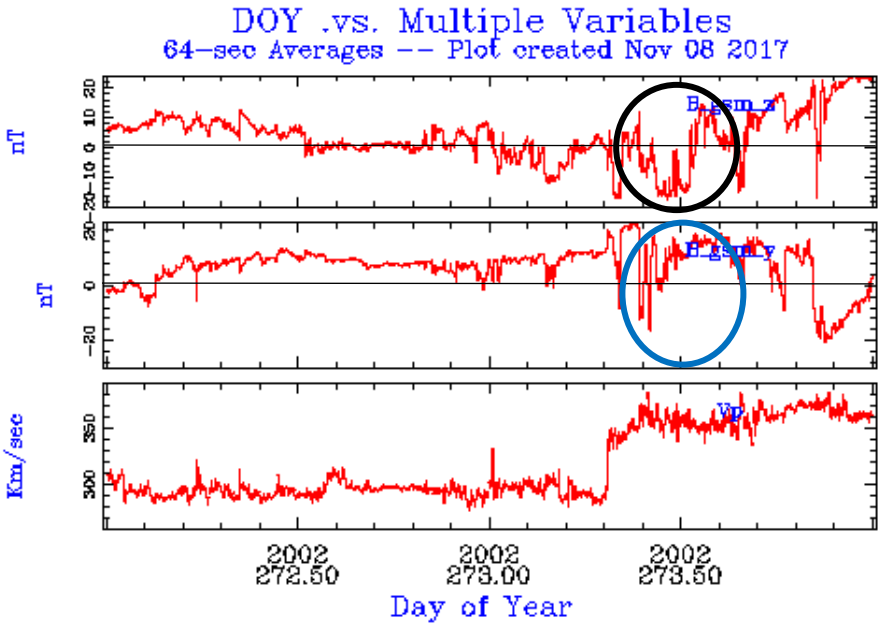

Figure 38 - A plot from ACE Science centre produced from the magnetometer and Solar Wind Electron, Proton, and Alpha Monitor aboard the ACE spacecraft. The plot shows the B_z and B_y components of the interplanetary magnetic field and the velocity, temperature and density of the H^+ ions or protons. There is a significant change in magnetic field from the quiet and stable field on the 29 (day number 272) September 2002 to the 30 September 2002. There is variability in the B_y component exhibited during the morning hours of 30 September 2002 before stabilizing to a positive B_y component during the time of interest (marked by a blue oval). The B_z component exhibits longer periods of negativity than 29 September but also shows more fluctuation between negative and positive during the times of interest (marked by a black oval). On the 30 (Day number 273) September 2002 at about 07:00 UT there is a sharp increase in velocity of the protons in the solar wind.

6.2.2 Kp Index

The 3-hourly Kp values for the 29 and 30 September are shown in Figure 39 beginning at 00:00 UT on the 29 September. A clear difference is seen between the two days with 29 September being quiet and 30 September being disturbed. During 29 September, the Kp index never reached above 2.0, meaning it was always at a low level of geomagnetic activity. On the 30 September at 03:00 UT there is an increase seen of the Kp index, meaning the ionosphere was suddenly becoming more active. This activity continuously increased until the Kp index

reached its highest value at 09:00 UT, and persisted at this level until 15:00 UT. The former day was used as a baseline for the values of the following day.

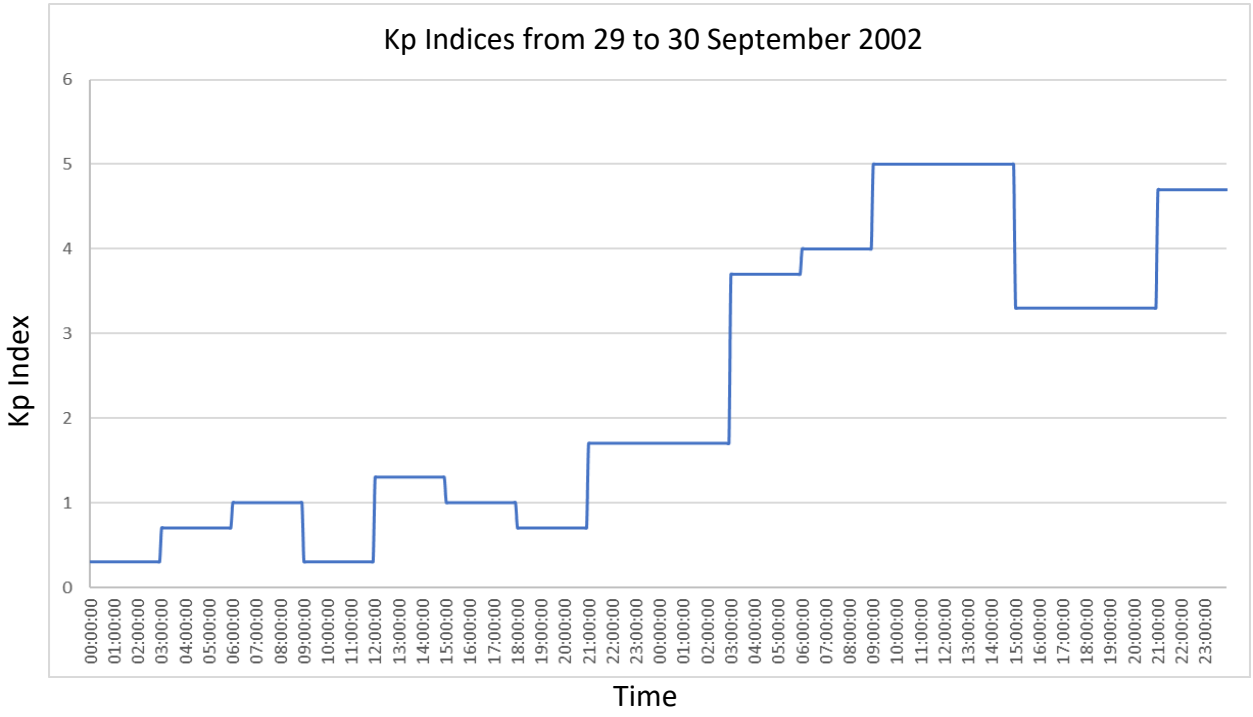

Figure 39 - A plot showing the Kp indices from 29 September through to the end of the 30 September. The 29 September was a quieter day, representative of the smaller Kp index values (between 0 and 2) exhibited globally this day. On the 30 September the Kp levels increase reaching its highest value at 09:00 UT, which has been previously described as levels of high geomagnetic activity. While not experienced the whole day, it did persist at these levels for 6 hours.

6.2.3 Dst Index

Figure 40 shows the hourly Dst, disturbance storm time index for 29 and 30 September 2002. On 29 September 2002 it is seen that the Dst index were positive and small in value, suggesting there was no active storm at this time. On 30 September 2002, beginning at 04:00 UT, a shift to negative indices is noted, and an increase in value, reaching a minimum of -49 nT at 15:00 UT.

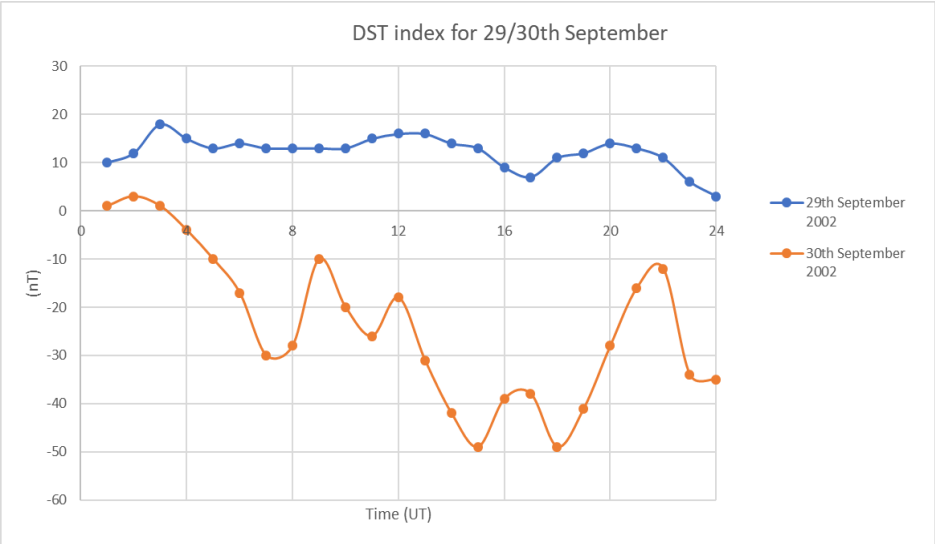

Figure 40 - A plot showing the Dst index values for the 29 and 30 September 2002. The Dst index between the quiet and active day are substantially different. The largest dip in the Dst occurs after 12:00 UT with values decreasing until to 15:00 UT.

6.2.4 AE Index

The AE index values for 29 and 30 September 2002 are shown in Figure 41. The disturbances to the magnetic field in the auroral zone on the 30 September are substantially greater than those seen on 29 September. The increase of approximately 200 nT in magnetic field variation is seen to begin from 04:00 UT. A maximum in magnetic field variation, value of 900 nT, is reached 14:00 UT, after which the variation begins to decrease rapidly and is gone by 20:00 UT.

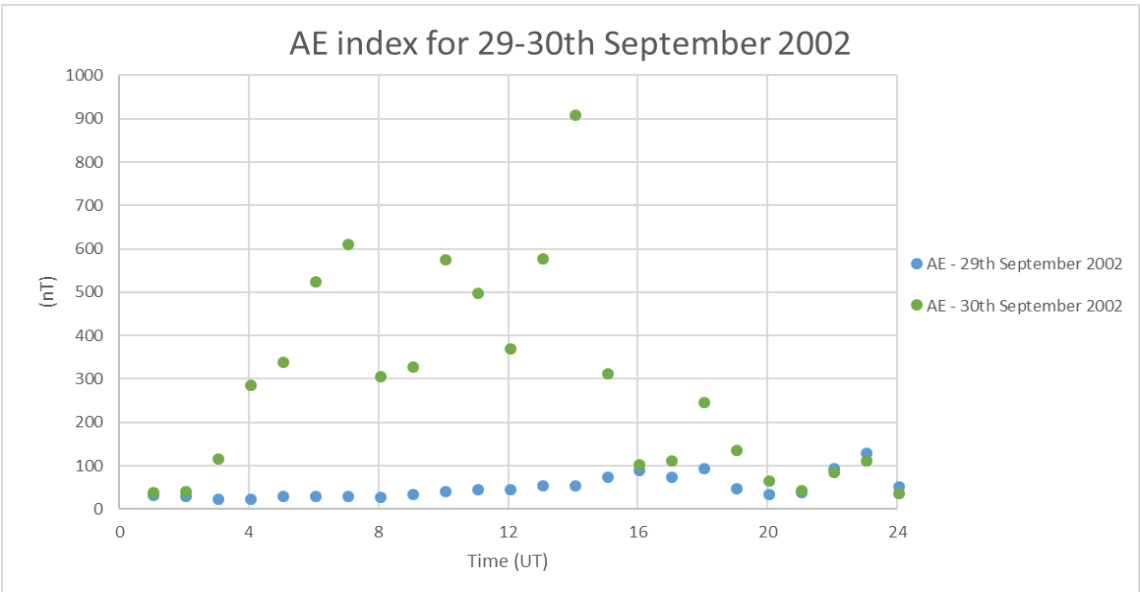

Figures 41 – The AE index for the 29 and 30 September is presented. The 29 September shows little variation in the AE index. The 30 September exhibited large variations in the magnetic field at the auroral zone.

6.2.5 EDAM

As previously mentioned, EDAM was used to assimilate the GPS data into a 3-D electron density grid with VTEC maps being produced on a latitude versus longitude grid. In this study VTEC maps were produced to identify the ionospheric phenomena, the SED and TOI on the 30 September 2002.

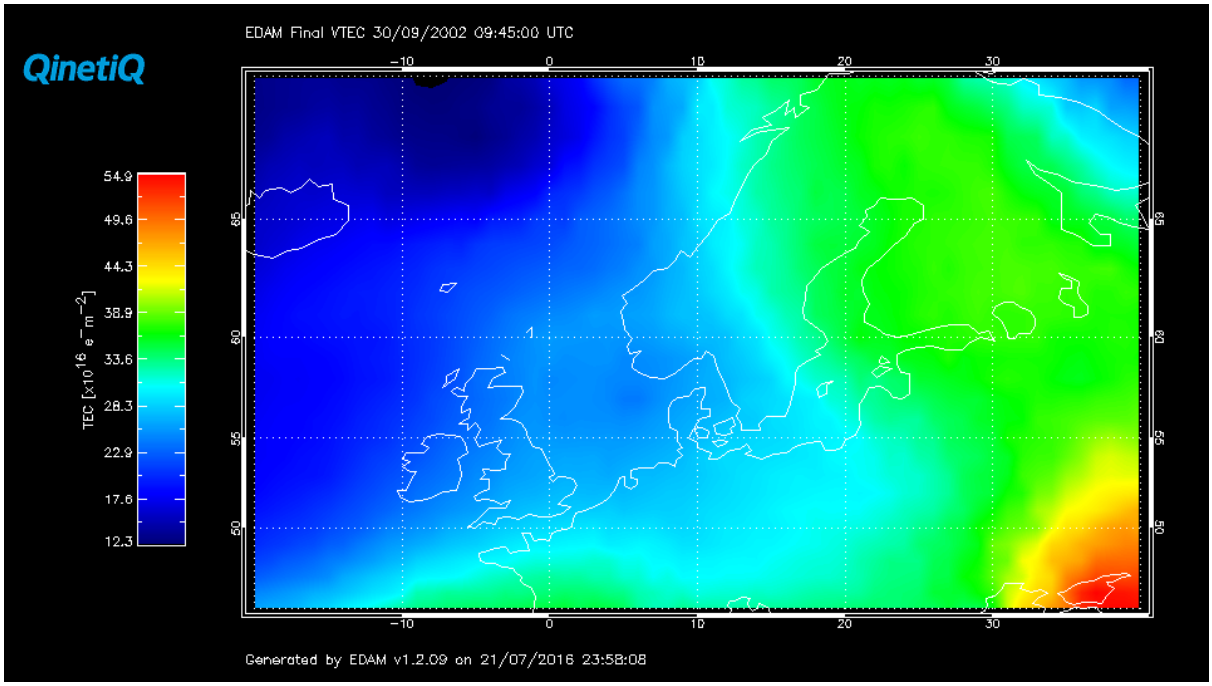

Figure 42a - VTEC map on the 30 September 2002 at 09:45 UT showing the TOI between 10 and 30 degrees longitude. The TEC levels are greater than the surroundings in this region, and the TEC appears to be extending to higher latitudes, beyond the upper limit of the grid at 70°N.

An example of a VTEC map on this day is shown in Figure 42a. The TEC scale in this case covers 12.3 to 54.9 TECU, automatically set by EDAM to cover the range of values in the modelled ionosphere. For further figures in this chapter a strict scale has been defined between 5 and 45 TECU for consistency between the figures and to see the evolution of the ionospheric phenomena in better detail. Also produced alongside these VTEC maps were EDAM difference maps, where the TEC from the 29 September has been subtracted from the TEC from the 30 September, where it was much quieter, to see the modelled difference between the two days and to show the ionospheric phenomena and where they occur more clearly.

Height profiles of modelled electron density differences were also used at the latitude of the base of the SED plume, as defined by Coster et al. (2007). The height profiles show the electron density difference between the 30 September and 29 September over the height range of EDAM, between 100-1000 km. These are utilised to help show if there are increased densities in the topside ionosphere between 30 September and 29 September, which is a signature of SED as described in Section 6.1.1. An example of the height profiles is shown in Figure 42b.

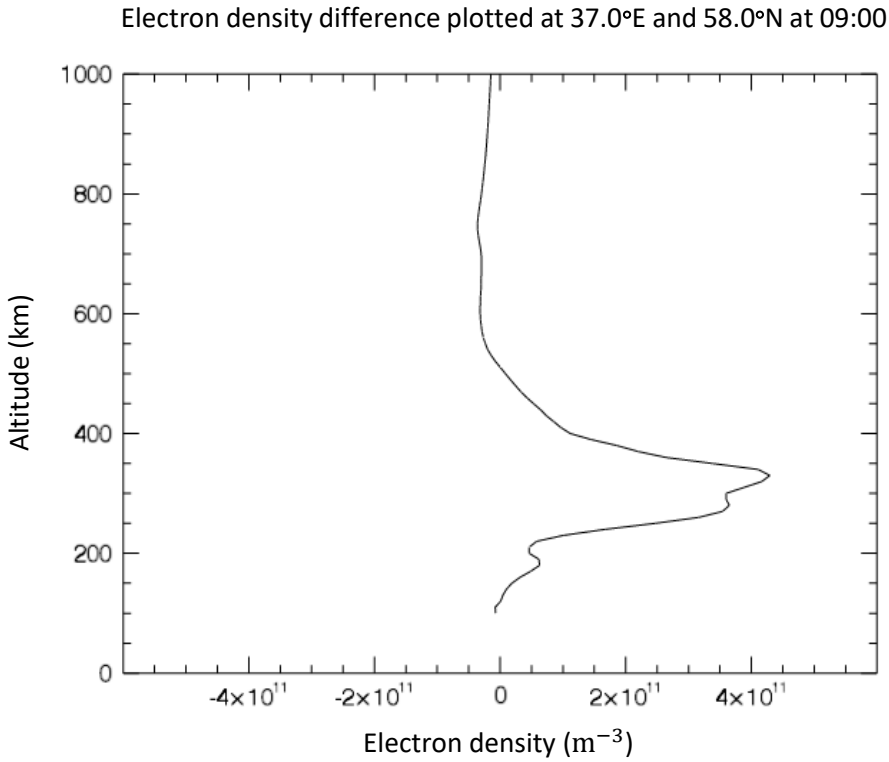

Figure 42b – An example height profile of modelled electron density differences between 29 and 30 September 2002 at 09:00 UT showing maximum increases in electron density at roughly 350km. The difference is taken at the latitude of the plume base, defined in this study at 37.0°E and 58.0°N.

6.2.6 SuperDARN potential plots

SuperDARN is a network of low-power HF radars, that looks at the mid-latitude to polar latitude ionosphere as previously described in Chapter 4.

SuperDARN electric potential plots have been used to study TOIs and SEDs notably in Thomas et al. (2013). Most of the studies using SuperDARN data with GPS TEC maps are for

ionospheric regions over North America. There is a significantly larger coverage of radars over this region compared to the European region. For this current study however, a link between the mid-latitude GPS TEC maps produced by EDAM for the European sector and the SuperDARN electric potential plots is made to present the TOI/SED feature on 30 September 2002.

The comparison uses the high-latitude electric potential patterns, for 30 September 2002 and the time period of 09:00 – 14:30 UT. The data are in the MLT and geomagnetic latitude co-ordinate system. The electric potential plots were at 2 min intervals with the main interest being the Iceland, UK and Scandinavian longitude sectors. An example plot is shown in Figure 43. Noon MLT is located at the top of the plot here. The B_z and B_y components of the interplanetary magnetic field are illustrated in the top right-hand corner underneath the date and time. The cross polar cap electric potential is at the bottom right of this plot. The green line surrounding the convection cell is the Heppner-Maynard boundary which is an approximation to the auroral oval, mentioned previously in Chapter 4.

The circular dots with lines extending from them indicate the position and velocity of the flow in relation to the scale shown in the bottom left. The colour of the these help to show the length of the line, which determines the value of the flow. Intense flows are red and of the order of approximately 1000 ms^{-1} with colours going into orange, yellow green down to blue which display the smallest velocity values. Starting at 60° geomagnetic latitude on the outer edge of the plot, the intervals are in 10° working inwards to 90° geomagnetic latitude at the centre of the plot. These potential plots were provided by Dr Suzie Imber from the Department of Physics and Astronomy at the University of Leicester.

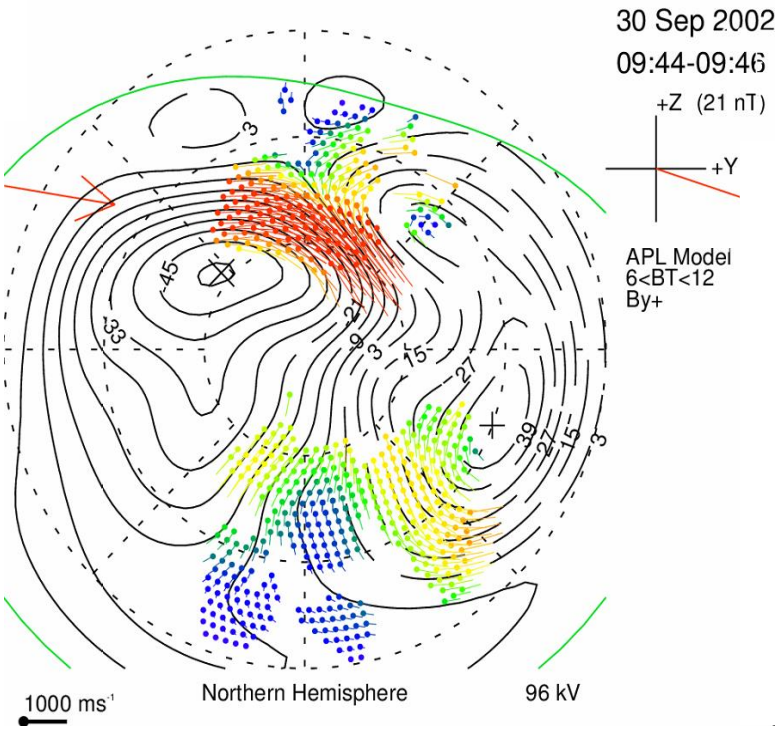

Figure 43 - A SuperDARN electric potential plot on 30 September 2002 at 09:44-09:46 UT in a magnetic co-ordinate system. Noon MLT is located at the top of the plot, where the drift velocities show the plasma to enter the polar cap into the polar cap can be seen. This plot, in time, corresponds to Figure 42a where the increased TEC values are shown to extend north of 70° latitude. The flow is shown from this latitude to enter the polar cap at 70° latitude and 20°E.

For this current study the electric potential plots are adapted by rotating them 180° so that noon MLT is located at the bottom of the plot. This is done to line up and compare with the EDAM GPS VTEC maps. The interplanetary magnetic field magnitude and direction, the date and time are also removed from the plot, but the date and time are given in each caption. The cross polar cap electric potential is located at the top right of the plot.

SuperDARN electric potential plots were compared with EDAM GPS assimilated VTEC maps, EDAM VTEC difference maps and difference height profiles of modelled electron density from EDAM. They are shown in the results section (Section 6.3).

6.3 Results

Figure 44a shows the SuperDARN plot for between 09:00 and 09:02 UT. There is a strong flow of charged particles at near a latitude of 75°N and 10 MLT entering the polar cap. The blue cross near 12 MLT shows the position of Tromsø (69.6°N geographic latitude or 66.7° geomagnetic latitude). This is approximately 10° south of the observed velocity vectors of the plasma flow into the polar cap. The orange cross shows the region directly below the entry of plasma into the polar cap on the modelled map. The green cross shows the approximate location of Iceland (64.9°N geographic latitude or 69.4° geomagnetic latitude). The black cross approximately marks the position of the UK (55.4°N geographic latitude or 57.7° geomagnetic latitude), south of the electric potential magnetic latitude grid. These crosses are also shown on the geographic grid of the EDAM VTEC plots, with the orange cross representing the longitude here for the flow into the polar cap as the EDAM grid does not extend to flows latitudes. The GPS TEC plot in Figure 44b shows an enhancement between roughly 55-65°N in latitude and between 30-40°E in longitude. This enhancement is outlined, and the intense enhancement in the centre is tracked, to show the alignment of the enhancement. The boundary is set by following a TEC value of approximately 35 TECU, defined by the yellow/orange colour scale. The centre is where the maximum TEC value lies in the boundary, defined by the redder colour, which is approximately 40-45 TECU. These boundaries are also illustrated on the SuperDARN electric potential plot. It appears that the VTEC enhancement is broadly aligned with the region where the flow enters the polar cap.

Figure 44c shows a difference map between a quiet day, the 29 September 2002 subtracted from the more disturbed day of the 30 September 2002. In this difference map, the region of enhancement noted for Figure 44b is the region where a small but significant TEC

enhancement is seen of roughly between 5-8 TECU. The small red cross defines where the SED plume base has been set, as this is the largest difference seen between the two days. Defining the plume base here helps mark the centre line in the boundary region shown in Figure 44b. On the west side of this enhancement the ionosphere is depleted by comparison, showing differences of approximately -10 TECU. Figure 44d shows the vertical profile for the difference between the two days in modelled electron density (Ne) over 58°N latitude and 37°E longitude, the region marked by the red cross showing the plume base. There is an increase in the electron density of the F-region, most notably around 350 km where there is an increase of greater than $4x10^{11}$ m^{-3}. Care may be required in this interpretation as there were no ionosonde measurements assimilated into the model, making it more difficult to map out the electron density height profile. This location defined by the red cross was used for consistency in all following electron density difference height profiles shown in this study.

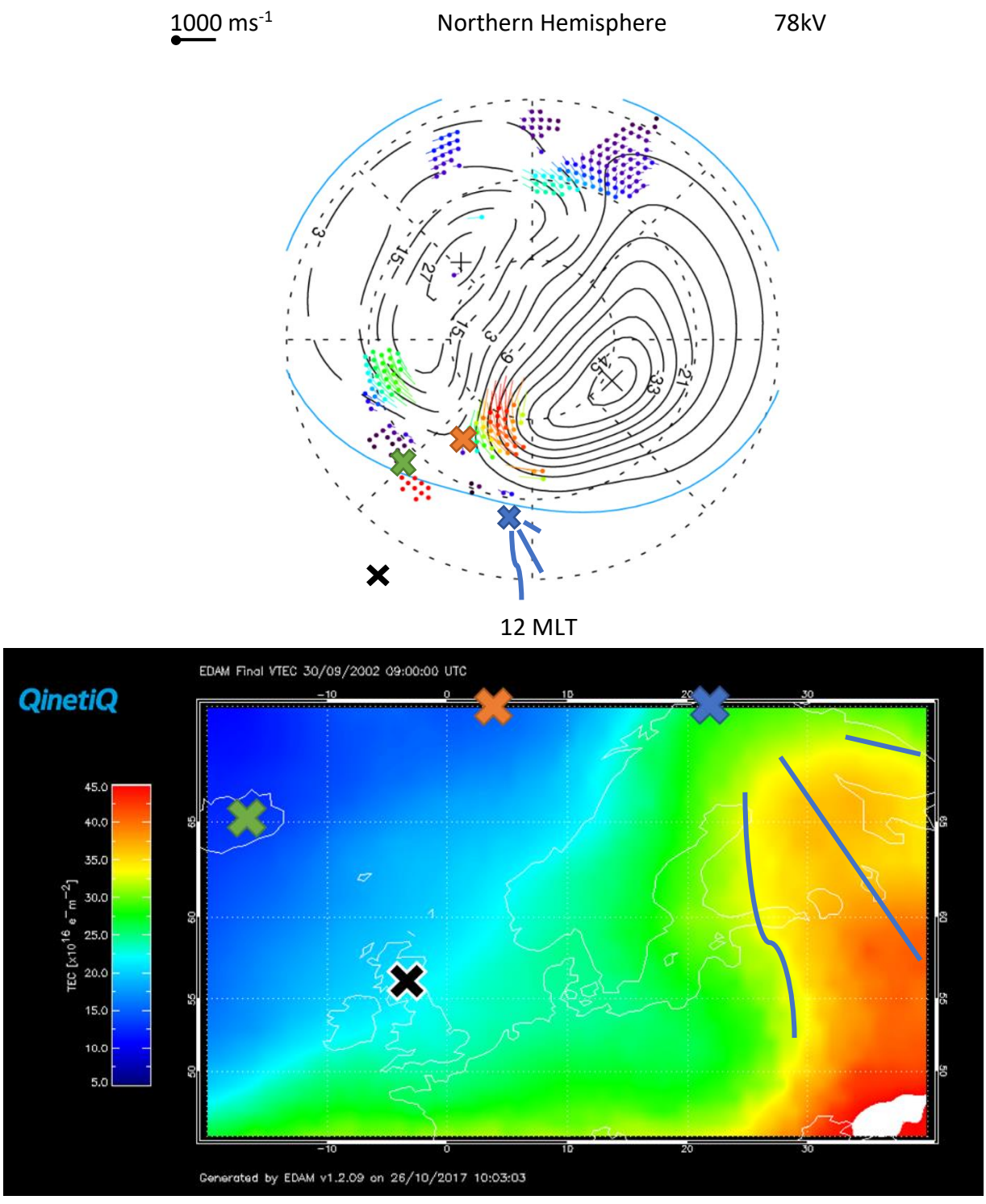

Figure 44a and b – Figure 44a displays the SuperDARN electric potential plot and plasma flow between 09:00 and 09:02 UT. Figure 44b displays a GPS VTEC map for 09:00 UT. The maximum geographic latitude of the grid is 70°N. The markings on the plot show the boundary of the identified SED plume and its centre, with its base being near 60°N latitude. These are also shown on 44a.

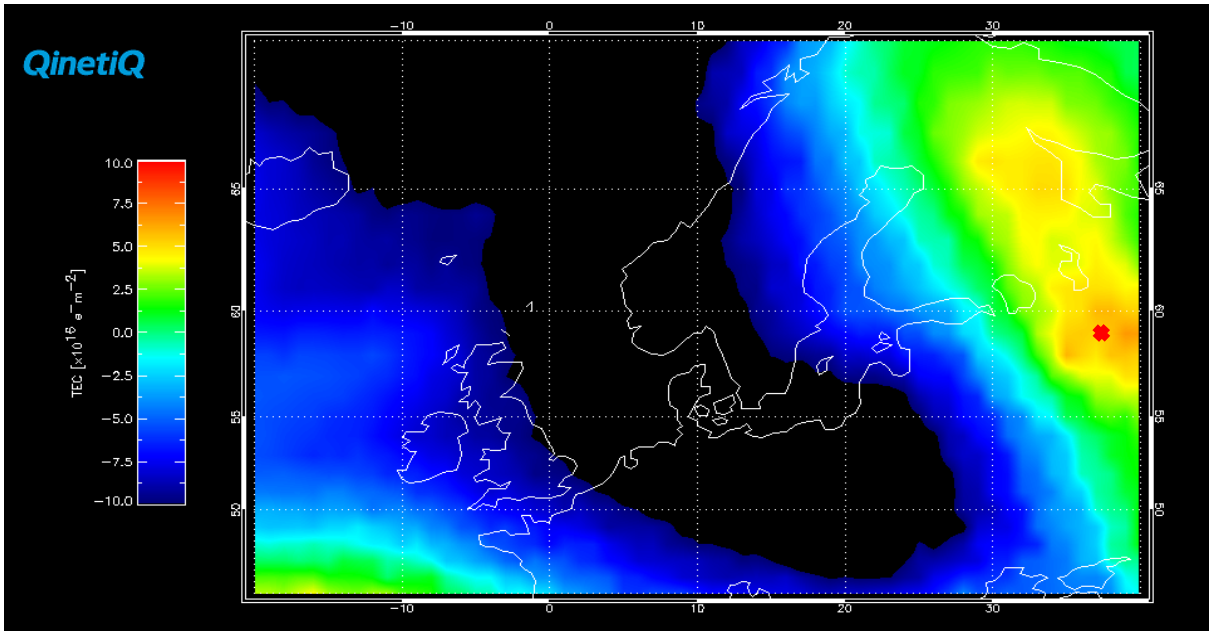

Electron density difference plotted at 37.0°E and 58.0°N at 09:00 UT

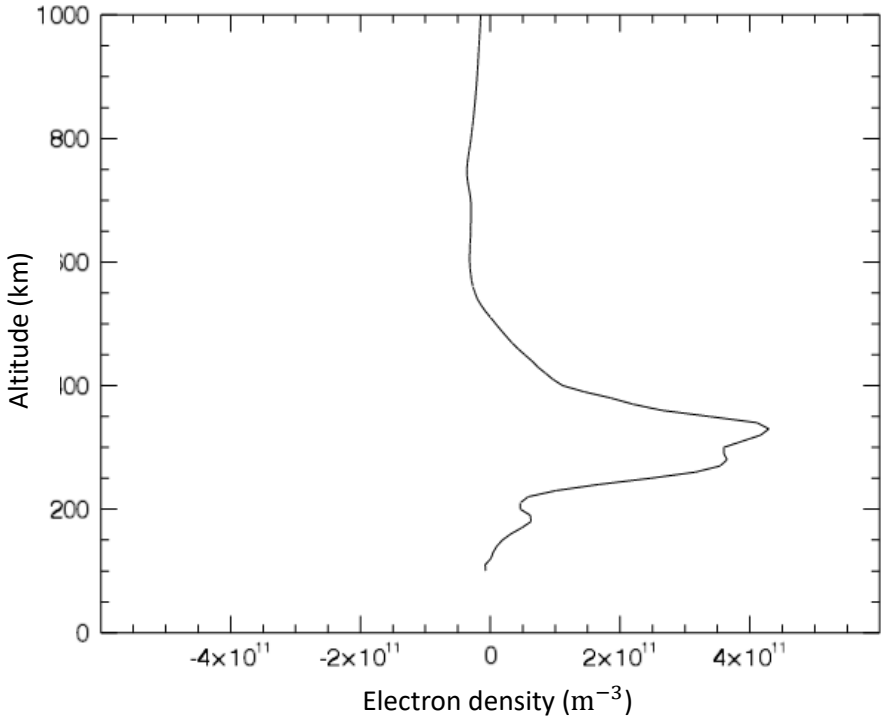

Figure 44c and d – Figure 44c displays the EDAM GPS TEC difference map between 29 September 2002, quiet day, and 30 September 2002, active day at 09:00 UT. There is an increase in difference VTEC marked by the red cross and its surrounding areas up to 70°N latitude. To the left of the enhancement is a 'hole' in the VTEC where the active day showed a large decrease in VTEC in comparison to the quiet day. Figure 44d shows the electron density difference height profile above the marked location in 44c. There is a large increase in difference electron density at about 350 km.

Figure 45a shows the SuperDARN plot for 09:30 – 09:32 UT. The orange cross has been removed from the plots to focus on the marked locations of Tromsø, Iceland and the UK. The electric potential plot shows the flow up the channel and over the polar regions with large velocities also seen at 24 MLT at geomagnetic latitudes 80-70° where the plasma flows out of the polar region. The throat region in Figure 45a can be clearly seen north of Tromsø in geomagnetic latitude. The data in Figure 45b shows the ionisation appearing to come from lower latitudes and aligned with the channel into the polar cap. This is indicative of a TOI of ionisation being transported from lower latitudes where the magnetic field lines are closed to the open field lines of the polar cap.

The difference VTEC map in Figure 45c shows that the largest enhancement value is at around 65°N geographic latitude, between 5-8 TECU, which is at a higher latitude when compared to the previous time step. There are minor but significant enhancements at lower latitudes. The depletion in VTEC difference, seen in the previous time step, is still evident west of the enhancements. Figure 45d, the electron density difference height profile, shows there are large increases in electron density difference at just below 200 km and at around 400 km and above.

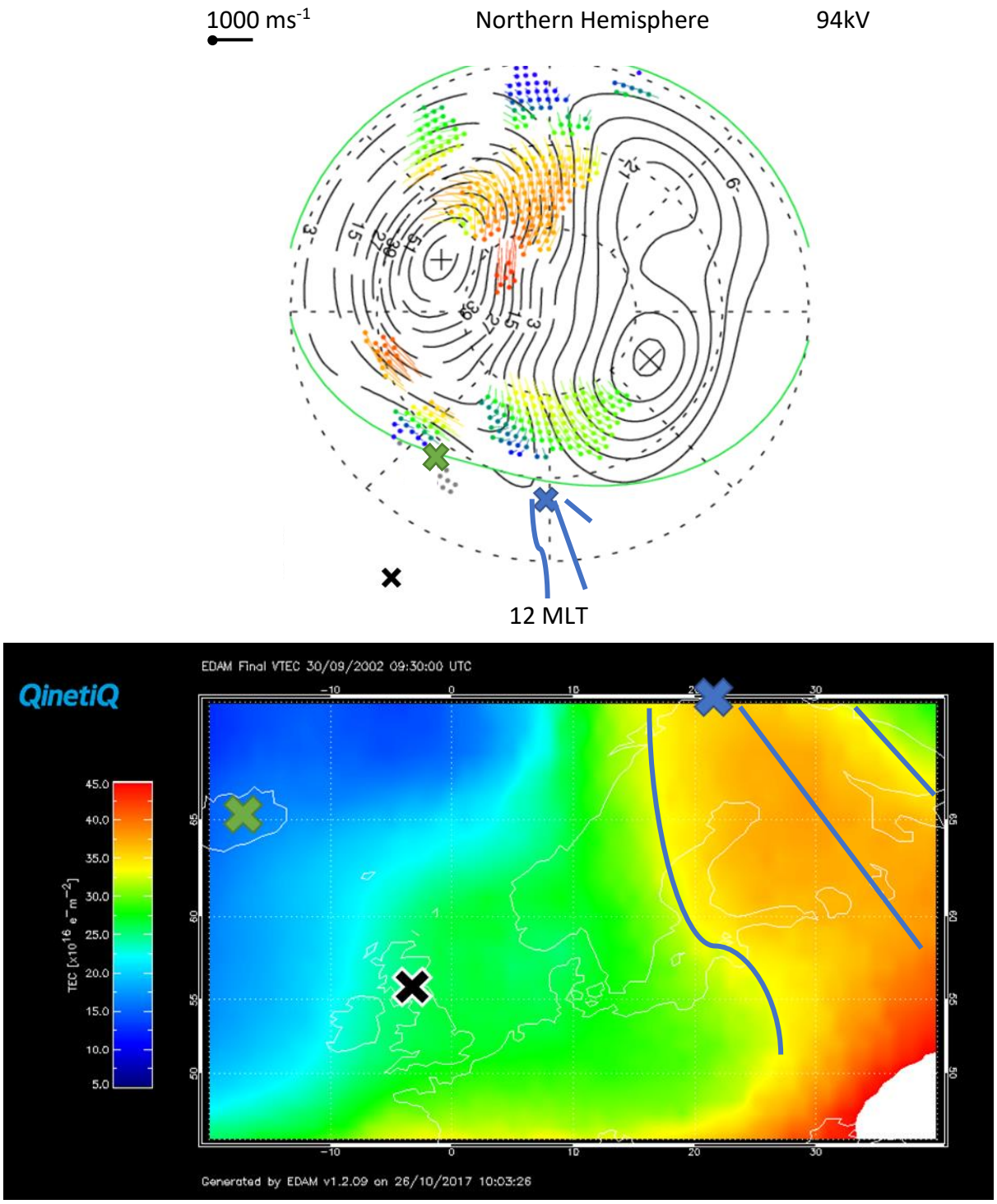

Figure 45a and b – Plots displaying the data for 09:30 UT, a time step of 30 minutes after the previous Figure, with each cross changing in location on the MLT co-ordinate system in 45a. The speed and direction of the plasma flow show the plasma was moving north of Tromsø into the polar cap. In Figure 45b, the marked boundary and centre line show where the largest VTEC values are located in the ionosphere in this region.

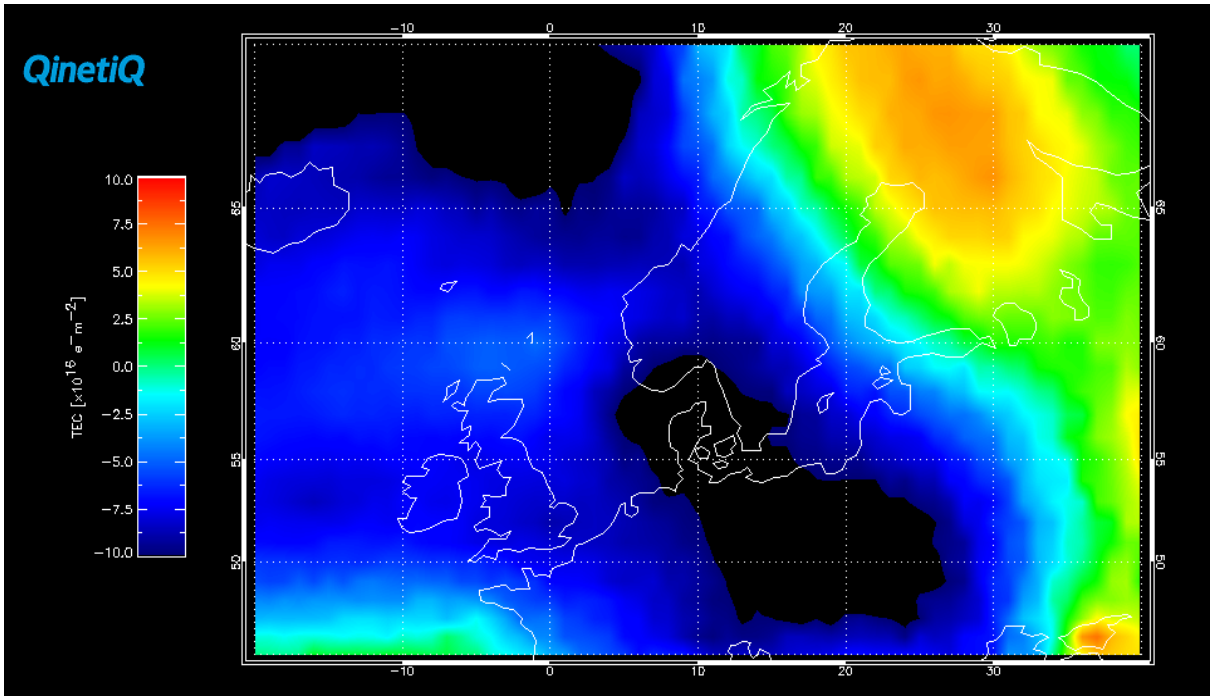

Electron density difference plotted at 37.0°E and 58.0°N at 09:30 UT

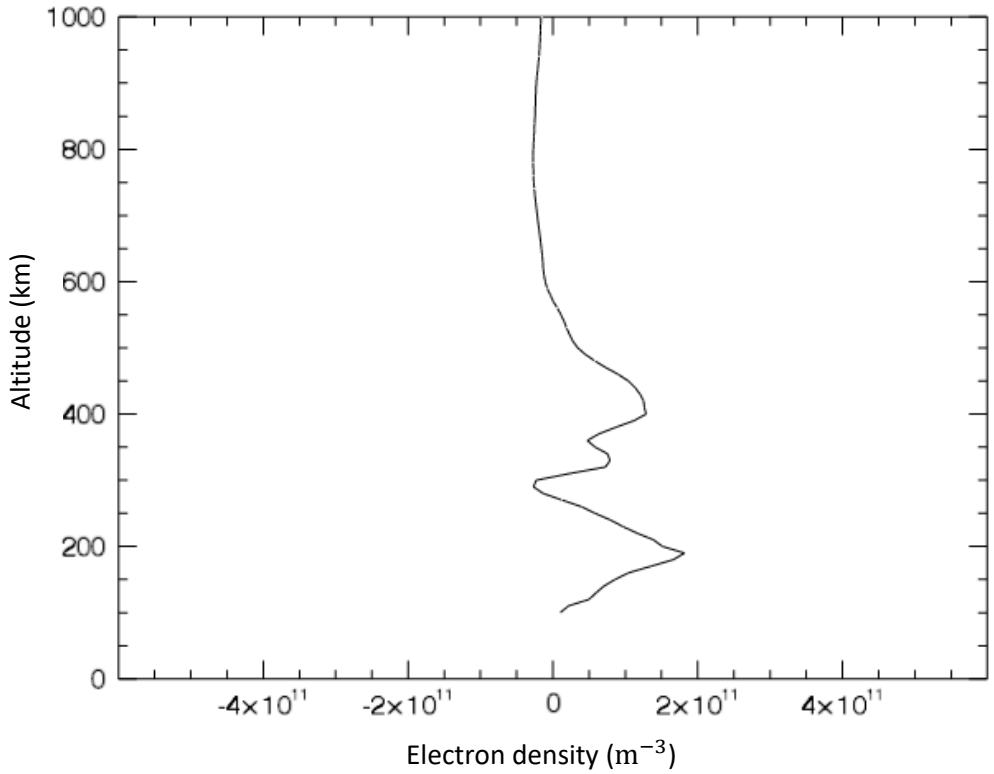

Figure 45c and d – Figure 44c displays the EDAM GPS VTEC difference map at 09:30 UT. There is an enhanced region of VTEC difference at 65°N latitude and between 25-30°E longitude. To the left of the enhancement is a 'hole' in the TEC continued from the previous time step. (d) shows the electron density difference height profile which shows a large increase in electron density difference at just below 200 km and above 400 km.

Figures 46a and 46b show the SuperDARN electric potential plot and EDAM VTEC map for the following time step at 10:00 UT. In the electric potential plot, the blue cross of Tromsø is at the edge of the convection cell, inside the modelled auroral oval boundary. The velocity vectors marked on the potential plot, show the flow of the ionisation at the latitude and longitude of Tromsø and into the polar region. The channel has been outlined in the GPS TEC map in Figure 46b and marked to the approximate position in Figure 46a. The centre line appears to line up with the velocity vectors of Figure 46a. This is again indicative of the TOI being prominent after 30 minutes over Scandinavian latitudes.

Figure 46c shows the VTEC difference map for 10:00 UT where the location of the SED plume base is identifiable at between 55°N and 60°N latitude at 40°E longitude where the increased ionisations densities are located. The channel is shown to extend from this region and the increased VTEC difference here, match the larger TEC values seen in (b). The increased TEC values also support the previous statement of the TOI flowing into the polar regions, seen in (a). The 'hole' of difference VTEC, mentioned in the previous timesteps is still evident and located to the west of the identified plume/TOI. In Figure 46d the electron density difference height profile is shown. The increased electron density differences appear from roughly 200-250 km, with the maximum at near 300 km.

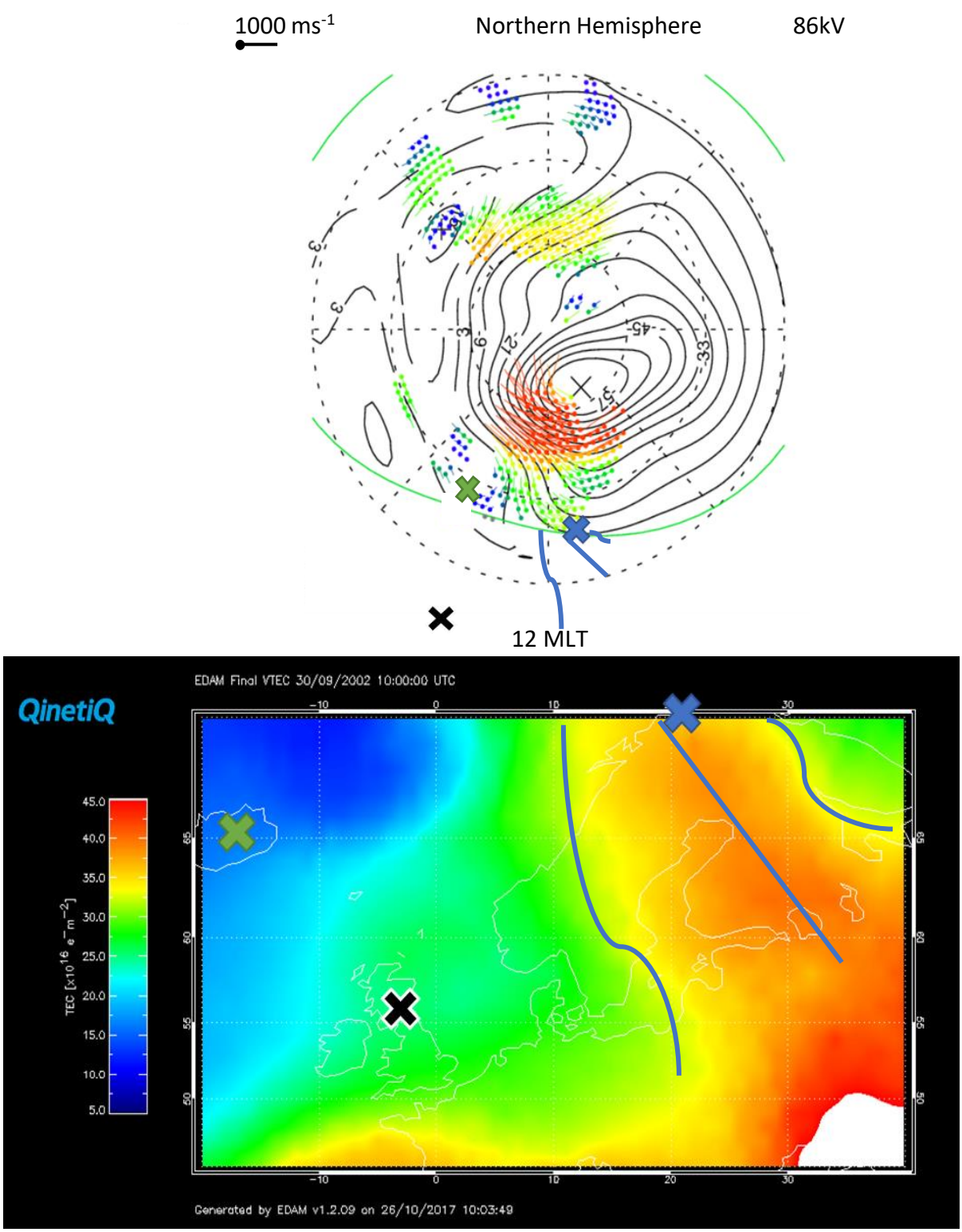

Figure 46a and b – SuperDARN electric potential plot, (a), and EDAM VTEC map, (b), for 10:00 UT. Tromsø is at the edge of the convection cell in the electric potential plot and in the marked boundary of the TOI, also shown in the EDAM VTEC map.

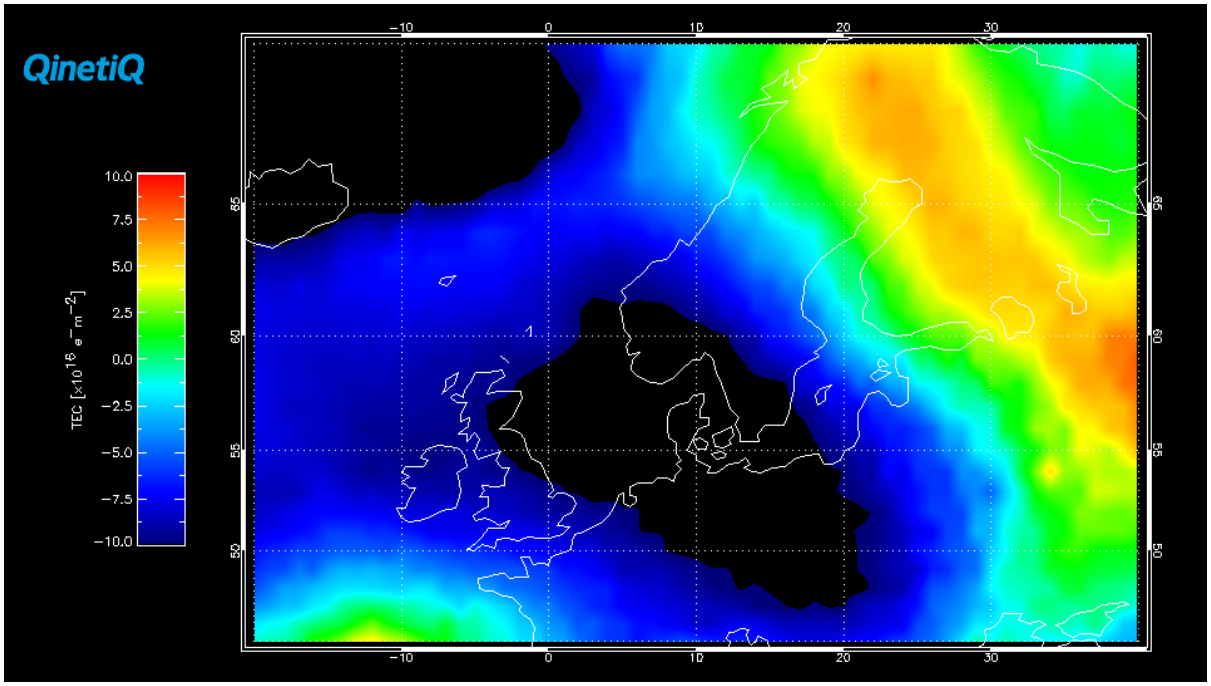

Electron density difference plotted at 37.0°E and 58.0°N at 10:00 UT

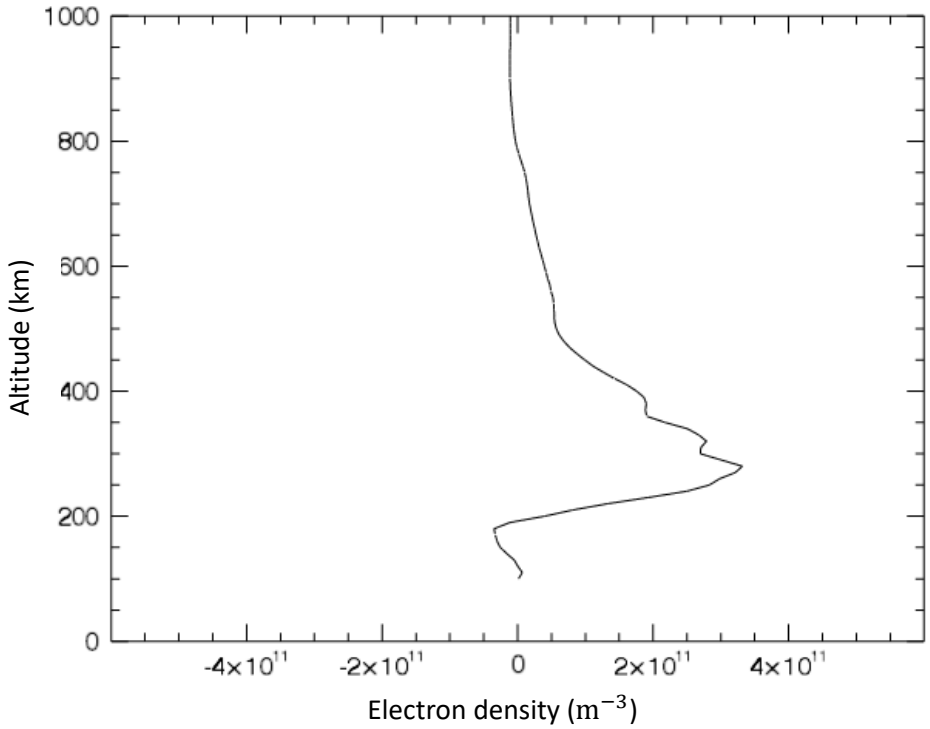

Figure 46 c and d – Figure 46c shows the VTEC difference plot for 10:00 UT. The increased VTEC difference can be seen more as a channel. The base of the largest TEC differences is at between 55° N and 60° N degrees latitude. There is still 'hole' of TEC over Europe to the west of the indicated TOI/SED plume. In Figure 46d there is an increased electron density difference between 300 and 400 km. This extends to higher altitudes.

Figures 47a and 47b show the electric potential plot and EDAM VTEC map for 10:30 UT. The outline for the TOI and plume is marked with the centre line. The centre line used to indicate the largest VTEC values in the marked boundary which, when marked onto the SuperDARN potential plot, matches up with the velocity vectors that flow into the polar cap. The defined TOI has been evident in the current data for one hour.

Figure 47c shows the EDAM VTEC differences between 29 and 30 September 2002 for 10:30 UT. The region where the largest difference occurs is shown to be at higher latitudes. The white colour on the difference map shows that the difference has exceeded 10 TECU. The channel in the difference matches with the region seen in Figure 47b. Figure 47d shows the electron density difference height profile, where the increased electron density differences are located between 200 km and at 500 km. The maximum difference is located at near 300 km with a difference value of roughly $4x10^{11}$ m^{-3}

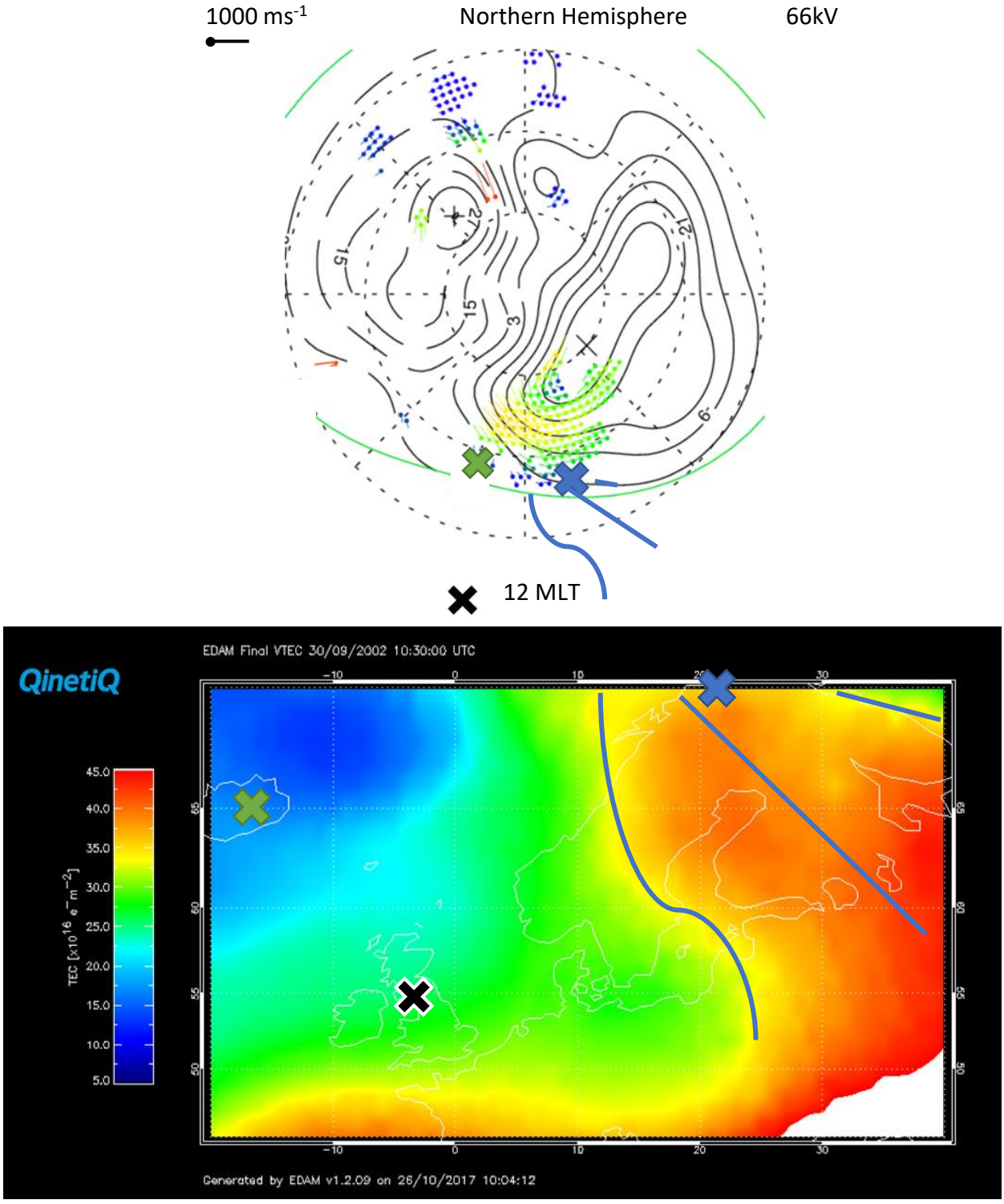

Figure 47a and b – SuperDARN electric potential plot, Figure 47a, and EDAM VTEC map, Figure 47b, presented for 10:30 UT. Tromsø is now located on the marked central line of the channel. In Figure 47b the VTECs are still roughly 40-45 TECU in the channel and appear to extend north of Tromsø.

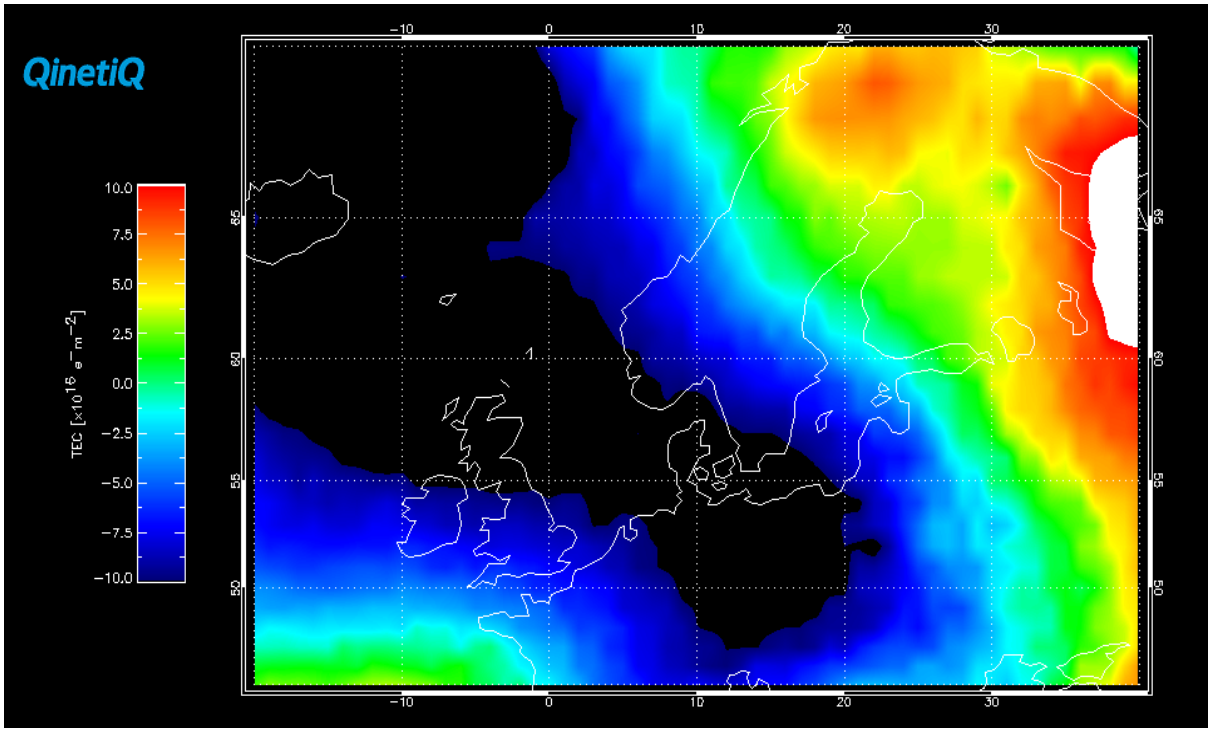

Electron density difference plotted at 37.0°E and 58.0°N at 10:30: UT

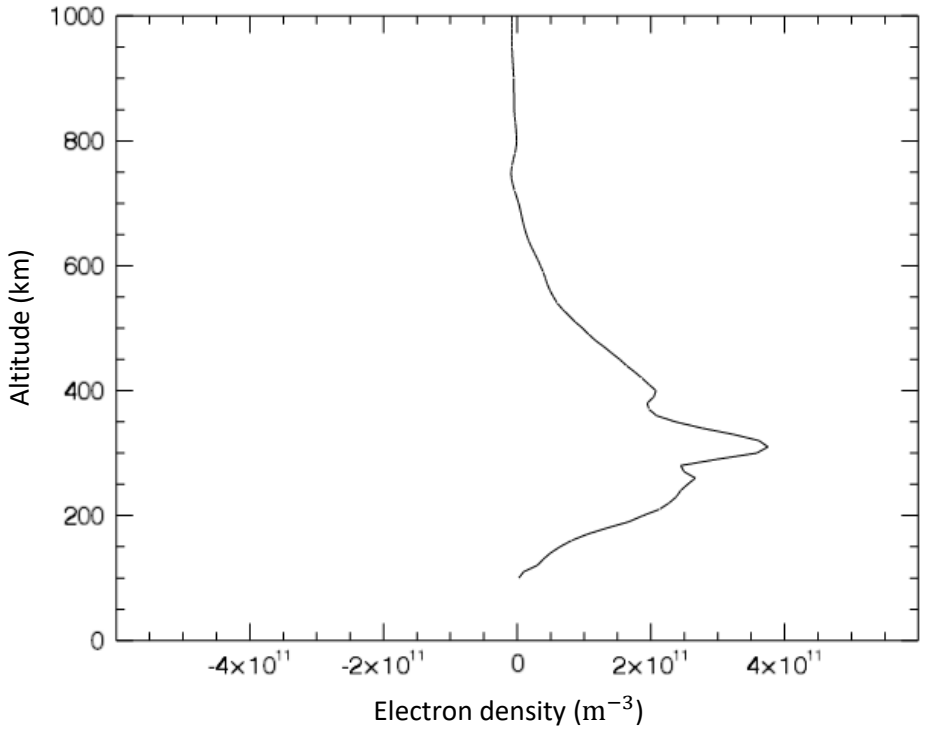

Figure 47c and d – EDAM VTEC Difference plot and electron density difference height profile for 10:30 UT. The channel marked in Figure 47b can be seen in the VTEC difference map, Figure 47c. The increased VTEC difference can be seen at latitudes of between 60° N and 65°N where the VTEC difference is greater than 10 TECU. In Figure 47d, there are positive electron density differences exhibited up to 600 km between 29 and 30 September. The maximum difference is seen at near 300 km with a value close to 4x10^{11} m^{-3}.

Figures 48a and 48b show the GPS VTEC maps and the SuperDARN electric potential plots for 11:00 UT. The convection cell in Figure 48a has changed in structure. Tromsø lies in the afternoon convection cell. The marked boundary of the channel aligns with the direction of the velocity vectors of the plasma. The GPS TEC map in Figure 48b shows the channel of enhanced VTEC between roughly 0°E and 40°E in longitude and 55°N extending beyond 70°N. The VTEC values in the centre of the channel are between 40 and 45 TECU. The western most boundary of the channel is now marked at near 0°E, 10° more west than the previous time step.

In Figure 48c the VTEC difference map for 11:00 UT shows the largest differences, of near 10 TECU, to be at the centre of the channel shown in Figure 48b. The depletion to the west of the channel is still noticeable at this time, but the VTEC difference values near the channel are decreasing, closer to -5 TECU difference rather than greater than -10 TECU. Figure 48d shows the electron density difference height profile. The largest differences in electron density are identified at approximately 250 km with a value of approximately $3x10^{11}$ m^{-3}. This is a smaller difference when compared to Figure 47d.

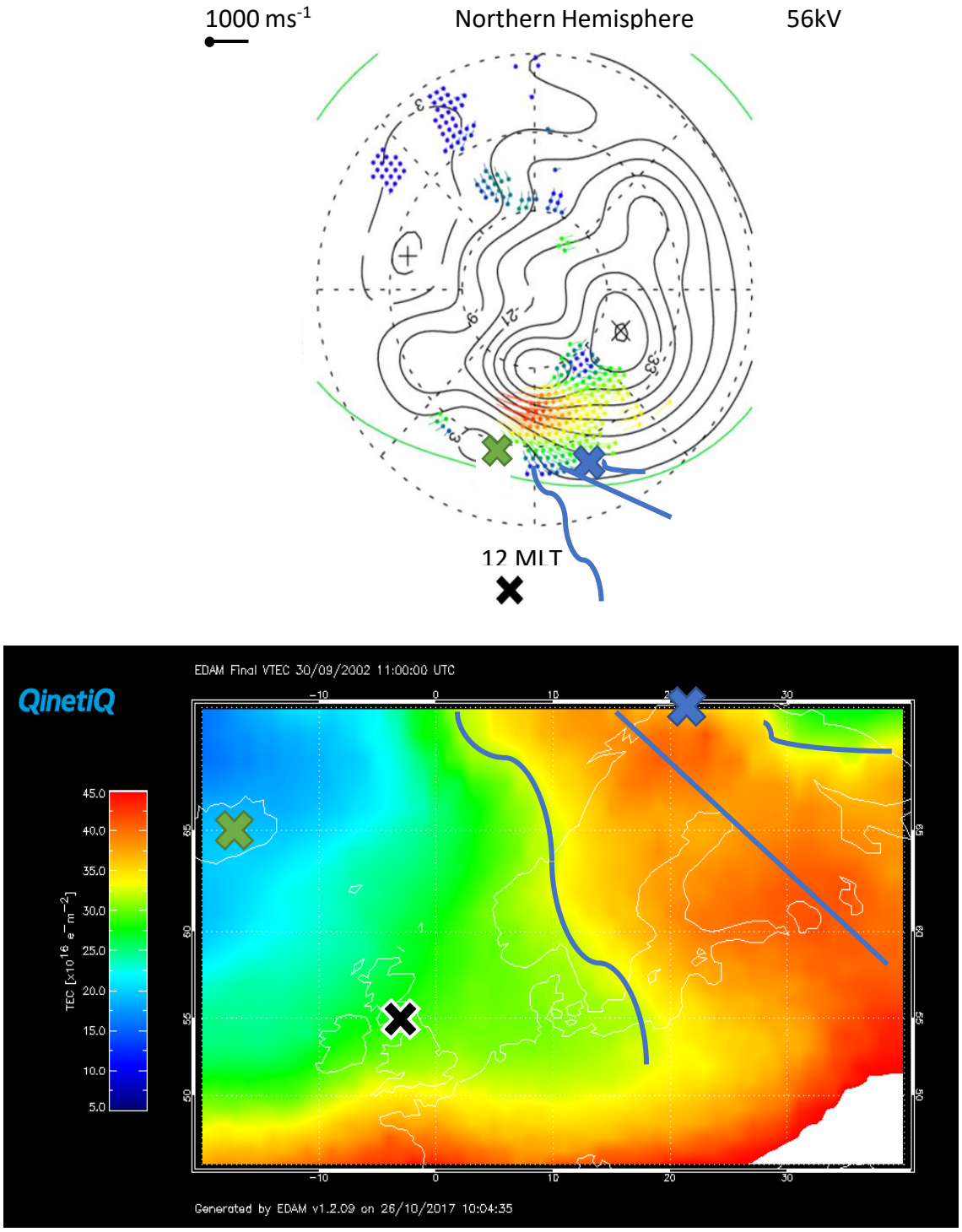

Figure 48a and b – SuperDARN electric potential plot, Figure 48a, and EDAM VTEC map, Figure 48b, for 11:00 UT. In 48a Tromsø is located in the afternoon convection cell. The marked boundary and centre line of channel align with the direction of the velocity vectors of the plasma. In 48b, the VTECs of the centre line are between 40 and 45 TECU. The western most boundary of the channel is now marked at near 0°E.

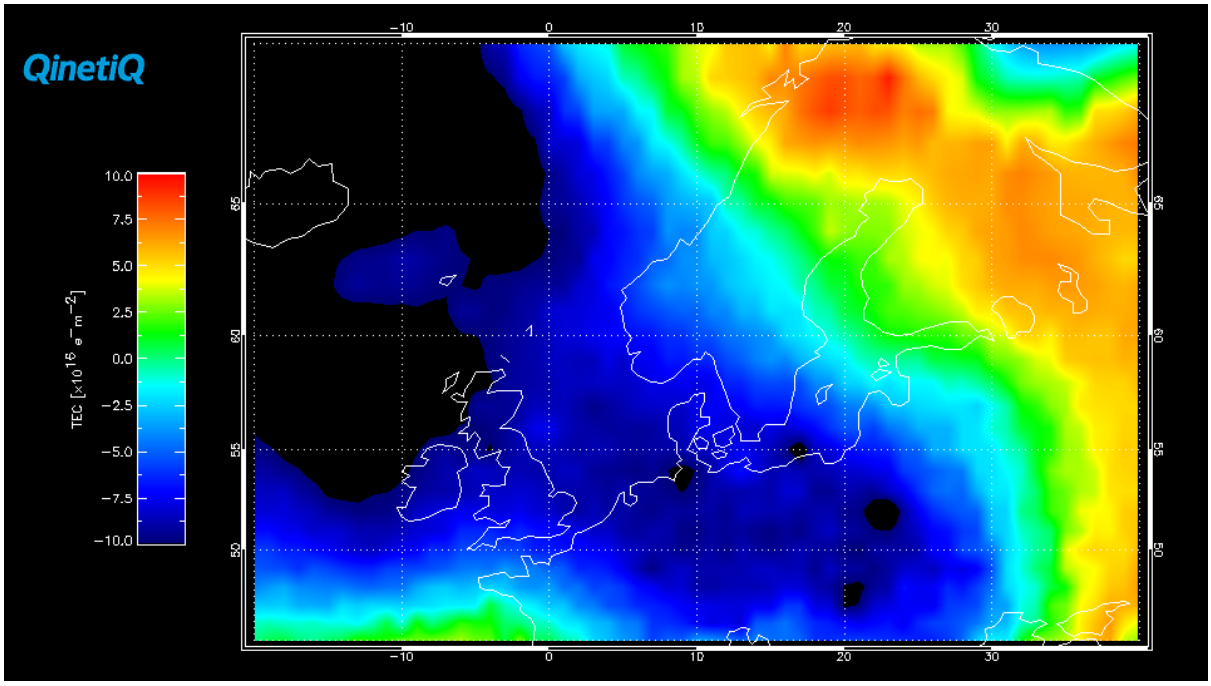

Electron density difference plotted at 37.0°E and 58.0°N at 11:00 UT

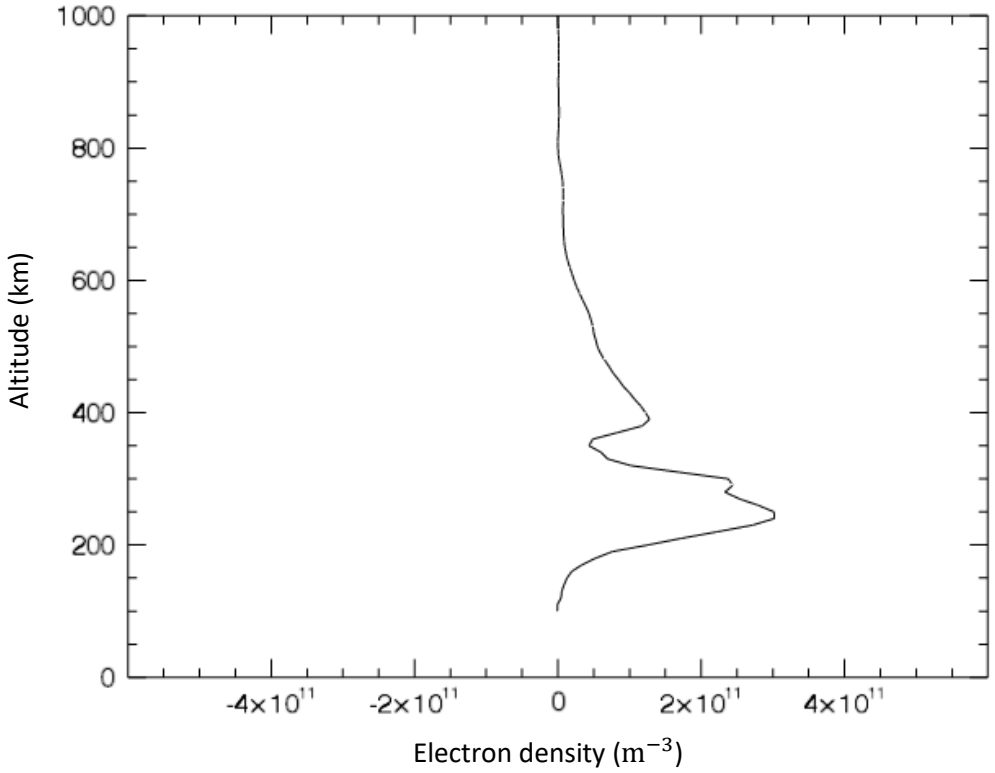

Figure 48c and d – EDAM VTEC Difference plot, Figure 48c, and electron density difference height profile Figure 48d, for 11:00 UT. The channel is still noticeable in the VTEC differences for this time period. The depletion to the west has increased in VTEC values, with a difference between the two days now at -5 TECU. In Figure 48d the electron density differences show a maximum difference at approximately 250 km with a value of $4x10^{11}$ m^{-3}.

Figures 49a and 49b show the SuperDARN electric potential plot and GPS VTEC map for 11:30 UT. Tromsø is still located in the afternoon convection cell, in the auroral boundary approximately given by the green line. It still appears that the marked boundary for the channel aligns with the direction of plasma flow shown by the velocity vectors on the electric potential plot. In Figure 49b, the high TEC values, between 40 and 45 TECU are along the centre line of the channel. The western boundary is now located further to the west, beyond 0°. The centre line and eastern boundary also follows this trend. The centre of the channel is beginning to become more horizontal, shown by the centre line.

The VTEC difference map in Figure 49c shows agreement with the marked boundary in Figure 49b with the centre of the channel becoming more horizontal. The VTEC differences along roughly the centre line is still large, near 10 TECU. The plume base, defined at the start of the study, is still within the larger VTEC differences. The VTEC differences in the channel appear to extend to lower latitudes. In Figure 49d there is a very large peak seen in the electron density difference at between 250 and 300 km. The value of this difference exceeds the x-axis limit of $6x10^{11}$ m^{-3}.

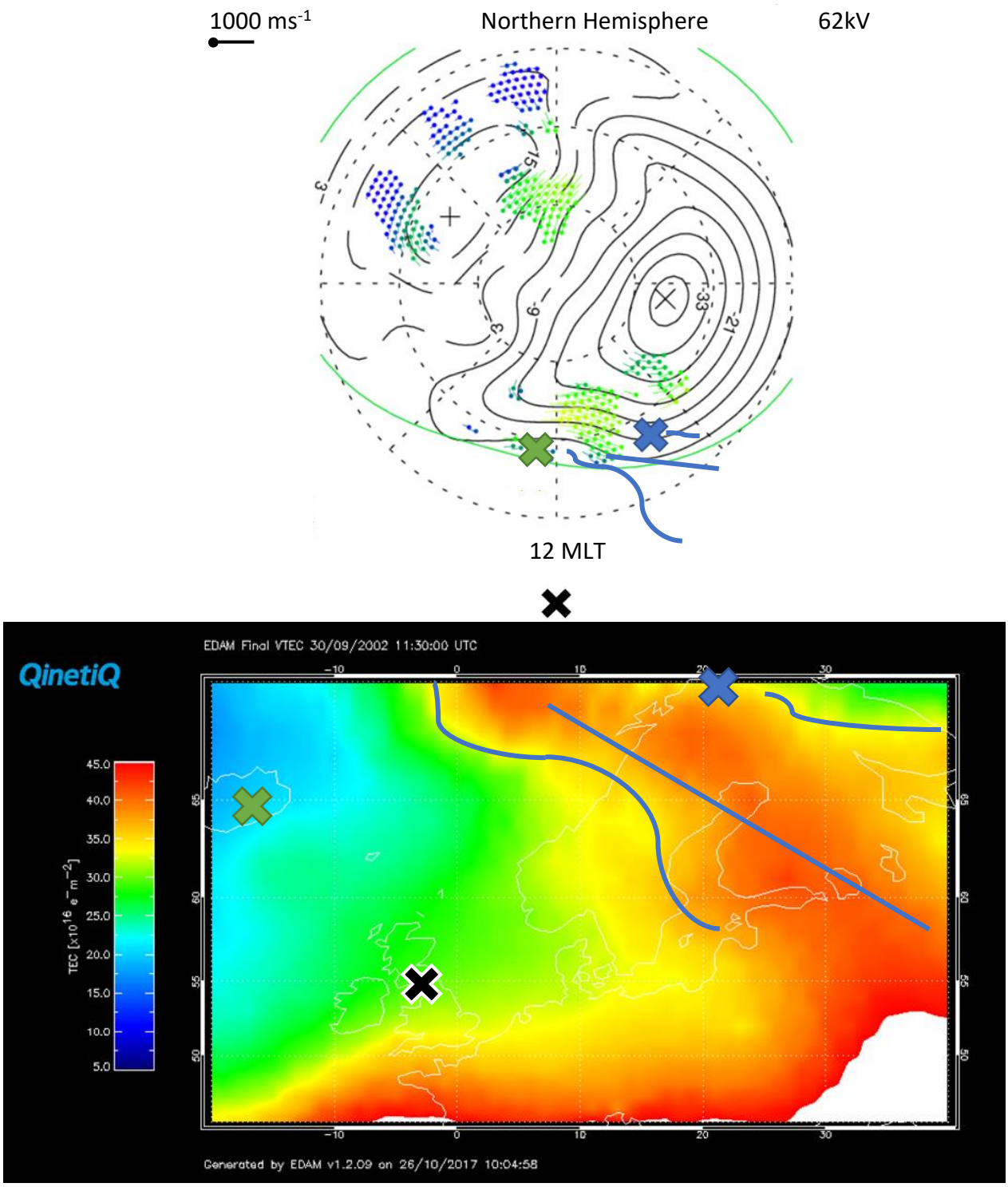

Figure 49a and b – SuperDARN electric potential plot, Figure 49a, and EDAM VTEC map, Figure 49b, for 11:30 UT. In (a), Tromsø is still located in the afternoon convection cell and the marked boundary for the channel aligns with the direction of plasma flow. In Figure 49b the high TEC values, between 40 and 45 TECU are along the centre line of the channel. The centre of the channel is beginning to become more horizontal compared to earlier times, shown by the centre line.

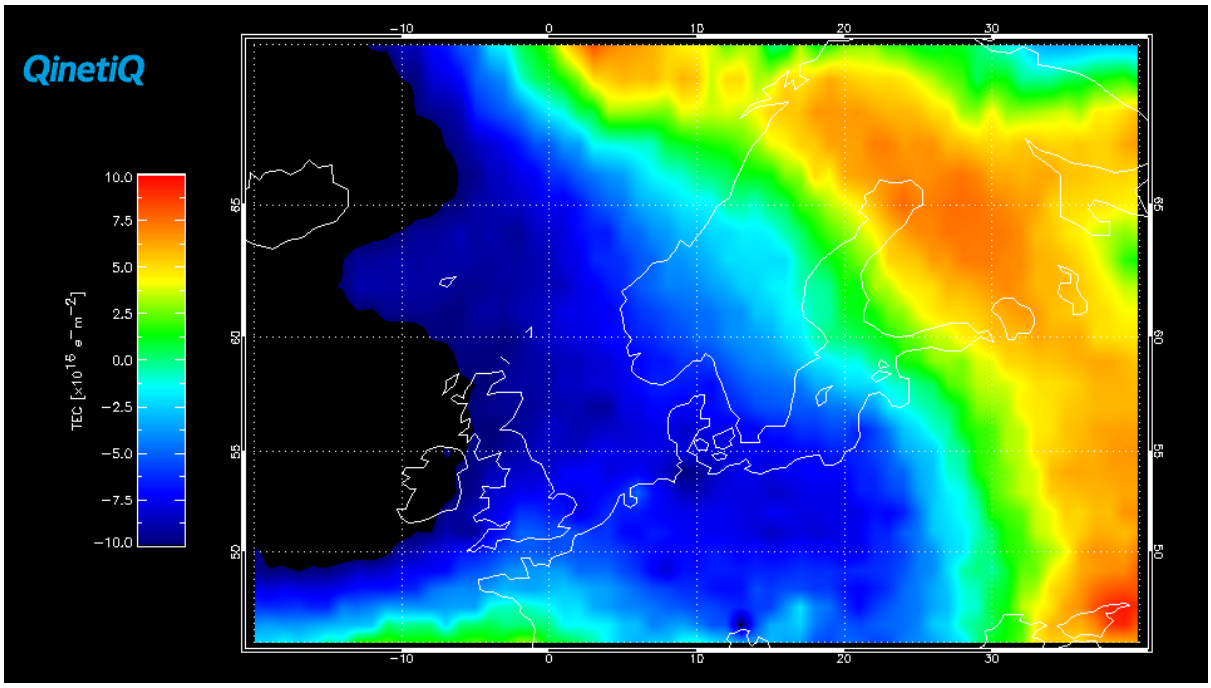

Electron density difference plotted at 37.0°E and 58.0°N at 11:30 UT

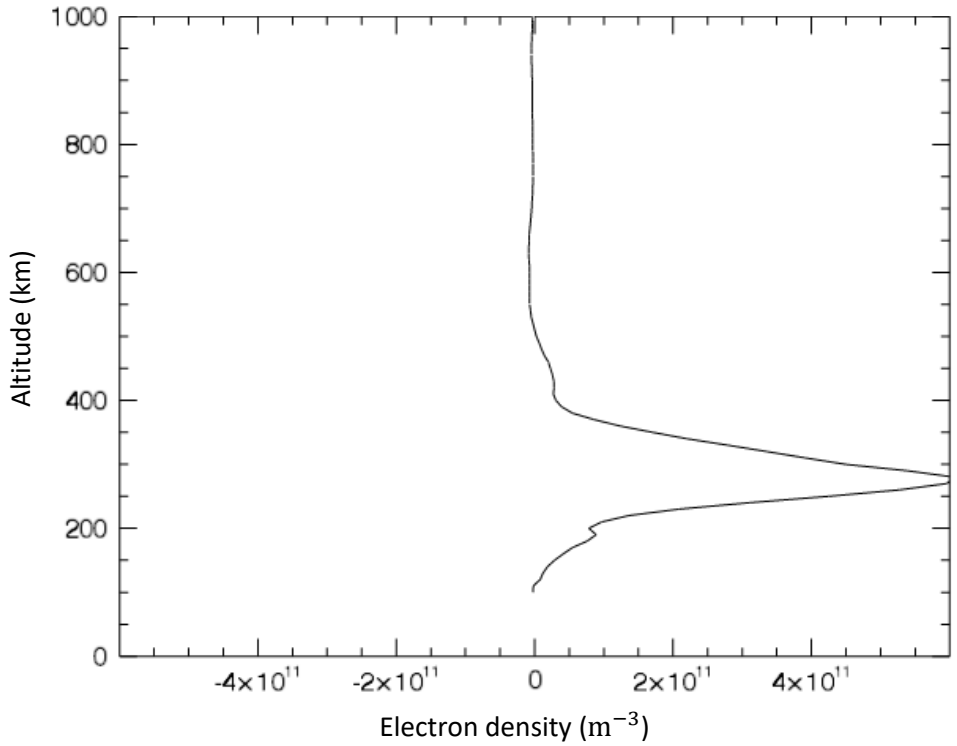

Figure 49c and d – EDAM VTEC Difference plot, Figure 49c, and electron density difference height profile, Figure 49d, for 11:30 UT. VTEC difference map in Figure 49c shows agreement with the marked boundary in Figure 49b. The plume base is still within the larger VTEC differences, values of near 7.5 TECU. In Figure 49d there is a large density difference located between 250 and 300 km with a value exceeding 6x10^{11} m^{-3}.

Figures 50a and 50b show the SuperDARN electric potential plot and EDAM GPS VTEC map for 12:00 UT. The electric potential plot in Figure 50a shows the plasma flow moving with the afternoon cell. The marked boundary of the channel aligns with this plasma flow. Tromsø again lies in the convection cell, north of the auroral oval and now Iceland is beginning to be located on the edge of this convection cell on the auroral oval boundary line. In Figure 50b the marked boundary for the channel no longer extends to the upper boundary of the latitude grid. The channel now extends to approximately 67°N latitude which is further south than all other previous times. The VTEC values for the centre of the marked channel however are still between 40 and 45 TECU.

Figure 50c shows the VTEC difference map for 12:00 UT. The VTEC differences agree with Figure 50b, with the channel not as structured and easily identifiable now. There is however large VTEC difference, values exceeding 10TECU, that has appeared in this time step at approximately 58°N latitude. The depletion to the west of the channel is still evident in the VTEC difference map, with differences of -5 TECU. Figure 50d shows the electron density difference height profile for 12:00 UT. The maximum of electron density difference is located at near 300 km with a value of near $5x10^{11}$ m^{-3}. Between 350 km and 700 km there is a positive electron density difference, but it is a gradual decline in difference value from 350 km.

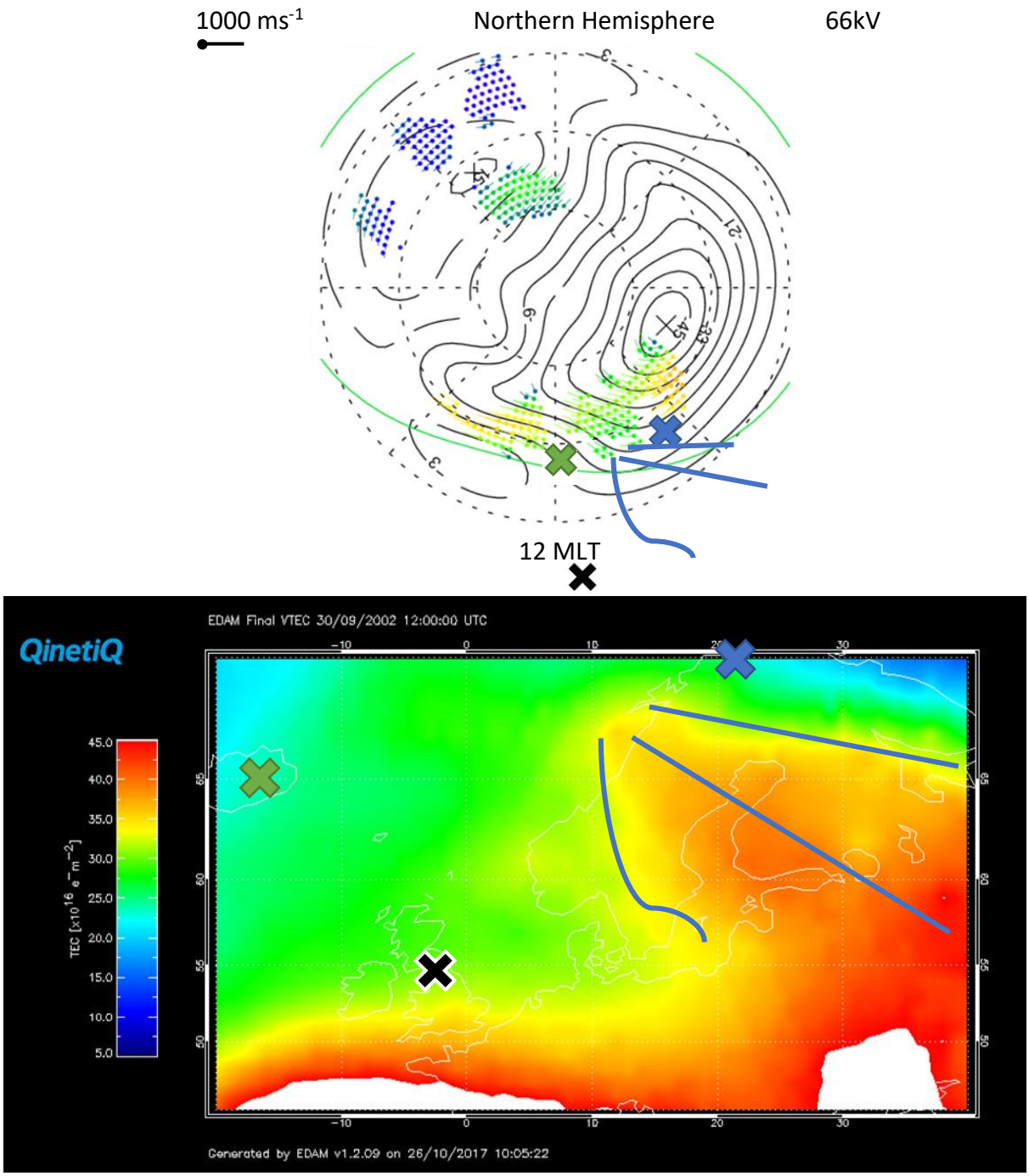

Figure 50a and b – SuperDARN electric potential plot, Figure 50a, and EDAM VTEC map, Figure 50b, for 12:00 UT. In Figure 50a the plasma flows with the afternoon cell. Tromsø again lies in the convection cell, north of the auroral oval and now Iceland is located on the edge of the convection cell on the auroral oval boundary line. In (b) the marked boundary for the channel no longer extends to 70°N.

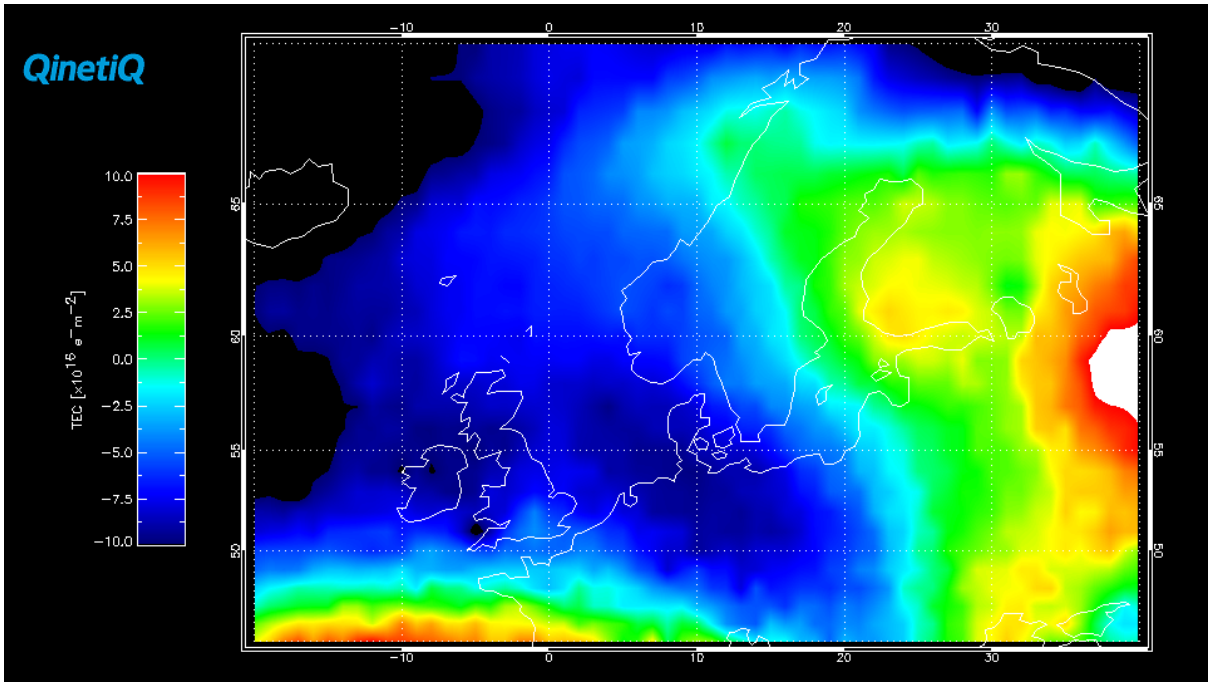

Electron density difference plotted at 37.0°E and 58.0°N at 12:00 UT

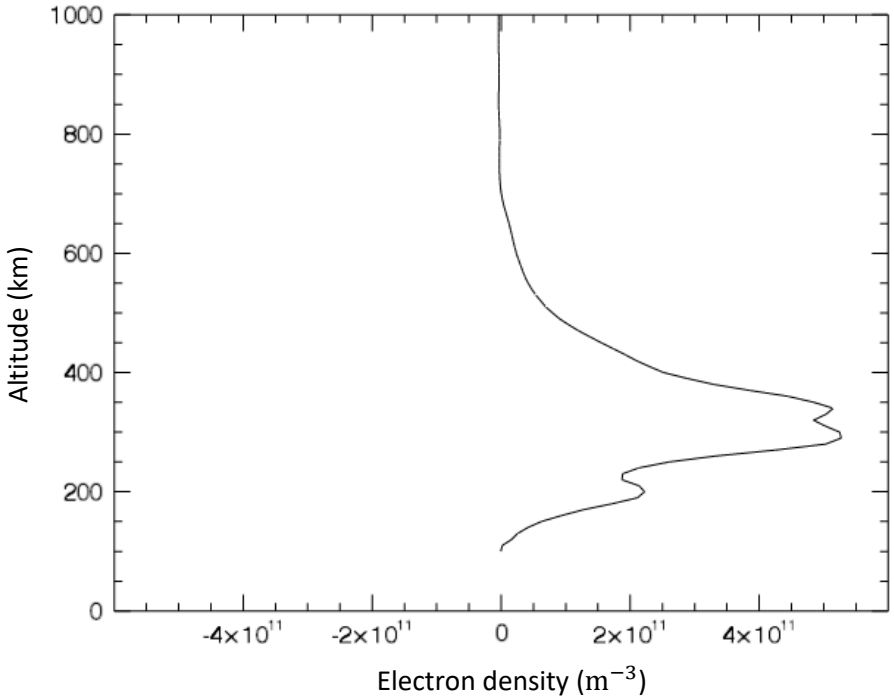

Figure 50c and d – EDAM VTEC Difference plot, Figure 50c, and electron density difference height profile, Figure 50d, for 12:00 UT. The difference TEC map in Figure 50c VTEC differences agree with Figure 50b. Large VTEC difference, values exceeding 10TECU, that have appeared at approximately 58°N latitude. In Figure 50d the maximum of electron density difference is located at near 300 km with a value of near 5x10^{11} m^{-3}.

Figures 51a and 51b present the SuperDARN electric potential plot and the EDAM GPS VTEC map for 12:30 UT. In Figure 51a Iceland is located to the east of the throat between the two convection cells. Tromsø is located well within the afternoon convection cell and north of the marked boundary of the channel. There appears to be strong plasma flow into the polar cap, shown by the red velocity vectors in the electric potential plot. In Figure 51b, EDAM would now be unable to see the TOI from this time step with it being located to the west of the EDAM grid. However, the channel of larger VTEC values has appeared more horizontally. The boundary the larger VTEC values, in both figures 51a and 51b, consistent with the flow entering the polar regions to the west of the grid, confirmed by Figure 51a.

Figure 51c shows the VTEC difference map for 12:30 UT. The large VTEC difference values seen in Figure 50d in the east are still present for this time step. The channel seen in the VTEC map in Figure 51b however does not come through as strong in the VTEC differences. There are some positive VTEC difference values located north of the UK latitudes, but these values are small in comparison. The values are approximately 2 TECU. The depletion that was seen to the west of the channel in earlier on in the day is still present to the west of the large VTEC differences and now because of the change in position of the channel is between the north marked boundary and the equatorward edge of the grid. Figure 51d shows the electron density difference height profile. The maximum electron density difference is at approximately 200 km with a value of near $4x10^{11}$ m^{-3}. The positive electron density differences are shown up to 600 km.

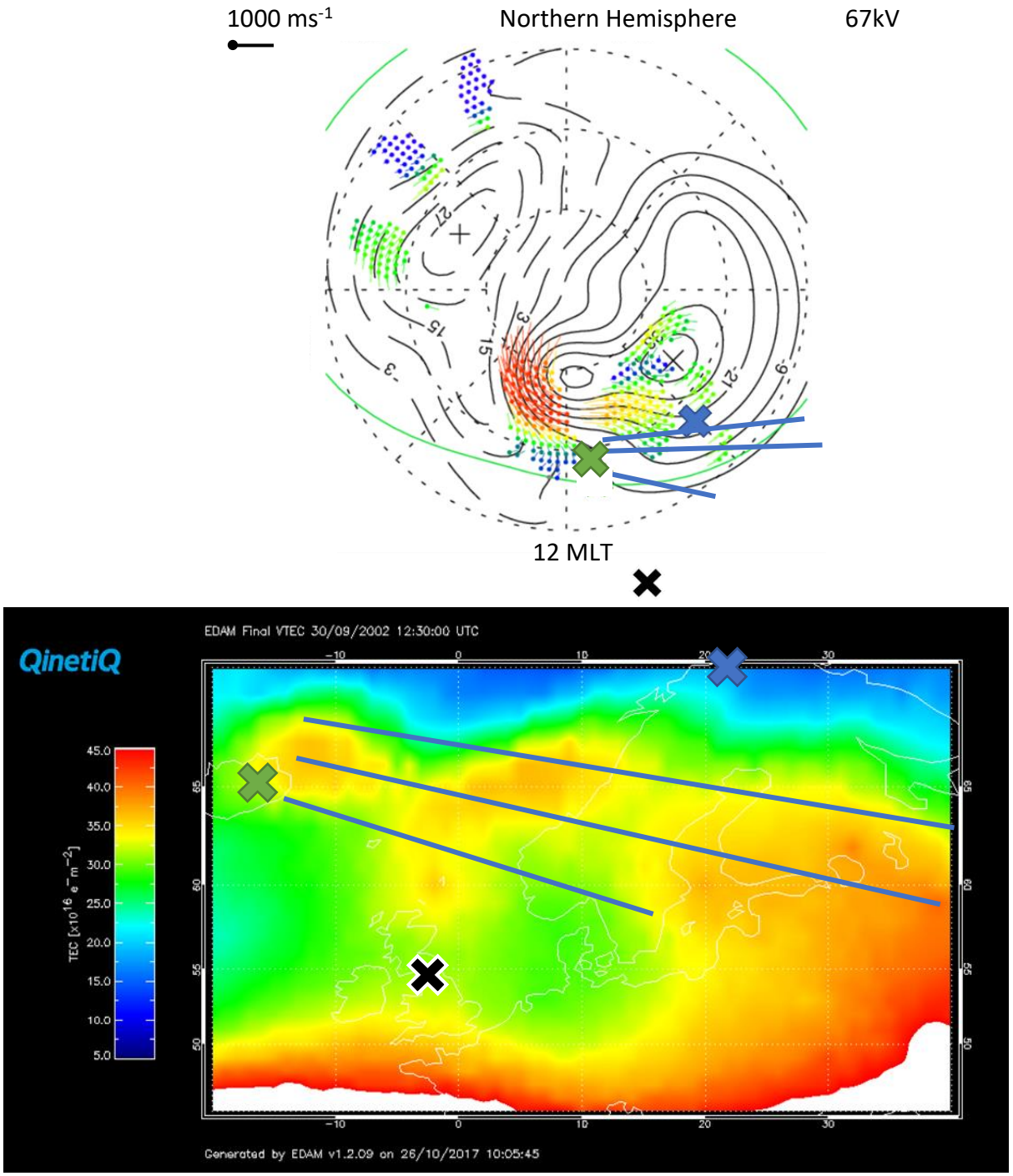

Figure 51a and b – SuperDARN electric potential plot, Figure 51a, and EDAM VTEC map, Figure 51b, for 12:30 UT. In Figure 51a Tromsø is located well within the afternoon convection cell and north of the marked boundary of the channel. There appears to be strong plasma flow into the polar cap to the west of Iceland. In Figure 51b the TOI would be located to the west of the EDAM grid so it no longer visible in EDAM. The marked boundary and centre line of the channel is located more horizontally on EDAM compared to earlier times. The VTEC values of the centre line are smaller compared to previous times, with values of approximately 35 TECU.

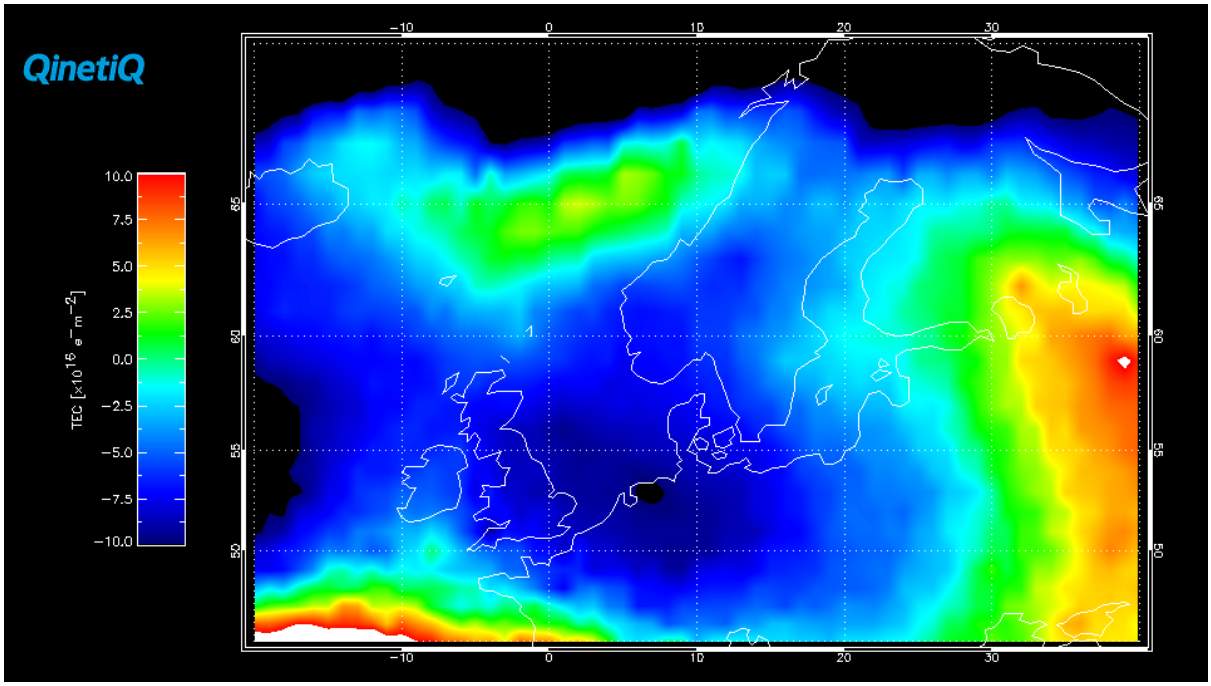

Electron density difference plotted at 37.0°E and 58.0°N at 12:30 UT

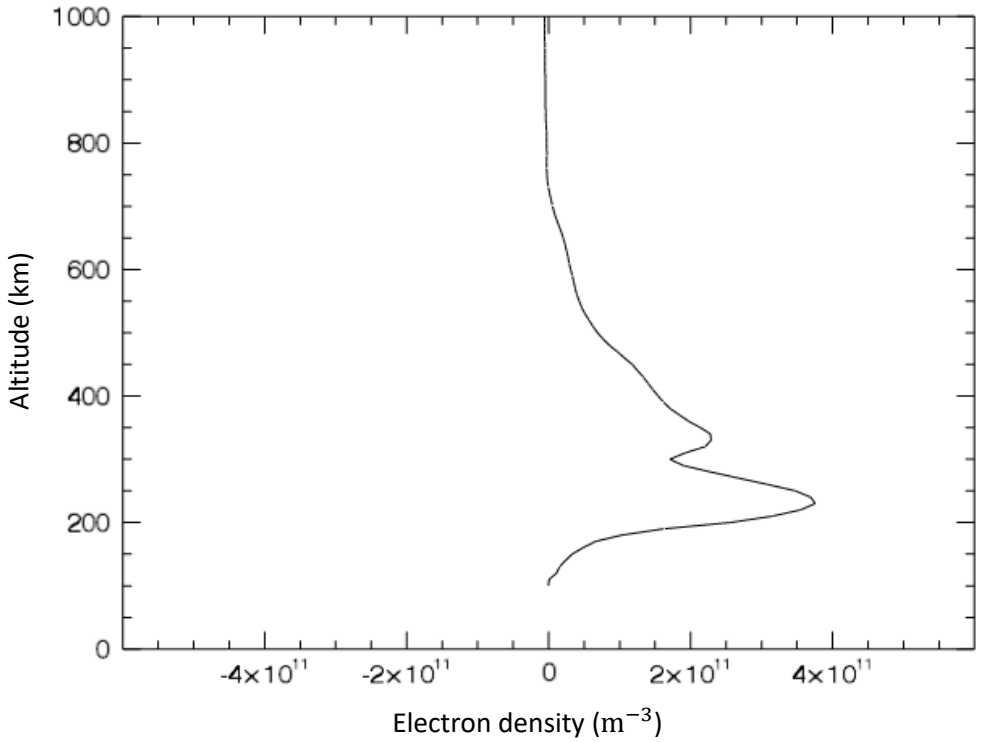

Figure 51c and d – EDAM VTEC Difference plot, Figure 51c, and electron density difference height profile, Figure 51d, for 12:30UT. The channel seen in the VTEC map in Figure 51b however does not come through as strong in the VTEC differences. The depletion that was seen to the west of the channel in earlier on in the day is still present south of the channel and to the west of the larger VTEC difference values. In Figure 51d the maximum electron density difference is at approximately 200 km with a value of near $4x10^{11}$ m^{-3}.

Figures 52a and 52b show the SuperDARN electric potential plot and EDAM GPS VTEC map for 13:00 UT. Figure 52a shows the location of Iceland slightly to the south-east of the throat region between the afternoon and morning convection cell. The plasma flows with the afternoon cell and into the polar cap. Tromsø is fully enveloped in the afternoon convection cell and is north of the marked channel. The direction of the marked channel in Figure 52a aligns with the direction of the plasma flow. In Figure 52b VTEC values, between 40-45 TECU, appear to be more extended in longitude rather than latitude compared to earlier plots, just like in Figure 51b. The largest VTEC values seen in this channel are now located at Icelandic latitudes and longitudes. A development of larger VTEC values is appearing closer to UK latitudes where it appears the channel VTECs are joining with the equatorial VTECs. This leaves less of a trough of VTEC between the two regions.

Figure 52c shows the VTEC difference map for 13:00UT. The channel stands out more in the difference VTEC values compared to the last time step. The largest VTEC difference values are in the marked channel of Figure 52b, with values of 5 TECU at the latitude and longitude of Iceland. At the plume base region, the VTEC difference values are of a similar magnitude. The depletion is still there to the south of the channel and west of the plume base. VTEC difference values of greater than 10 TECU is seen at the lowest latitudinal extent of the EDAM grid, 50°N latitude, and at 10°W longitude. Figure 52d shows the electron density difference height profile. The maximum electron density difference value is at approximately 250 km with a value of near $4x10^{11}$ m^{-3}.

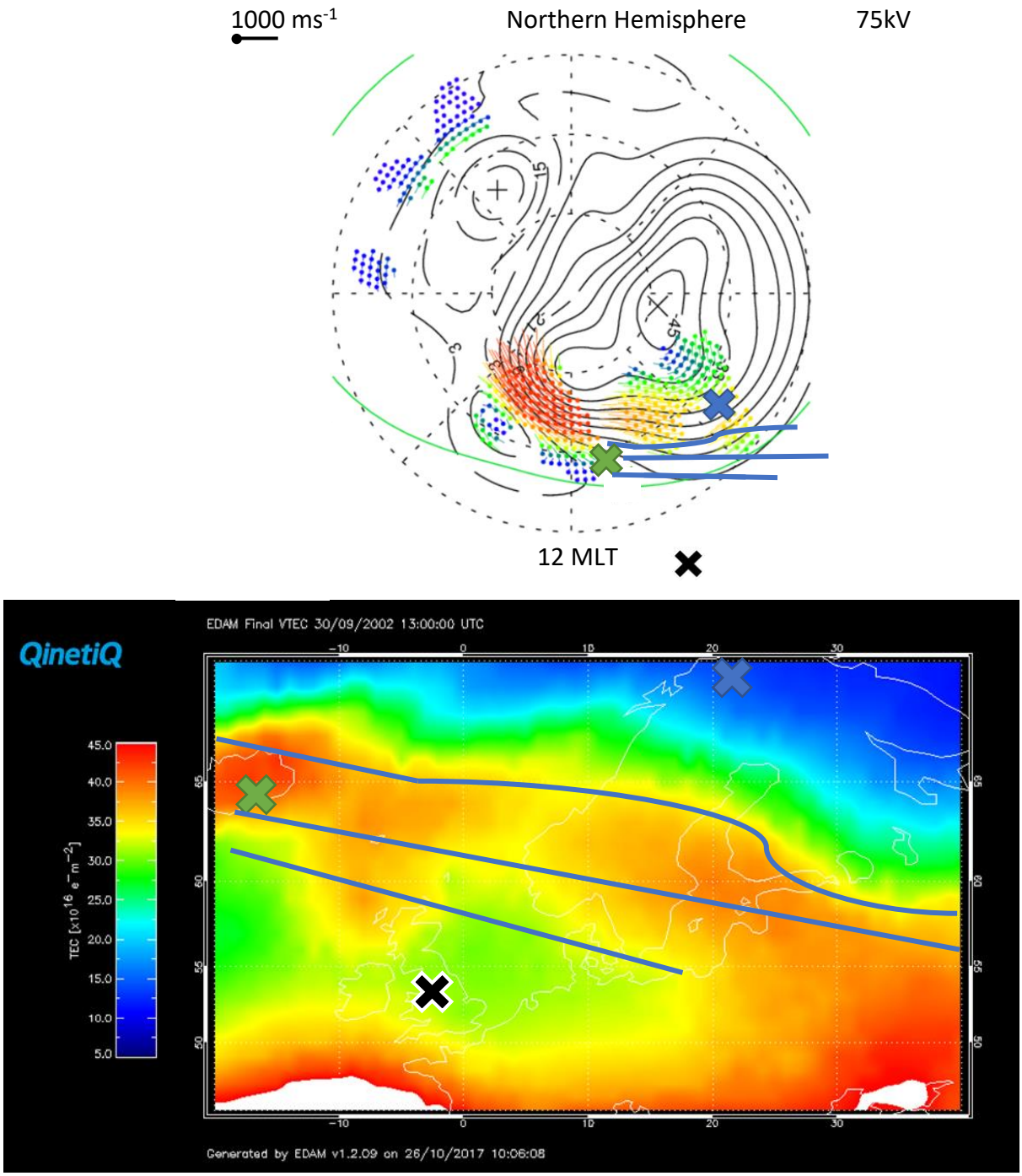

Figure 52a and b – SuperDARN electric potential plot, Figure 52a, and EDAM VTEC map, Figure 52b, for 13:00 UT. In Figure 52a location of Iceland slightly to the south-east of the throat region between the afternoon and morning convection cell. The largest VTEC values seen in this channel are now located at Icelandic latitudes and longitudes, values of 40 to 45 TECU.

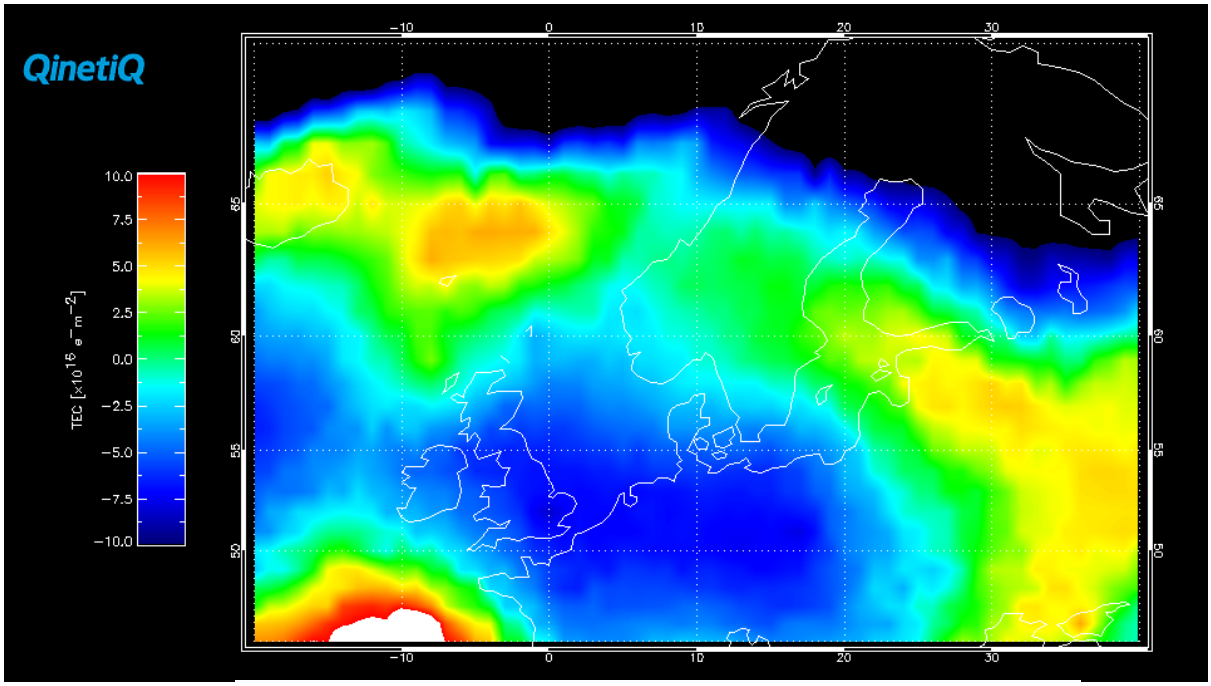

Electron density difference plotted at 37.0°E and 58.0°N at 13:00 UT

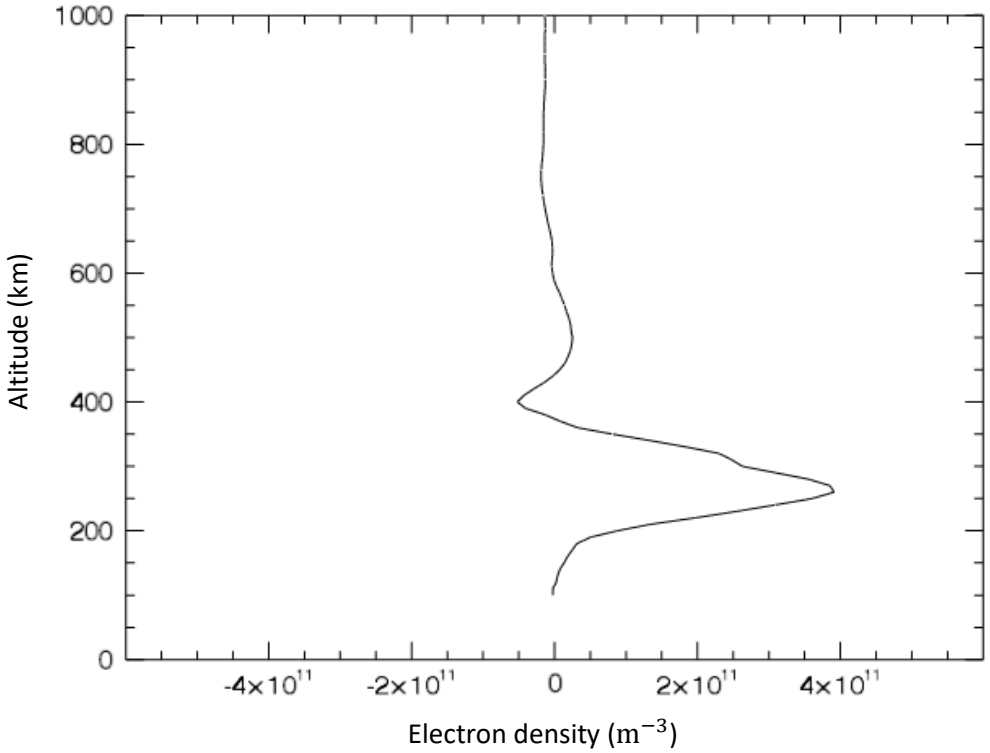

Figure 52c and d – EDAM VTEC Difference plot, Figure 52c, and electron density difference height profile, Figure 52d for 13:00 UT. In Figure 52c, the largest VTEC difference values are in the marked channel of Figure 52b, with values of 5 TECU at the latitude and longitude of Iceland. VTEC difference values of greater than 10 TECU are seen at 50°N latitude, and at 10°W longitude. In Figure 52d, the maximum electron density difference value is located at approximately 250 km.

The SuperDARN electric potential plot and EDAM GPS VTEC map for 13:30 UT are presented in Figures 53a and 53b. Figure 53a shows the position of Iceland on the edge of the afternoon convection cell. Surrounding this cell are strong plasma flows, with directional velocity vectors to the west, flowing into the polar cap. The marked channel on this plot aligns with the velocity vectors of the electric potential plot. Tromsø is again located deep within the afternoon convection cell and far north of the channel. Figure 53b shows the marked channel of VTEC values of 40 to 45 TECU. The channel is very similar in structure compared to the previous time step. The potential merging of the channel and the equatorial region is more evident in this time step when looking at the VTEC values. There is still a small trough of VTEC between the two regions, located at roughly 55°N latitude and near 0° longitude.

In Figure 53c, the VTEC difference map, the values of the marked channel are small by comparison of the previous time step with values between 0 and 2.5 TECU. At the location of the plume base, the values are of a slightly higher magnitude but show more variation in the region, with values between 0 and 5 TECU. The merging of the channel and equatorial region is less noticeable in the VTEC difference values as the depletion is still prevalent in the same region. However, the gap between the two larger, positive VTEC difference values at UK altitudes is decreasing. Figure 53d shows the electron density difference height profile for 13:30 UT. The maximum difference value is located at 350 km with a value of approximately 2.5×10^{11} m^{-3} which is significantly smaller than the previous time step.

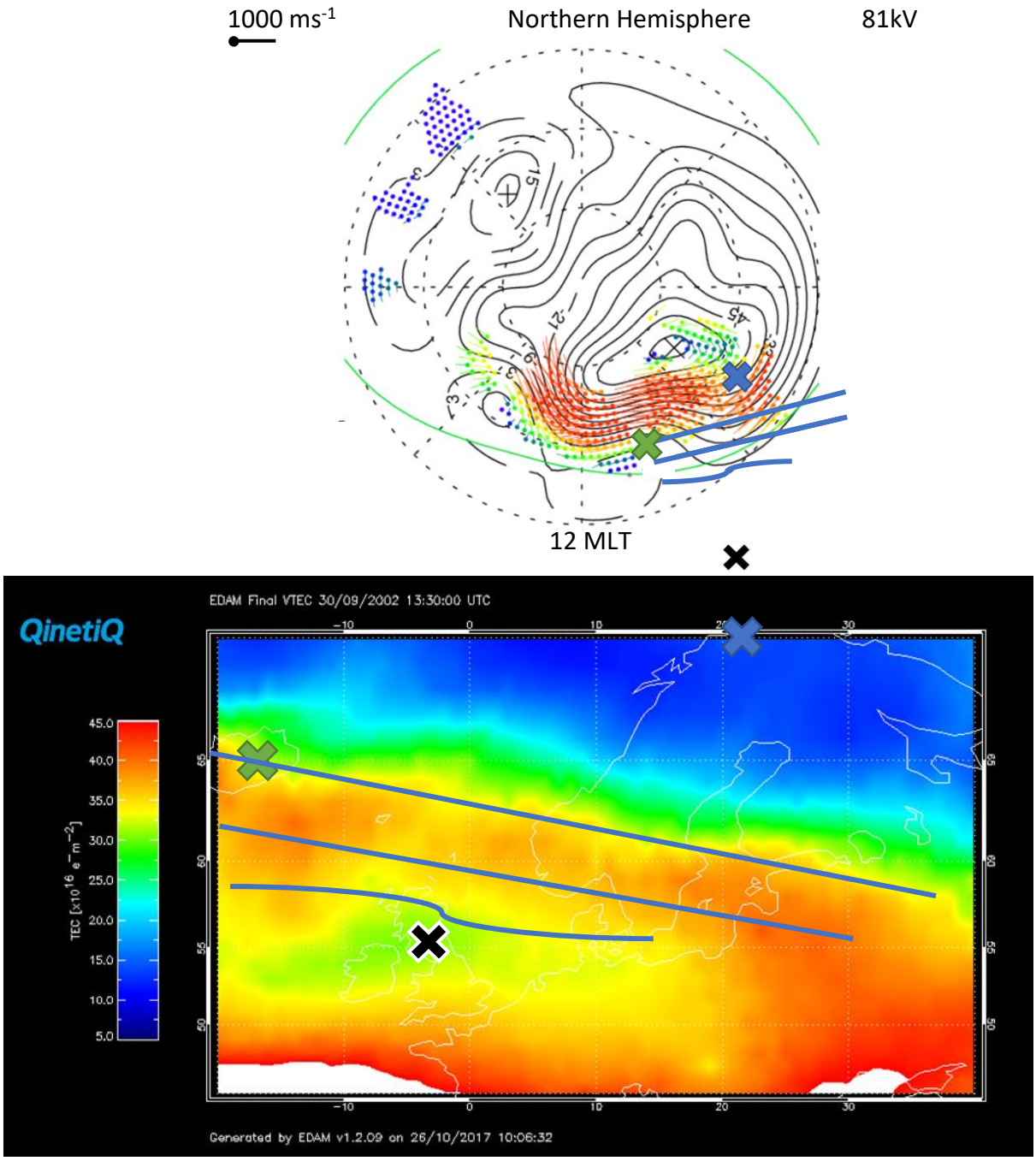

Figure 53a and b – SuperDARN electric potential plot, Figure 53a, and EDAM VTEC map, Figure 53b, for 13:30 UT. In Figure 53a the position of Iceland is located on the edge of the afternoon convection cell. Figure 53b shows the marked channel of VTEC values to be 40 to 45 TECU.

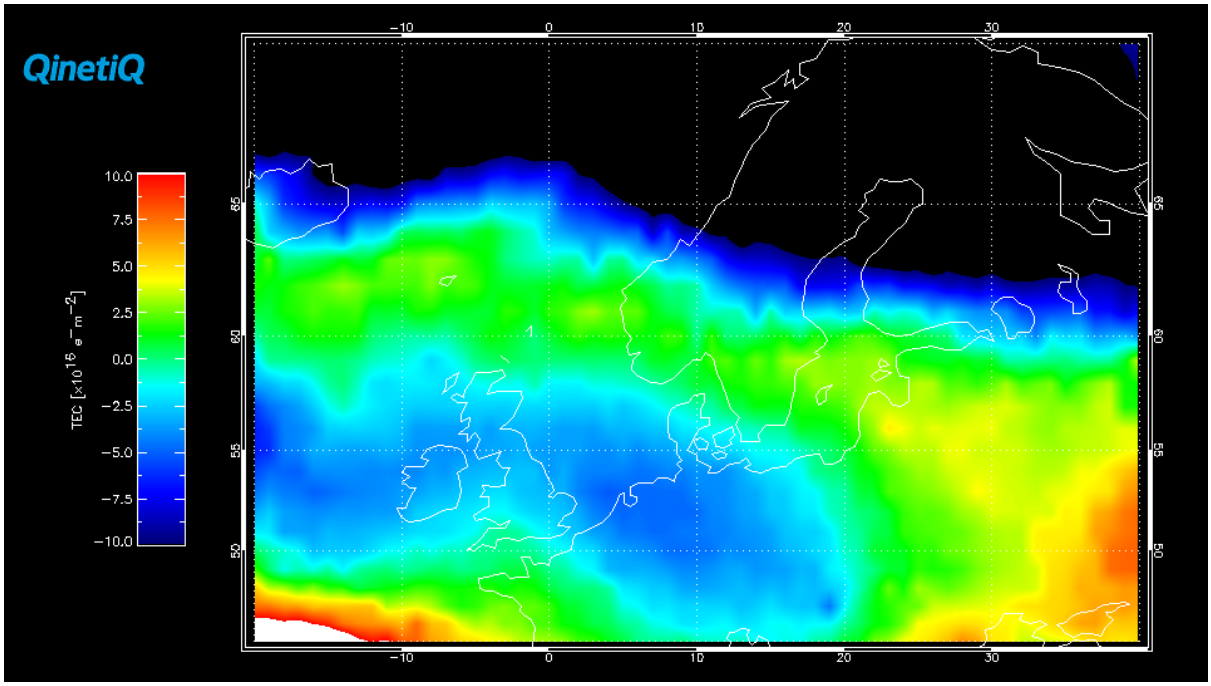

Electron density difference plotted at 37.0°E and 58.0°N at 13:30 UT

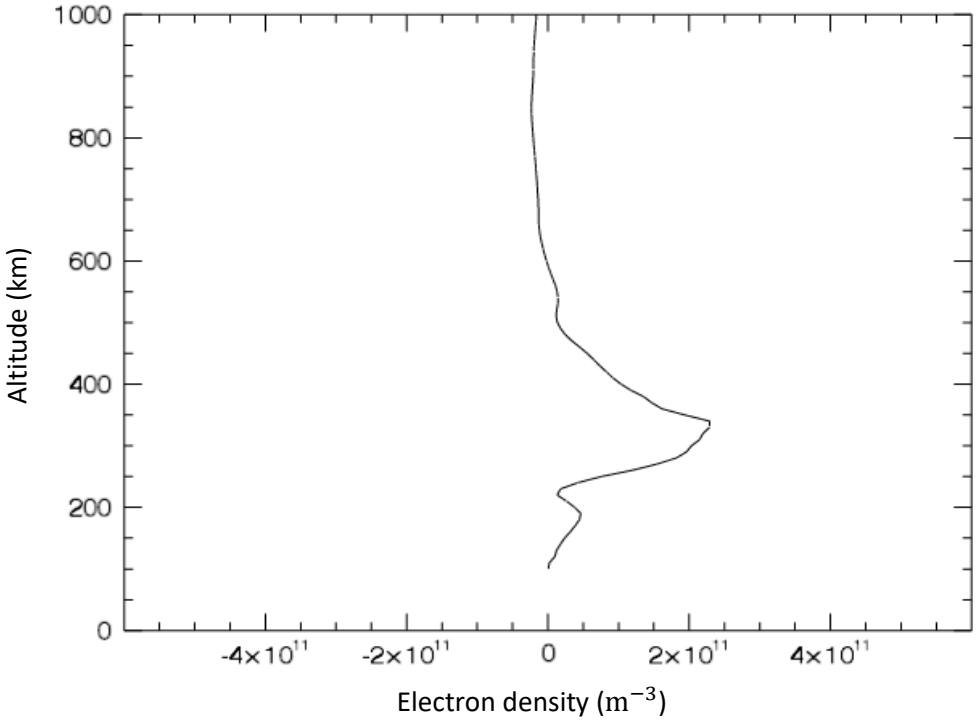

Figure 53c and d – EDAM VTEC Difference plot, Figure 53c, and electron density difference height profile, Figure 53d, for 13:30UT. In Figure 53c, the values of the marked channel are small, between 0 and 2.5 TECU. The maximum electron density difference value is at approximately 350 km.

Figures 54a and 54b show the SuperDARN electric potential plot and EDAM GPS VTEC map for 14:00 UT. Figure 54a shows Iceland on the edge of the dominant afternoon cell and north of the auroral boundary. The velocity vectors over this region show the directional flow of the plasma to be to the west, following the afternoon cell. The convection cell structure is broken up on the morning side, so it is difficult to tell where the plasma enters the polar cap. The marked channel aligns with the directional flow of the plasma at the latitude and longitude of Iceland. In Figure 54b the marked channel is still evident by the large VTEC values of 40 to 45 TECU. However, at roughly the midway point of the marked channel, roughly 0° longitude and 60°N latitude, there appears to be a decrease in the VTEC value compared to the rest of the VTECs in the channel, with values less than 35 TECU. The trough region between the channel and the equatorial region is still evident at UK latitudes in this time step.

Figure 54c, the VTEC difference map for 14:00 UT, shows the split of the channel much clearer, with VTEC difference values in this region of approximately 2.5 TECU. Just below the channel the VTEC difference values are approximately -2.5 TECU, indicating the quieter day modelled VTEC values greater than 30 September. The region to the north of the channel shows a large depletion in VTEC difference of values greater than -10 TECU. At the location of the plume base the VTEC difference values are 10TECU and greater. Figure 54d shows the electron density difference height profile for 14:00 UT. There is a big shift in this height profile with the maximum difference value being approximately -2×10^{11} m^{-3} at approximately 300 km. This indicates the defined location is now exhibiting lower electron density values on 30 September compared to 29 September. There is a positive maximum electron density difference at 200 km at this latitude and longitude with a value of 1×10^{11} m^{-3}.

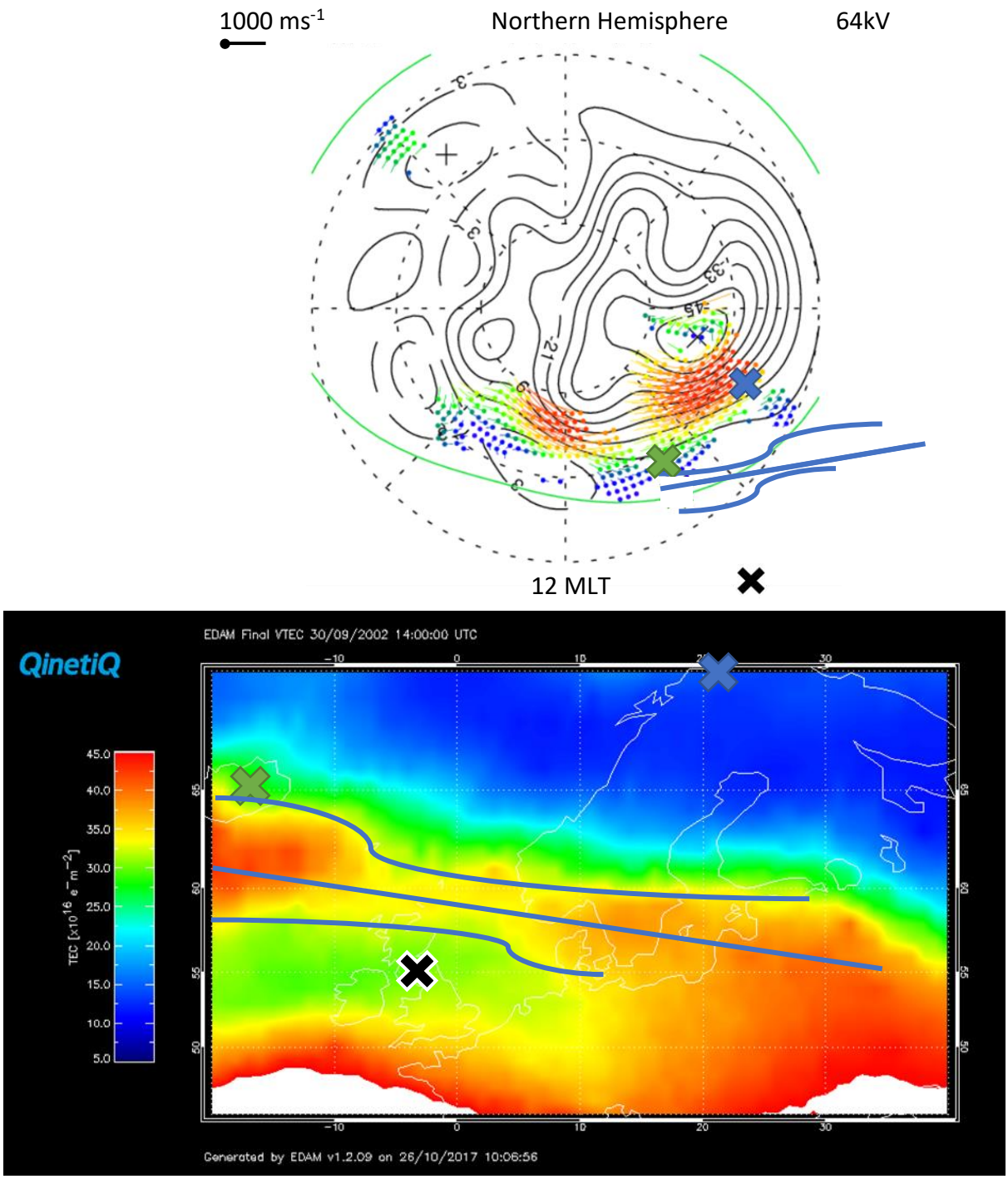

Figure 54a and b – SuperDARN electric potential plot, Figure 54a, and EDAM VTEC map, Figure 54b, for 14:00 UT. Figure 54a shows Iceland on the edge of the dominant afternoon cell and north of the auroral boundary. Figure 54b shows the marked channel is still evident by the large VTEC values of 40 to 45 TECU.

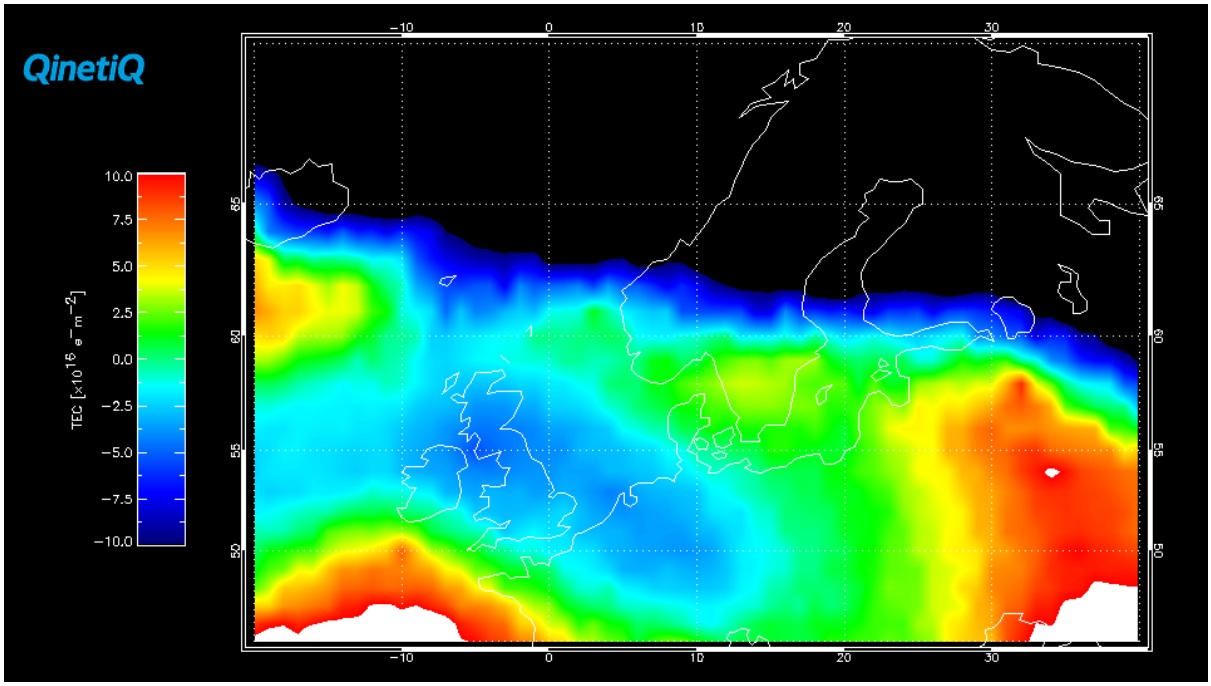

Electron density difference plotted at 37.0°E and 58.0°N at 14:00 UT

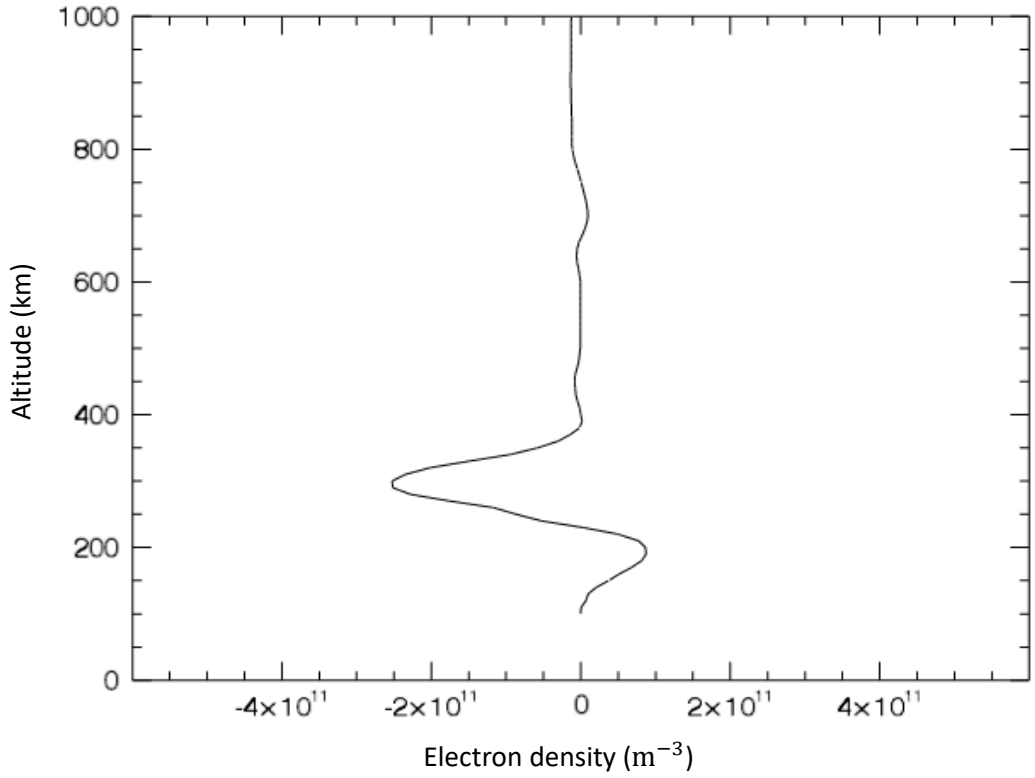

Figure 54c and d – EDAM VTEC Difference plot, Figure 54c, and electron density difference height profile, Figure 54d, for 14:00 UT. In Figure 54c, the channel is shown with VTEC difference values in this region of approximately 2.5 TECU. The region to the north of the channel shows a large depletion in VTEC difference values, greater than -10 TECU. In Figure 54d the maximum difference value is approximately -2x10^{11} m^{-3} at approximately 300 km.

Figures 55a and 55b show the SuperDARN electric potential plot and EDAM GPS VTEC map for 14:30 UT. These series of figures mark the end of the comparison. Figure 55a shows the dominant afternoon convection cell, with Iceland located on the edge of this cell. The plasma is shown to flow over this region, given by the direction of the velocity vectors on the plot. The flow of the plasma is shown to travel far to the west of these longitudes, following the afternoon cell. The marked channel on this plot is located to the south of Iceland and the afternoon cell and no longer aligning with the flow of the plasma. Figure 55b shows the marked channel, with much lower VTEC values, approximately 35 TECU, and begins to merge with the larger VTEC values at the lower latitudes.

The VTEC difference map in Figure 55c confirms what has been said in Figure 55b. The channel marked in Figure 55b is not nearly as noticeable in the VTEC difference values, and the channel region appears to join with the lower latitude region. The region in between 50° latitude and 60° latitude, seen at the south eastern corner of the grid still shows larger VTEC differences. The depletion north of the UK is still prominent with VTEC difference values greater than -10 TECU. Figure 55d shows the electron density different height profile. There is a maximum density difference seen between 250 km and 300 km, with a value greater than $4x10^{11}$ m^{-3}. There is a smaller second maximum modelled at 450 km but this time with an electron density difference greater on the 29 September with a value of near $-2x10^{11}$ m^{-3}.

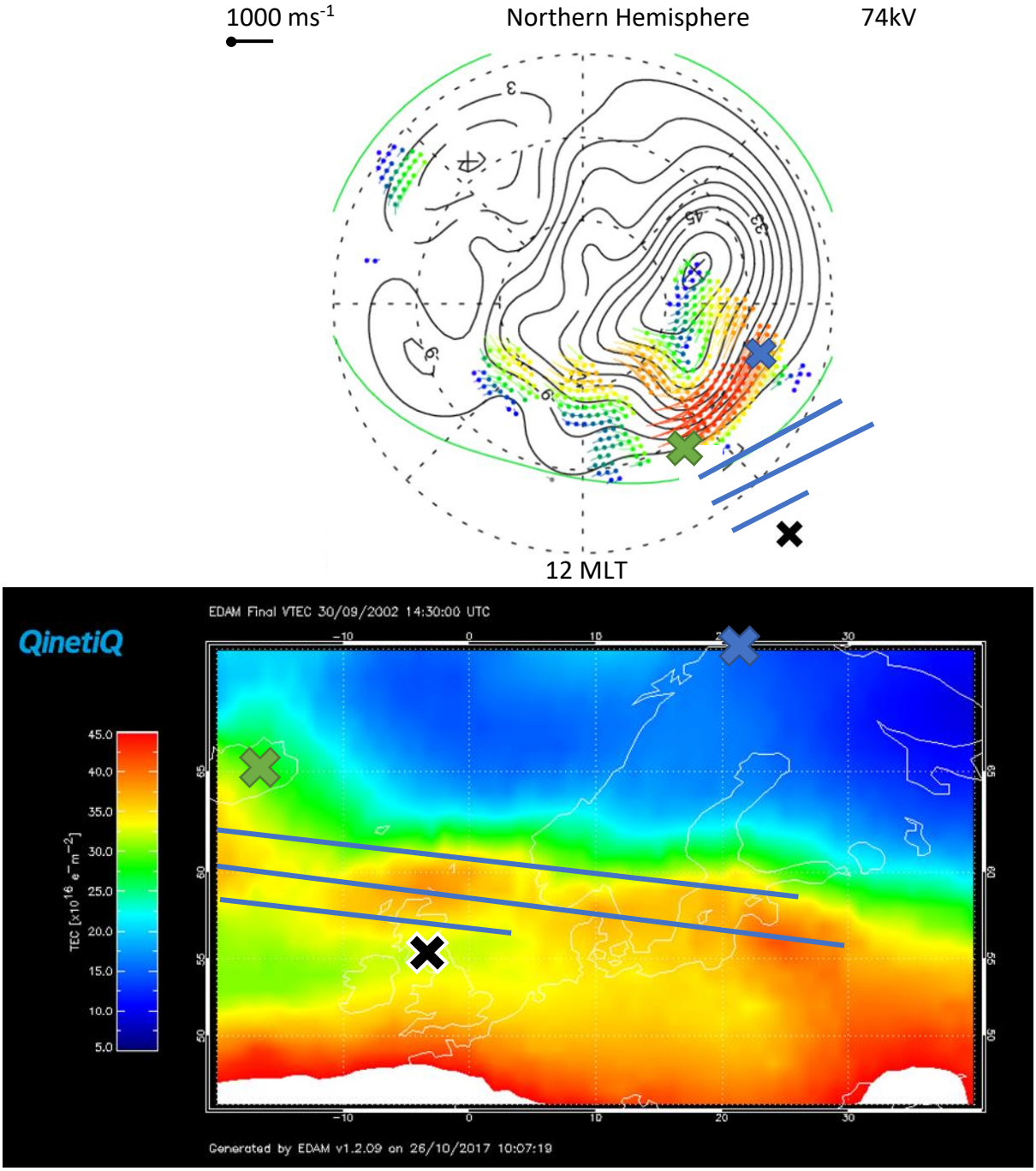

Figure 55a and b – SuperDARN electric potential plot, Figure 55a, and EDAM VTEC map, Figure 55b, for 14:30 UT. Figure 55a shows the dominant afternoon convection cell, with Iceland located on the edge. Figure 55b shows the marked channel with VTEC values of, approximately 35 TECU. The channel begins to merge with the larger VTEC values at the latitudes of around 50°N.

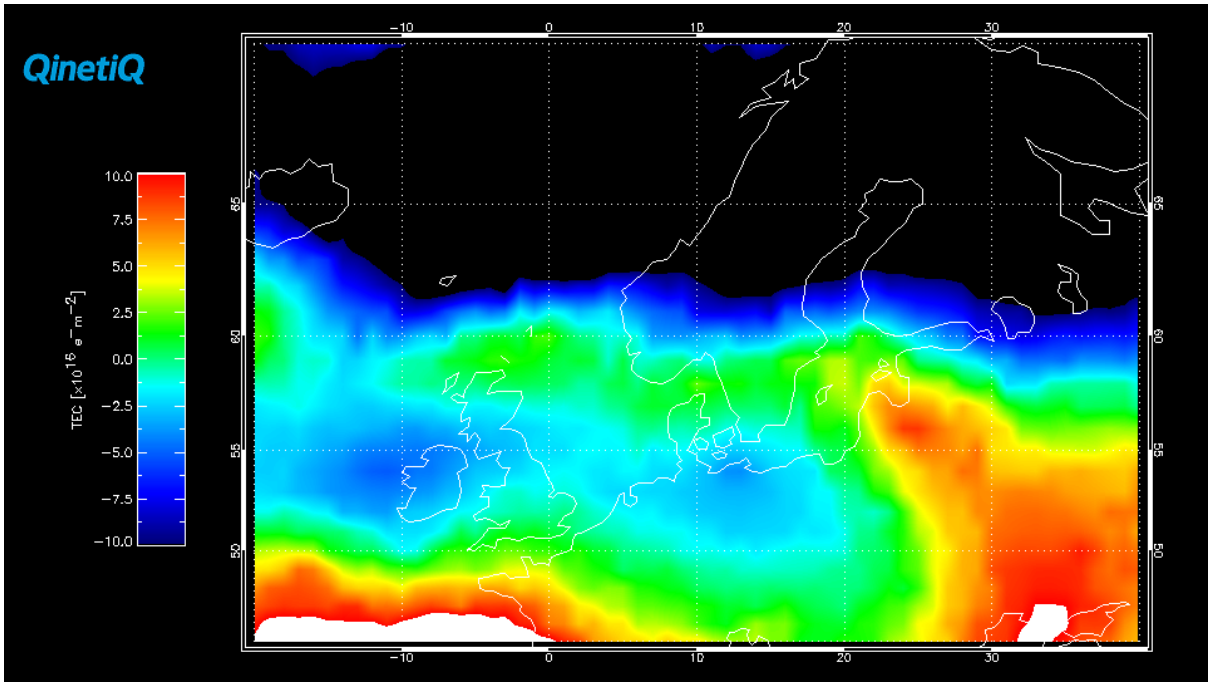

Electron density difference plotted at 37.0°E and 58.0°N at 14:30 UT

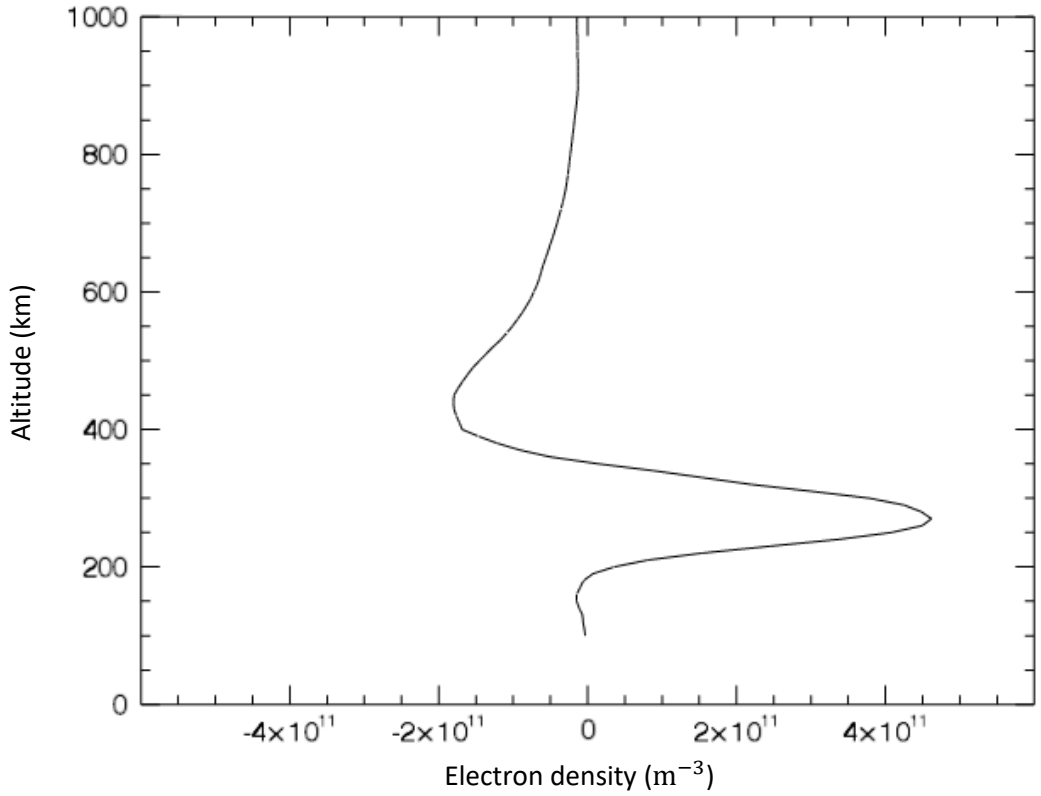

Figure 55c and d – EDAM VTEC Difference plot, Figure 55c, and electron density difference height profile, Figure 55d, for 14:30 UT. In Figure 55c, the channel is not nearly as identifiable in the VTEC difference values. The depletion to the north of the UK latitudes is evident with VTEC difference values greater than -10 TECU. In Figure 55d, there is a maximum density difference seen between 250 km and 350 km, with a value greater than $4x10^{11}$ m^{-3}.

6.4 Discussion

Observations of the TOI (Figure 44 to 52) and an SED plume (Figure 44 to 55) have been presented on the 30 September by use of GPS VTEC maps from EDAM and SuperDARN electric potential plots. EDAM VTEC, difference maps between the active and quiet day were presented along with electron density difference height profiles. The Kp index (Figure 39) and the Dst index (Figure 40) set the scene for the activity on 30 September 2002. The increasing value of the Kp index compared to the previous day displayed the increase in geomagnetic activity, confirmed by the changes in the Dst index, before the observations presented in section 6.3.

The TOI cannot be identified definitively in the early morning, 09:00UT, when comparing the EDAM VTEC grid and the electric potential plot (Figures 44a and 44b). The location of the marked channel is too far south in latitude on the electric potential plot, meaning the connection between the channel and the convection cells cannot be made, only assumed due to the defined direction of the channel. The VTEC values (Figure 44b) that haven't been marked in the channel, 70°N latitude and between 20°E and 40°E longitude with values of approximately 30 TECU, provide a hint of the extension of the channel but due to the definition of the boundary were not marked. The location of the channel is also to the east of the marked throat region of the convection cell (Figure 44a), so it could only be inferred in this time step that the plasma is picked up at higher latitudes, and convected towards the polar cap, which is the signature of the TOI. (Knudsen, 1974)

While the TOI could only be inferred from the electric potential plot and the VTEC map, data from the Defense Meteorological Satellite Program (DMSP) F13 satellite provides the evidence for the presence of a TOI. Figure 56 shows the DMSP F13 high latitude data survey

plot for 30 September 2002 between 08:50 UT and 09:20 UT. The region of interest in this pass is marked by the black vertical lines. This depicts the auroral boundary with the higher energy electrons and ions marking the equatorward edge and the lower energy electrons and ions being within the polar cap, in the pass of the satellite (Redmon et al., 2017; Yuan et al., 2008). Inside the marked region looking at 09:05 UT marks the closest to the times of the plots of Figure 44a and 44b. In this region the horizontal component of the ion drift velocity is strongly negative. A positive horizontal component would always be sunward and perpendicular to the direction of the flight. This means a negative horizontal component, like in the marked region, shows the ions are drifting in the opposite direction. The vertical component of the velocity for this region should be negative, downward ion flow, if the satellite has passed over the TOI as this would be consistent with other observations (Foster et al., 2005; Yuan et al., 2008) from the North American region. This is an important factor for keeping the electron density of a TOI at a high level as it passes over the polar cap. At approximately 09:02 UT, the values could be of the order of -100 ms^{-1} but the scale is too large to see this on Figure 56.

However earlier on in the pass, 09:00 UT, when the pass was over the auroral boundary, the ion up-flow velocity was strongly positive. Yuan et al. (2008) concluded from their results that a TOI, that is driven from an SED, can lead to strong up-ward ion flows at the auroral zone and polar cap boundary. This is evident in this pass.

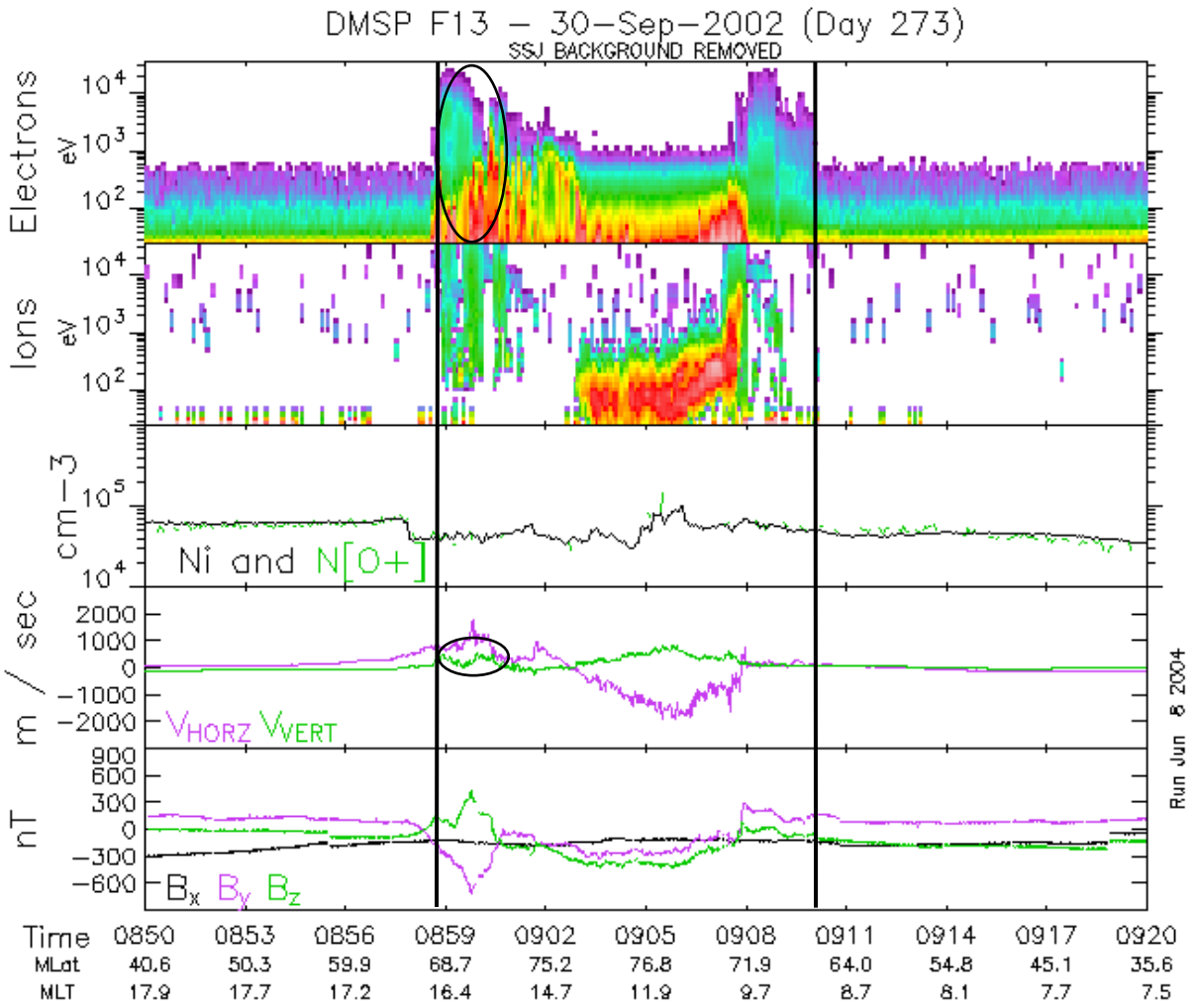

Figure 56 – A DMSP high latitude data survey plot for the pass of F13 satellite between 08:50 UT and 09:20 UT. The spectrogram results (1st and 2nd row from the top) show the flux at the considered energies of the electrons and the ions. The third row shows the ion density and the O^+ density, which are very similar because O^+ constitutes most of the ion density. The 4th row shows the horizontal (positive being perpendicular to the satellite flight) and vertical (positive being upward flow) components of the ion drift velocity. The final row shows the magnetic field components measured from the satellite. The black vertical line indicates the region of the auroral boundary into the polar cap. The region that has been circled shows the positive up-flow ion drift velocity in both vertical and horizontal components in the 4th row and the corresponding energy of electrons.

In the next DMSP F13 pass, shown in Figure 57, in the northern hemisphere, at roughly 77 magnetic latitude, 10 MLT and 10:50 UT, the vertical component of the ion drift velocity is negative to the order of 100 ms^{-1}. This value is what is seen in Yuan et al. (2008) and Foster et al. (2005) to suggest that the satellite has passed over a TOI. Using those results and these DMSP passes the TOI presence can be confirmed and the time it persists can be determined.

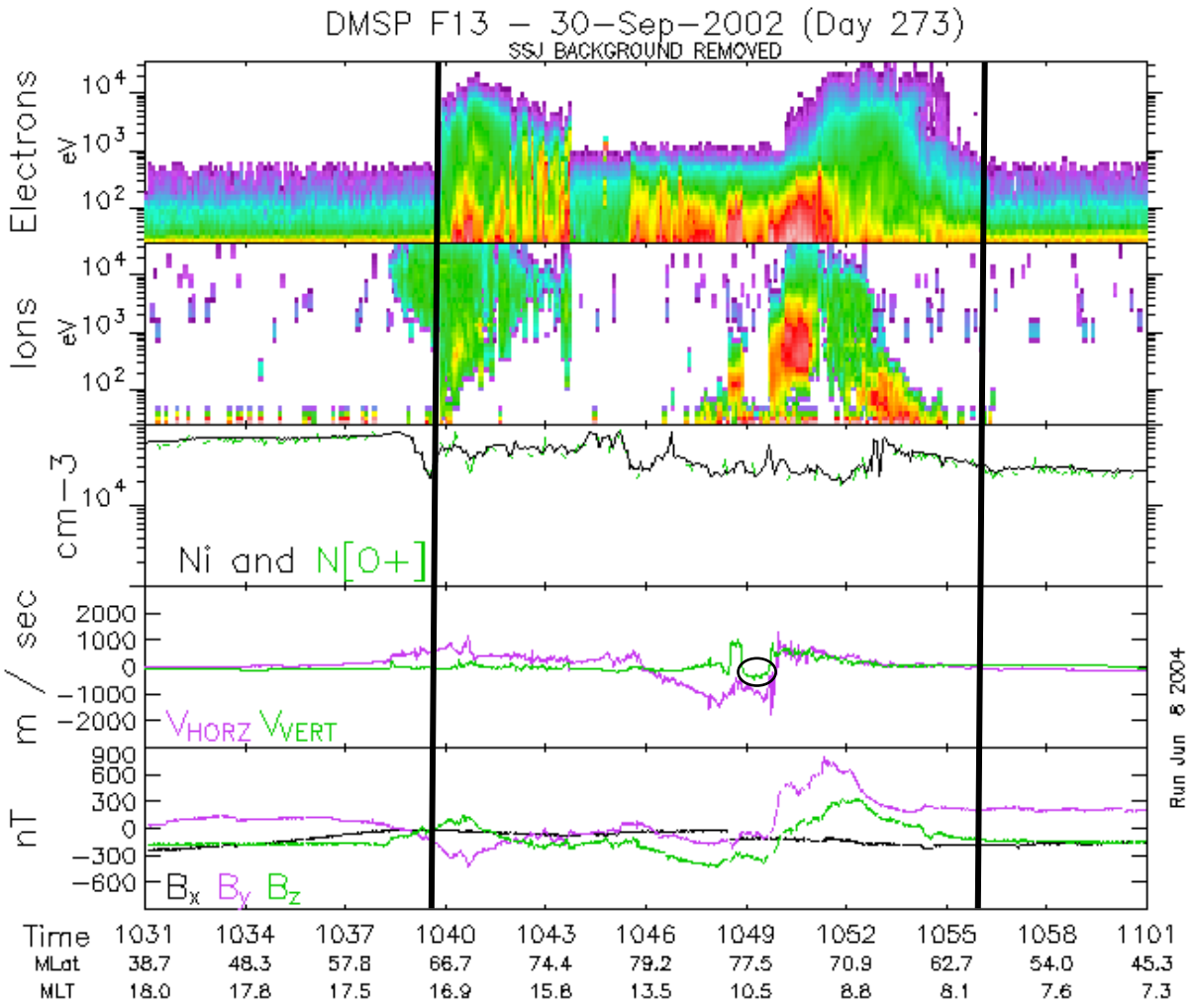

Figure 57 – A DMSP high latitude data survey plot for the pass of F13 satellite between 10:31 UT and 11:01 UT. The auroral boundary has been marked by two vertical black lines and the ion drift vertical velocity component that's negative is marked by a black circle.

Confirming the TOI leads to the next step, which was to find the source, based on a number of results, including for example Foster et al. (2005), Hosokawa et al. (2010), Thomas et al. (2013) and many other results. The conclusions of the mentioned literature, as described in the introduction of this chapter (Section 6.1), pointed towards SEDs as the source of the ionisation flow over the polar cap.

Deciding on the location of the SED plume base for this current study, shown by the small red cross in Figure 44c, was based on the results from Coster et al. (2007) and Yizengaw et al. (2006). The latitudes for the plume base in Figure 3 of Coster et al. (2007) from the number

of different events had a linear line that was fitted to the data. This linear line of best fit suggested that at 09:00 UT the SED base would be at approximately 65° geographic latitude. Using Figure 1 of Coster et al. (2007) the geographic longitude is roughly between 30°-40°E. This shows the location of the SED plume base to be lie outside of the EDAM grid. The VTEC difference maps (Figure 44c) however, shows that the largest VTEC difference was at lower geographic latitudes. The plume base was seemingly closer to 60°N latitude. The SED plume base outlined by Yizengaw et al. (2006) in Europe was also at roughly 60°N geographic latitude during September, but in the year 2005. This latitude agrees more with the findings in this current study for 09:00 UT. Yizengaw et al. (2006) clearly outlines the plume of ionisation separating from the main daytime ionisation at lower latitudes. This helps to outline the base of the plume.

While the latitude of the plume in this current study agrees with Yizengaw et al. (2006), the location of the plume base in the earlier study is more to the east, which is outside of the EDAM grid. While this potentially means the plume base cannot be directly seen in the EDAM VTEC, the location chosen with the help of Coster et al. (2007) and Yizengaw et al. (2006) provides guidance of where the SED plume base is located in the EDAM grid. Also due to the two results showing different locations for the SED plume base, this shows variability in the findings of the position of the SED plume base. The Kp indices for both are at similar levels, Kp index of 6, and both events occur in the Autumn. The difference between the two is in year with one being in 2001 and the other event in 2005 indicating a difference in the solar cycle. The year 2001 was closer to a solar maximum while 2005 was closer to a solar minimum. (Solomon et al., 2018)

The electron density differences between the active day and the quiet day (Figure 44d) shows a notable increase in maximum electron density at altitudes of 300-400 km with smaller positive differences shown up to 600 km. According to the results from Evans (1970) and Foster et al. (1993) the SED is indicated in vertical profiles of electron density by an elevated F region peak altitude and enhanced topside densities with respect to a quiet day. While the electron density differences of the current study must be taken with caution due to no ionosonde input, the increases in values of electron density seen at topside altitudes of the ionosphere show agreement with these findings. Having also established that the chosen SED plume base for this study could be to the west of the true location, it is likely that the values will be seen much stronger and clearer at the location of the plume base.

In the GPS VTEC difference map (Figure 44c) there is a region of VTEC that is significantly depleted on 30 September compared to 29 September 2002. This region, referred to as a 'hole', is present in Liu et al. (2016). It could also be present in Coster et al. (2007) and Thomas et al. (2013) but it is more difficult to confirm because the GPS TEC maps do not show the difference to a previous, quieter day. The 'hole' is not easy to identify but the locations of where it should lie are confirmed east of the TOI/SED in this current study and Liu et al. (2016). Liu et al. (2016) obtained the TEC data from the Madrigal database and produced absolute TEC difference maps between a storm time day and a quiet time day, similar to what was done for this study. That data showed an electron density hole either side of the observed SED and TOI. They then used the NCAR-TIEGCM model, which is a time-independent, three-dimensional, thermosphere-ionosphere coupled model, to compare with the GPS absolute TEC differences. The interesting result from this was that the model could not reveal the hole that was evident in the GPS. The model displayed TEC values that were very similar to the quieter day or only slightly lower. EDAM in this study, using GPS assimilated data, could model

this VTEC hole. It is explained in Liu et al. (2016) that this hole is a cause of the quiet day exhibiting enhanced TEC values which when looking at the EDAM VTEC difference maps do show this to be the case. For this explanation to be the case something must be happening the day before in preparation for a storm time event to raise TEC values in the mid-high latitude ionosphere and more studies are required to verify that this occurs for most TOI/SED events.

The evolution of the TOI and SED plume is clearly shown in the results of this study (Figures 44 to 55), showing the TOI persisting for several hours with the SED as the driver of the ionisation from lower latitudes. Starting from Figure 50 it is not obvious that the TOI is still present in the VTEC map. However, when comparing the map to the electric potential plot, the plasma is picked up in the convection cell and then transported across the polar cap to the west of Iceland. This is not in the grid range of the VTEC map but the idea that this occurs can be seen due to the direction of the marked channel and the line of enhanced VTEC in this channel. It is only at 14:00 UT and beyond (Figures 54 and 55) that the TOI can no longer be perceived in the VTEC map. The VTEC difference maps for these times also begin to show a break up in the channel and a merging of the lower latitude VTECs with the channel VTECs indicating it is no longer extending out from the bulk of lower latitude plasma like before.

The TOI in this study was observed to have persisted from 09:00 UT to 14:00 UT. TOIs are variable in how long they persist for. In Thomas et al. (2013) the TOI observed in their study only lasted for approximately 1 hour during a weak geomagnetic storm with sustained positive IMF B_y component and a strong negative IMF B_z component. Hosokawa et al. (2010) showed a TOI continuing for approximately 4 hours during an intense geomagnetic storm with a prolonged southward IMF B_z component. In Liu et al. (2015) a TOI was observed that lasted

for approximately 5 hours, the same length as the observed TOI in this study. It was observed during a period of weakly negative B_z component in the IMF. The structure of the TOI was only confined in the polar cap, meaning within 70°N magnetic latitude with an extension in width of 10°. Another TOI observed by Foster et al. (2005) lasted 3 hours during the early and main phases of the superstorm in November 2003. The negative B_z component of the IMF was much stronger, approximately -50 nT, and was more extended than the TOI observed by Liu et al. (2015) in both latitude and longitude. The results from other studies coincide with negative B_z components in the IMF and during geomagnetic storms. In this current study, Figure 38 showed periods of negative B_z component in the IMF from the approximately 10:00 UT lasting until approximately between 13:00 and 14:00 UT. In Figure 39, the Kp indices for 30 September, show a sustained value of 5 Kp index from 09:00 to 15:00 UT indicating high levels of geomagnetic activity using the Kp levels defined in Chapter 5. The Dst index in Figure 40 showed negative deviations from 0 nT from as early as 04:00 UT, with maximum deviations of -49 nT exhibited at 15:00 UT. This variation in the Dst index suggests a weak to moderate geomagnetic storm is taking place, using the definitions for a geomagnetic storm in Section 2.7.1.

The TOI is no longer evident from approximately 14:00 UT as previously mentioned, but there is still an enhanced density region at approximately 55°N latitude that is extended in longitude by approximately 30°, from approximately 10°E to 20°W. This suggests that it is possible the SED is still present, but there is no longer a TOI structure forming from the SED. This is a 'fossil' SED discussed by Thomas et al. (2013). The idea of the 'fossil' describes many features seen by Coster et al. (2006) where a TOI did not form from a SED. This 'fossil' SED is said to occur because the B_z component sharply switches from negative to positive, and

dayside reconnection is no longer present, meaning there is no mechanism allowing the ions and electrons to be drawn antisunward and transported across the polar cap, with the plasma to move from closed to open field lines (Cowley and Lockwood, 1996). This causes the SED plume to stagnate with no TOI. The sharp turning of the B_z component said to be required for the fossil SED of the IMF is observed in Figure 38, at approximately 14:00 UT, confirming this is the most likely explanation of the remnant feature seen as the TOI vanishes from the GPS TEC maps.

For the fossil feature to be present, it is noted in Thomas et al. (2013) that the source mechanism for the SED that formed the TOI and allowed the plasma to be transported across the polar cap with the convection cell must be no longer active in the SED region. This leads to the question of what is the source mechanism for the SED. The majority of the studies of SEDs and TOIs related these features and structures to sub-auroral polarization streams (SAPS). These are sub-auroral electric fields causing strong westward plasma convection at sub-auroral latitudes (Foster and Vo, 2002). The mechanism of the SED is beyond the scope of this current study.

6.5 Conclusion

Observations of the TOI and SED have been presented using EDAM assimilated GPS VTEC maps, difference VTEC maps, electron density difference height profiles and SuperDARN electric potential plots. The evolution of the TOI and SED plume has been presented over the Western European sector on 30 September 2002 between 09:00 UT and 14:30 UT. The results have also considered IMF and solar wind data from ACE, Indices such as the Kp index, Dst index and DMSP data plots.

The results have shown the evolution of the TOI beginning from 09:00 UT up to 14:00 UT where the feature is no longer identifiable in the VTEC maps. The TOI was observed in the EDAM VTEC map at 09:00 UT but could only be inferred with the evidence from the VTEC maps and the electric potential plots. DMSP helped confirm that a TOI was present during this time, agreeing with the results from Foster et al. (2005), Redmon et al. (2007) and Yuan et al. (2008). The causes of this TOI were also confirmed to be as a result of a SED, using the VTEC maps and the results of Foster et al. (2005), Hosokawa et al. (2010) and Thomas et al. (2013). The TOI was shown to persist for approximately 5 hours. The resulting SED that persisted in the ionosphere as show in Figure 54c existed as a 'fossil' or remnant SED. This agrees with the results presented by Thomas et al. (2013) where they observed the TOI for a time before a fossil feature lingers after a sharp transition in the IMF B_z component from negative to positive.

This is the first time that EDAM assimilated GPS alongside SuperDARN electric potential plots has been used to study a TOI and SED. Previous studies have used GPS TEC maps and different models to produce the generated TEC maps that have studied TOIs and SEDs during storm time conditions. The model methods however would be different, and the majority of the studies took place in the North American sector. EDAM has shown the capability to model these features using GPS data in Europe and is supported by the results found in the literature. It is possible EDAM can be improved by assimilating other data sources to help model the correct altitudinal profile and help enhance the interpretation of the mechanisms for the generation of the SED.

Given the global coverage of EDAM and the number of GPS receivers in operation the study shows the potential for the model to be used in other sectors across the world to study these

ionospheric phenomena and also the potential to produce statistical studies on these features, for example those done by David at el. (2016). There is potential to start looking further in detail on these features and their relation to other factors such as time of year, solar conditions, geomagnetic conditions and if there is any difference in the southern hemisphere.

Chapter 7

Evaluation of EDAM using Modified Taylor Diagrams

7.1 Introduction

To verify the performance of EDAM and give substance to how well it has performed in both Chapter 5 and Chapter 6, Modified Taylor Diagrams (MTDs) (Elvidge et al., 2014) were used to display calculated statistics, described in the following section, that compares the TEC values modelled by EDAM with GPS data that has not been assimilated in the model. This excluded data is called the 'truth' data in the study and will fairly compare with the modelled data with GPS data. The background model described in Chapter 3 and 5, IRI, is also used as a comparison with the 'truth' data to see how EDAM compares with IRI.

7.1.1 Modified Taylor Diagrams

Taylor diagrams are used to summarize how closely modelled measurements match observations (Taylor, 2001). This is done by displaying statistics that show these comparisons on a diagram.

The correlation coefficient is the statistic that is used the most often to represent the pattern similarity between datasets. The correlation coefficient between two sets of data, f and g, is defined as:

$$R = \frac{\frac{1}{N}\sum_{n=1}^{N}(f_n - \bar{f})(g_n - \bar{g})}{\sigma_f \sigma_g}, \qquad \textbf{[Equation 34]}$$

where $\bar{f}$ and $\bar{g}$ are the mean values, σ_f and σ_g are the standard deviations of the datasets f and g, f_n and g_n represent nth element of the data sets datasets f and g, R is the correlation coefficient and N is the number of points in each data set.

That statistic often used to quantify differences between two data sets is the RMS difference, E, which for data sets f and g is defined as:

$$E = \left\{\frac{1}{N}\sum_{n=1}^{N}[f_n - g_n]^2\right\}^{\frac{1}{2}}. \qquad \textbf{[Equation 35]}$$

The RMS difference, E, can be split into two components, the bias and the centred pattern RMS difference. The overall bias between f and g is simply defined as the difference of the means of the two data sets as in Equation 36:

$$\bar{E} = \bar{f} - \bar{g}. \qquad \textbf{[Equation 36]}$$

The centred pattern RMS difference is defined by Equation 37:

$$E' = \left\{\frac{1}{N}\sum_{n=1}^{N}\left[\left(f_n - \bar{f}\right) - \left(g_n - \bar{g}\right)\right]^2\right\}^{\frac{1}{2}}. \qquad \textbf{[Equation 37]}$$

As two patterns become more alike, in this case as two data sets become more alike, the centred pattern RMS difference approaches zero. The bias squared, $\bar{E}^2$, and the centred pattern RMS difference squared, E'^2, add together to yield the RMS difference squared, E^2.

The correlation coefficient, defined in Equation 34, and the centred pattern RMS difference, defined in Equation 37, provide complementary statistical analysis that shows the relationship between two data sets. For a complete comparison and understanding of the data sets the standard deviations of each data set must also be used. It is possible to display all the statistics on a single diagram by recognizing the relationship between the statistical quantities and the cosine law, as shown in Equation 38 and 39.

$$E'^2 = \sigma_f^2 + \sigma_g^2 - 2\sigma_f\sigma_g R, \qquad \textbf{[Equation 38]}$$

$$c^2 = a^2 + b^2 - 2abcos\phi. \qquad \textbf{[Equation 39]}$$

This geometric relationship can be represented by a b and c being the lengths of a triangle and ϕ is the angle opposite of side c. Using the statistical equivalents of this cosine law, the triangle that comes from the geometric relationship, established by Taylor (2001) is displayed in Figure 58.

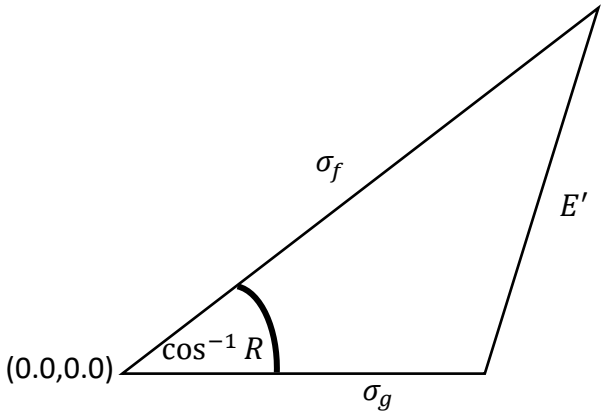

Figure 58 – A diagram showing the geometric relationship between the statistics involved in the setup of the Taylor diagram. Adapted from Taylor (2001).

Figure 58 is used to show the relationship in Equation 38. To explain Figure 58, one data set will be considered as an observed data set, σ_g, and the other shall be a modelled data set, σ_f. The radial distance from the origin, (0.0,0.0), on the diagram to a point plotted on the diagram represents the standard deviation of that data set, where the line represented by σ_g in the diagram is for the observed data and the line represented by σ_f is for the modelled data. The angle $\cos^{-1} R$ of line represented by σ_f gives the correlation coefficient between the two data sets. The centred pattern RMS difference is given by the length E' on the diagram.

For the purposes of this study the data sets mentioned previously are the slant TEC (sTEC) values of the ionosphere over a latitude and longitude to be defined later in the thesis. The data sets would include all sTEC values over a given range of time. When statistics are

computed on the modelled data sets, they are all normalised by the standard deviation of the observed, 'truth', sTEC values, adapting Equation 38 to:

$$\left(\frac{E'}{\sigma_g}\right)^2 = \left(\frac{\sigma_f}{\sigma_g}\right)^2 + \left(\frac{\sigma_g}{\sigma_g}\right)^2 - 2\left(\frac{\sigma_f}{\sigma_g}\right)\left(\frac{\sigma_g}{\sigma_g}\right)R. \qquad \textbf{[Equation 40]}$$

This allows multiple modelled data set comparisons with observed data to be plotted onto the same diagram enabling the comparison of both EDAM and IRI modelled sTECs with the observed data, each represented by one point. As previously stated, f, in Equations 34 to 40 and Figure 58 is for the modelled data sets, to be compared with the observed sTEC values, g, in Equations 34 to 40 and Figure 58.

Modified Taylor Diagrams are used in this study and the code to produce these diagrams was provided by QinetiQ. An example of the Modified Taylor Diagram is seen in Figure 59, taken from Elvidge et al. (2014). The radial distance of a data point from the origin is the model's normalised standard deviation, $\frac{\sigma_f}{\sigma_g}$. The angle of that radial distance gives the correlation between the two standard deviations of the modelled and observed data sets, $\cos^{-1} R$, and the axis that show the corresponding correlation values are displayed on the outer circular line of the Modified Taylor Diagram. The dashed line, at (1.0,1.0) is for a normalised standard deviation of 1, where the standard deviation of the modelled sTEC values would equal the observation sTEC values with both y and x-axis displaying the standard deviation values. The dotted semi-circles, centred at (1.0,0.0) seen shows the normalised standard deviation of the model error, which is equal to the normalised centred pattern RMS difference, $\frac{E'}{\sigma_g}$. The colour bar at the top shows the normalised bias of the model, $\frac{\bar{f}-\bar{g}}{\sigma_g}$, which is what makes them 'modified'.

The example in Figure 59 has been previously published (Elvidge et al., 2014) where hmF2, foF2 and h(0.8foF2) is used rather than the sTEC mentioned so far. The key at the right side defines each point used in the diagram, for the example shown in Figure 59, EDAM is represented by the letter E, GPSII is represented by G, IRI represented by I and MNeQuick is represented by NQ. The square represents hmF2, height of the peak frequency for the F2 region, circles represent foF2, the peak frequency of the F2 layer, and diamonds represent h(0.8foF2), the height at $\frac{4}{5}$ at the peak frequency of the F2 region. This means the square point marked by an E on the diagram represents the statistical comparison of EDAM hmF2 data with observed hmF2. It also includes the normalisation factors, the standard deviations of the observed data sets, which can be used to revert any of the data points to its original value.

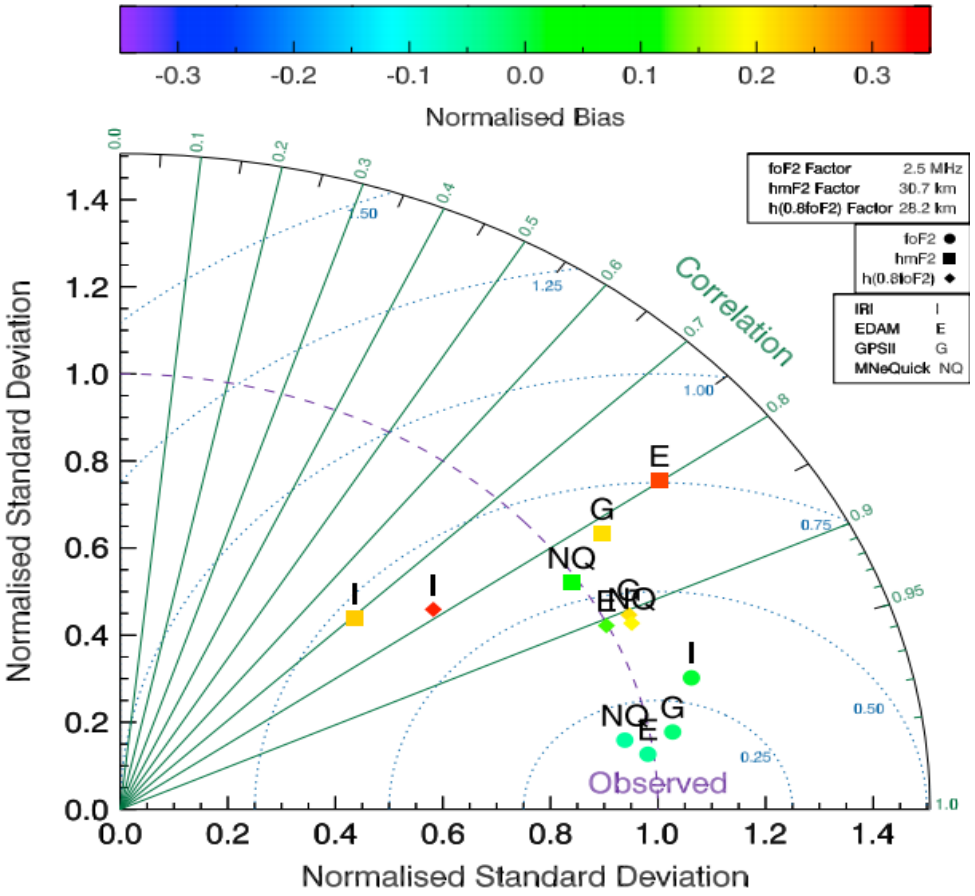

Figure 59 – An example modified Taylor diagram taken from Figure 2 of Elvidge et al. (2014). This plot showcases the statistics that can be represented on the diagram and therefore the use of this method. This diagram shows the performance of EDAM compared to three other models using hmF2, height of the peak density for the F2 region, foF2, the peak frequency of the F2 layer, and h(0.8foF2), the height at 4/5 at the peak frequency of the F2 region.

7.2 Data Analysis

The observed data set, known as the 'truth' data, is obtained from a GPS receiver called HERS, located at Hailsham 50.9°N and 0.3°E. This means that this GPS data has not been assimilated by EDAM. In Section 3 it was mentioned that products of the EDAM assimilation were files that held the difference grid, meaning the electron density differences between the background model and modelled electron densities after the assimilation. These files were produced for September 2002 and August 2003 that held the modelled densities on the latitude, longitude, altitude grid which was used in Chapters 5 and 6.

To be able to calculate the statistics for the MTDs, firstly some other steps must be taken. The sTEC files for the truth station must be collected from the RINEX files, mentioned in Chapter 3, for each satellite and for every day from September 2002 to August 2003. This used the satellite ephemeris and biases for the receiver to calculate the sTEC values as explained in Chapter 3. The sTEC data was downloaded from the Rinex files for 5-minute intervals along with the satellite number (the number of the defined GPS satellite), the time epoch (the array that holds the time, day, month, year of the current time step), the GPS satellite position (the latitude, longitude and altitude of the satellite) and the station position (the latitude, longitude and altitude of the receiver). Due to the nature of the satellite pass in view of the receiver, when plotted for a given satellite the data tends to form an arc, over a prolonged period. Examples of the satellite passes split into multiple arcs are displayed in Appendix C. Hence the outputted files for each satellite are split into arcs for each day, for each month and for September 2002 to August 2003. TECs were calculated along the same satellite-to-receiver paths through the electron density grids of the EDAM and IRI models.

Three different studies were performed with the results shown in the Modified Taylor Diagrams. The first was to look at the how the models were performing at different times of the day. The data were split up into four time sectors and a data point obtained for the whole day. This was to see what time influenced the performance the most. The four sectors are Dawn, 3 UT ≥ t ≤ 8 UT, Dusk, 15 UT ≥ t ≤ 20 UT, Night, 21 UT ≥ t ≤ 2 UT and finally Day, 9 UT ≥ t ≤ 14 UT, where t is the time. Each 5-min calculated sTEC value would lie within one of these sectors. The second study was to look at satellites individually, to see how each satellite was performing. The final study was a consideration of how EDAM was affected by the level of geomagnetic activity. For this the Kp index for each 5-minute period for September 2002 to August 2003 was used to organise the data into three categories, Low Kp, Kp ≤ 2+, Mid Kp, 3- ≥ Kp ≤ 4 and High Kp, 4+ ≥ Kp.

The diagrams were produced for the whole statistical study region, from September 2002 – August 2003, for each season in this year beginning with winter 2002, for each month and finally for each day for specific months. These revealed different levels of detail. The diagrams for each of these are presented and discussed in the next section.

7.3 Modified Taylor Diagram Results

7.3.1 Introduction

The statistical results are considered to compare the results from EDAM and IRI with the truth data from the HERS receiver. The first comparison looks at the modelling in four different times of day. The second uses EDAM and considers each of the satellites. The third again uses EDAM and considers different levels of geomagnetic activity. The final section uses data from

the receiver at Tromsø to see how EDAM performs when satellite-receiver paths pass through ionospheric features, such as the main ionospheric trough, which is known to affect radio propagation.

7.3.2 Results for the year

Figure 60 displays the statistical results in the Modified Taylor Diagram for EDAM and IRI sTEC statistics between September 2002 and August 2003. The four-time sectors defined in the previous section are considered – dusk (the diamond point), dawn (the square point), day the (left-pointed triangle point), and night (the right-pointed triangle point). The circle point on the diagram represents all times of day taken together.

Figure 60 shows the correlation for all of the EDAM points are above 0.90, indicating the EDAM modelled sTECs show a close similarity with the 'truth' data while IRI lies approximately between 0.80 and 0.90. The EDAM day, EDAY, dusk, EDU, dawn, EDA and all-time data points, E, have normalised standard deviations greater than 0.90 meaning that EDAM has a similar variation of the sTEC data to the truth sTEC data from the HERS receiver. The EDAM night, EN, point however does not perform to this standard. The standard deviation for the EDAM night point is at approximately 0.88.

For the IRI equivalent points, defined with an I in the Figure rather than the E of EDAM, the correlation values are below 0.90 except for the IRI all times point, I, which has a correlation of approximately 0.90. The normalised standard deviations for all the IRI points are also less than 0.90.

EDAM in the dawn sector, EDA, has the best normalised standard deviation, approximately 0.98, which is very close to 1.00. EDAM in the day sector, EDAY, however has the best correlation of approximately 0.97. The normalised biases in this diagram, given by the colour of the point that matches the colour bar at the top of the diagram, are negative for both models, EDAM and IRI, and in all time sectors. This means there is an overall underestimation of the sTEC value compared to the truth data set, as the normalised biases are the differences in the mean sTEC values, $\frac{\bar{f}-\bar{g}}{\sigma_g}$. Caution should be taken in reading the normalised bias scales as it changes from figure to figure.

The largest negative normalised biases, with values greater in magnitude than -0.25, are EDAM and IRI in the night sector, EN and IN. In conclusion from this diagram is that EDAM is modelling the sTEC values better than IRI along the same satellite-receiver paths.

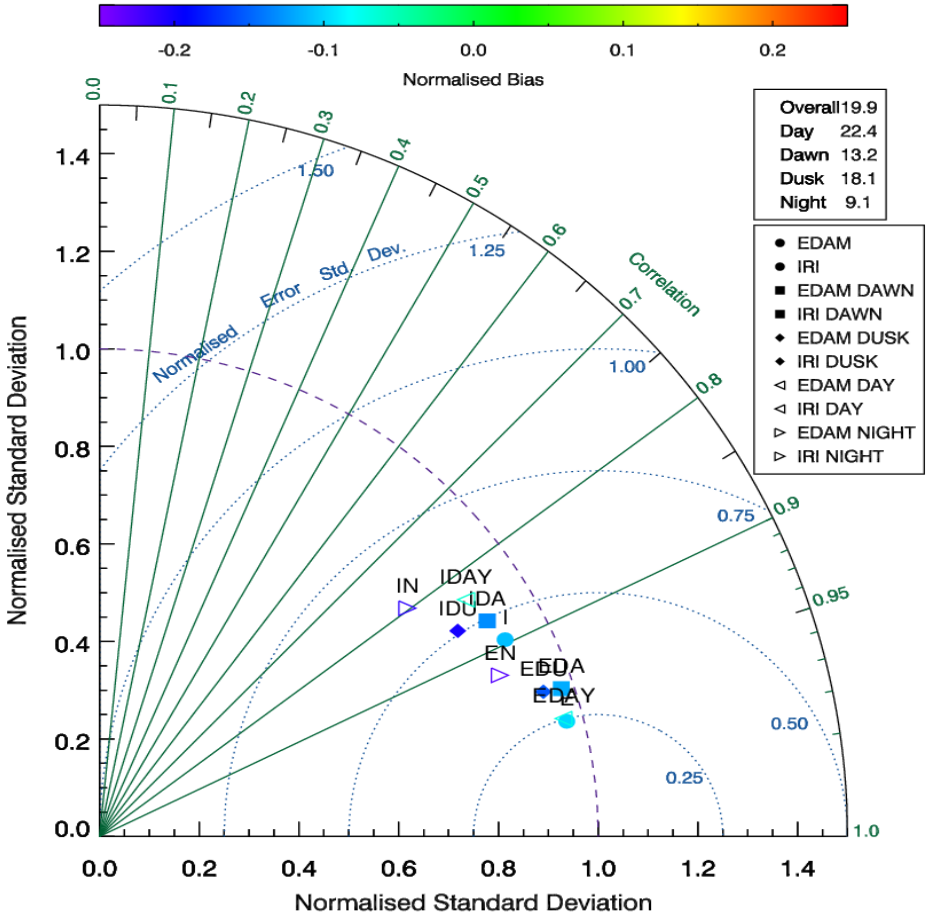

Figure 60 – A Modified Taylor Diagram showing the statistical results for the EDAM and IRI models compared to the truth data from the HERS receiver, between September 2002 and August 2003 for the time sectors defined in the text. The radial distance from the origin to the data points on the diagram give the normalised standard deviation of the modelled sTEC data, the line from the angle between the x-axis and that radial distance gives the correlation, the semi circles, centred at (1.0,0.0), give the normalised error in the standard deviation described in the text and the colour bar gives the normalised bias of the models compared to the truth data. The normalisation factors in units of TECU are marked in the top right of the diagram and are appropriately labelled for overall, dawn, dusk, day and night. The EDAM point for all times is labelled E, for the dawn sector it's EDA, for dusk it's EDU, for day it's EDAY and for night it's EN. It is the same for IRI but instead of E at the beginning of the label it is I.

7.3.3 Results at 3-monthly intervals.

Figure 61 shows the same statistical analysis as for Figure 60 but this time for a restricted time period of September 2002 to November 2002. The best performance is EDAM in the dawn sector, EDA, with a normalised standard deviation of close to 1.00, and a correlation of approximately 0.99. The day and dusk sectors, EDAY and EDU, also perform extremely well as well as the all times point, E, with normalised standard deviations of roughly 0.95 and

correlations of 0.98. The worst performing EDAM point is the night sector, with a standard deviation of 0.85 and a correlation of roughly 0.89. Even though this is considered the worst point in EDAM's performance, compared to IRI in the night sector, which has a standard deviation of 0.60 and a correlation of roughly 0.70, EDAM is performing much better. On the whole EDAM is outperforming IRI across the whole day, with the IRI best performing sector never increasing above 0.90 correlation. The biases of the values are all negative, for both models, indicating an underestimation of the truth TEC value. The IRI night sector point, IN, shows the largest negative normalised bias values of roughly -0.30. EDAM in the dawn sector, EDA, is the closest to a normalised bias of 0.00 with values around -0.05.

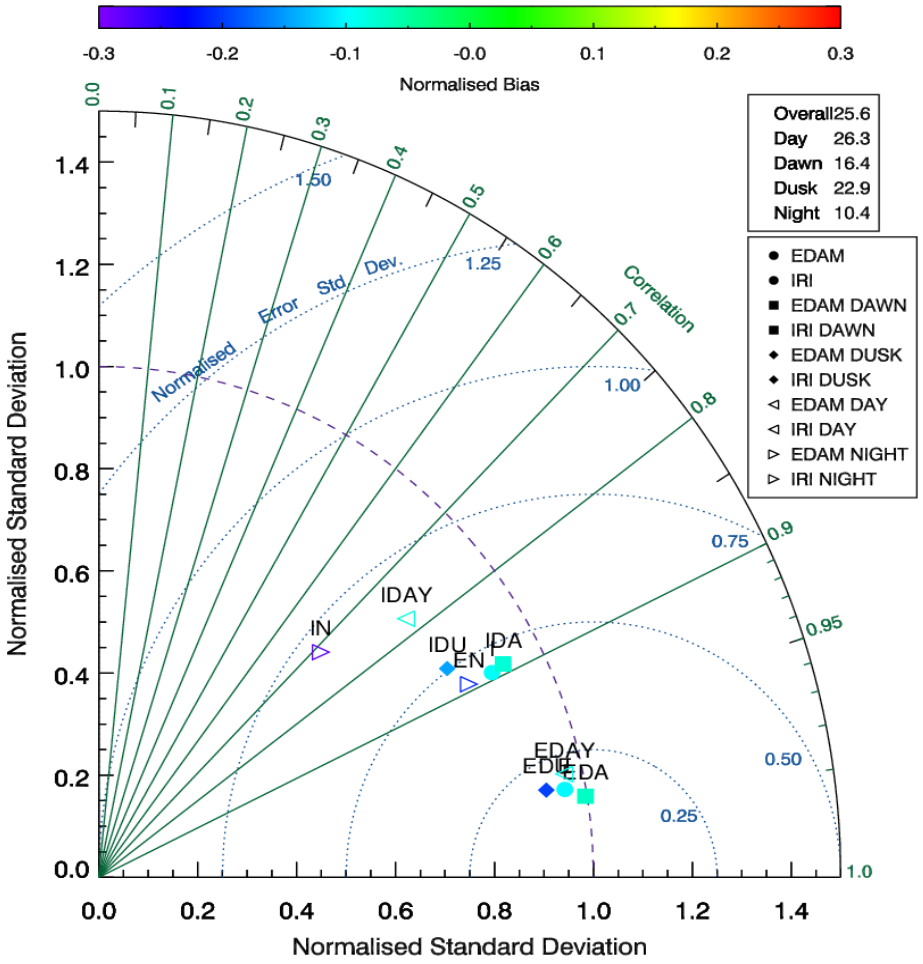

Figure 61 - Modified Taylor Diagram for September to November 2002, showing the statistics performed on sTEC between the HERS receiver and all satellites in view for both EDAM and IRI. EDAM in the dawn sector, EDA, shows the best performance in this period when compared to the truth data.

Figure 62 shows the Modified Taylor Diagram for December 2002 to February 2003. In this diagram it is the EDAM overall data point, E, with normalised standard deviation of 0.95 and correlation of 0.98 that provides the most accurate result. By comparison the IRI overall point, I, also performs better compared to Figure 61, with a correlation of 0.92 and a normalised standard deviation of approximately 1.05 compared to values of 0.90 for correlation and approximately 0.90 for normalised standard deviation in Figure 61. The IRI overall point, I, outperforms EDAM in the night sector, EN, and EDAM in the dawn sector, EDA, as although the correlations are comparable, values of 0.92, EDAMs normalised standard deviation is roughly 0.85 which is further away from 1.00 than IRI. The normalised biases here are negative for the most part, ranging from values of 0.00 to -0.20. IRI in the night sector however shows the largest negative normalised bias with values of approximately -0.60.

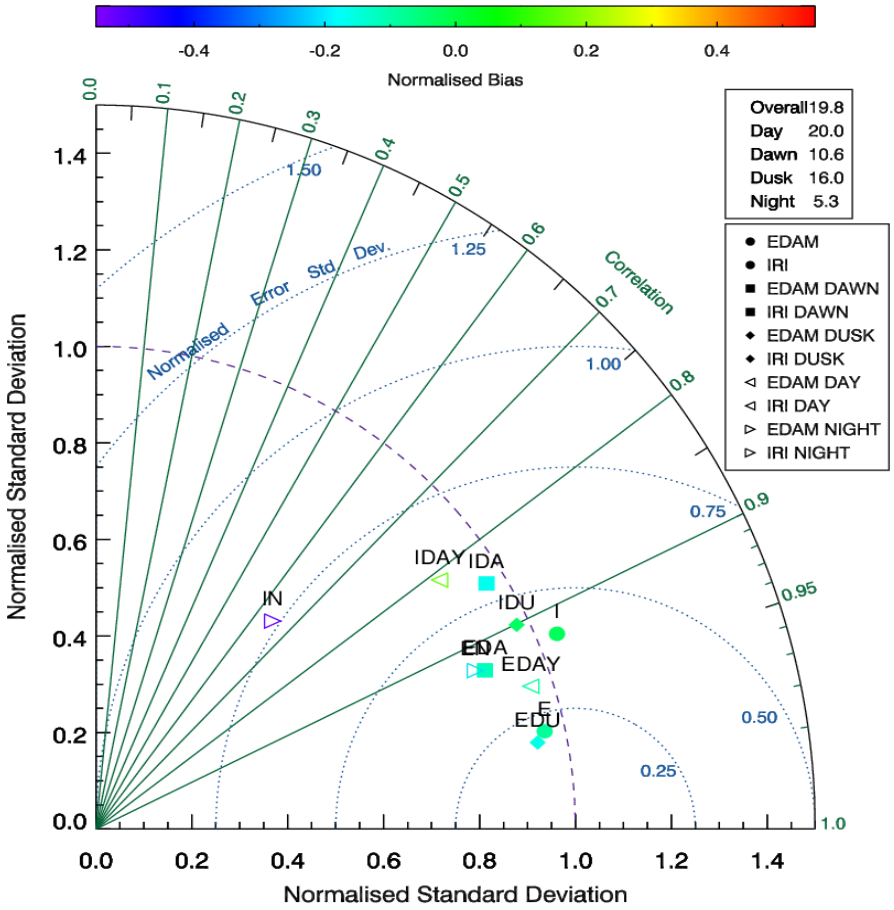

Figure 62 - Modified Taylor Diagram representing the statistics performed on sTEC between HERS receiver and all satellites in view for both EDAM and IRI for the December 2002 to February 2003. The EDAM overall point is performing the best in this period with standard deviation of 0.95 and correlation of 0.98.

The Modified Taylor Diagram shown in Figure 63 gives the statistics performed on the data set for March 2003 to May 2003. EDAM in the day sector, EDAY, shows the best performance with a correlation of 0.97 and a normalised standard deviation of 0.95. EDAM in the dusk sector, EDU, and the overall data set point, E, almost lie on top of the day data point, with a correlation that's approximately 0.97, but has the same normalised standard deviation of 0.95. The points for all of the IRI sectors lie between 0.80 and 0.90 for correlation, and normalised standard deviations of approximately between 0.75 and 0.80. Both models show negative values for the normalised biases for all time sectors, with the largest negative normalised bias in IRI in the dusk sector with a value of approximately -0.30.

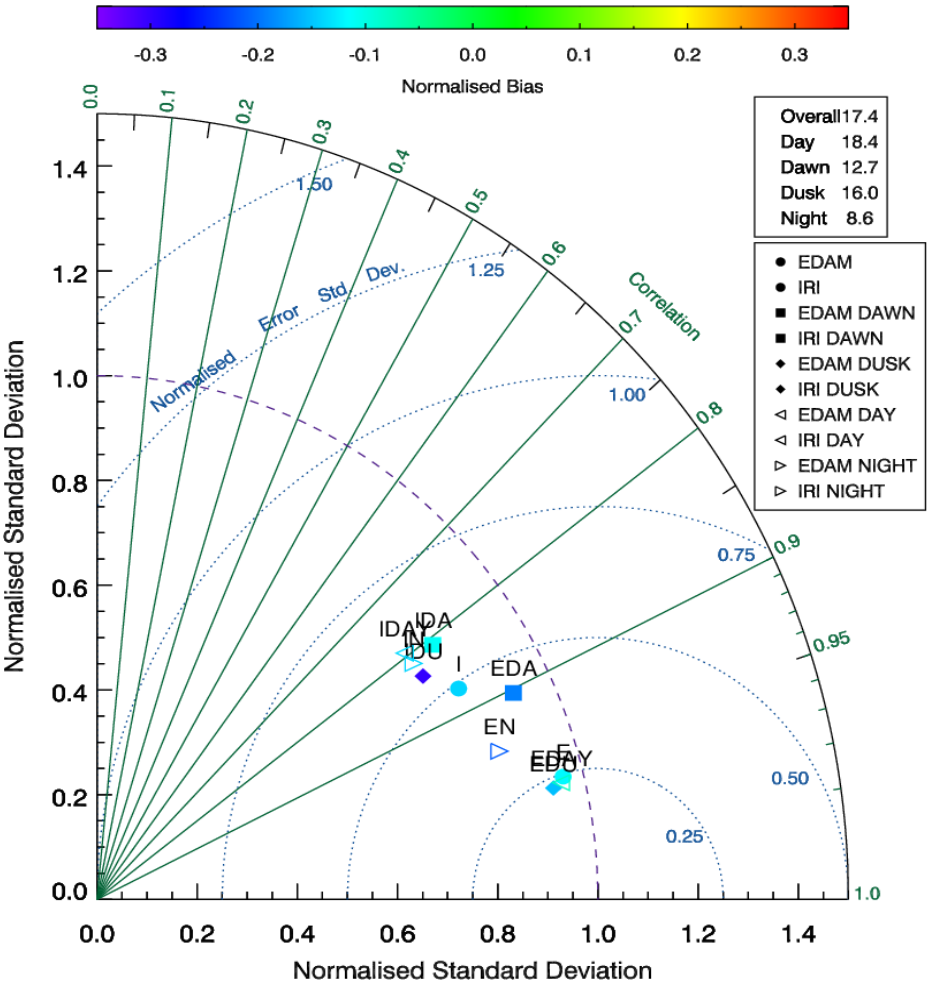

Figure 63 - Modified Taylor Diagram representing the statistics performed on sTEC between HERS receiver and all satellites in view for both EDAM and IRI for March 2003 to May 2003. EDAM in the day sector shows the best performance with a correlation of 0.97 and a normalised standard deviation of 0.95.

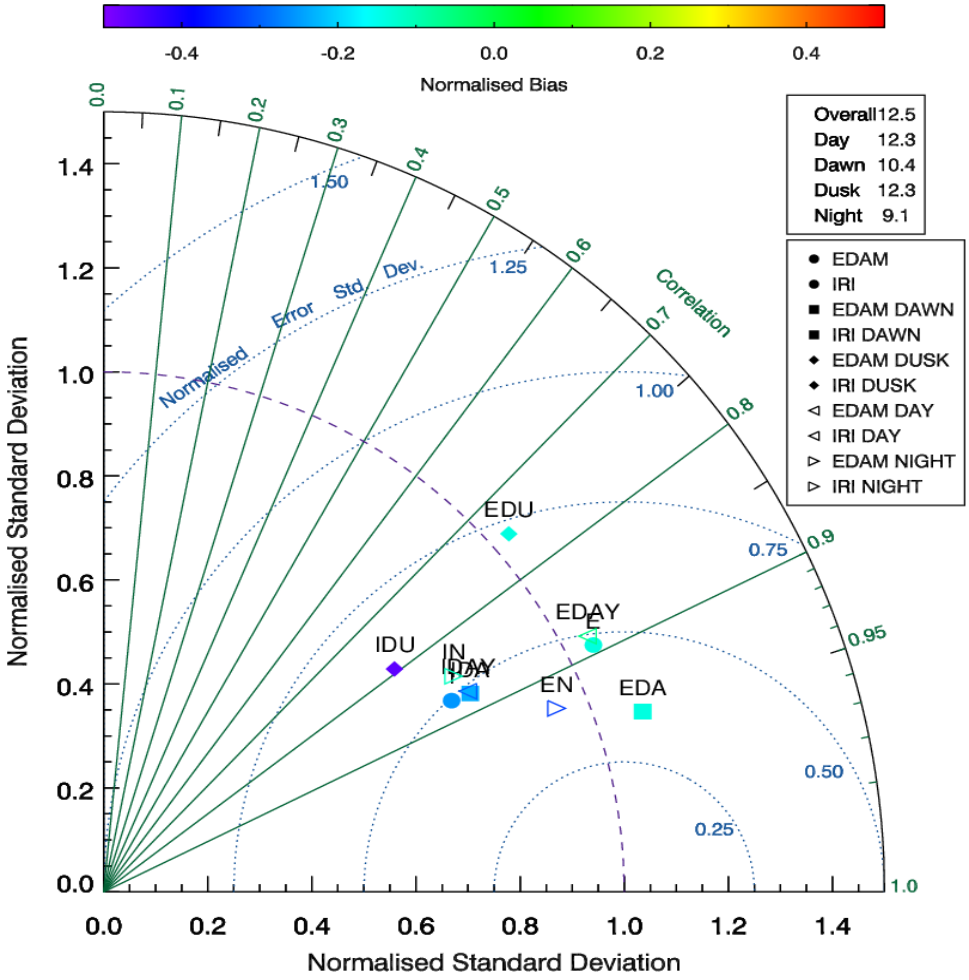

Figure 64 - Modified Taylor Diagram representing the statistics performed on sTEC between HERS receiver and all satellites in view for both EDAM and IRI for June 2003 to August 2003. EDAM in the dawn is the best performing sector with a correlation of 0.94 and a normalised standard deviation of 1.10.

Figure 64 shows the Modified Taylor Diagram for June 2003 to August 2003. EDAM in the dawn sector, EDA, is the best performing sector with a correlation of 0.94 and a normalised standard deviation of 1.1. EDAM in the dusk sector, EDU, is considerably worse in Figure 64 compared to the previous Modified Taylor Diagrams with a correlation of roughly 0.75, however it does have a normalised standard deviation close to 1.00. IRI in the majority of the time sectors and the overall data set lie within the 0.80 to 0.90 boundary in correlation with the truth data set, however IRI in the dusk sector has a similar correlation to the EDAM counterpart of less than 0.80. The normalised standard deviation for the IRI model in the dusk sector however is much worse, at a value of approximately 0.70. The normalised biases show

similarities with the previous Modified Taylor diagram with the normalised bias values being negative for both models in all time sectors.

Chapter 8 will focus on June 2003 to August 2003 as it is clear from the analyses above, with the higher variability in the performance of EDAM, something interesting is happening.

7.3.4 Individual Satellite Results for EDAM

Figure 65 shows the Modified Taylor Diagram for the data modelled through EDAM and the HERS truth data for each individual satellite during the period September 2002 to August 2003. The points for the majority of the satellites lie in a region, defined with a black circle, with the correlation coefficient ranging from 0.97 to 0.99 and the normalised standard deviation from 0.95 to approximately 1.00.

As for Figure 60 the statistical analyses were collectively applied to the whole year. The correlations and normalised standard deviations of the individual satellites in Figure 65 are approximately equal with the normalised standard and correlations for the EDAM points in Figure 60. Only one satellite in Figure 65 can be considered an outlier. That outlier is satellite number 21 with a correlation of roughly 0.82 and a standard deviation of approximately 0.90. The normalised biases for all the satellites are negative, with the majority lying between the region of values of 0.00 and -0.20. Satellite 21 however has the largest negative normalised bias of approximately -0.30. The normalisation factors are not included on the diagram as there would be a factor for each of the satellites and cause the diagram to look cluttered.

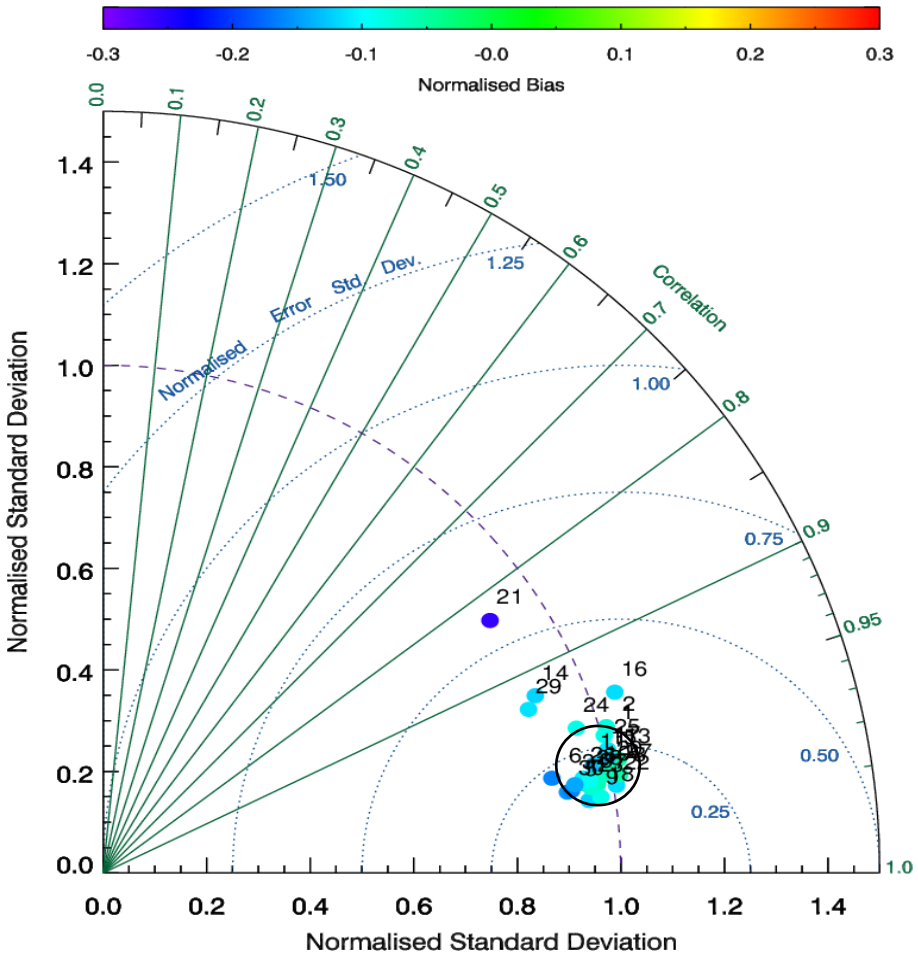

Figure 65 - A modified Taylor diagram for the satellites performance between September 2002 and August 2003. Each satellite that has been in view of the receiver HERS over the course of the year is included in these statistics, and the majority of the satellites lie around 0.95 to 1.00 normalised standard deviation, with correlations ranging from 0.97 to 0.99.

Figure 66 is the modified Taylor diagram September and November 2002. This is comparable to Figure 61. Nearly every satellite is showing a correlation greater than 0.96 with varying normalised standard deviations, ranging from 0.80 to 1.05. The biases are shown to be all negative, which agrees with the biases shown in Figure 65. The only outlier from the group is satellite 14 with a correlation value of 0.91.

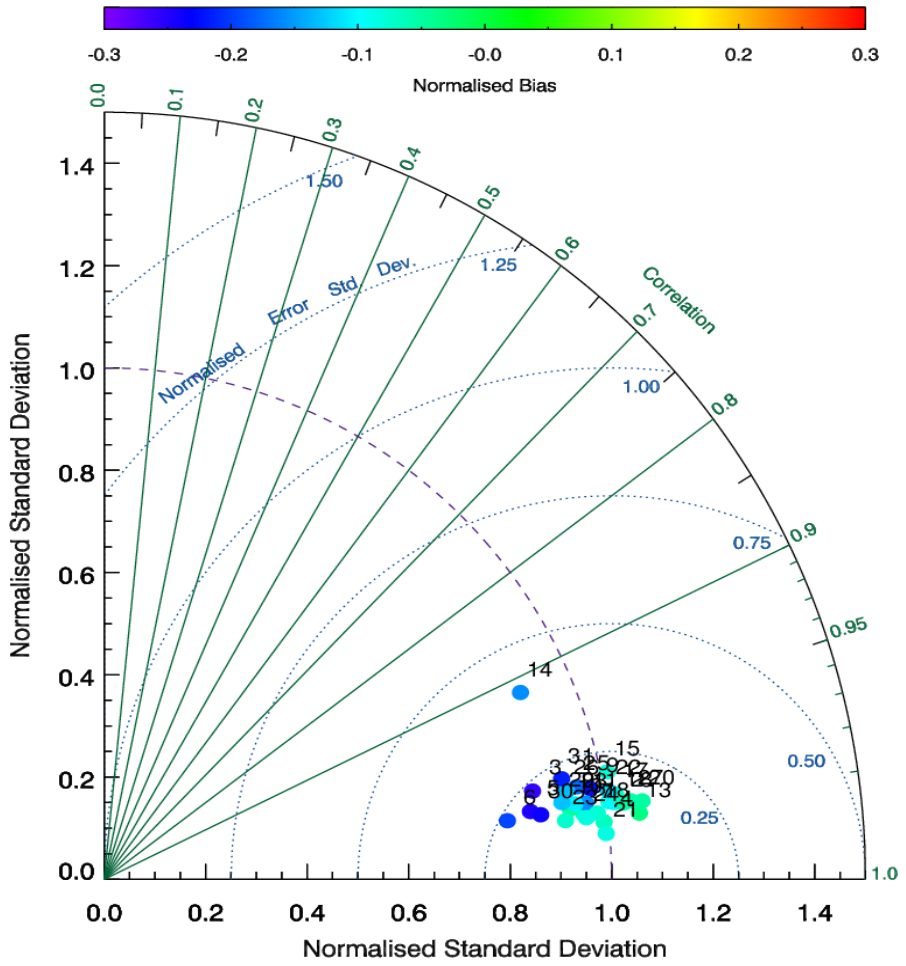

Figure 66 - Modified Taylor Diagram showing the satellites performance between September and November 2002. The performance here of EDAM in modelling the sTEC between each satellite and HERS is shown to have correlations greater than 0.96.

A Modified Taylor Diagram showing the satellites performance between December 2002 and February 2003 is displayed in Figure 67. Like the previous figure, most satellites are being modelled extremely well by EDAM with correlations great than 0.95 and normalised standard deviations greater than 0.85 and less than 1.05. The one considered outlier from this data series is the satellite 14, just like in Figure 66. This time however the correlation is slightly worse with a value of approximately 0.87. The majority of the normalised biases in the data shown in Figure 67 are negative, with values between 0.00 and -0.20 suggesting that EDAM overall underestimates the TEC values, agreeing with the biases shown in Figure 65 and 66.

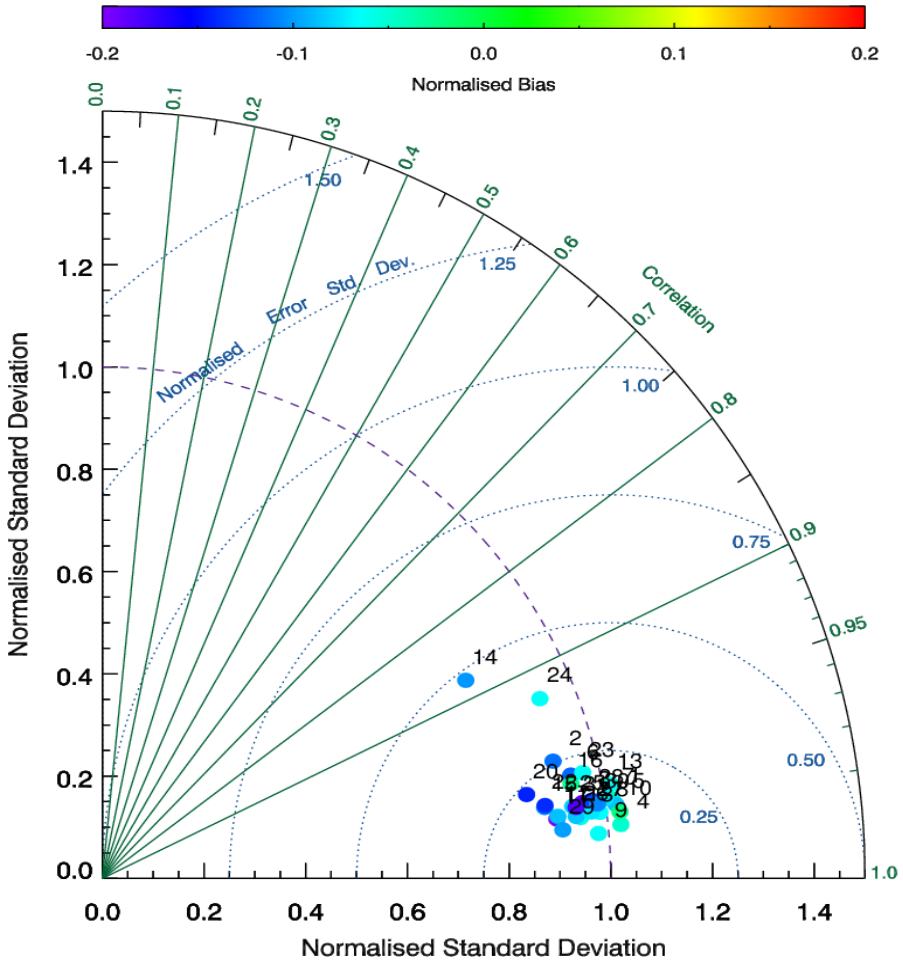

Figure 67 - A Modified Taylor Diagram showing the satellites performance between December 2002 and February 2003. The performance here of EDAM in modelling the sTEC between each satellite and HERS is shown to be great with correlations greater than 0.95 with only two satellites, satellite numbers 14 and 24, not performing to this standard.

Figure 68 shows the Modified Taylor Diagram for the March 2003 to May 2003. Again, many of the satellites have correlations greater than 0.95 and normalised standard deviations between 0.85 and 1.05. One outlier can be clearly seen in the diagram, satellite number 21. The correlation of this point is approximately 0.60 with a standard deviation of 0.45. It also has an extremely large negative normalised bias of around -0.50. The normalised biases for the rest of the satellites range from 0.00 to -0.30.

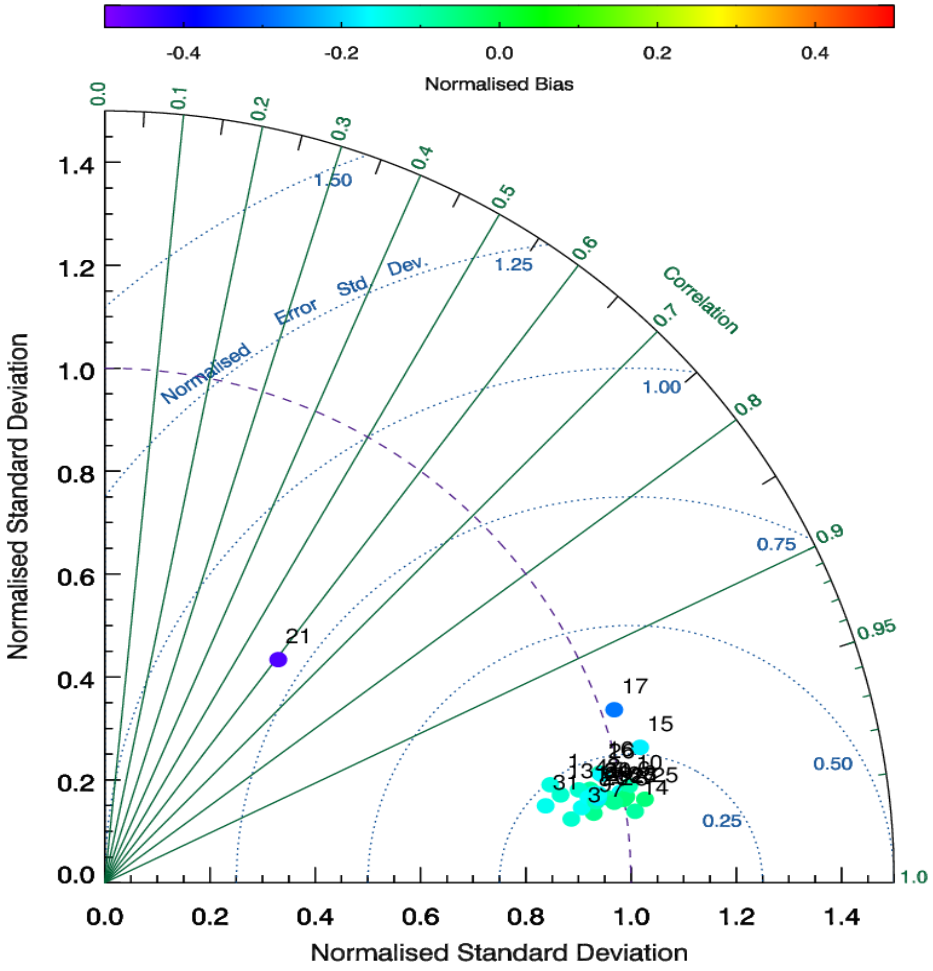

Figure 68 - A Modified Taylor Diagram showing the satellites performance between March and May 2003. The performance here of EDAM in modelling the sTEC between each satellite and HERS is shown to be great with correlations greater than 0.95 with only two satellites not performing to this standard. One satellite is a complete outlier.

Figure 69 shows EDAM's performance for the individual satellites between June and August 2003. There are significant differences compared to the previous figures in this case. The majority of points now lie either side of 0.90 correlation, showing a clear decrease in performance. The range of normalised standard deviations has also increased, and now extends from 0.80 to 1.20. A few satellites show up as major outliers. Satellite 29 has a correlation value of roughly 0.50 and a normalised standard deviation of approximately 0.55. The other considered outliers have a normalised standard deviation of roughly 1.3. This three-month period will be discussed later.

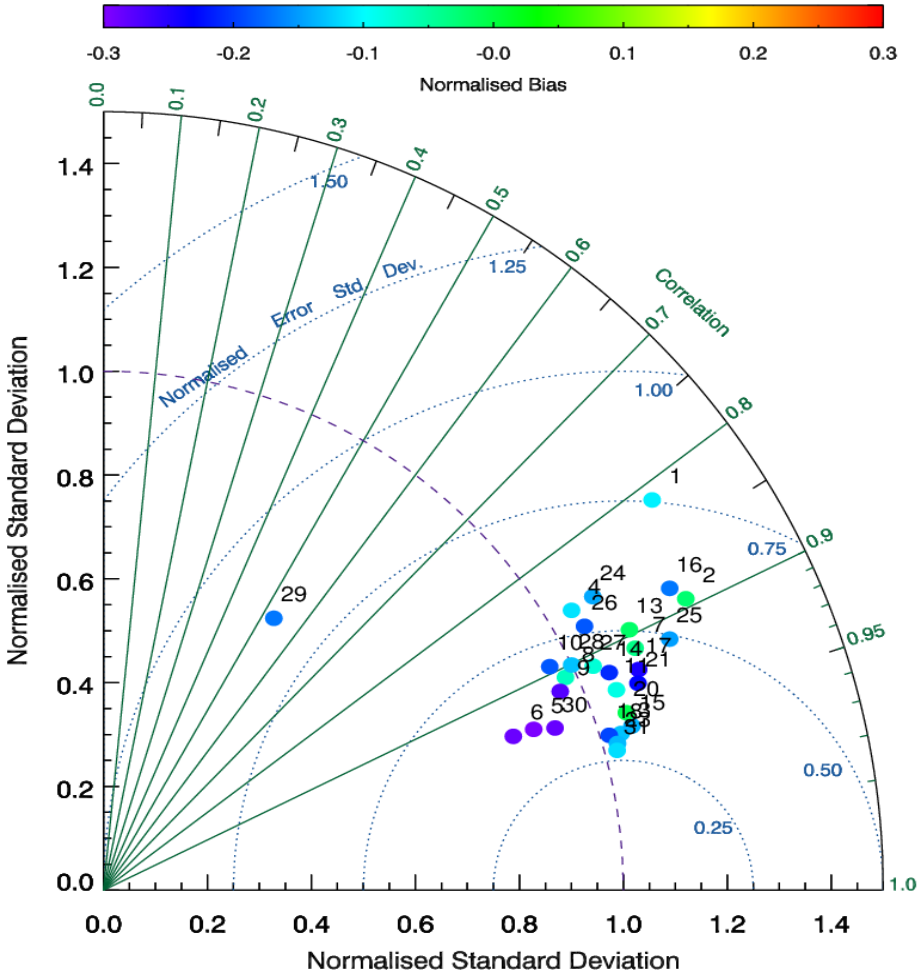

Figure 69 - A Modified Taylor Diagram showing the satellites performance between June and August 2003. The performance here of EDAM is very different compared to the previous time periods. The bulk of the satellite's performance lie around the 0.90 correlation, either side of the line. There are more considered outliers in the period too, different satellites to before.

7.3.5 Results for Kp Index

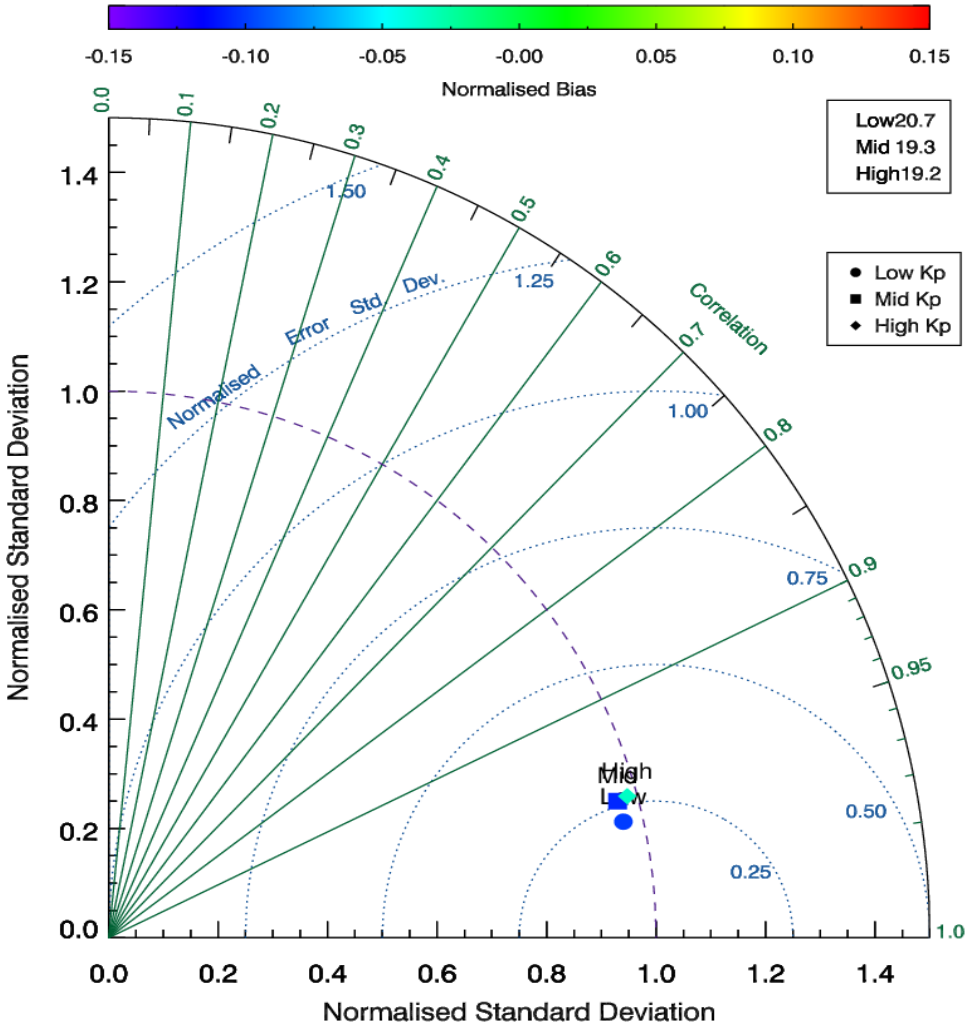

Figure 70 - A Modified Taylor Diagram showing the performance of EDAM in defined ranges of Kp levels with Low Kp, Kp ≤ 2+, Mid Kp, 3- ≥ Kp ≤ 4 and High Kp, 4+ ≥ Kp, between September 2002 and August 2003. There is little difference in how EDAM performs under the different levels of geomagnetic activity. The correlations are typically 0.97 and normalised standard deviations of 0.95.

The data displayed in Figure 70, shows how EDAM performs under different levels of Kp, in the Modified Taylor Diagram between September 2002 and August 2003. The three points are for each of the three data sets related to Low Kp, Mid Kp and High Kp respectively. These are set as being Low Kp, Kp ≤ 2+, Mid Kp, 3- ≥ Kp ≤ 4 and High Kp, 4+ ≥ Kp. All three points have roughly the same normalised standard deviation of 0.95 and correlation of 0.97. A conclusion from this figure is that the quality of modelling of EDAM is not dependent on the geomagnetic activity. Looking at the normalised bias, the Mid and Low Kp points appear to

have normalised biases similar to each other, which are -0.10. The High Kp has a bias closer to -0.05.

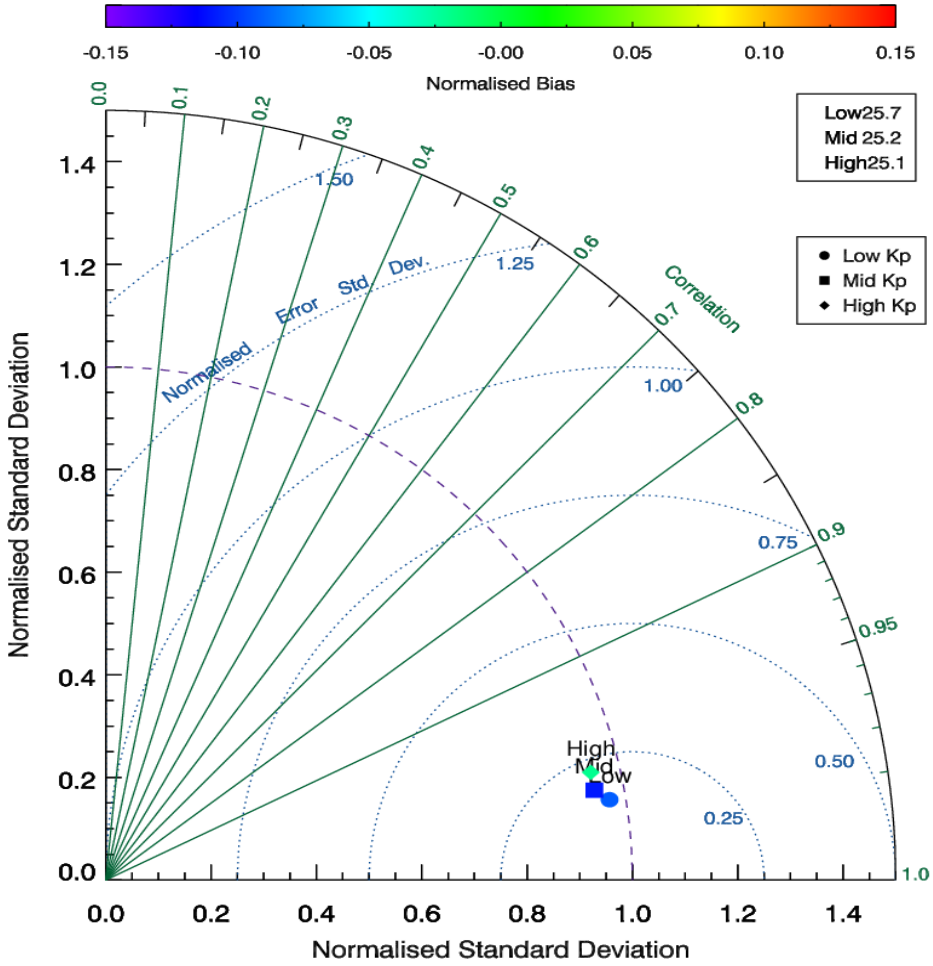

Figure 71 - A Modified Taylor Diagram showing the performance of EDAM with respect to the Kp index, between September 2002 and November 2002. There is little difference in how EDAM performs under the different levels of geomagnetic activity. The correlations are close to 0.99 and 0.95 for normalised standard deviations.

Figure 71 shows the Modified Taylor Diagram for the period between September and November 2002. Comparing with Figure 70 the normalised standard deviations are the same at around 0.95 but the correlations have slightly changed to 0.99. The marked difference here is the positive bias, of roughly 0.70, for the High Kp data point. A positive normalised bias suggests that EDAM is in general overestimating the values for the TEC in this Kp range for active geomagnetic conditions.

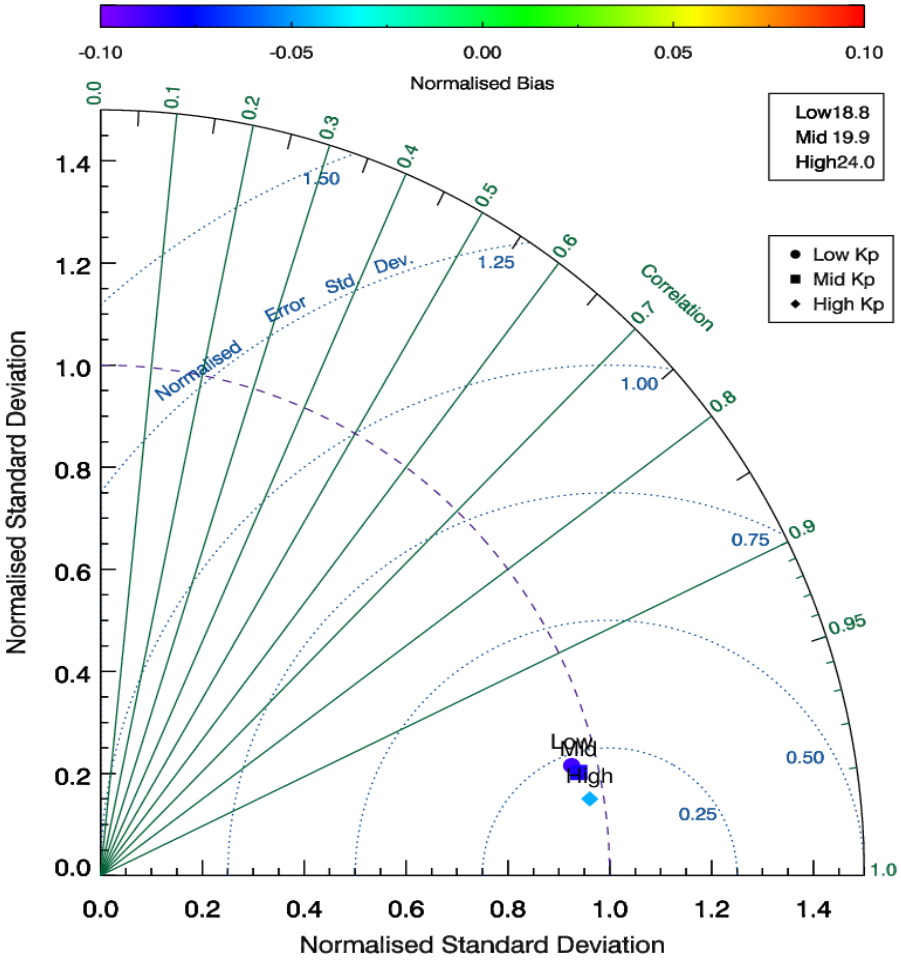

Figure 72 - A Modified Taylor Diagram showing the performance of EDAM with respect to the Kp index, between December 2002 and February 2003. All point show roughly the same correlation value of 0.98 with a normalised standard deviation value of 0.95.

Figure 72 displays the Modified Taylor Diagram for December 2002 to February 2003 for the Kp data sets. Performance of all data sets are roughly at a correlation of 0.98 and a normalised standard deviation of 0.95. The normalised biases for each Kp range are negative with similar values ranging approximately between -0.10 and -0.05.

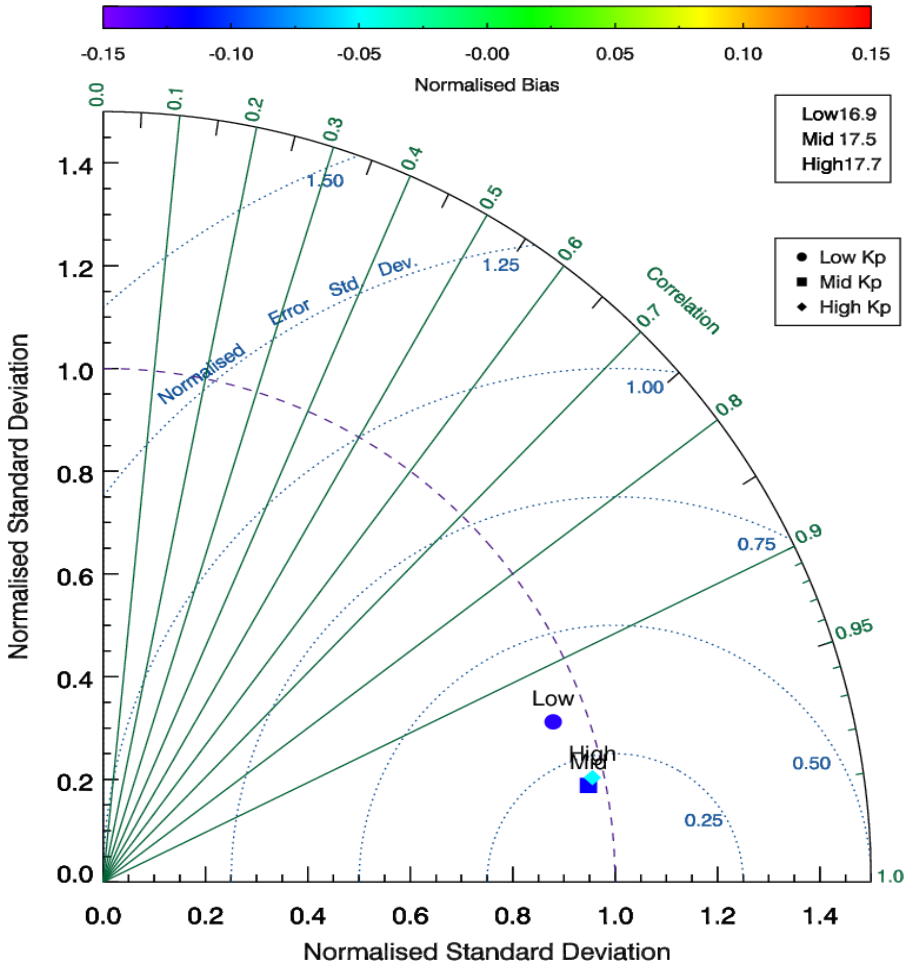

Figure 73 - A Modified Taylor diagram showing the performance of EDAM with respect to the Kp index, between March 2003 and May 2003. Mid and High Kp are showing the best performance overall with correlation values of roughly 0.98 and a normalised standard deviation of near 1.00.

For the Modified Taylor diagram in Figure 73, with data sets for March 2003 to May 2003, there is a notable separation of the points from each other. Low Kp shows the worse performance with a correlation of roughly 0.94 and a normalised standard deviation 0.94. The other two data sets have correlation values of 0.98 and a normalised standard deviation of approximately 1.00. The normalised biases are negative for all points, with Mid Kp being roughly -0.10 while High Kp is at roughly -0.05 and with Low Kp at approximately -0.10.

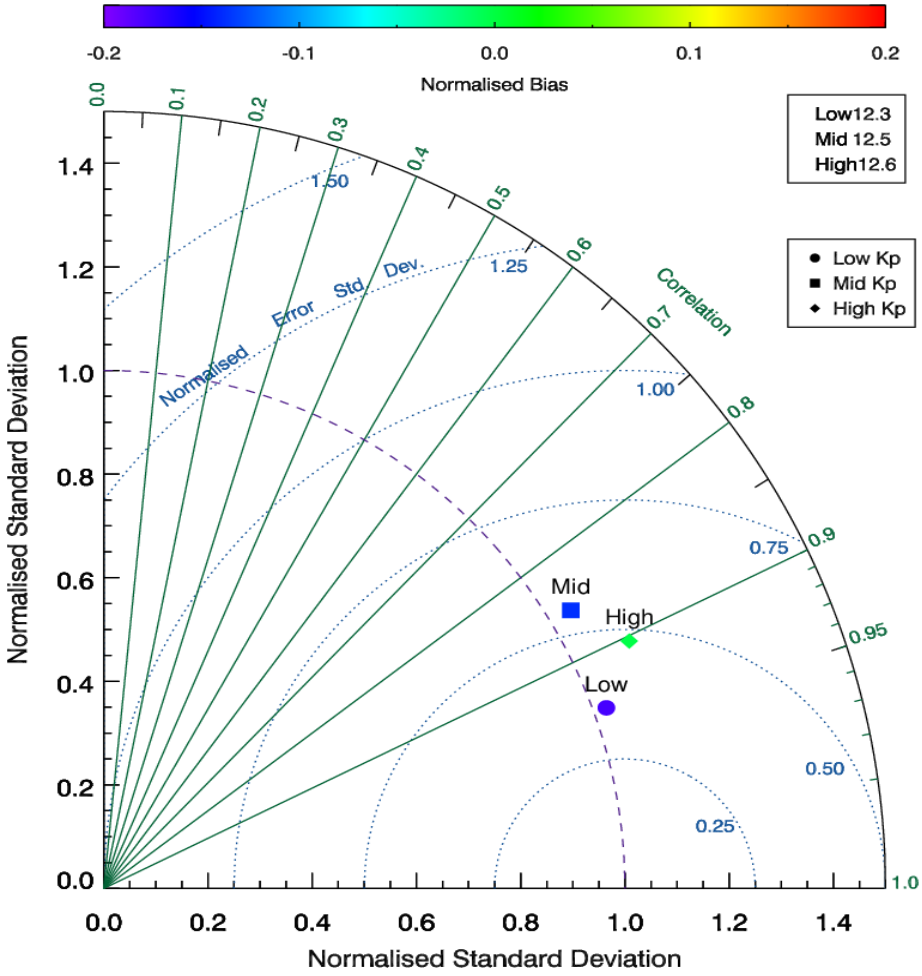

Figure 74 - A Modified Taylor Diagram showing the performance of EDAM with respect to the Kp index, between June 2003 and August 2003. Low Kp is now the best performing data set with a standard deviation of close to 1.00 and a correlation of 0.94.

Figure 74 displays the Modified Taylor Diagram for June 2003 to August 2003, for the Kp indices. The correlation of the Mid Kp point is approximately 0.85, the first time a data set in this section on Kp results has gone below 0.90 correlation. The standard deviation of this point is 1.05. The best performing point is Low Kp with a correlation of 0.94 and a standard deviation approximately 1.00. The High Kp point has a correlation of 0.9 and a normalised standard deviation of approximately 1.15. The normalised biases are predominately negative, with values of approximately -0.20 for Low and Mid Kp while it is positive for the High Kp data set at a value of approximately 0.05.

7.3.6 Tromsø Receiver

The results of the previous sections using HERS receiver data as truth for comparison had shown EDAM performing well, normalised standard deviation values between 0.90 and 1.00 and correlation values between 0.90 and 1.00 for the most part, at mid-latitudes. One of the purposes to complete a statistical study of EDAM using modified Taylor diagrams was to see the performance of EDAM when ray paths passed through large scale features, as this would affect radio propagation. In the case of the HERS receiver, ray paths were unlikely to pass through the large-scale structures as they travelled to the satellites.

Another study was conducted, by using data from a receiver at a higher latitude. The chosen receiver was TRO1 (69.6°N latitude, 18.9°E longitude) in Tromsø. In this case data measured by the receiver had been assimilated into EDAM. The purposes here were to focus on how it performed in modelling a higher latitude receiver, where the ray paths would be passing through large scale structures, such as the main ionospheric trough. The TRO1 data were considered 'truth' data for this study.

For the receiver TRO1 three modified Taylor diagrams were produced. The first plot compares with Figure 60 showing the EDAM and IRI statistical results for all previously defined time sectors, for between September 2002 and August 2003. The second diagram compares with Figure 65 and shows the EDAM statistical results for all individual satellites for between September 2002 and August 2003. The final diagram shows the EDAM statistical results for defined Kp levels for between September 2002 and August 2003.

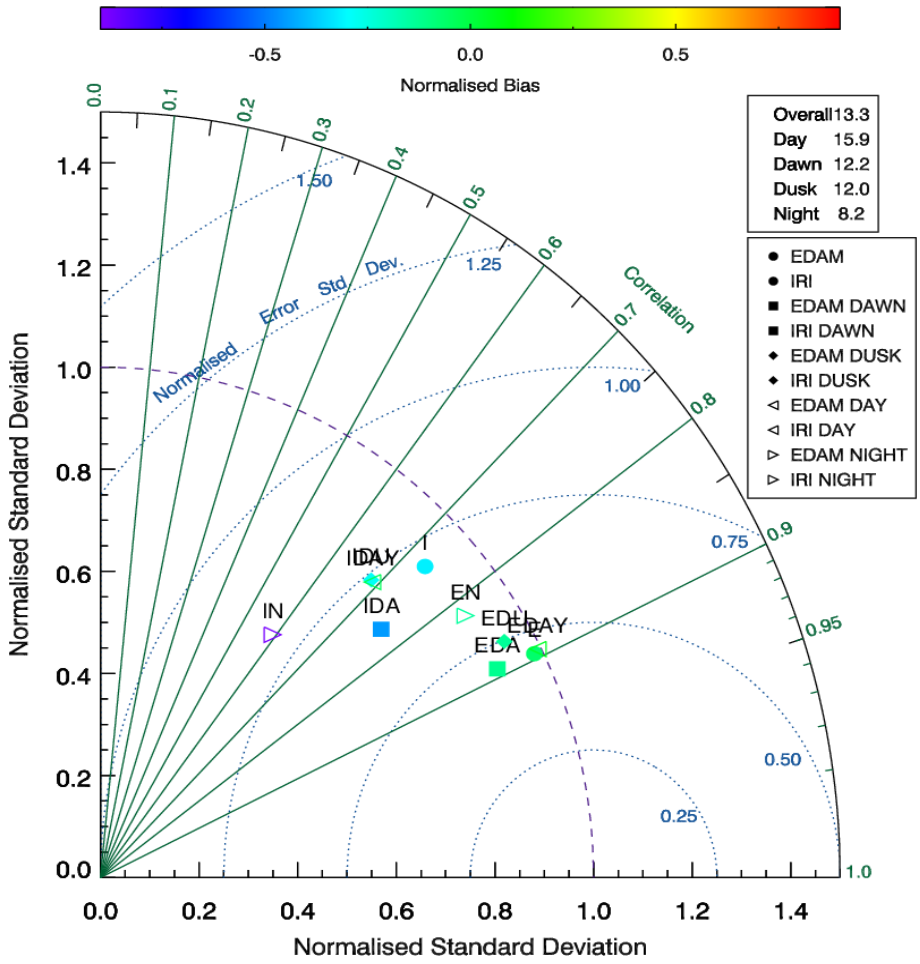

Figure 75 - A Modified Taylor Diagram showing the statistical results for TRO1 receiver as truth, between September 2002 and August 2003 for each of the defined time sectors. The performance of EDAM is between 0.80 and 0.90 correlation and normalised standard deviations between 0.90 and 1.00. EDAM in the day sector, EDAY, is the best performing sector in EDAM with a normalised standard deviation value of approximately 1.00 and a correlation value of approximately 0.90. The normalised biases are primarily negative for both IRI and EDAM across all time sectors.

Figure 75 shows the Modified Taylor Diagram for TRO1 receiver between September 2002 and August 2003 for each defined time sector. Overall the performance of EDAM has correlation values between 0.80 and 0.90 with normalised standard deviations between 0.90 and 1.00 and biases close to 0.00. IRI has correlation values ranging from approximately 0.60 to approximately 0.80, normalised standard deviations between 0.50 and 0.90 and biases that go strongly negative reaching a maximum value of approximately -0.90. These values show overall EDAM is performing better than IRI compared to the truth data located at higher latitudes. The night sector for both models, EN and IN, is performing the worst out of the time

sectors in Figure 75. The EDAM night sector, EN, has a normalised standard deviation value of 0.90 and a correlation value of approximately 0.82. The normalised bias of this value is approximately -0.05. The IRI night sector, IN, has a normalised standard deviation value of approximately 0.50, a correlation value of approximately 0.59 and a normalised bias of approximately -0.90. EDAM in the day sector, EDAY, is the best performing sector in EDAM, with a normalised standard deviation value of approximately 1.00 and a correlation value of approximately 0.90.

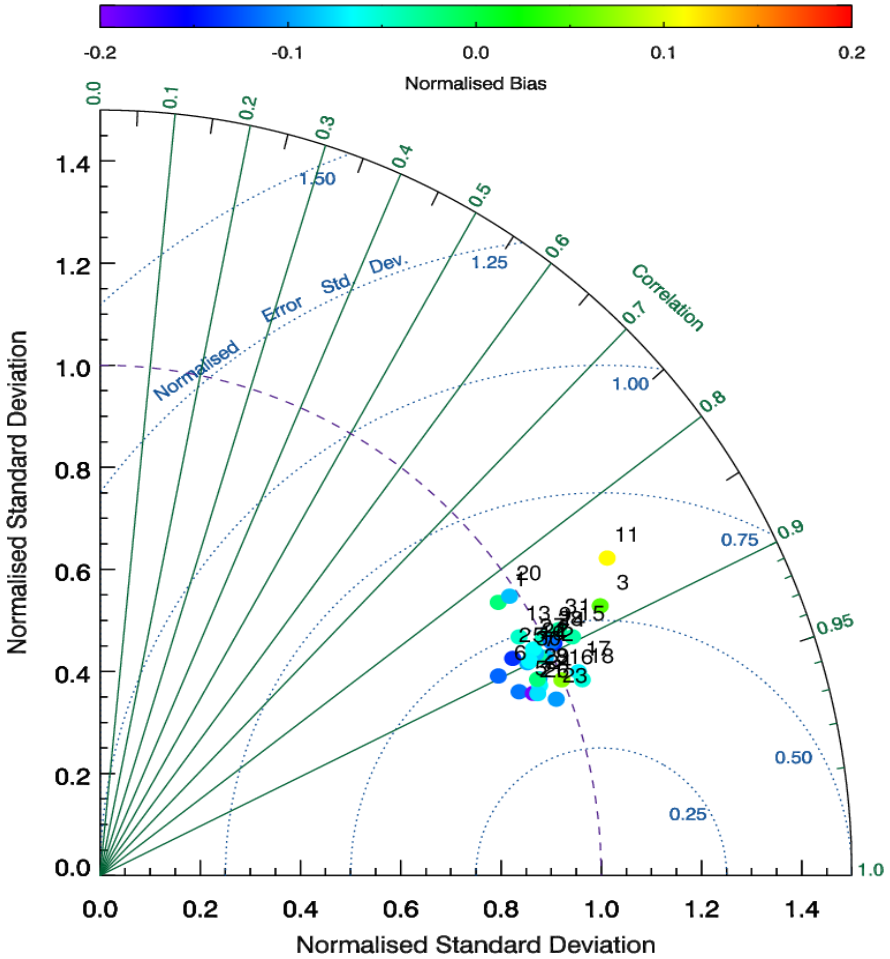

Figure 76 - A Modified Taylor Diagram for all satellites in view of TRO1 receiver between September 2002 and August 2003. Many of the satellites data points have correlation values of approximately 0.9. A few satellites, numbers 1, 20 and 11, perform closer to 0.80 correlation. The normalised standard deviations of the individual satellites range between 0.90 and 1.20. The normalised biases for all the satellites are quite variable, ranging from positive values of 0.10, to strongly negative values of -0.20.

Figure 76 shows the Modified Taylor Diagram for the satellite's performance between September 2002 and August 2003. The majority of the satellites all have approximate correlation values of 0.90. Satellites numbered 1, 20 and 11 however have correlation values closer to 0.80. Most of the individual satellites have normalised standard deviation values ranging from 0.90 to 1.05. Satellites 3 and 11 however have normalised standard deviations greater than 1.05. There is a wide variability in the normalised biases of each satellite ranging from very positive normalised biases, at 0.10, to strongly negative normalised biases, values of -0.20. What is evident in Figure 76 is that the performances of all the individual satellites are all close together on the diagram. There are no real discernible outliers in these data.

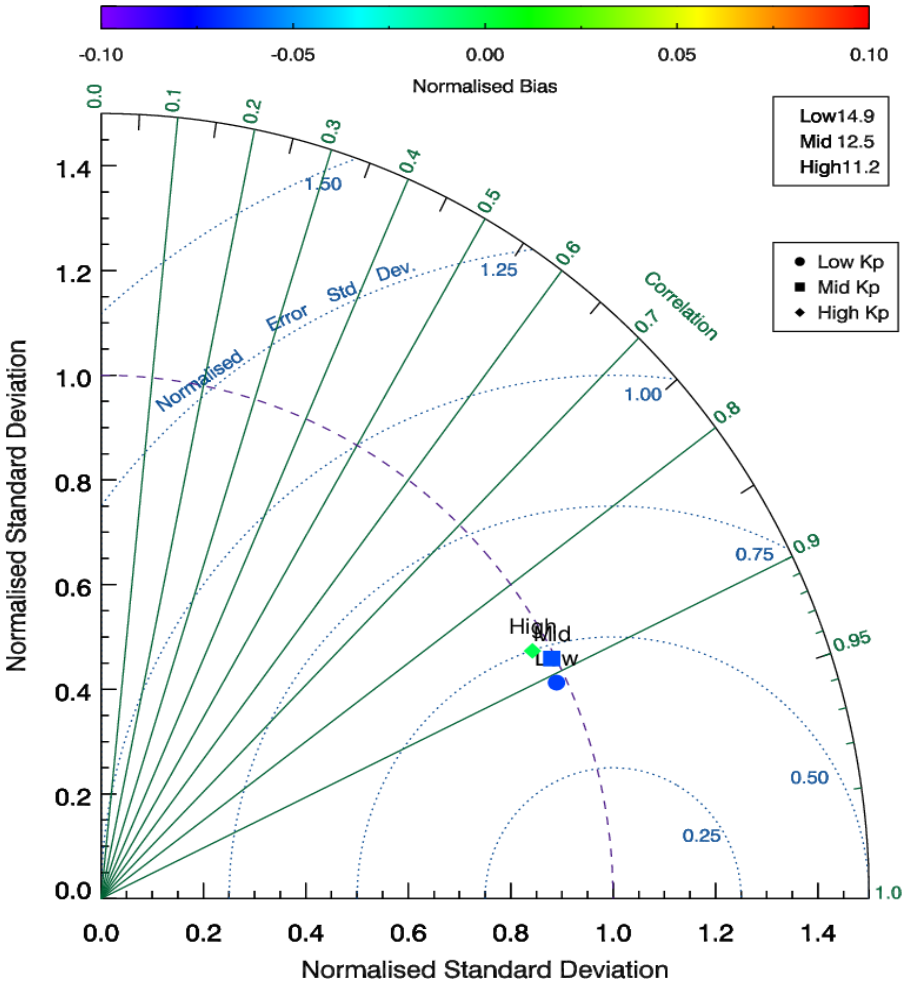

Figure 77 - A Modified Taylor Diagram for Kp indices between September 2002 and August 2003. The performances with respect to Kp index here all have a correlation value of approximately between 0.85 and 0.90 and normalised standard deviation values of approximately 1.00. The High Kp index point has the largest positive normalised bias, with a value of 0.05. The normalised bias values for the Mid Kp index and High Kp index are approximately -0.10.

Figure 77 shows the Modified Taylor Diagram for the defined Kp index levels between September 2002 and August 2003. Each of the Kp levels have a correlation value of between 0.85 and 0.90 and a normalised standard deviation value of approximately 1.00. The normalised bias for the Low Kp index is negative, with a value of -0.10. For the Mid Kp index, the normalised bias is roughly the same as the value for the Low Kp index. Finally, the High Kp index has a normalised bias value of approximately 0.05.

7.4 Discussion

Modified Taylor Diagrams have been used to present statistical results comparing the models EDAM and IRI with truth data measured at the HERS receiver. The statistical data displayed on the Modified Taylor Diagrams were split into four different time sectors and for all times during the day to compare performances over the whole year and three-monthly. The data were then considered in comparisons between EDAM and truth for individual satellites and for Kp index ranges. Due to few, if any, satellite-to-receiver ray paths passing through large scale ionospheric structures from the HERS receiver location, data from another receiver, TRO1 located at Tromsø, were considered and statistical results displayed in Modified Taylor Diagrams. The data were again considered by different categories to compare performances for the time of day, individual satellites and Kp index ranges.

Figures 60-64 showed the performances of EDAM and IRI compared to the truth data measured at the HERS receiver for each defined time sector for the whole year and split into three-monthly data sets. EDAM performed better in modelling sTEC data along satellite-to-receiver paths to the HERS location better than IRI. This is evident in the correlation values for each defined time sector.

Figure 78 displays the comparison between the correlation values for EDAM and IRI compared to the truth data for the whole year of data, split up into each month. Here the correlation values of IRI are subtracted from the EDAM values to compare performances.

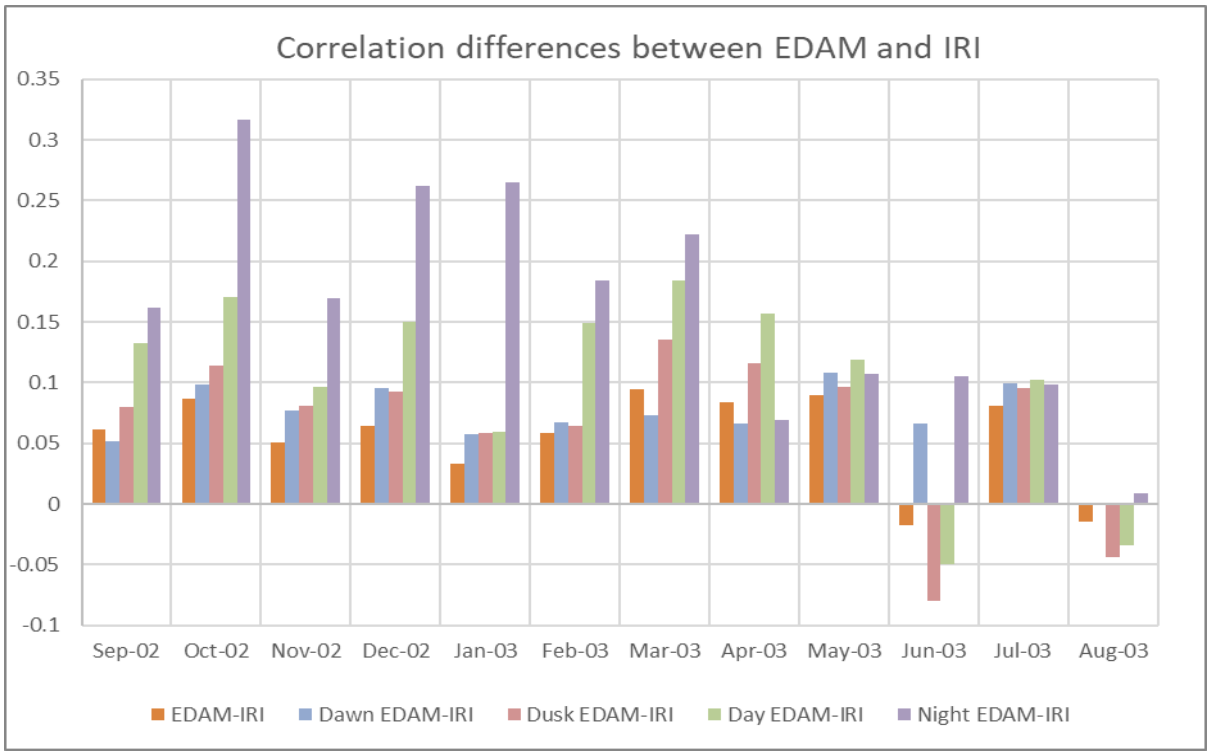

Figure 78 – A Bar chart showing the differences between EDAM and IRI correlation values for all defined time sectors of the day. For 10 out of the 12 months EDAM is showing a clear better correlation with the truth compared to IRI. It is primarily EDAM in the night sector, EN, that is outperforming the performance of IRI the most showing correlation differences greater than 0.15 for most of the year.

For 10 out of the 12 months EDAM shows a clear better correlation with the truth data compared to IRI. EDAM in the night sector performs the best compared to IRI showing correlation differences greater than 0.15 for most months. It is the only EDAM time sector that consistently performs better than IRI for the whole year. The model IRI-2007 is used here for the comparison and is used as the background model for EDAM. The newer IRI model is not adapted to currently work as a background model so was not considered for this study. The IRI-2012 model (Bilitza et al., 2014) with another ionospheric model, NeQuick2, were compared to GPS TEC data in the South American sector (Venkatesh et al., 2014). One of the noticeable differences in that data was the underestimation of TEC from IRI-2012 in the late

evening hours, defined in this thesis in the night sector. This is displayed in Figure 6 of Venkatesh et al. (2014). The IRI model is adapted in EDAM by the measured TECS and so, in principle, this is also consistent with EDAM outperforming IRI in the night sector when comparing with truth.

Figures 79a, 79b and 79c show the mean sTEC values for each month, for each defined time sector for both IRI and EDAM and the truth receiver, HERS. Of particular note in the mean sTEC values is the comparison of EDAM in the night sector and IRI in the night sector. Particularly over the winter months, the mean sTEC value modelled from IRI is lower than the mean sTEC value modelled from EDAM. This suggests IRI is underestimating the TEC when compared to EDAM. It is underestimating even more so when compared to the truth data, by approximately 3 or 4 TECU. This agrees with what is found in Venkatesh et al. (2014). Kumar (2016) found that in the year 2012, across low latitude and equatorial regions, the IRI-2012 model was underestimating TEC values in the winter. This was attributed to the non-inclusion of the plasmasphere electron content in the IRI model. This could account for disparity between the IRI and EDAM model mean sTEC values as the GPS assimilated data would include plasmaspheric TEC due to the long lengths of the satellite to receiver ray paths. Caution must be taken with these statements due to the different latitude and longitude of the data that are being compared and the differences between the IRI-2007 and IRI-2012 models.

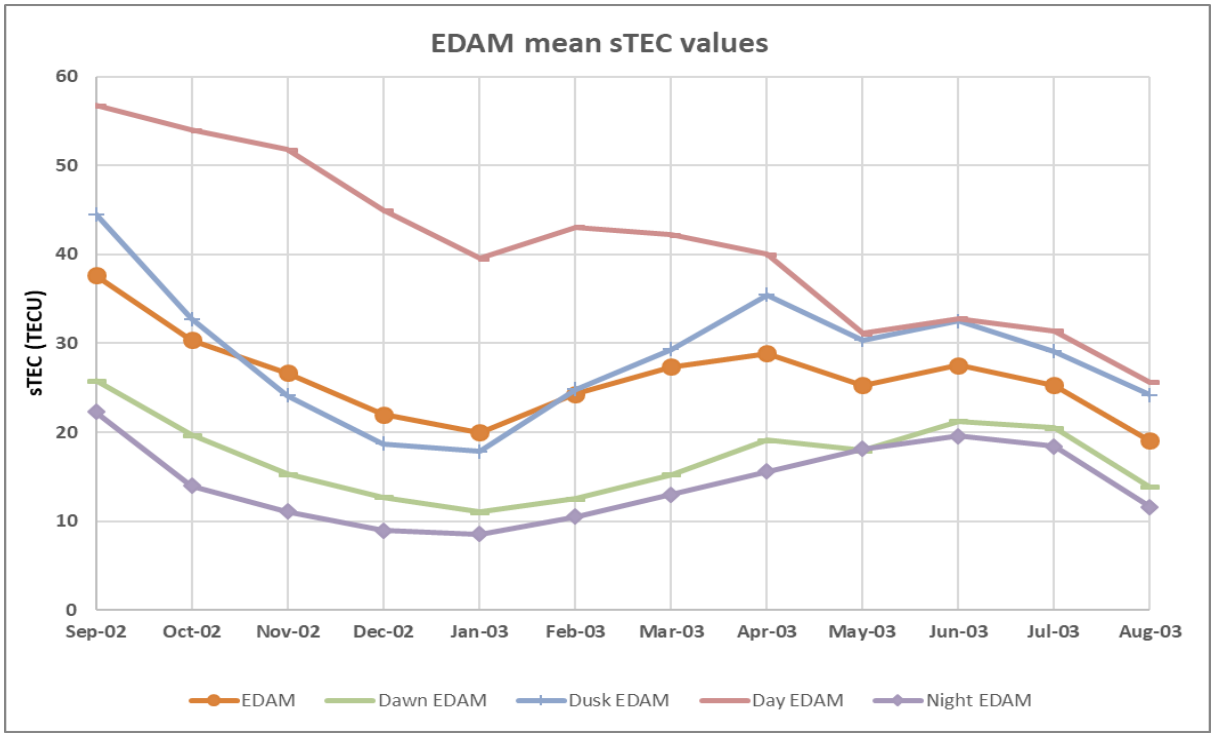

Figure 79a – EDAM mean sTEC values are displayed for each of the defined time sectors for the HERS receiver. An interesting trend throughout the year is the consistent decrease in the mean sTEC value for the day sector. All other time sectors experiences decrease in mean sTEC value until January before increasing in value until June. A final decrease in sTEC occurs until the end of the defined year in August.

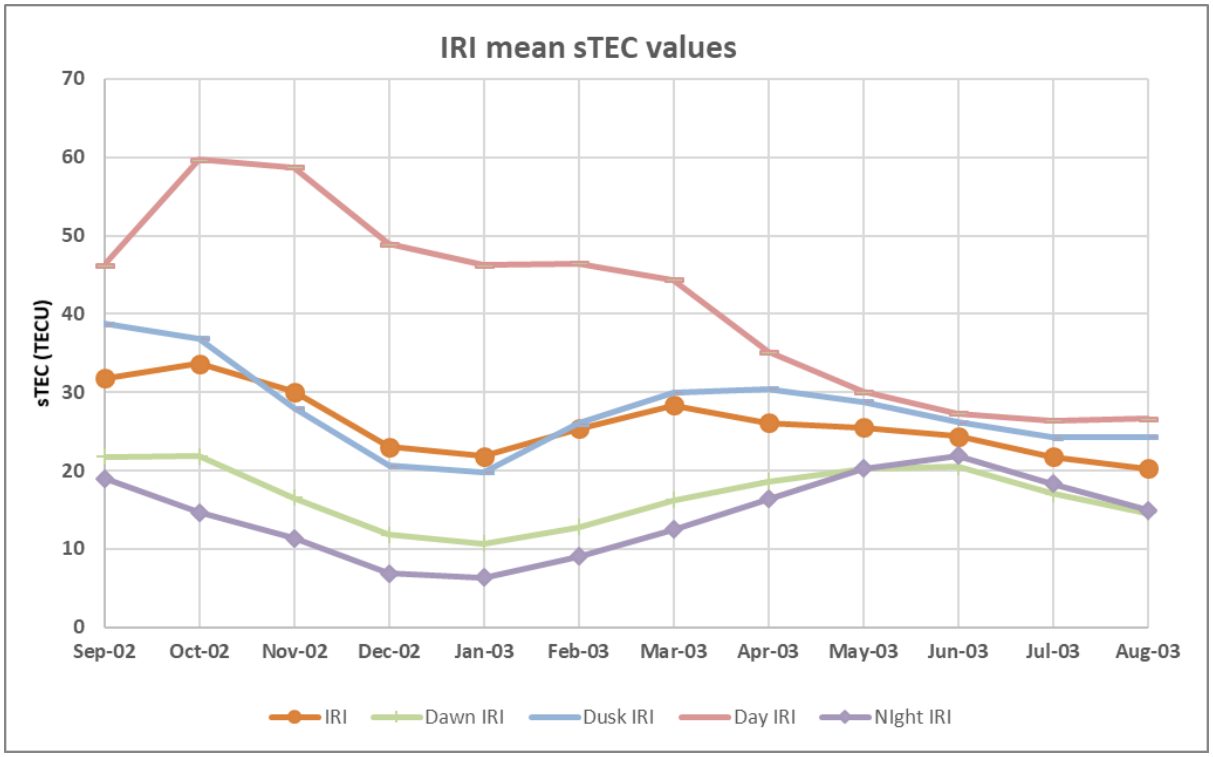

Figure 79b – IRI mean sTEC values are displayed for each of the defined time sectors for the HERS receiver. Comparing to Figure 77a, in December and January the night mean sTEC value is approximately 3 TECU smaller than the EDAM mean sTEC value. The reverse is true in May and June where IRI is larger by approximately 2 TECU.

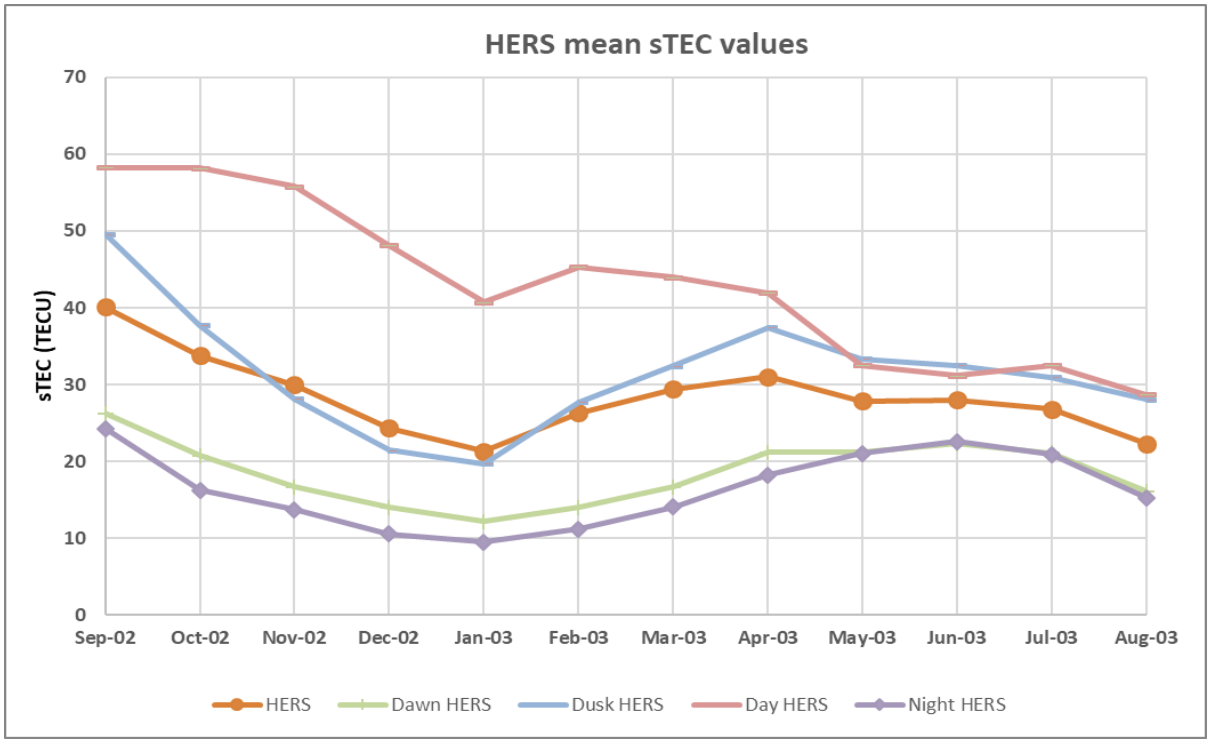

Figure 79c – HERS mean sTEC values are displayed for each of the defined time sectors at the location of the HERS receiver.

As previously mentioned, the background model that EDAM uses as a base ionosphere to assimilate GPS measurements into is the IRI model (Angling and Jackson-Booth, 2011; Bilitza and Reinisch, 2008). Therefore, it should be expected that EDAM with assimilated GPS sTEC performs better than IRI when compared to the truth data. Figure 5 of Angling and Jackson-Booth (2011) displays a comparison performance of residual TECs, the model TECs minus the GPS truth observations, for EDAM and IRI. The residual TECs modelled by EDAM with assimilated GPS are closer to 0 than IRI-2007 model, which modelled residual TEC more negative in morning and evening, but more positive during the day.

Figures 60 and 75 shows that there is a substantial difference between the performance of EDAM and IRI at the HERS receiver at mid-latitude, and their performance at the TRO1 receiver at high-latitude. Figure 60 shows the correlation of EDAM compared to truth for all defined time sectors to be between 0.90 and 1.00. Figure 75 however shows the correlations

values for the same points to be between 0.80 and 0.90. In the high-latitude ionosphere there are more structures present than in the mid-latitude ionosphere that can affect radio propagation (Hunsucker, 1992; Pryse et al., 1996; Park et al., 2012; Jin et al., 2014). This can account for the disparity between EDAM and the truth data.

Comparing Figures 65 and 76, the individual satellites performance, also show a big change in correlation between EDAM and truth. For TRO1 the correlation values of the individual satellites are centred around 0.90 correlation while for HERS the correlation values were located in the region around 0.96. There is a huge change in bias between the two. There are more individual satellites showing positive biases in Figure 76 compared to the predominantly negative biases in Figure 65. This is also evident when comparing the defined Kp levels in Figures 70 and 77.

Feltens et al. (2011) compared EDAM with three other ionospheric models. Rather than just one truth station, this paper compared the modelled data to multiple GPS stations across the world. Figure 80 shows the results of one of the comparisons conducted in Feltens et al. (2011), in December 2006 night time results, which is 18:00-05:59 local time. HRM1 is a receiver located at 51.4°N latitude and 1.28°W longitude and TRO1 is the same receiver used in this study. In a similar fashion, standard deviation values rather than normalised standard deviation, of differential slant TEC were compared for different time sectors and in different years. The differential slant TEC used by Feltens is like the residual TEC from Angling and Jackson-Booth (2011). The results from Feltens et al. (2011) show EDAM to be one of the top performing models using assimilated GPS, with standard deviation values smaller than the majority of receivers, when compared to several truth receivers across the world.

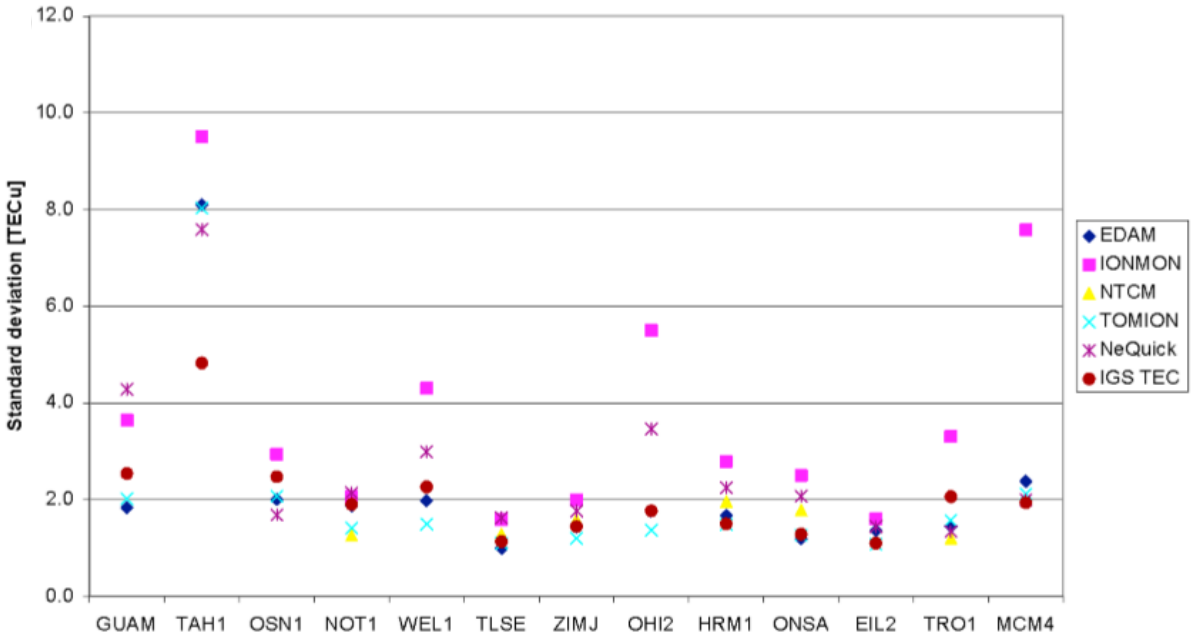

Figure 80 – December 2006 night time results displaying the standard deviation of the differential slant TEC taken from Feltens et al. (2011). The stations are ordered by geomagnetic latitude.

Across the board for all receivers EDAM is performing well, being very close to the IGS TEC point in Figure 80, which represents the truth data from the receiver. These results agree with the findings of the Modified Taylor Diagram study which showcases the performance of EDAM to be near agreeable with the truth data. Figure 80 also shows that EDAM is one of the more consistent and better performers of modelling the data by using assimilated GPS data compared to other models that use different techniques to assimilate the data. The exception that can be seen is for TAH1 receiver, which is in Tahiti. This was put down to the station being isolated from the input GPS data that is assimilated into the models.

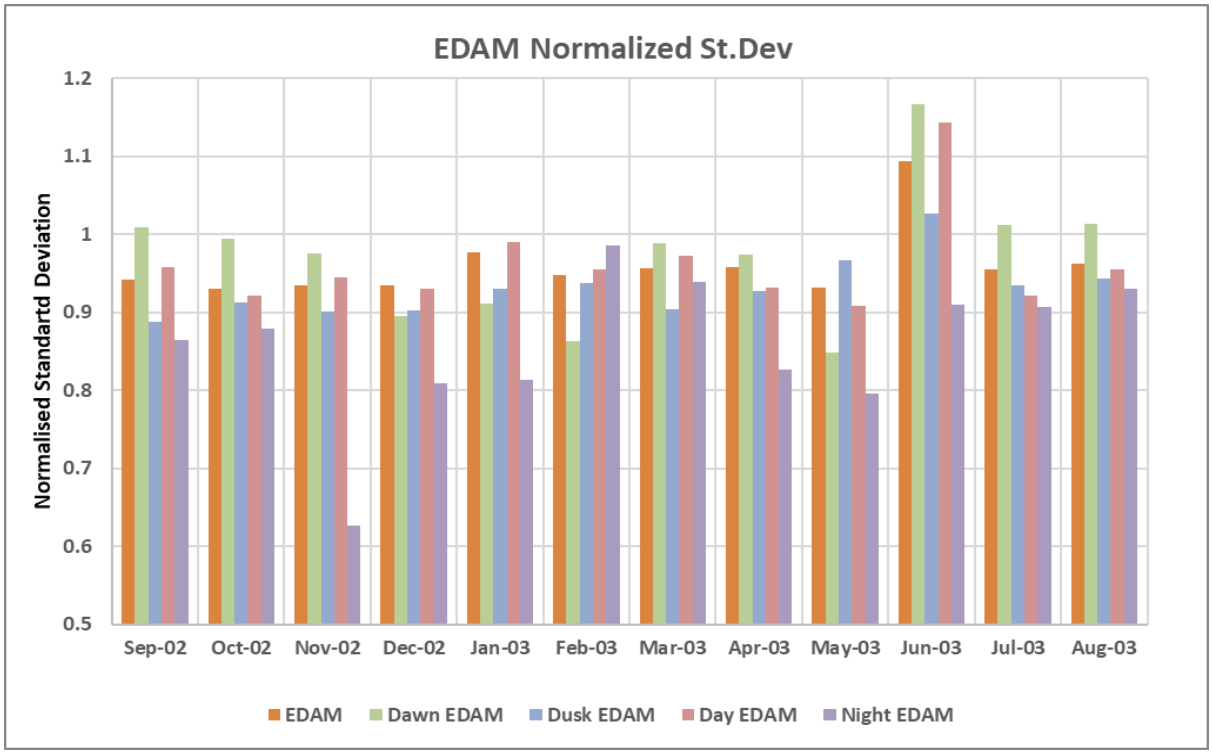

Figure 81 – Normalised standard deviation values for EDAM is displayed for all defined time sectors. For most months and time sectors the normalised standard deviation values are between 0.90 and 1.00. EDAM in the night sector shows the lowest normalised standard deviation in the plot, with a value of approximately 0.62 in November. June 2003 shows the values for the dawn and day time sectors surpass 1.10 for the only time during this year.

Figure 81 displays the normalised standard deviations of EDAM for each month and defined time sector. Comparing Figure 81 and 80, while different data are used, the results show that the standard deviations of EDAM and the truth are almost 1.00 and indicate that both studies agree that EDAM is performing well modelling the ionosphere using assimilated GPS data. Looking at June 2003 in Figure 81, it is the only time that the normalised standard deviations are substantially greater than 1.00, suggesting that EDAM is modelling more variability in the TECs than what is being observed at the HERS receiver.

The two months that EDAM is showing poor performances compared to the rest of the study, evident in Figure 78, is June and August 2003. Figure 81 also shows that June 2003 is a month where EDAM is underperforming by noticeable differences, with normalised standard deviations values greater than 1.10.

7.5 Conclusion

Modified Taylor diagrams have been used to show the performance of EDAM and IRI with respect to a truth receiver, HERS, between September 2002 and August 2003. The diagrams were categorised into three different parameters to focus on; the time of day, individual satellites, and Kp index.

Figure 78 shows that EDAM is generally outperforming IRI with larger correlation values. EDAM in the dawn sector, EDA, in Figure 61 is the best performing point in the whole study with a correlation of approximately 0.99 and normalised standard deviation of approximately 1.00. The EDAM correlation values are mostly between 0.90 to 1.00. The bias values exhibited by all EDAM points are predominately negative and the normalised standard deviation values are mostly between 0.80 and 1.00.

The comparison with the results from the TRO1 receiver shows that the more variable ionosphere is more difficult to model, with EDAM correlation values decreasing to between 0.80 and 0.90. The biggest difference between the two receivers is the normalised biases. Results from TRO1 shows variability in the biases between positive and negative, while for HERS data, EDAM is negatively biased for the whole year.

June 2003 is a big outlier in performance for the EDAM model, noticeable in the correlation comparison in Figure 78, where IRI is outperforming EDAM in some of the time sectors, and the EDAM normalised standard deviation values displayed in Figure 80, for the day and dawn sectors are greater than 1.10. June 2003 will form the discussion of the next chapter.

Chapter 8

June 2003 – A period when EDAM underperforms.

8.1 Introduction

Modified Taylor Diagrams (MTD) in the previous chapter (Figure 64) MTD for June 2003 to August 2003, showed unusually poor performances of EDAM compared to truth observations. The behaviour was not evident in the other three-monthly periods considered for 2002-2003. June 2003 provides the focus of the case study in the current Chapter. Figure 78 in Chapter 7 showed that June 2003 was one of the main causes for the poor performance in that period with IRI performing better than EDAM in the day and dawn sectors. The Modified Taylor Diagrams for the month, the days of the month for the defined time sectors and the individual satellites are presented to find the cause of this performance.

Modelling results for July 2003 are used as a baseline to show how EDAM should be performing during these summer months. The chapter therefore opens with the Modified Taylor Diagrams for July 2003 for comparisons with the MTD for June 2003.

8.2 Results for July 2003

Figure 82 shows the Modified Taylor Diagram for EDAM and IRI compared to the 'truth' data for July 2003. The diagram displays little variability in the correlation values of the five EDAM points, with all points for the time sectors residing near correlation values of 0.97 and 0.98. The normalised standard deviations of the different time sectors show slightly more variation in the night sector, EN, having a normalised standard deviation value of approximately 0.92 and the dawn sector, EDA, a normalised standard deviation value of approximately 1.02. The normalised biases for all EDAM points are slightly negative, with values between 0.00 and -0.20. The IRI points are also all close together, with a normalised standard deviation of

approximately 0.75. The correlations of the points are between 0.85 and 0.90 and normalised biases are negative, at approximately -0.40. EDAMs performance here is comparable with the correlation and normalised standard deviation values exhibited throughout Chapter 7.

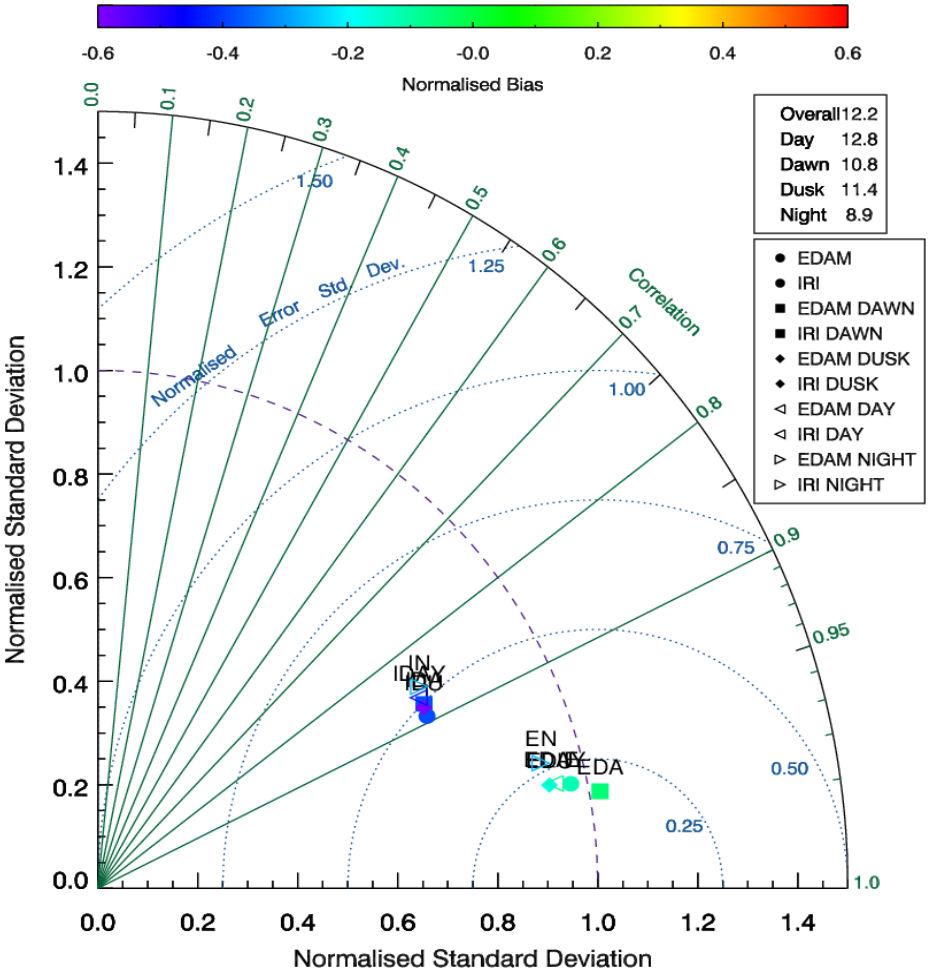

Figure 82 - A Modified Taylor Diagram showing the statistical performances of EDAM and IRI compared to the 'truth' data for July 2003. Correlations for EDAM around 0.97 and 0.98 while IRI points are between 0.85 and 0.90. EDAM exhibits minor differences in normalised standard deviation with values ranging from approximately 0.92 to 1.02.

Figure 83 shows the same data for EDAM as in Figure 77 but categorised by individual satellites. The points are clustered around a normalised standard deviation value of 1.00 with correlation values ranging between 0.95 and 0.99. The points are more scattered compared to the points for the defined time sectors in Figure 82 although the performance is again very consistent. The points also exhibit a negative normalised bias, ranging from 0.00 to approximately -0.25, with no satellite showing a positive bias.

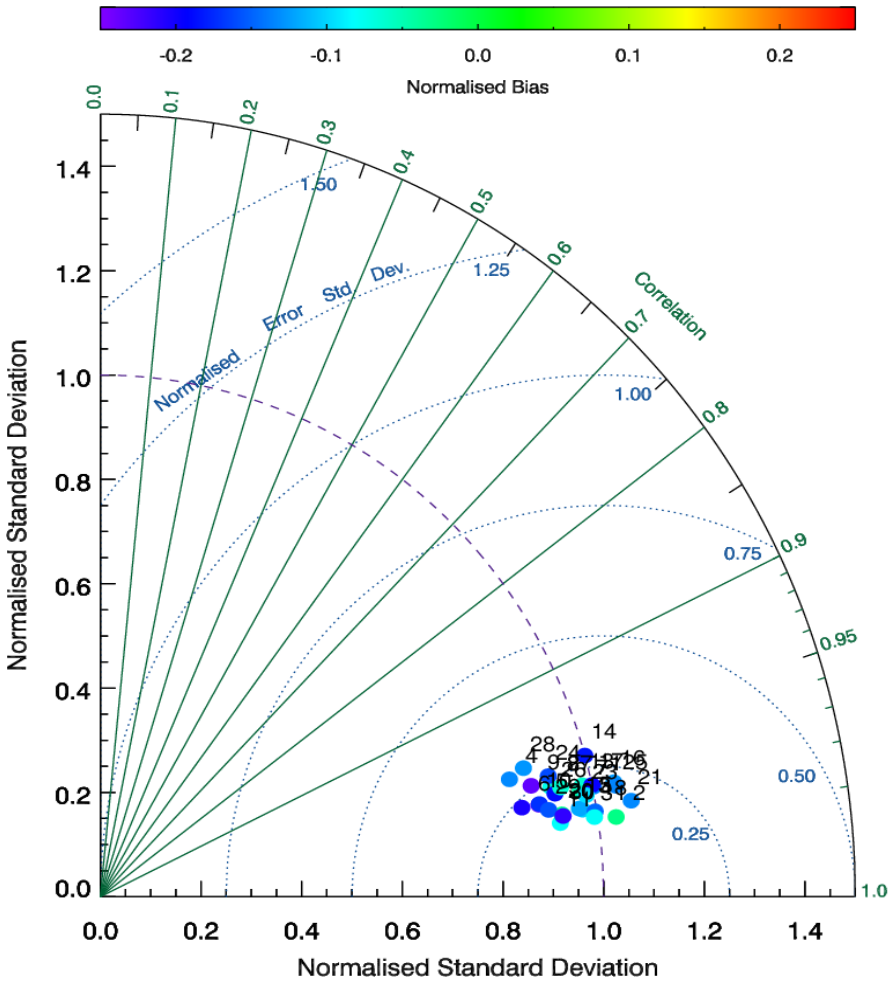

Figure 83 - A Modified Taylor Diagram showing the statistics for every satellite compared to 'truth' data for EDAM. The points are clumped together in their performance with a range of 0.95 to 0.99 in correlation and 0.85 and 1.10 for normalised standard deviation. The normalised biases for all the points are negative.

Figures 84a and 84b shows Modified Taylor Diagrams for 1 July 2003. Figure 84a shows the diagram for the defined time sectors and Figure 84b for the individual satellites. In Figure 84a, the diagram shows the clumping of the results from EDAM for most of the time sectors, correlation values of approximately 0.98 and normalised standard deviation value of approximately 1.00. EDAM in the dusk sector, EDU, is the only one offset from this with a correlation value of 0.96 and a normalised standard deviation of 0.90. These differences are very small between the group and the dusk point and is not considered as an outlier point. The IRI points are also clumped together, but with correlation values around 0.95 and normalised standard deviations of approximately 0.75.

Figure 84b shows the performance of EDAM for each individual satellite compared to the 'truth' for the same day. The majority of satellites are bunched close together, around the 1.00 normalised standard deviation, values between 0.90 and 1.10, and with correlation values between 0.97 and around 0.99. There are two offset points from this group, satellites 28 and 4, that have smaller standard deviations around 0.80 and less with correlation values that are 0.95 and less.

The biases for both Modified Taylor Diagrams show that EDAM is negatively biased, agreeing with the what was seen for the whole month. Comparison of the correlations and standard deviations in Figure 84a with these in Figure 82, for the whole month, shows that both EDAM and IRI have similar values of correlation and normalised standard deviation. The individual satellite comparison is slightly different. The individual satellites in 84b are clumped with similar correlation and normalised standard deviation values to those seen in Figure 83. The two outlying satellites however are not visible in Figure 83.

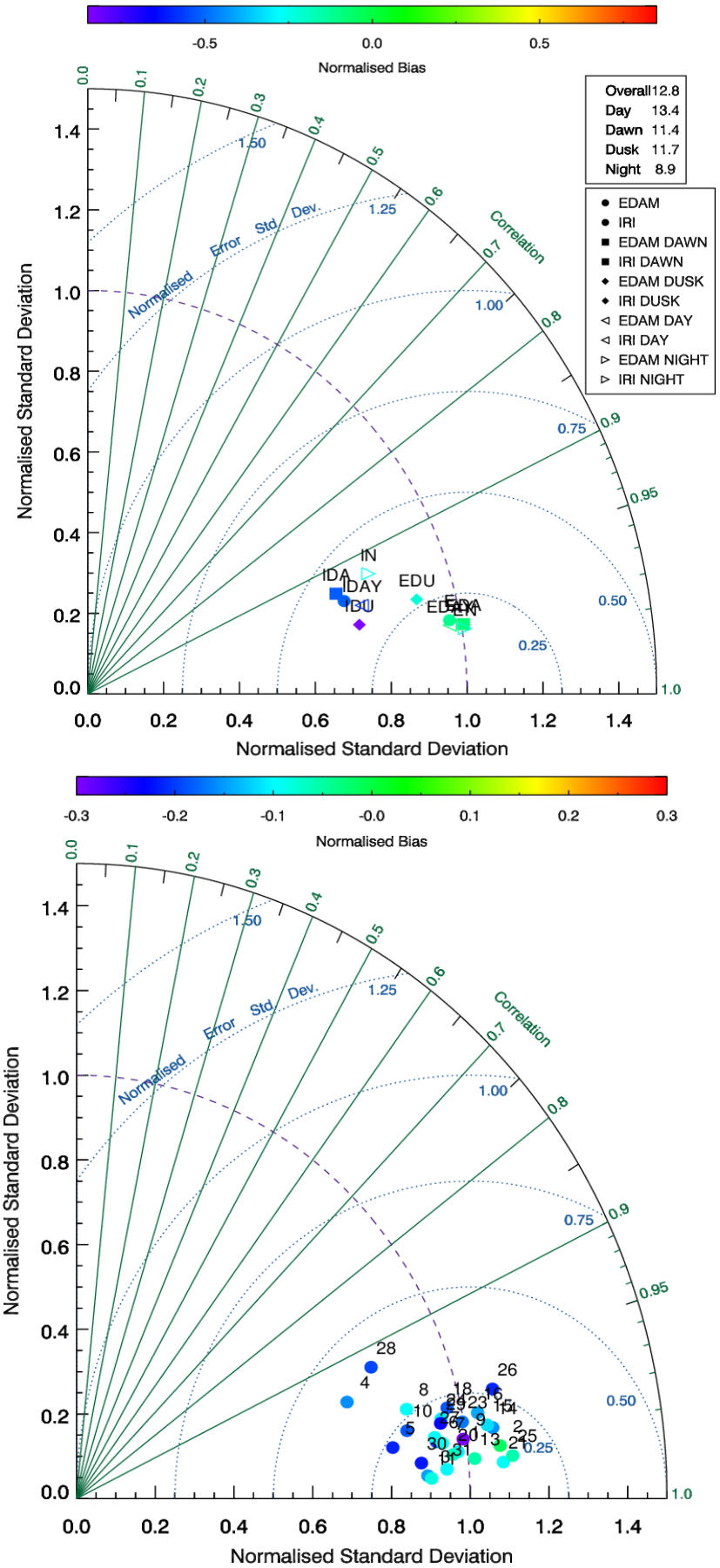

Figure 84a and b – Modified Taylor diagrams that show the performance of EDAM and IRI compared to the 'truth' for each defined time sector and individual satellites on 1 July 2003. Figure 84a shows the times of day performances, with a group forming around 1.0 normalised standard deviation and correlation of 0.98. The dusk sector is the outlier to this, with a slightly worse correlation of 0.96 and a worse normalised standard deviation of 0.90. IRI is also clumped together but with correlation values around 0.95 and normalised standard deviations of approximately 0.75. Figure 84b shows the satellites' performance, with a group, with correlations between 0.97 and 0.99, and normalised standard deviations between 0.90 and 1.10. There are two noticeable points that are outliers to this group, satellites 28 and 4, with correlation values slightly greater than 0.90 and normalised standard deviation values less than 0.80.

The second day that was chosen was 31 July 2003. Modified Taylor Diagrams for this day are shown in Figures 85a and 85b for the time sector and individual satellites. Figure 85a shows the Modified Taylor Diagram for the time sector performance of EDAM and IRI compared to the 'truth' data. There is a little difference here between this diagram and Figure 84a. The correlations for the EDAM points are all approximately the same, 0.98 to 0.99. The differences are in the normalised standard deviation, and in the biases of each time sector. The range in the normalised standard deviation is from 0.85 for the EDAM night point, EN, to 1.05 for the EDAM dawn point, EDA. EDAM at all times, E, lies at approximately 1.00 normalised standard deviation with a correlation value of 0.98. The normalised bias for the EDAM night point is strongly negative, approximately -0.40, with the EDAM dawn point close to 0.00. The other time sectors are in-between this range. There is much more variability in IRI points for this

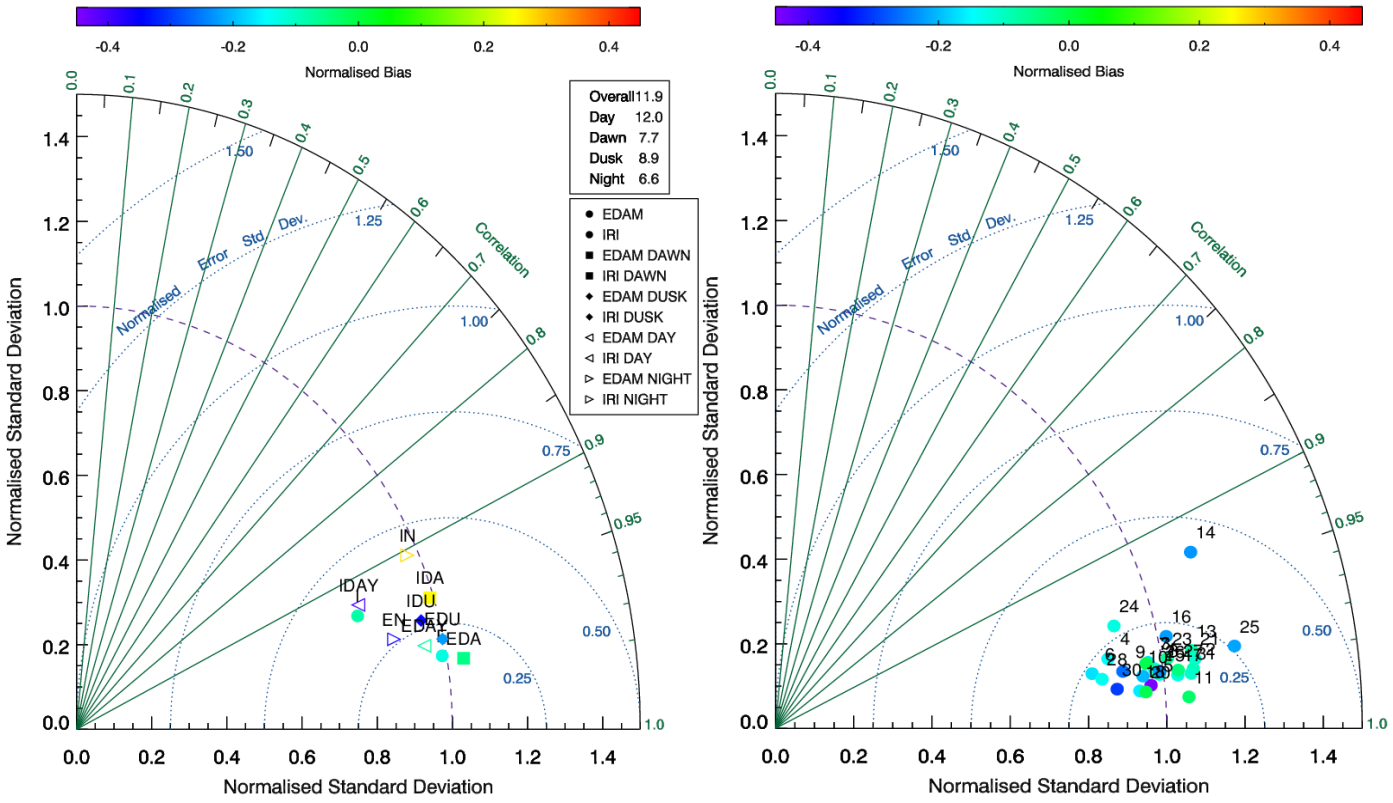

Figures 85a and b – Modified Taylor diagrams that show the performance of EDAM and IRI compared to the 'truth' for the defined time sector and individual satellites on 31 July 2003. The correlation values for EDAM are 0.97 to 0.99. The normalised standard deviation values range from between 0.85 to 1.05. There is also a range in the bias, where for the EDAM night point, EN, it is approximately -0.40, while the EDAM dawn point is approximately 0.00. Figure 85b shows the performance for the individual satellites modelled by EDAM compared to 'truth'. There are two outliers to grouped region, satellites 14 and 25. These two satellites have normalised standard deviations of 1.15 and 1.20. The correlation values for these satellites are of 0.93 and 0.98

day, compared to Figure 82 and Figure 84a. The biases for the IRI night point, IN, and the IRI dawn point, IDA, are positive. This is different when compared to Figures 82 and 84a. The normalised standard deviations values are between 0.80 and 1.10 for these points but correlations are comparable to Figures 82 and 84a with values of at 0.90 and 0.94.

Figure 85b shows the individual satellite performance modelled by EDAM compared to the 'truth'. This performance is very similar to the Figure 84b with two outliers, satellites 14 and 25 this time. The two outliers in this diagram have normalised standard deviation values of 1.15 and 1.20. These correlation values are 0.93 and 0.98 respectively. The normalised biases for the majority of the points are negative, with the bias of a few satellites being approximately 0.00.

8.3 June 2003

With June 2003 being established as a problematic month in the study of Chapter 7, this will be the focus for this section.

8.3.1 June 2003 as a whole

Figure 86 shows the Modified Taylor Diagram displaying statistics for the June 2003 sTEC data through EDAM and IRI compared to the truth data. The EDAM dawn, EDA, and EDAM night, EN, points are performing well in comparison to the other time sectors with correlation values greater than 0.90 which is comparable with July 2003.

Looking at the points for IRI, the worst performing time sector is the dusk sector, IDU. The correlation value of the dusk point is approximately 0.70 and normalised standard deviation of 0.60, suggesting the variation away from the mean is smaller than the variation exhibited by the truth data. Figure 86 shows that the problems of EDAM in June are related to the dusk and day sector, where the dusk point for EDAM, EDU, has an even smaller correlation value when it is compared to the equivalent IRI point, IDU. The EDAM at all time sectors point, E, is based on the complete data set for June 2003 and is affected by the dusk and day time.

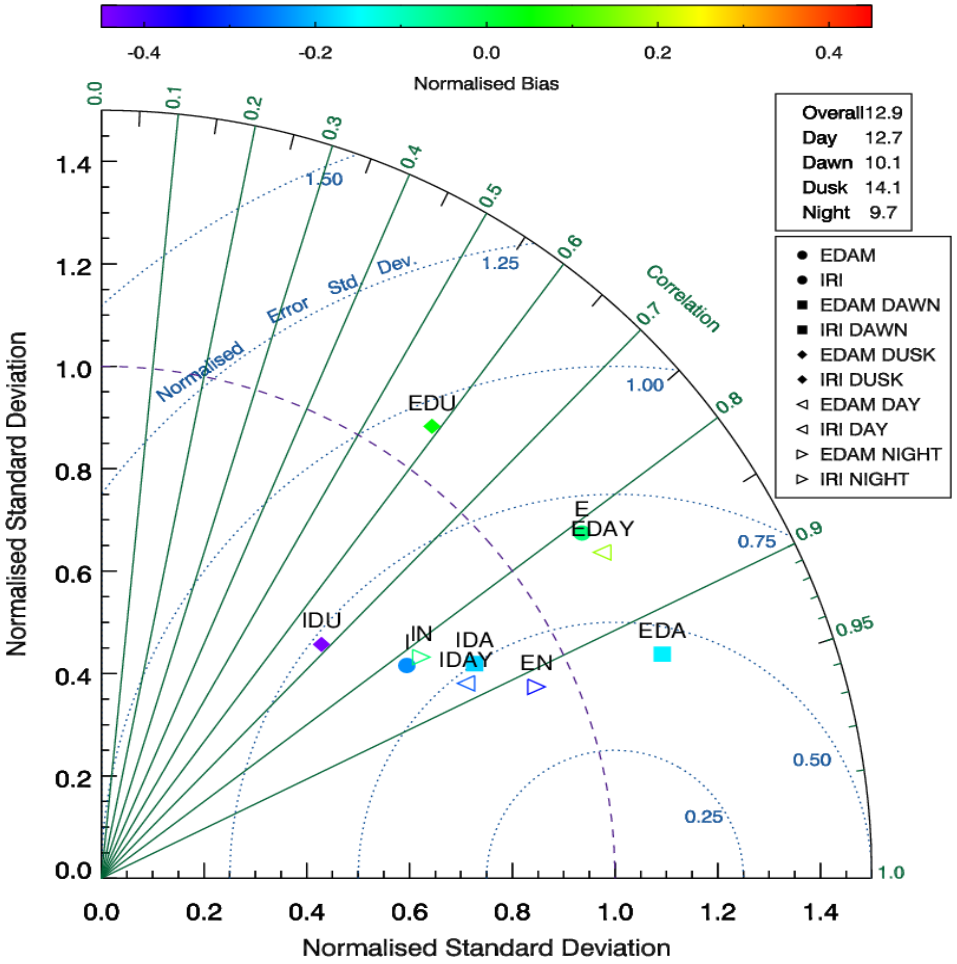

Figure 86 – Modified Taylor Diagram showing the defined time sectors for EDAM and IRI in June 2003. The performance here is for the month. The dawn and night points are the best performing sectors for EDAM with correlations greater than 0.90. Dusk is the worst performing sector for both models, but the IRI point has a greater correlation value, approximately 0.70, than the EDAM point, a value of approximately 0.60.

The biases for the EDAM points are also different when compared to the performance of July. There is a more positive bias for the performances of EDAM in the dusk and day time, where the worst performances are, while there is still a negative bias for the night and dawn sectors, the better performing sectors. This indicates EDAM in the two underperforming points is showing TEC values greater than there should be.

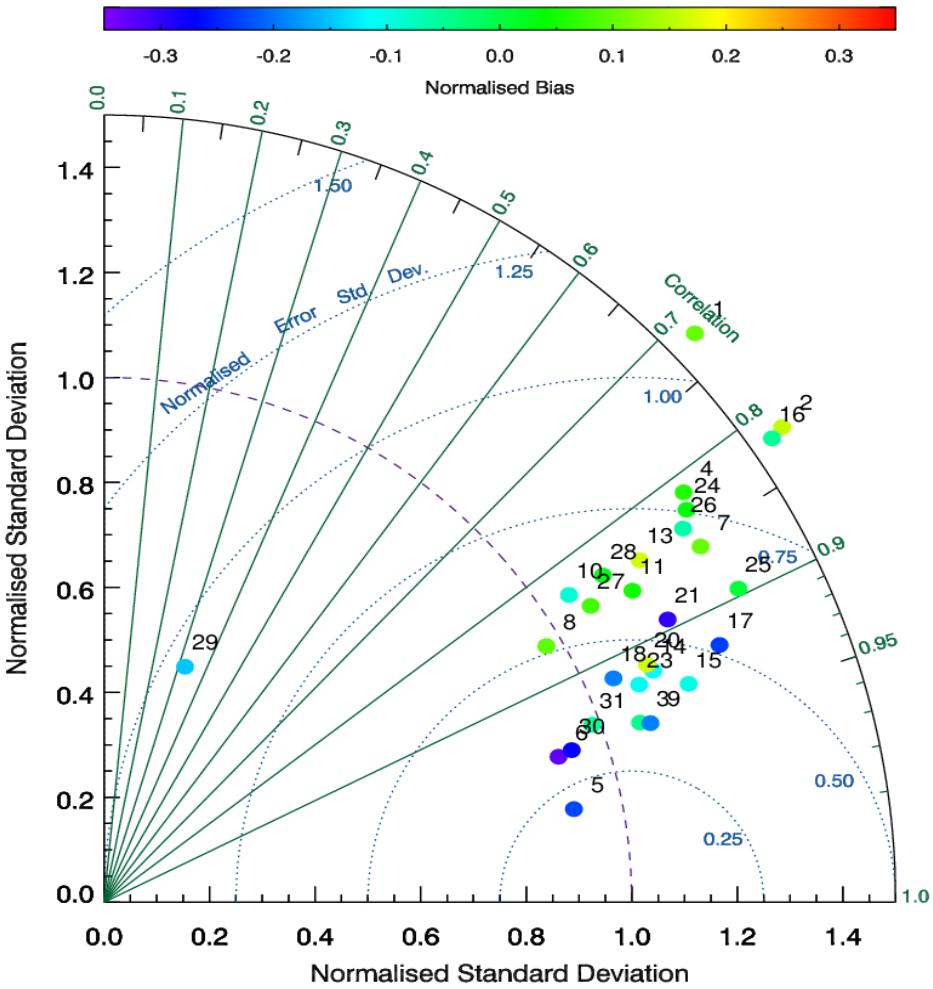

Figure 87 - Satellite statistical performance for June 2003. Satellite 29 is an outlier and in-depth research into this satellite showed there was little data for this month, so it can be disregarded in this diagram. The rest of the satellites are scattered between 0.70 and 0.98 correlation with an expansion in normalised standard deviation seen to extend beyond 1.50 for satellites 2, 1 and 16.

Figure 87 shows the Modified Taylor Diagram for the EDAM performance for the individual satellites, for June 2003. There is a large scatter in the points between correlations of 0.70 and 0.98. As the correlations get worse, the bias increases in positivity. Satellite 29 is a complete outlier, with little data available for this month. For the purposes of this study, it can be ignored when compared to the rest of the data set. Satellites 2, 1 and 16 exceed the axis limits for the normalised standard deviations, showing values great than 1.50.

8.3.2 13 – 20 June 2003

This section considers the EDAM performance for the satellites on individual days between 13 and 20 June 2003.

Figure 88 shows the EDAM satellite performance for 13 June 2003. The diagram shows that most of the satellites have a correlation value greater than 0.90, with a variation of roughly 0.20 either side of 1.00 in normalised standard deviation. The normalised biases for the individual satellites are mostly negative. Comparing the performance on this day with Figure 87 shows that the majority of the individual satellites have better correlation values on the 13 June than for the whole month, and they are more aligned with the correlation values shown in Figure 83 for July.

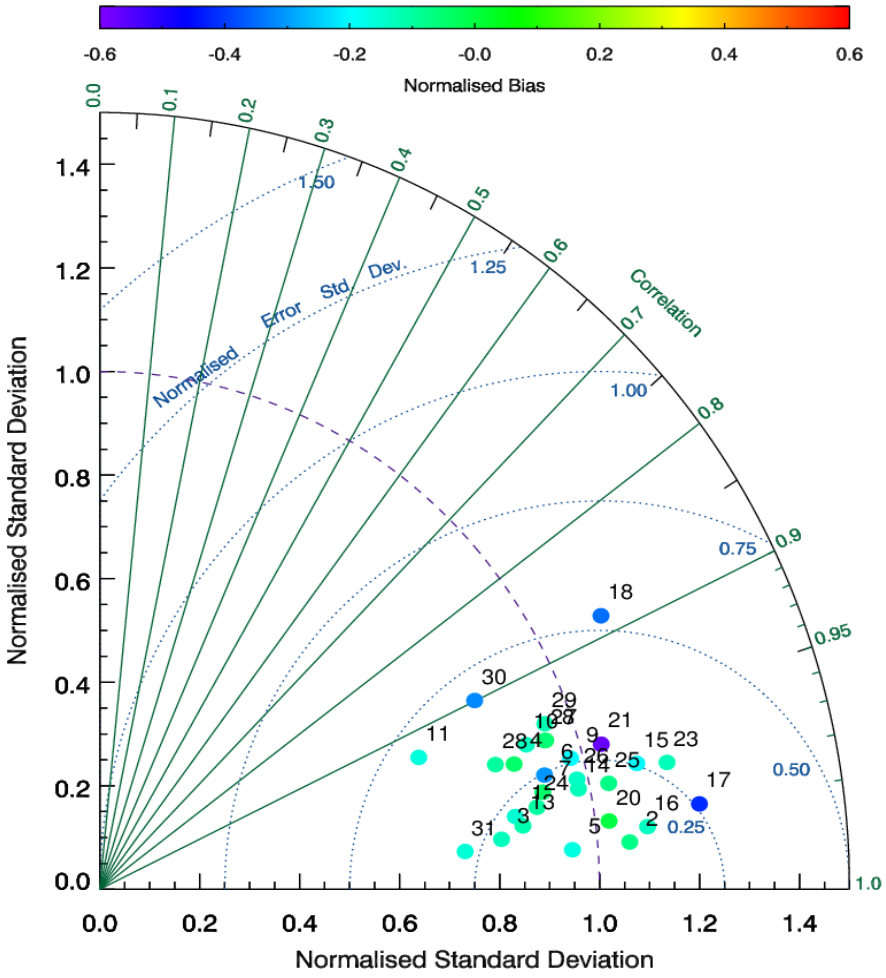

Figure 88 - Modified Taylor Diagram for 13 June 2003. While there is some scatter in the data points, the correlation values for the satellites are mostly within 0.90 and 1.00, with minor variations in normalised standard deviation and biases that are comparable to July.

A Modified Taylor Diagram for the following day, 14 June 2003, is presented in Figure 89. The scatter of the points has now increased dramatically covering a larger variation in both correlation and normalised standard deviation. The correlation values of the satellites now vary between 0.60 and 1.00. Individual satellites now have normalised standard deviation values greater than 1.50, the limit on the normalised standard deviation axis.

There is also a significant change in the normalised bias of each satellite between the two days. More individual satellites now have a positive bias, especially evident in the scattered points beyond 1.50 normalised standard deviation. Before delving into what is causing this, the rest of the days that experience this are displayed to show how long this performance in EDAM lasts for. The normalisation factors used for the statistics between 13 – 20 June are

shown in Table 2 in Appendix B. These factors give a measure of how the truth data are varying for the satellites between each day.

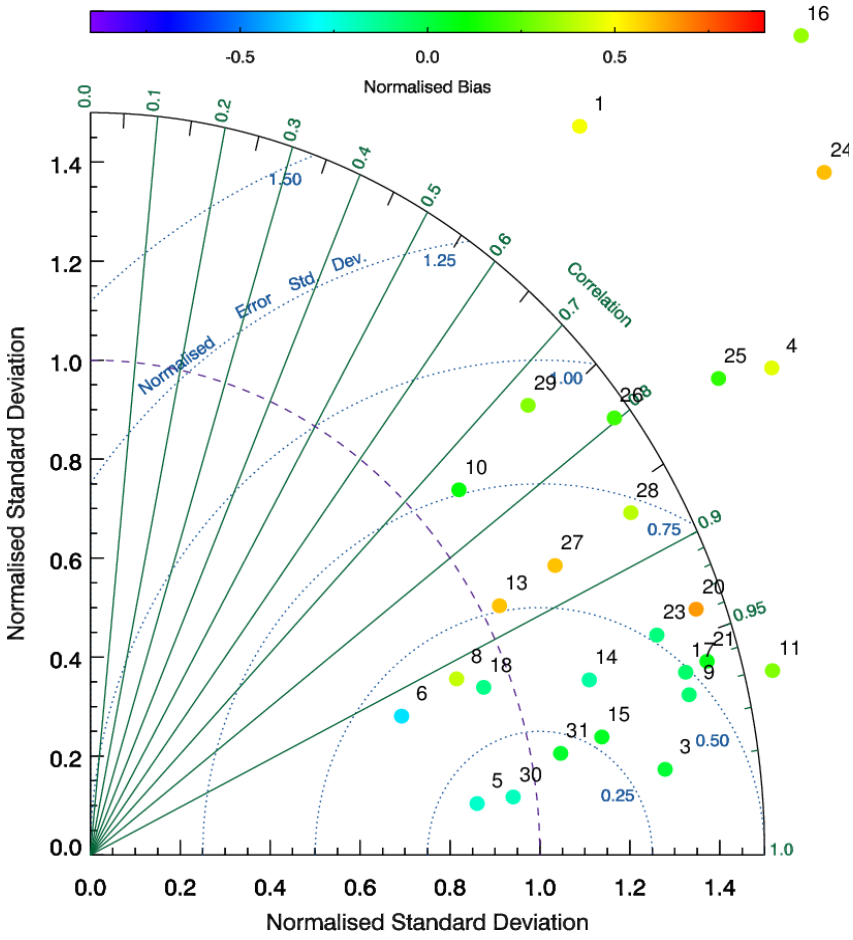

Figure 89 – EDAM performance for individual satellites on 14 June 2003. There is substantial variation and scatter in the performance of the individual satellites compared to Figure 88. There is large variation in correlation values of the points, 0.60 to 1.00. Large normalised standard deviations are observed, with many satellites exceeding values of 1.50. There is a shift in normalised bias from negative in Figure 88, to more satellites showing a positive bias here.

Figure 90 shows the Modified Taylor Diagram for 15 June 2003. Satellite 13 has a large normalised positive bias, with a value of approximately 1.00, which has not been evident in previous Modified Taylor Diagrams. This means that for this satellite EDAM is overestimating the TEC value. There is a decreased number of satellites present on the diagram, which is because of the increased values of normalised standard deviation for some of the individual satellites, values that are well beyond what can be shown on the diagram. The number of

satellites in the diagram is 23, while Appendix B shows the normalisation factors for 28 satellites, meaning that 5 satellites are missing from the diagram. Some of the satellites present on the diagram, satellite 13 for example, are beyond the 1.50 normalised standard deviation at the edge of the axis but the value is small enough to be shown on the diagram.

The performance in Figure 90 is noticeably worse than Figures 88 and 89, however there are some satellites, numbers 5, 6 and 30, that have correlation values between 0.98 and 1.00 and normalised standard deviation values of approximately 0.96. Their normalised biases are also around 0.00 to -0.25. These values are comparable with those of Figure 83 for the performances in July 2003.

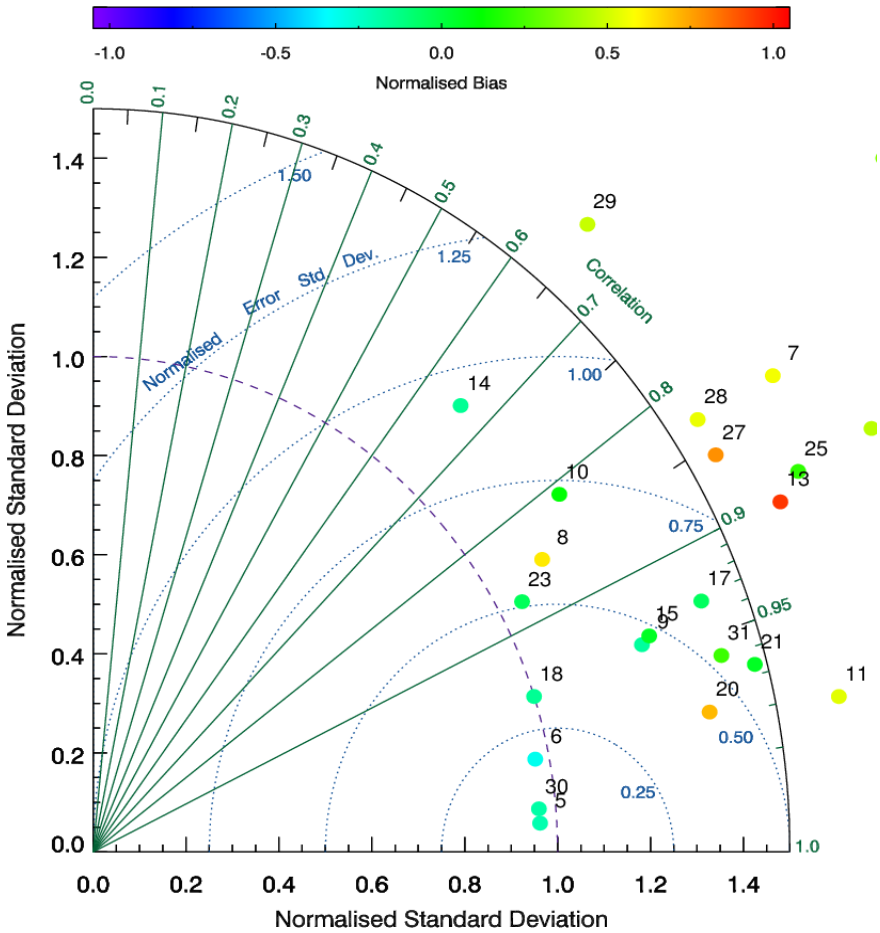

Figure 90 - EDAM performances for individual satellites for 15 June 2003. There are notable increases in normalised bias, for example satellite 13 now showing a normalised positive bias value of approximately 1.00. Several satellites with statistics available are not presented on this diagram due to a large normalised standard deviation, too large to be displayed on the diagram. The satellite numbers 5, 30 and 6 show EDAM is not underperforming for all individual satellites.

This situation is similar for the next few days up until the 20 June 2003. Figures 91a to 91d show the Modified Taylor Diagrams for the period 16 – 19 June 2003 (inclusive).

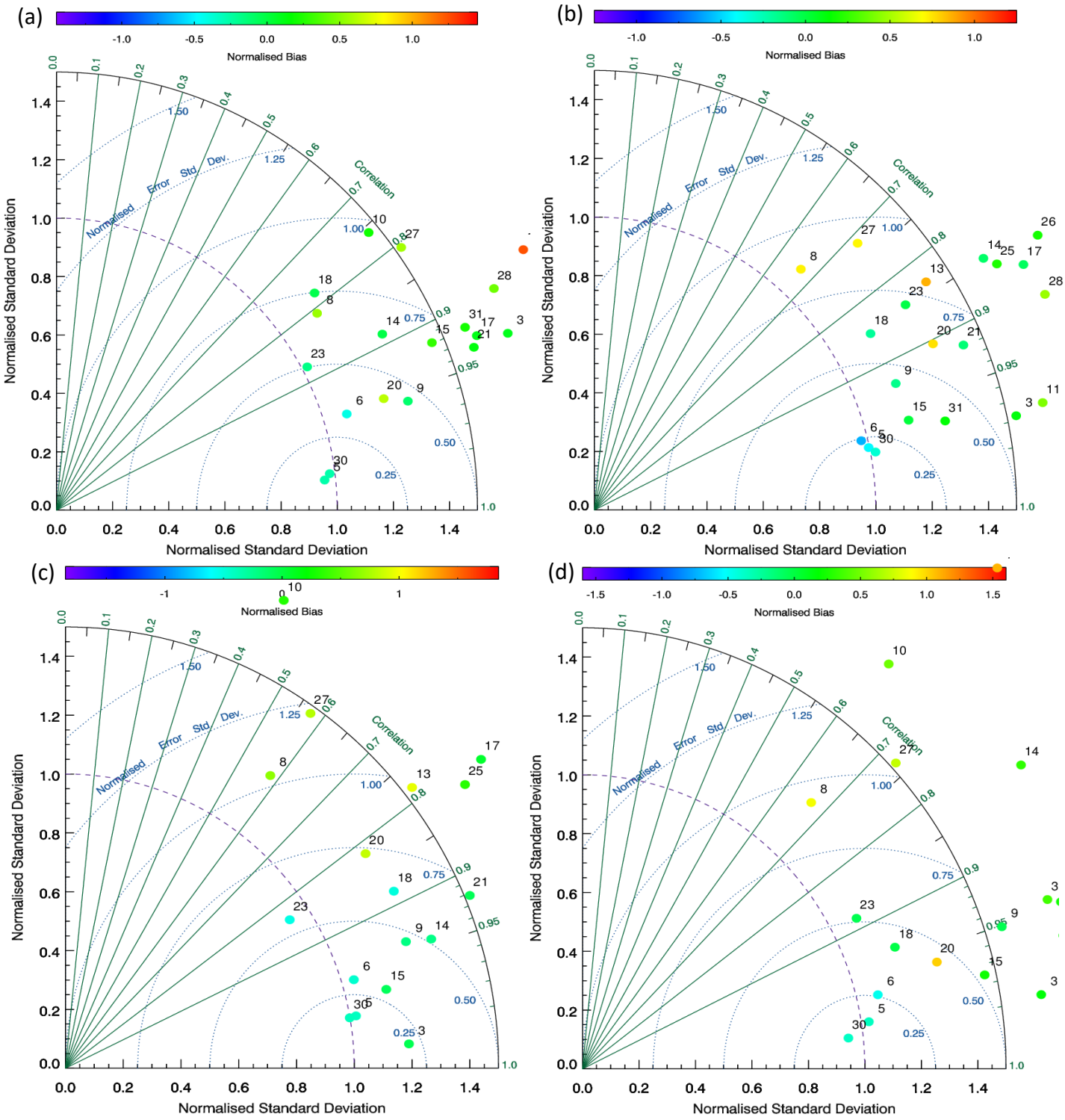

Figures 91 - Modified Taylor diagrams for 16 – 19 June 2003. The diagrams show the similar trends seen in Figure 90 with satellites missing due to large values of normalised standard deviation. However, there are satellites in each that continue to show the good performances of EDAM, for example satellite 30 in all diagrams with a correlation value around 0.98 and 0.99 with normalised standard deviation values of approximately 1.00.

On 20 June 2003 the performance of EDAM returns to a state that is similar to the result shown Figure 88. The Modified Taylor diagram for this day is presented in Figure 92. The next step was to focus on what happened between the 13 and 14 June 2003 that caused the drastic variability in performance to occur. To do this, other methods of approach to looking at the EDAM, IRI and truth data along with other data sources were considered to find where the variability in the satellite performances was occurring and if there was any variability in the ionosphere that could have been a cause for this.

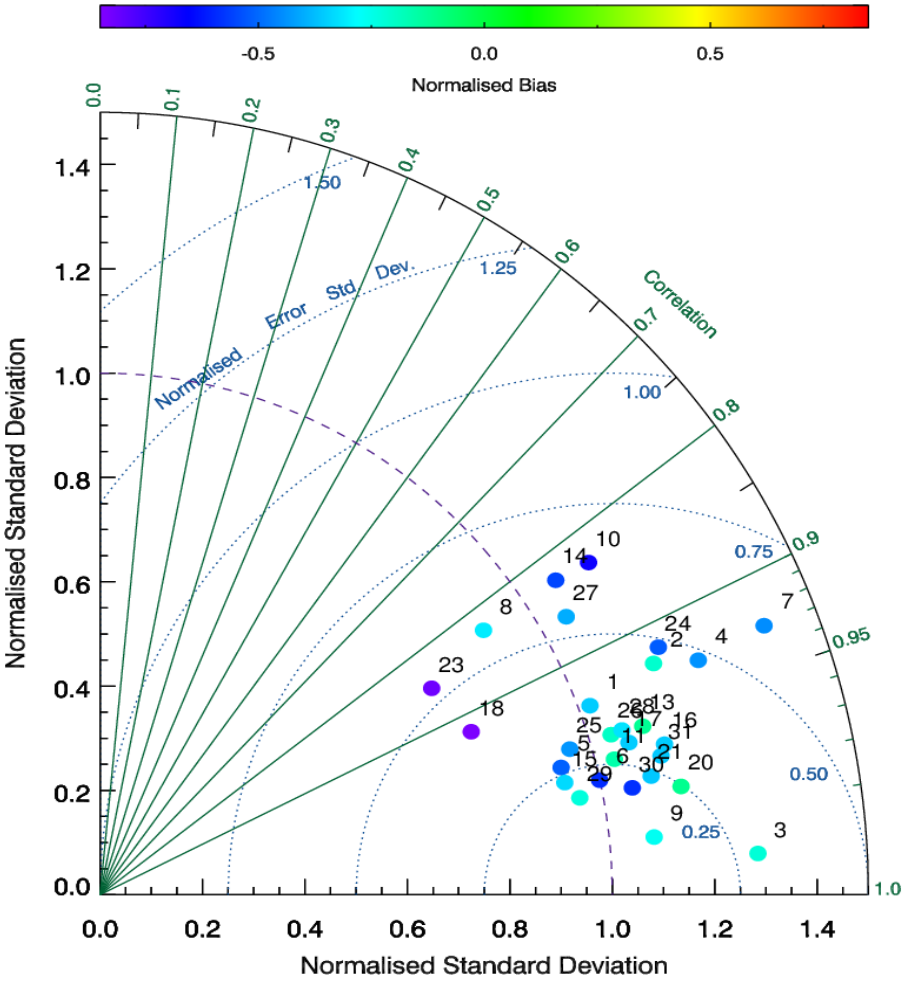

Figure 92 - EDAM individual satellite performance for 20 June 2003. There is still scatter in the EDAM performances for the individual satellites, however the scatter is much less compared to the previous figures. The biases have reverted to normal standards, with the values being primarily negative. The majority of satellites now have correlation values greater than 0.90, with all greater than 0.80.

8.3.3 sTEC Comparison of three satellites

Focussing on the period 13 to 20 June 2003, plots were produced of the sTEC between satellite and receiver. They were the measured truth observations, labelled as RINEX in the figures, and sTECs calculated through the EDAM model and calculated through the IRI model. The sTEC data is for each satellite. Each satellite follows a trajectory at an altitude of approximately 20,000 km. The receiver acquires the satellite signal when it is in the line of sight of the receiver. The plots can show the detail of where the model is inaccurate and give an explanation to some of the bias values shown in the previous section.

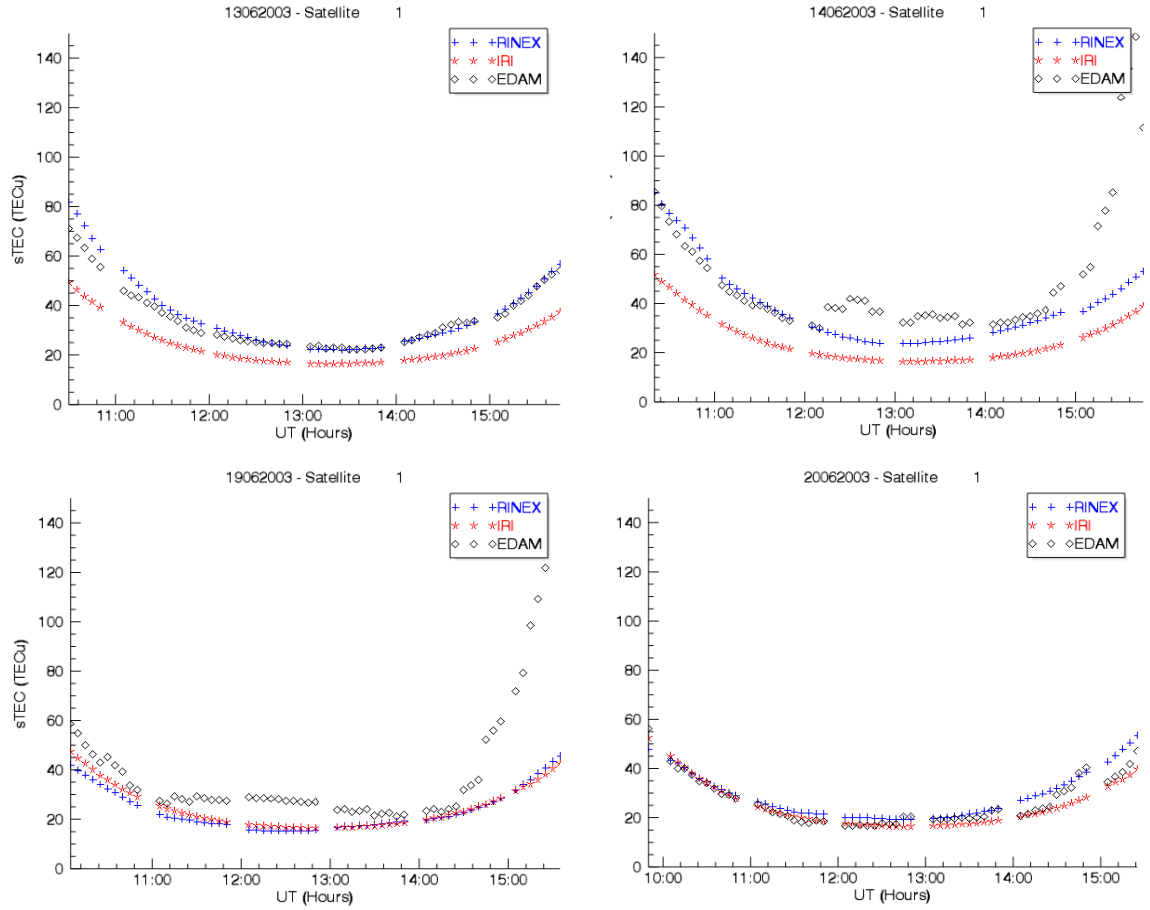

Figure 93 - Slant Total Electron content for satellite 1 on 13 June 2003 (a), 14 June 2003 (b), 19 June 2003 (c) and 20 June 2003 (d). The data show arcs for the truth (RINEX) data between HERS and the satellite shown by the blue crosses, the sTEC between HERS and the satellite through the IRI model shown by the red stars and the sTEC between HERS and the satellite through EDAM shown by the white diamonds. There is variation in the sTEC at the beginning of the arc, just before midday, to that of the arc later in the afternoon, from midday onwards, on 14 and 19 June. There are differences in excess of 80 TECU between the truth and EDAM at around 15:00 UT.

Figures 93 a – d show the evolution of one of the underperforming satellites in the Modified Taylor Diagram, satellite 1, on the 13, 14, 19 and 20 June 2003.

Figure 93a are the sTEC values of satellite 1 on 13 June 2003. This corresponds to a point on the Modified Taylor Diagram in Figure 88. Comparing the truth and EDAM sTECs show that EDAM is within 2 to 3 TECU of the truth value for most of the plot. The IRI sTECs show difference from the truth of approximately 10 TECU. The following day, 14 June 2003, in Figure 93b is for the day when the variability in EDAM started to occur. Shortly after 12:00 UT the sTEC values of EDAM increase by approximately 10 TECu, giving a difference between the truth and EDAM of approximately 10 to 15 TECU. This variability occurs for the hours following, with a decrease in the TEC levels around 14:00 UT. At around 15:00 UT there is another increase in sTEC of approximately 15 TECU, continuing to increase until the end of the plot showing values of 100 TECU greater than the values modelled at 14:00 UT. This gives differences between EDAM and the truth of about 100-110 TECU after 15:00 UT. IRI sTEC values does not show this increase and variability from 13 June to 14 June. This means during the time when EDAM shows large increases in sTEC, IRI becomes the more accurate model when compared to the truth. A similar outlook can be viewed in Figure 93c, 19 June 2003, with the sTEC value increase occurring slightly earlier in time. Of note in Figure 93c is that the truth sTEC values have decreased in comparison with Figures 93a and 93b. This causes a better comparison with IRI, with differences between the two now at approximately 3 TECU. EDAM has a difference of approximately 10 TECU from the truth data, but much greater at 15:00 UT and beyond where differences reach a maximum of 80 TECU. Figure 93d shows EDAM beginning to model the sTEC values for this satellite much better with difference values between EDAM and the truth returning to approximately 5 TECU.

Figures 93b and 93c begin to confirm that EDAM is performing poorly in this time period and in particular the midday to afternoon time sector. Satellite 1 is one of the worst performing satellites for the modelling at this time. A few other satellites also show underperformance on a similar scale to satellite 1 and will be discussed as well. The other satellites chosen are satellite 13 and satellite 24 as they show large positive biases and in Figure 86, they are not seen on some of the diagrams.

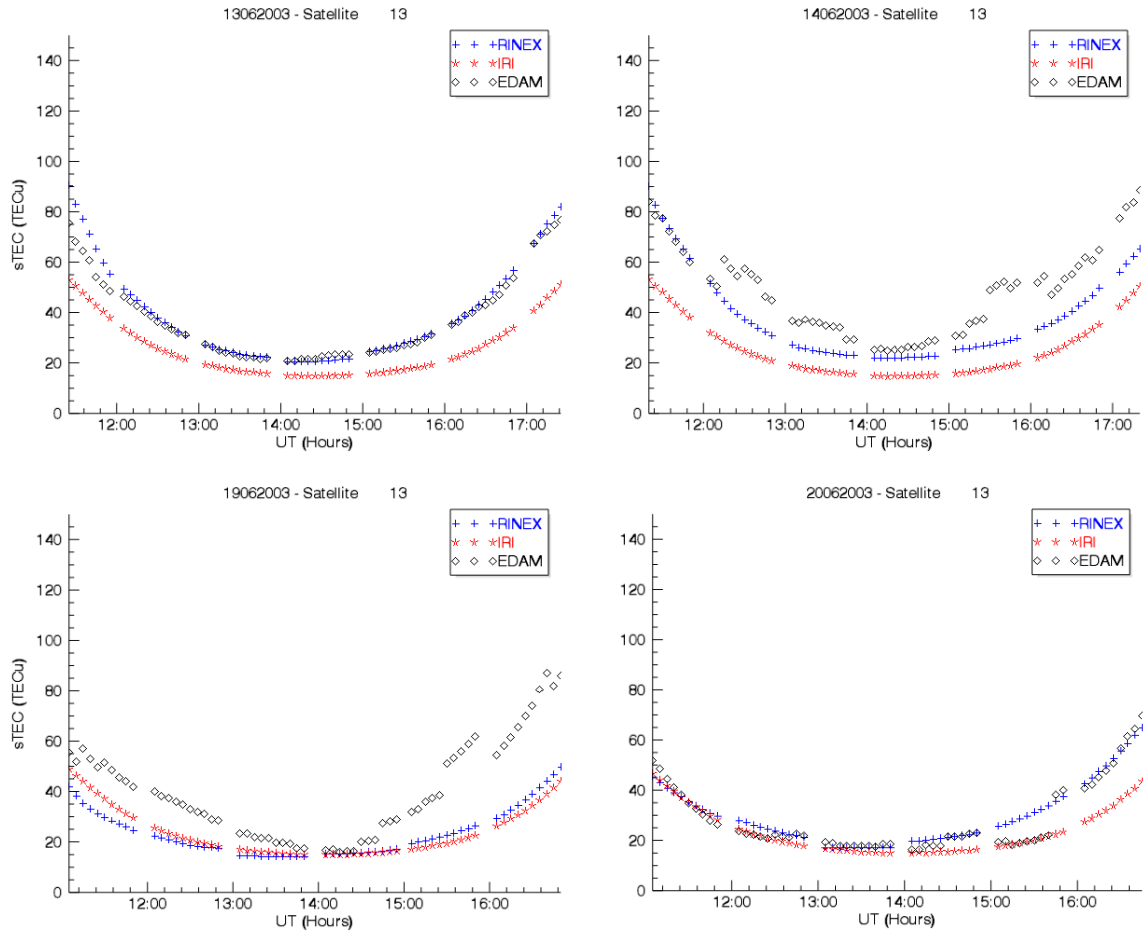

Figure 94 - Slant Total Electron content for satellite 13 on 13 June 2003 (a), 14 June 2003 (b), 19 June 2003 (c) and 20 June 2003 (d). A similar pattern emerges here as was shown for satellite 1 with the 13 June showing good performance by EDAM compared to truth, with 14 and 19 June showing EDAM sTECs much greater than anticipated from the truth with it beginning to reduce on the 20.

Figure 94 shows the sTEC arcs for satellite 13 on four different days; 13, 14, 19 and 20 June. The sTEC arcs for the 13 June in Figure 89a show very good agreement between EDAM and

truth sTEC values, with differences of about 1 to 2 TECU for most of the time. The IRI sTECs are lower when compared to EDAM and the truth sTECs, being some 5 to 10 TECU lower. The following day shows variability in the EDAM sTECs. Shortly after 12:00 UT in Figure 94b, the values of the EDAM sTECs increase by almost 20 TECU, which is a significant increase in such a short amount of time. The sTEC differences from the truth reduce to a few TECU just after 14:00 UT. After 15:00 UT the EDAM sTEC values increase again with some differences between the truth and EDAM of around 30 TECU. In Figure 94c for 19 June 2003, there is still variability noticeable in the EDAM sTECs. The differences between EDAM sTECs and truth sTECs range from 40 TECU on the edge of the arc to 5 to 10 TECU at around 13:00 to 15:00 UT (Figure 94c). The IRI values appear to show less variation and are much closer in value to the truth, approximately 2 TECU. The final plot, Figure 94d, shows the sTECs for 20 June 2003. The EDAM values of sTEC now match the truth better. There are interesting sTEC values just after 15:00 UT where the EDAM values align better with IRI than the truth. This only lasts for a few points before it becomes more aligned with the truth sTEC values. This pattern over the 4 plots is similar to that for satellite 1.

The final satellite in this comparison, satellite 24, confirms what has been seen by satellite 1 and 13. Figures 95a-d show EDAM is performing very similar to the results presented for satellites 13 and 1. EDAM models the sTEC values well compared to the truth on 13 June 2003, performs much worse on 14 and 19 June 2003, and then finally models well again on the 20 June. There are differences between satellites 24, 1 and 13, for example in Figure 95b where there is much more variability and larger increases in sTEC for the EDAM sTECs compared to satellite 13 before 14:00 UT. Before 14:00 UT, the difference between the EDAM sTECs and RINEX sTECs on 14 June 2003 are approximately 60 TECU. It then decreases to about 20 TECU

at 13:00 UT. This is likely to be because the start time for this satellite to be in view of the receiver is between 12:00 and 13:00 UT while the other two satellite started before 12:00 UT. As for satellite 13 there is a moment where the differences between EDAM and the truth are small, such as just after 14:00 UT.

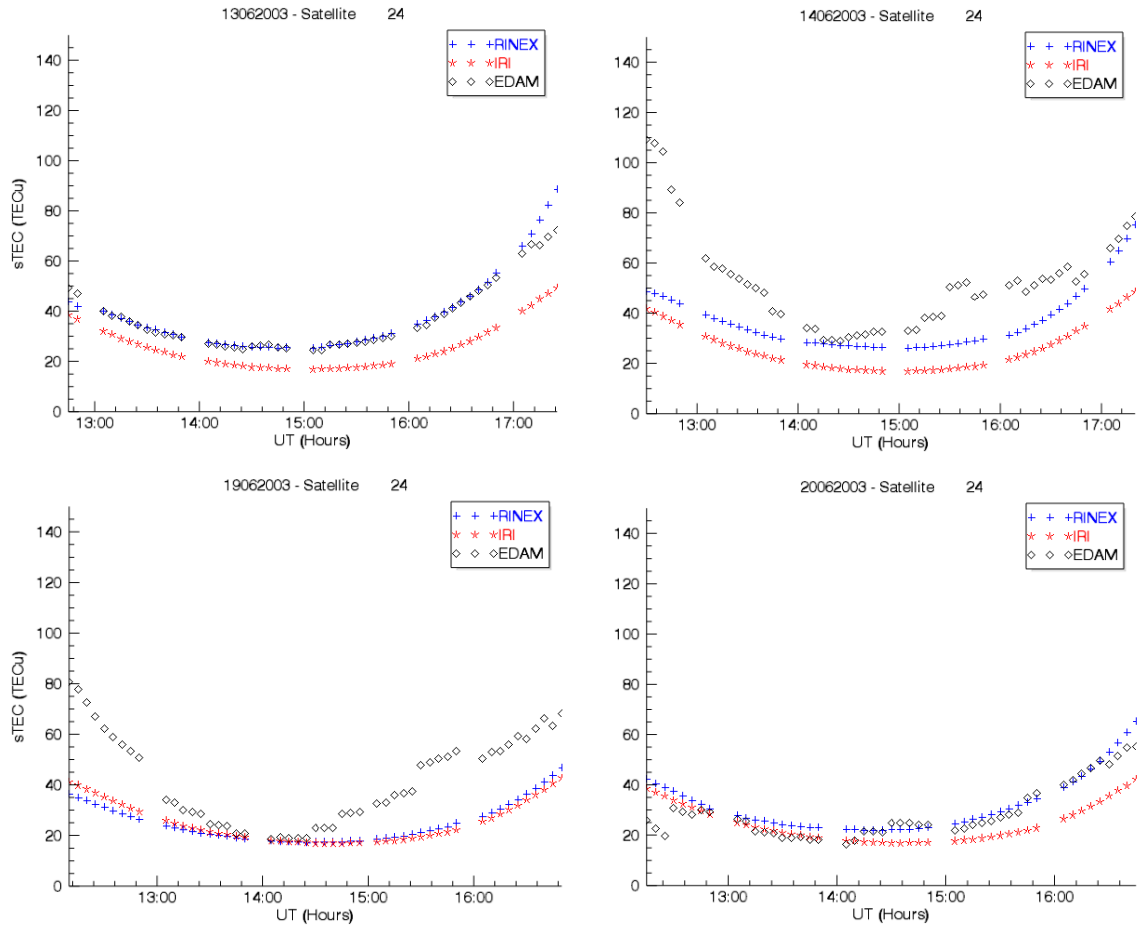

Figure 95 - Slant Total Electron content for satellite 24 on 13 June 2003 (a), 14 June 2003 (b), 19 June 2003 (c) and 20 June 2003 (d). A similar pattern emerges as was seen for satellites 1 and 13 in Figures 93 and 94 respectively, with the 13 June 2003 showing good performance by EDAM compared to the truth, 14 and 19 June showing EDAM sTEC values much larger than the truth, and the performance beginning to return to the usual performance on the 20 June.

This confirms that something is affecting EDAM when modelling the sTEC values in the region that the truth receiver, HERS, is observing. Having considered multiple satellites and analysed their performances, the time at which the poor performance occurs has been narrowed down to between 12:00 and 17:00 UT, with an improved performance at 14:00UT consistently for

all three satellites. With this information the next step was to look at other data sources to see if there were any external occurrences that could have caused the issues for the period 13 to 20 June.

8.3.4 Comparison using other data sources

The focus turned to these days in the middle of the month. More data was considered to help analyse the problems that were occurring. The first data source was the Kp indices, to consider global geomagnetic activity during the period.

Figure 96 shows the Kp indices for the 13 to 20 June 2003. It was noted in Chapter 7 that the Modified Taylor Diagram did not show a correlation between geomagnetic activity and the performance of EDAM. Constant variability in geomagnetic activity however would have an effect on the ionosphere, which could have an effect on the modelling performance.

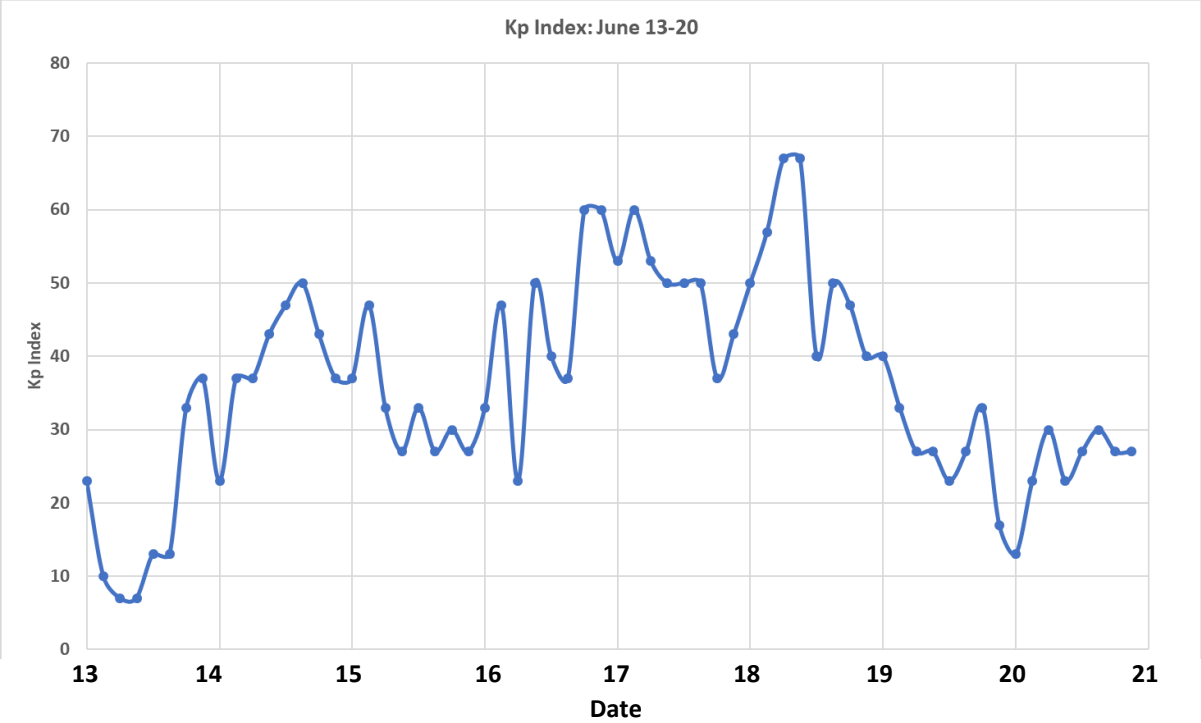

Figure 96 - The three-hourly Kp Indices between 13 and 20 June 2003 taken from UKSSDC with the Kp index values along the y-axis and the date along the x-axis.

On the 13 June, at the beginning of Figure 95, the Kp indices were relatively small lying between values of 7 and 23, which are 1- and 2+ as categorised previously in Chapter 5. This would relate to low Kp and therefore low levels of geomagnetic activity. Around the time of 14 June, the Kp indices rose to medium Kp levels, with values of 37 rising to a maximum value of 50 in the afternoon. There are fluctuations in the values of the Kp index for the next few days between 30 and 50. At the end of the 16 June the Kp rises to 60, classed as high Kp, before dropping in the afternoon of the 17 June. It then rises, from 37 Kp on the 17 June, to the maximum Kp value seen in this period of 67 on the 18 June in the morning. The Kp levels drop after this for the remaining two days until it remains at about 30 on 20 June. Whilst this does not explain the reason for the poor performance of EDAM, it gives an idea of some of the potential factors that could be considered. With the fluctuating levels of Kp and geomagnetic activity, it shows during this time the ionosphere was active and with the high

levels seen later in the period it was possible that a geomagnetic storm was in effect during this time period. Figure 97 shows the Dst indices for the same dates, 13 to 20 June 2003.

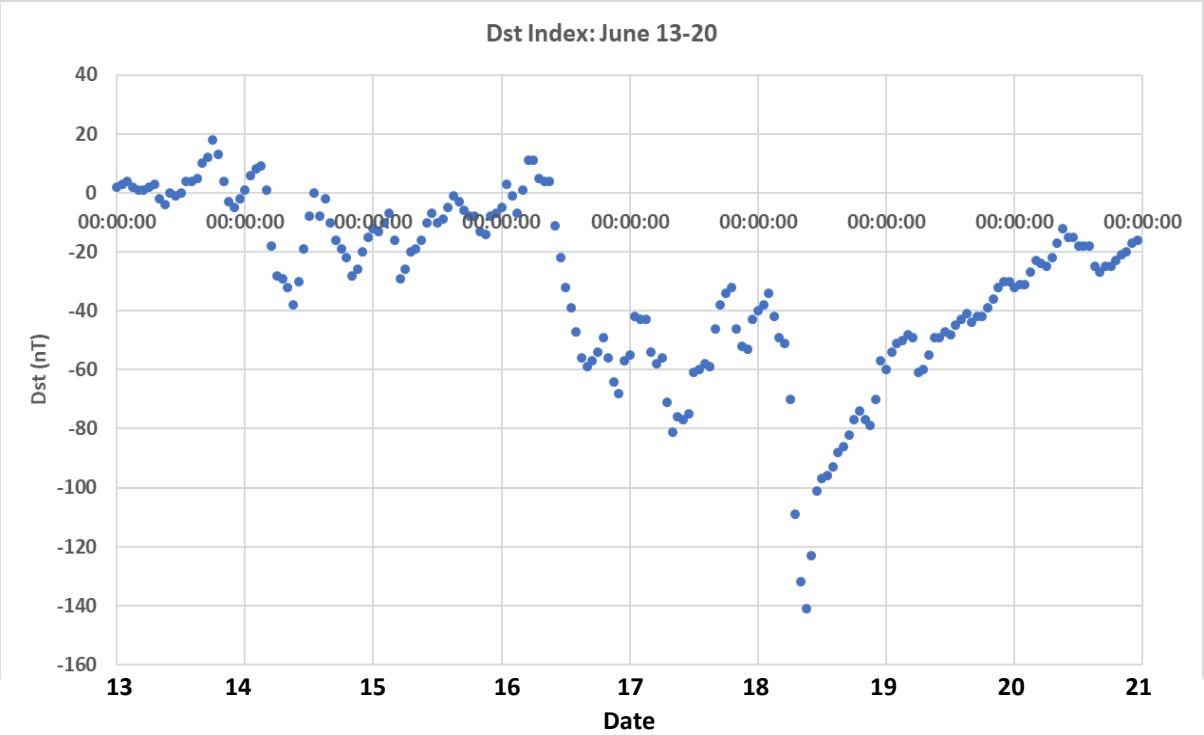

Figure 97 - The hourly Dst indices between 13 and 20 June 2003 taken from NOAA, with the dst plotted on the y-axis and the time on the x-axis.

Figure 97 shows that there is minimal disturbance in the Dst until the 16 June 2003. After this day the Dst starts to decrease to -60 nT, which stays through the 17 June 2003. On the 18 June 2003 the Dst reaches its lowest point of -140 nT during the morning before increasing gradually to -20 nT on the 20 June.

A cause of potential geomagnetic storms and ionospheric activity comes from the solar wind Thus, solar wind data were the next source that was looked at to help understand the current problem. Solar wind data from ACE gave the potential to see any variability in the interplanetary magnetic field along with ion velocity, density and temperatures in the solar wind. Figure 98 shows the plot of these variables.

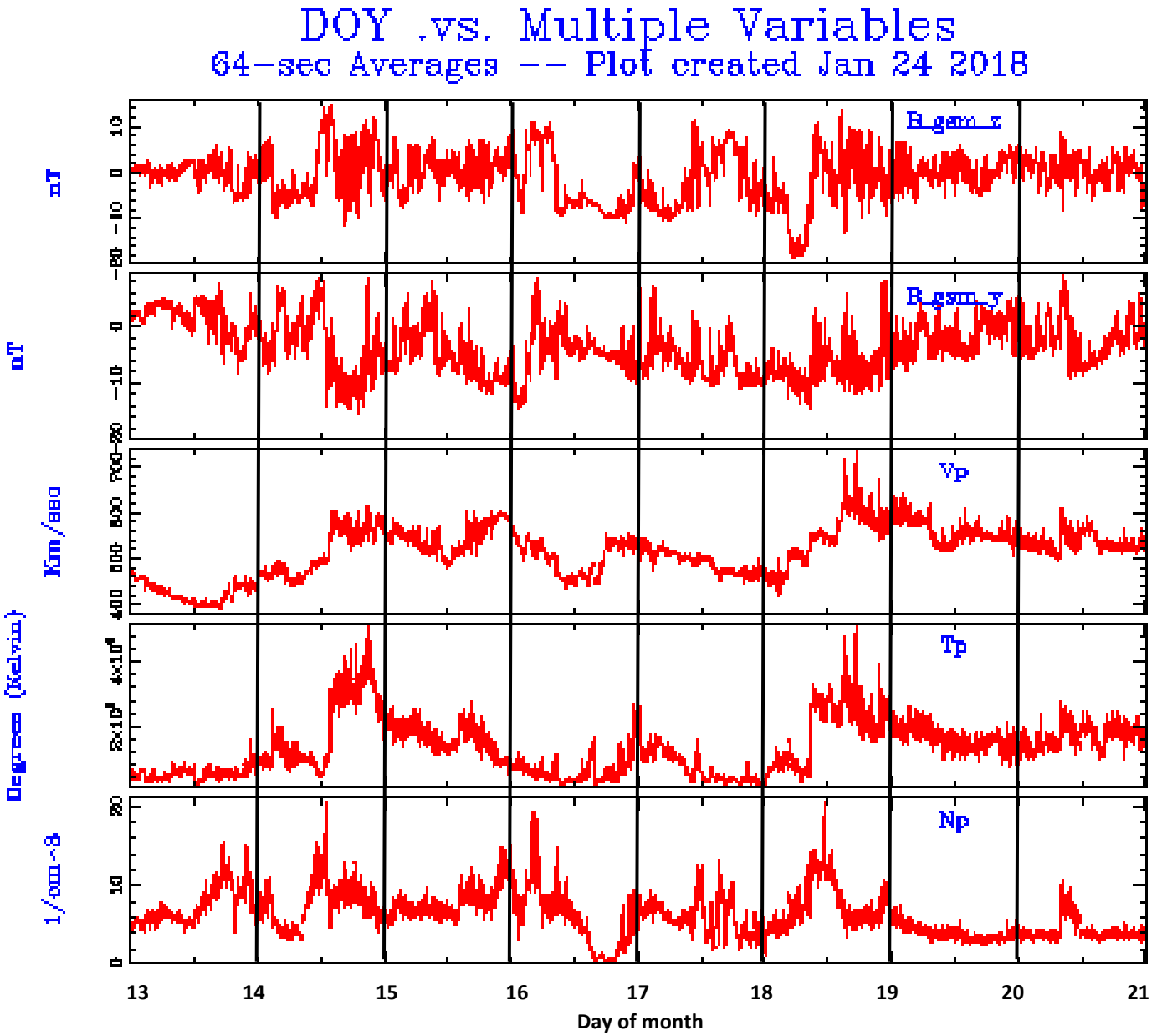

Figure 98 - Solar wind parameter and Magnetometer data plots using measurements from ACE instrumentation SWEPAM and MAG using http://www.srl.caltech.edu. The x axis shows the days in question from day 164 converted as 13 June to the end of day 171 or 20 June. Each day is marked by a black line. There is variability in the ion density, temperature and velocity in this time period while also experiencing major shifts in the direction of the magnetic field z and y components.

On 13 June 2003 the solar wind shows little fluctuation in the velocity, temperature and density of the ions and the interplanetary magnetic field components B_z and B_y. It was around midday on the 14 June, when fluctuation occurs in the solar wind. The density of the ions shows a population increase by over 10 cm^{-3}, and a temperature rise of over $2x10^5$ K. The

velocity of the ions increases by almost 200 kms^{-1} while magnetic field changes are also observed, with B_y turning negative and B_z turning positive. At the end of the 14 June the parameters return to the values prior to the fluctuations, with exception to the velocity which remains at 550 kms^{-1}. Another fluctuation in the solar wind and magnetic field occurs on the 18 June, day number 169. After a period of the negative B_z there is a sharp transition to where the component becomes neutral, and accompanying this is a sharp increase in velocity, to roughly 600 kms^{-1}, temperature, to approximately $3x10^5$ K, and density of the ions, to a maximum of 20 cm^{-3}. These events are not a definitive reason for the EDAM to underperform but it does show there were fluctuations in the solar wind and interplanetary magnetic field between 13 to 20 June 2003. These correspond to the fluctuations observed in the Dst index, Figure 97, and the changes in the Kp index, in Figure 96.

The next step was to consider the EDAM VTEC and electron density map. They were of the same grid as described in Chapters 5 and 6. The VTEC map gives the modelled EDAM values, between -20° to 40° longitude and 45° to 70° latitude. The electron density maps show the maximum electron density and the height of this density. Caution is needed in the interpretation of the heights of the maximum density as previously explained in Chapter 6, as no ionosonde observations were included in the assimilation. Figure 99 shows the VTEC map and Figure 100 shows the electron density maps and corresponding heights for 14 June 2003 at 13:45 UT.

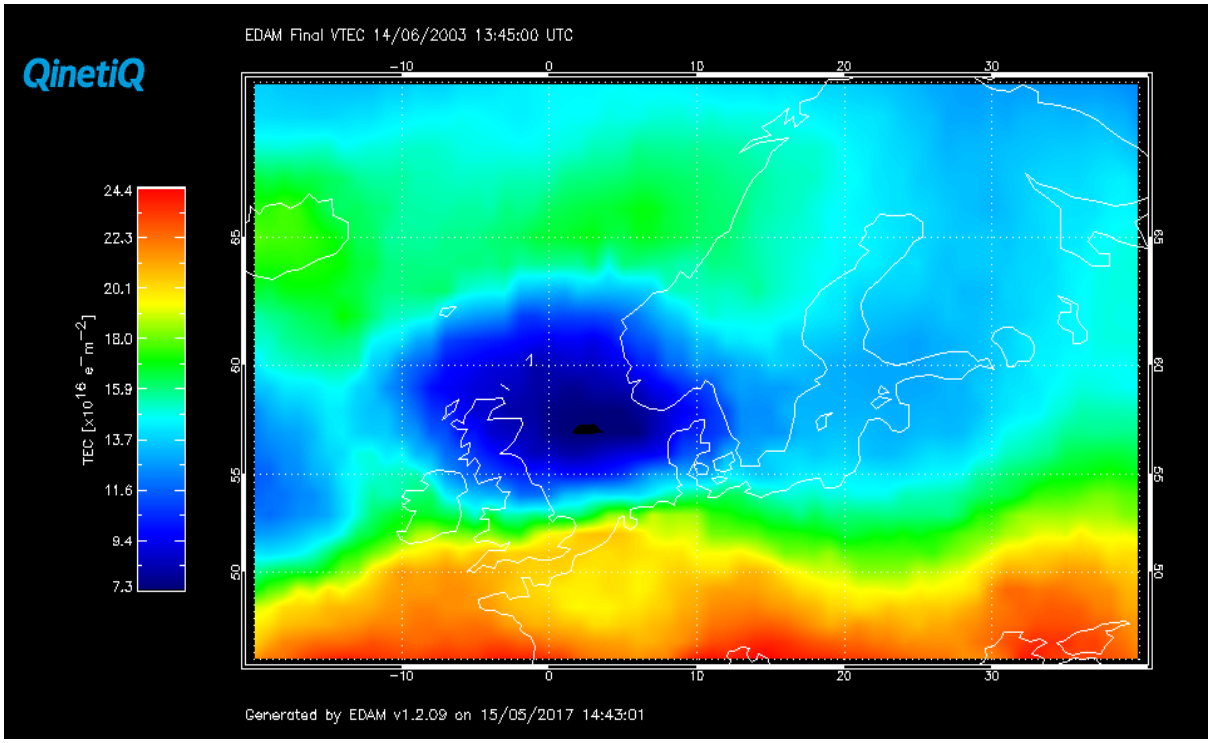

Figure 99 – The EDAM VTEC map for 14 June 2003 at 13:45 UT. Centred around 2-3° longitude and at 57° latitude, there is a sharp decrease in TEC compared to the surroundings but is not relevant to this study.

This EDAM VTEC map, Figure 99, is a representative of the model on the days 14 and 19 June 2003 and modelled at times between midday and 17:00 UT. GPS Satellites reach a peak orbital latitude of roughly 56°N; examples are shown in Appendix C for different dates of the year and for different satellites. With the location of the HERS receiver at 50.9°N and 0.3°E, the ray paths are more likely to intersect the ionosphere at an altitude of 1000 km at roughly 52°-53°N latitude. The depletion shown in Figure 99 does not affect the ray paths and is at the wrong location to affect the sTECs observed in figures 93-95.

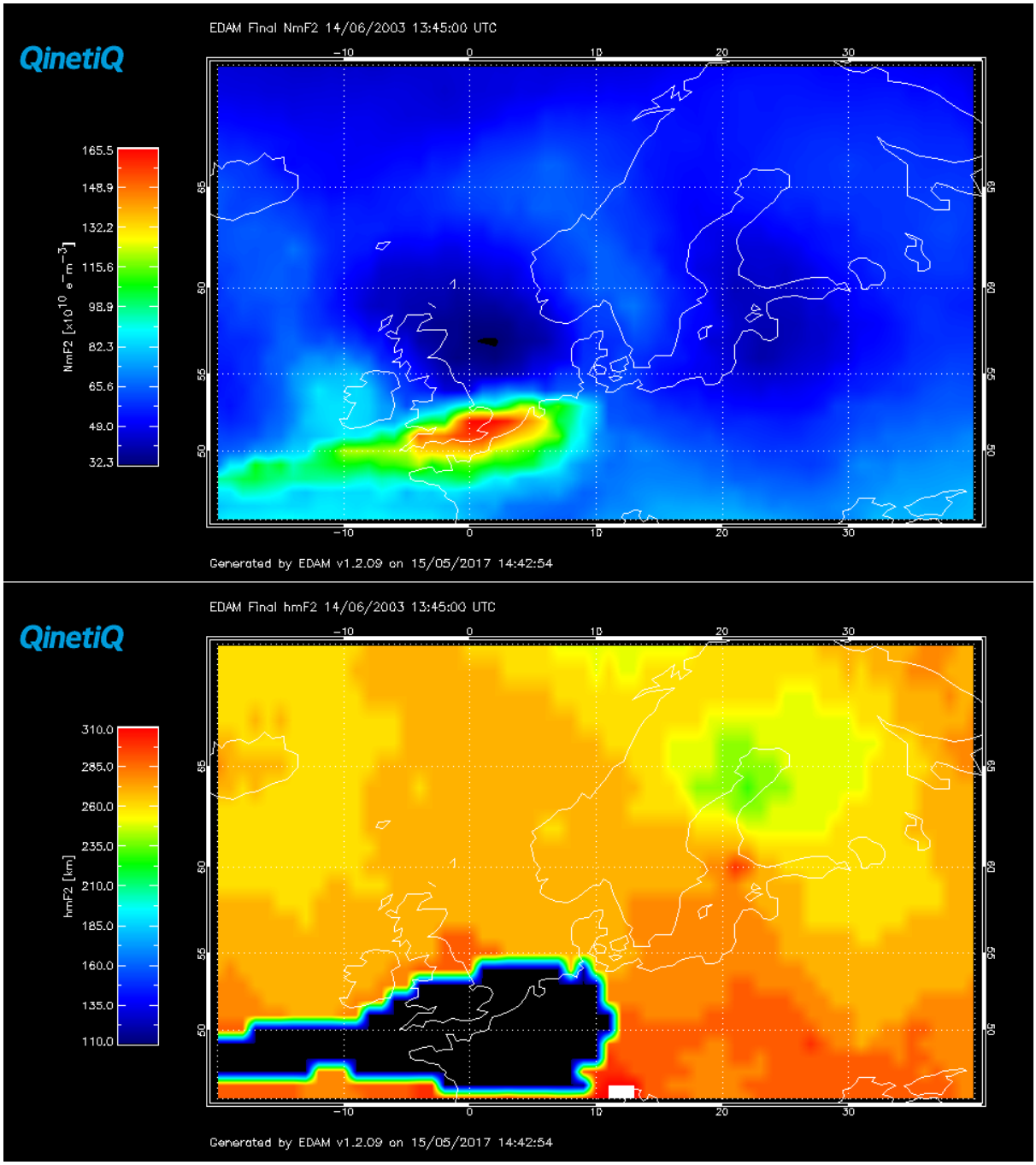

Figure 100 - (a) EDAM map of maximum electron densities and (b) map of the heights of the maximum electron density in (a). The map of maximum electron density shows a very intense region where the electron density is large on the southern edge of the UK. This would be considered the peak density for the F2 region as the electron density maps show NmF2 and hmF2. However, looking at the height map, (b), the height of this value corresponds to 110 km. These are heights normally associated with the E-region.

Figure 100 shows the maximum electron density, where the region that is causing the underperformance of EDAM becomes clearer. Figure 100a shows a maximum electron density value in the southern UK, a value of $165x10^{10}$ e^{-} m^{-3}. This would usually be considered for the peak of the F2-region. However, the height map, Figure 100b, shows the height of this value to be 110 km. This is the height of the E-region. This density is unusually large for the E-region, except for a phenomenon known as Sporadic E. Due to the receiver being at the same location of these large densities and low altitudes and, using Figures 93b, 94b and 95b, the ray paths at these times from these satellites to the HERS receiver would have intersected this region of high density.

Sporadic E was discussed in Section 2.6.2 with an example of the characteristics of sporadic E in Figure 11. Ionograms from the Chilton ionosonde, 51.70°N, 1.23°W, were considered between 13 to 20 June to verify if Sporadic E at the time of the EDAM modelled observations.

An example ionogram at 11:00 UT on 17 June 2003 is given in Figure 101. This shows that Sporadic E during the time period provided evidence that EDAM could be modelling this phenomenon.

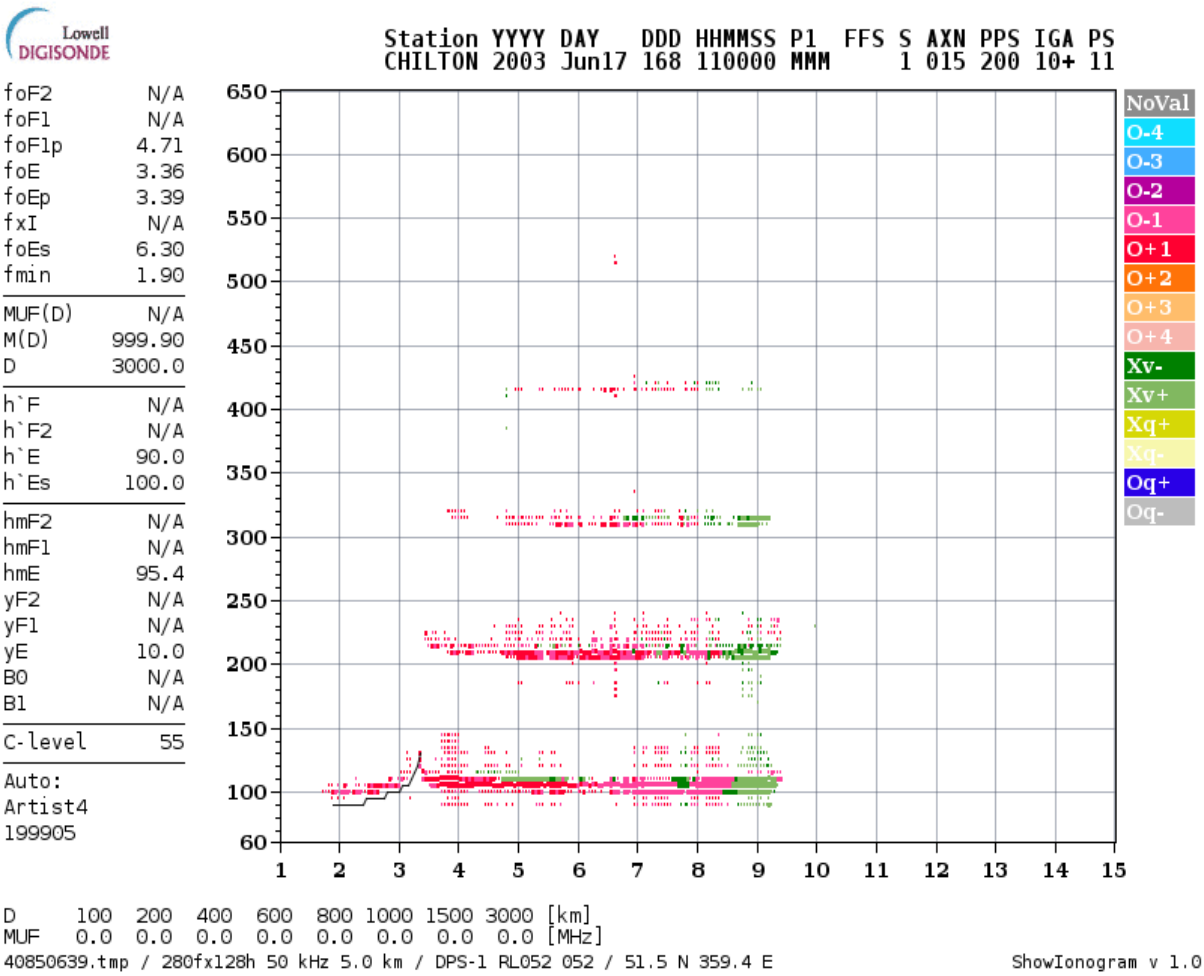

Figure 101 - Chilton Ionosonde ionogram from Lowell Digisonde International website on June 17, 2003 at 11:00 UT. foEs, the critical frequency of the sporadic E layer, is larger than the N/A foF2 value.

The maximum frequency observed on the ionogram and corresponding virtual height value for each ionogram, at 30-minute intervals between 13 and 20 June 2003 were considered. The same was done for EDAM, but for every 15 minutes. In this case the maximum electron density value of the vertical profiles was conducted, at the approximate location of Chilton ionosonde, 51.00°N, 1.00°W. The density was then converted to frequency for easier comparison with the ionosonde (Section 4.3).

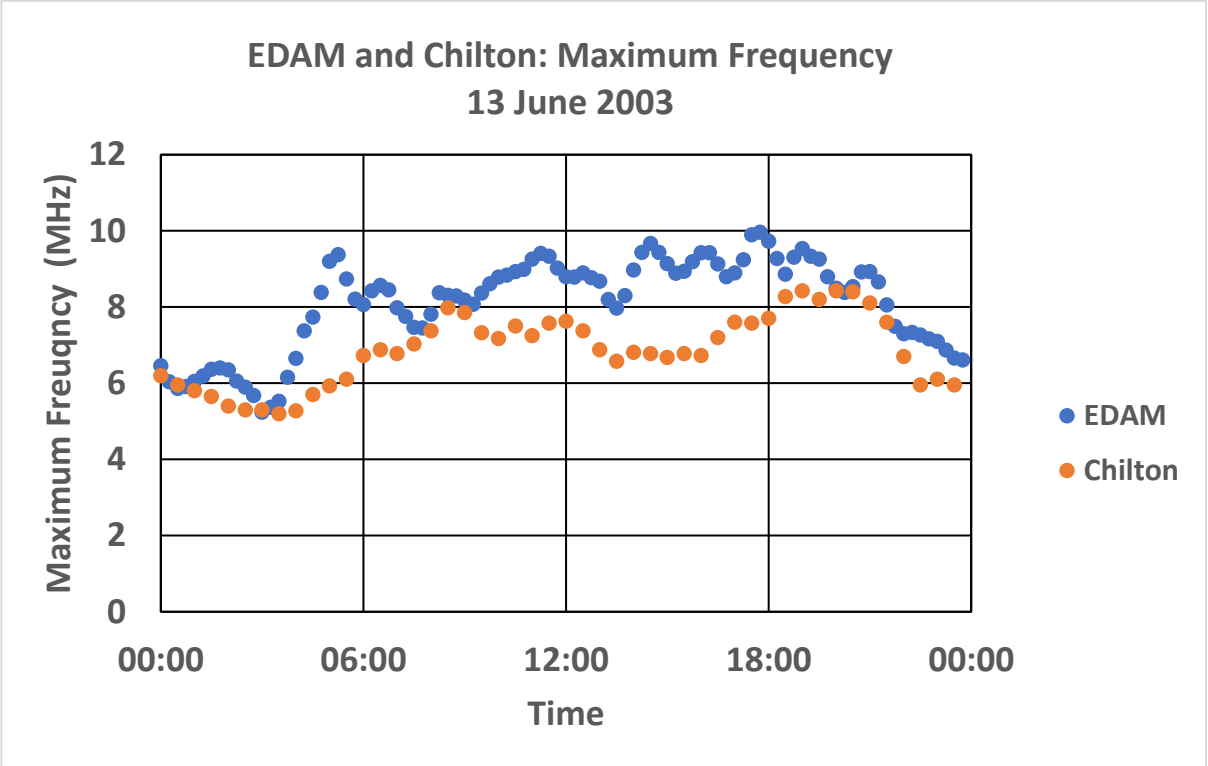

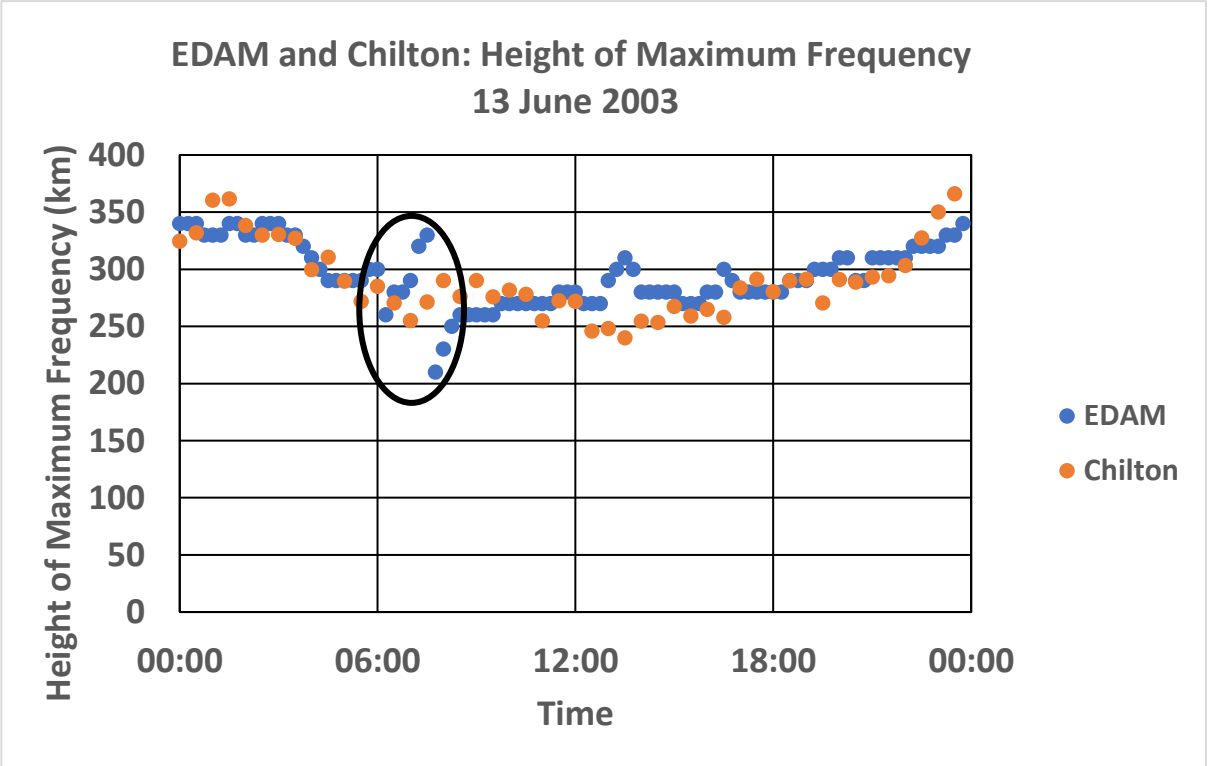

Figure 102 – Comparisons of maximum frequency (top) and height of the maximum frequency (bottom) between EDAM and Chilton ionosonde for the 13 June 2003. There are differences between the maximum frequency value. EDAM is performing within 5-20 Km with Chilton ionosonde in finding the correct location of the maximum frequency. There is no evidence of Sporadic E in this Figure.

Figure 102 shows the comparison of maximum frequency (top panel) and the height of that maximum frequency (bottom panel) between the converted electron density from EDAM, example plot in Figure 100, and the Chilton ionosonde for the 13 June 2003. This is the day before EDAM started to underperform. The maximum frequency obtained for EDAM is compared to the maximum frequency observed at the Chilton ionosonde. The general trend measured by the ionosonde is modelled by EDAM but with generally larger frequencies, by approximately 2 MHz.

The heights corresponding to the maximum frequency (bottom panel) from EDAM are similar to those from the ionosonde, with height values between 250 km and 350 km. A peculiarity is identified post 06:00 UT (black oval) where the EDAM height rises from 250 km to just below 350 km at 07:30 UT, where it then drops to 210 km. This drop of over 100 km was not observed by the ionosonde. The EDAM height then begins to increase, to approximately 250 km where it becomes closer to the ionosonde once again.

In general, this gives confidence in the ability to compare the maximum frequency converted from the electron density of EDAM and the height corresponding to this frequency with the observations from the Chilton ionosonde.

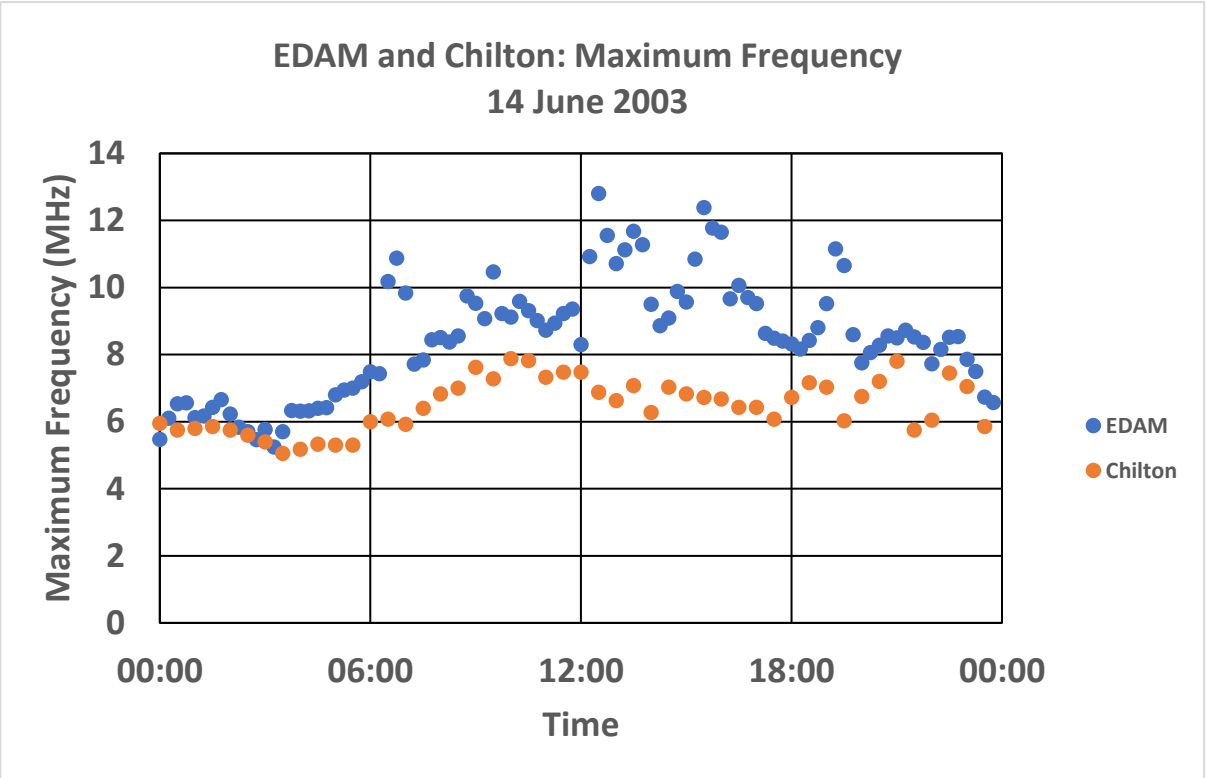

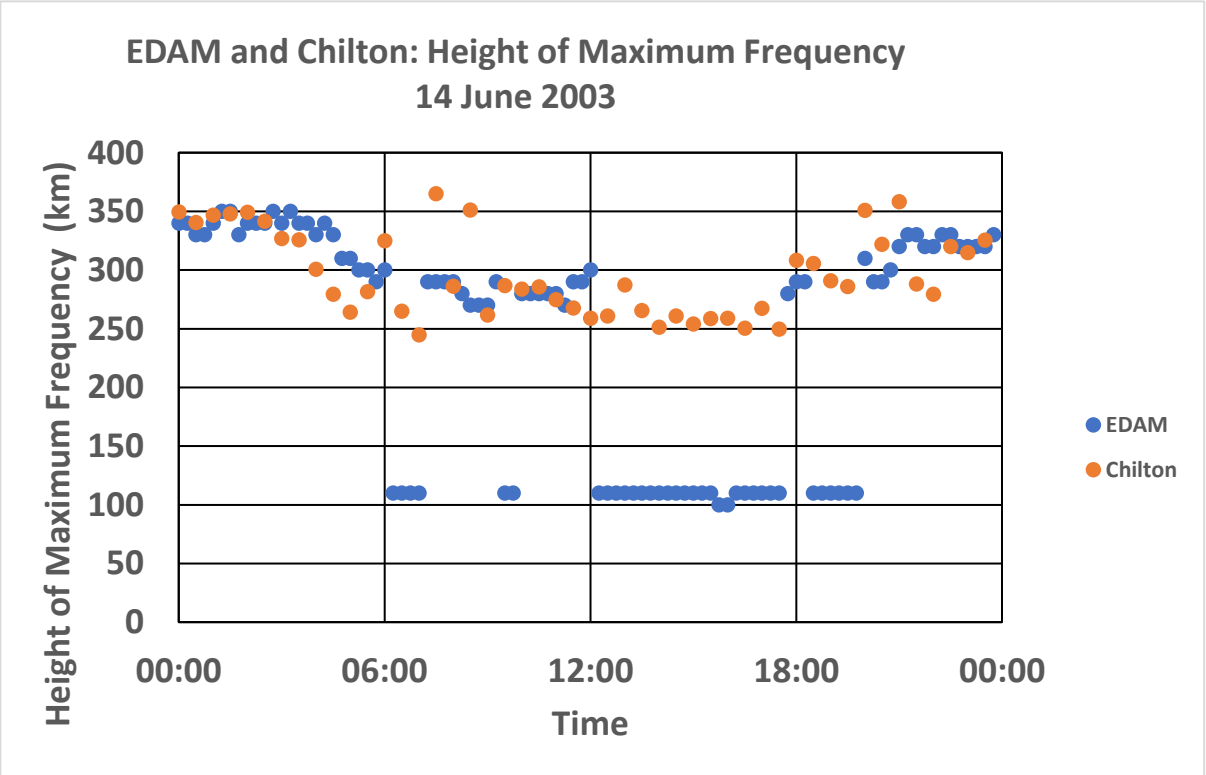

Figure 103 – Comparisons of maximum frequency (top) and height of the maximum frequency (bottom) between EDAM and Chilton ionosonde for the 14 June 2003. The differences in frequency are largely during the morning and daytime. There are now significant differences between the heights of the frequency with EDAM showing heights at E-region altitudes, values of 110 km, while the Chilton ionosonde did not observe this.

The maximum frequencies from the electron densities modelled by EDAM and those observed by the Chilton ionosonde for the 14 June 2003 are shown in Figure 103. A similar pattern to those of the previous day is observed in that EDAM has modelled electron densities that converted to larger frequencies than those observed by the ionosonde. Some of the EDAM values exceed 12 MHz, just after 12:00 UT, which is almost double the frequencies observed by the ionosonde. There is also a discrepancy in the heights of the maximum frequency coinciding with the large differences in the frequencies. The heights given by EDAM are at approximately 100 km. The heights remain at approximately 250 km to 350 km for the ionosonde. This doesn't provide evidence for sporadic E being present on this day and raises questions on what is causing the large electron densities modelled by EDAM and the corresponding low altitude.

On the 15 June 2003 (Figure 104) EDAM exhibits variability in the maximum frequency during daytime where the values show a zig-zag nature of increasing and decreasing between approximately 6 and 12 MHz every couple of hours between 06:00 and 18:00 UT. This is not observed in the ionosonde data. The heights from EDAM, during the day, are now predominately around 100 km altitudes, which corresponds to the variability in the maximum frequency. There is also variability in heights observed by the Chilton ionosonde. During the day some heights decrease to values around 200 km with one point reaching a low of 110 km to match with EDAM. There are more points at this altitude occurring later in the day, at around 18:00 UT.

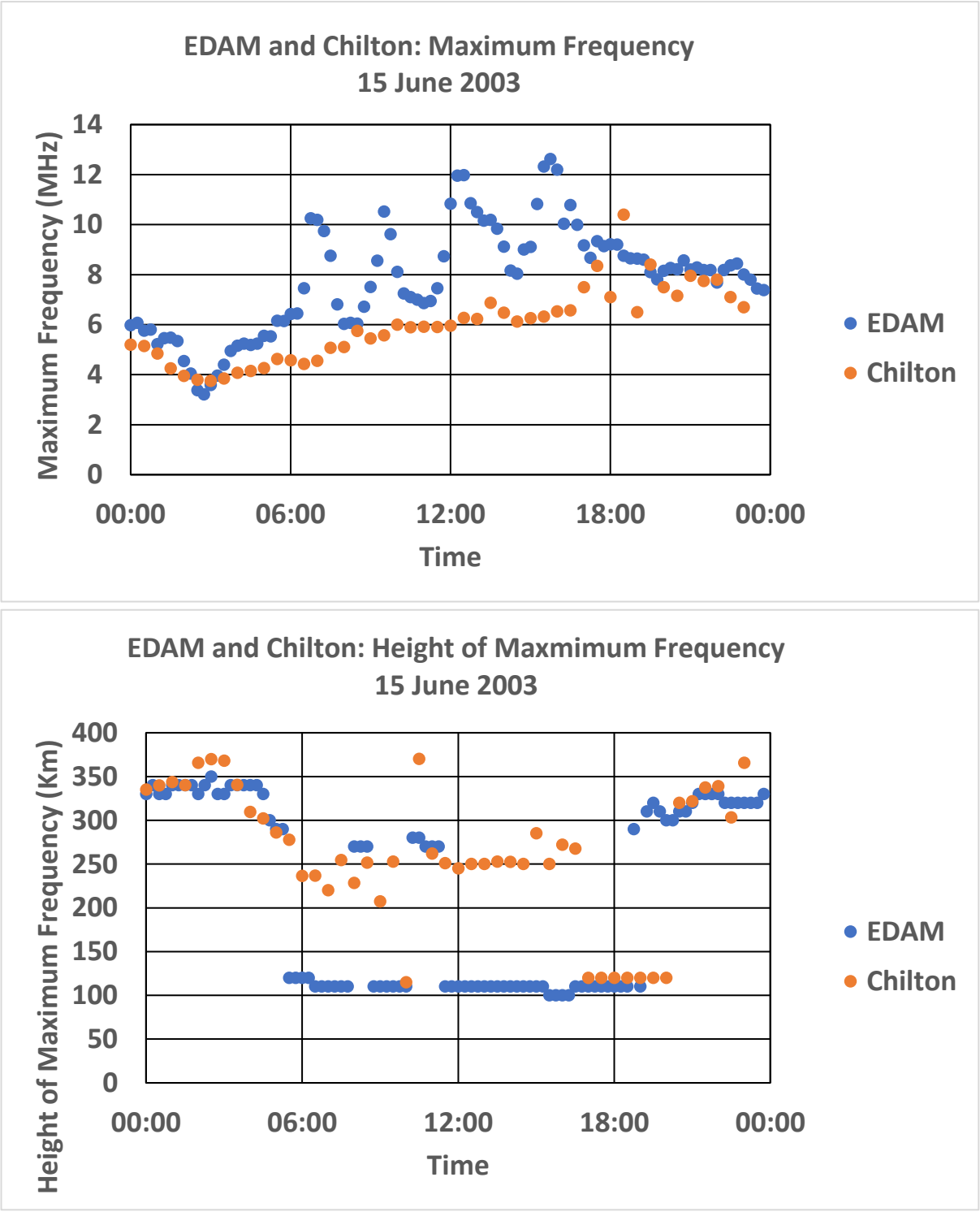

Figure 104 – Comparisons of maximum frequency (top) and height of the maximum frequency (bottom) between EDAM and Chilton ionosonde for the 15 June 2003. Variability is observed during the day in the EDAM maximum frequency series. This is not observed in the ionosonde data. EDAM is modelling the heights of the frequency at approximately 110 km. This is also observed by the Chilton ionosonde at approximately 18:00 UT.

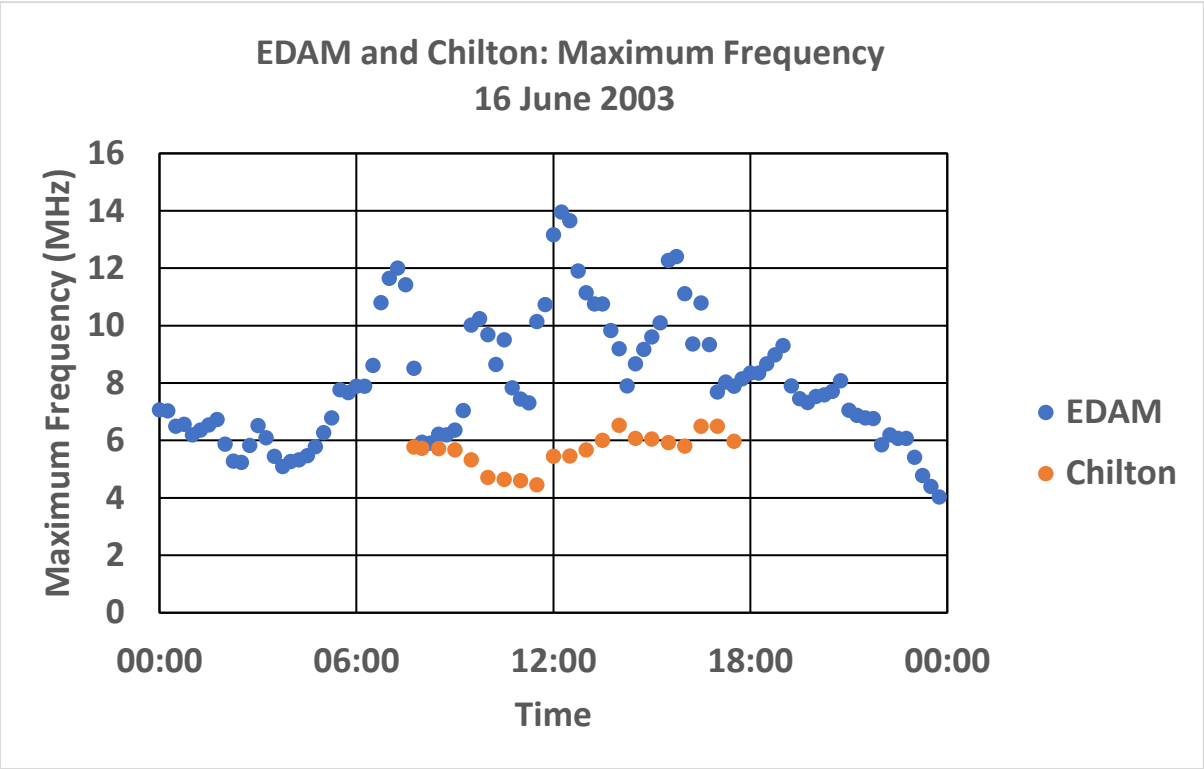

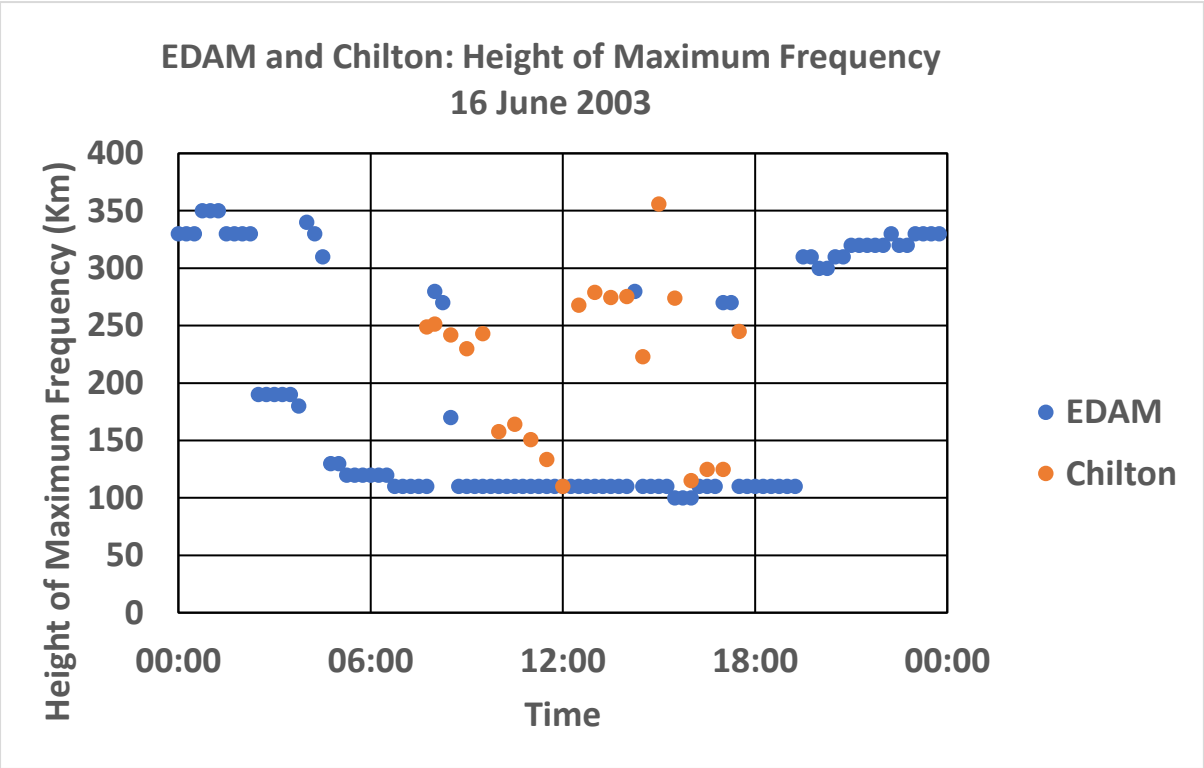

Figure 105 – Comparisons of maximum frequency (top) and height of the maximum frequency (bottom) between EDAM and Chilton ionosonde for the 16 June 2003. There is a lack of observations from the ionosonde in both the morning and evening sector. The variability observed in the EDAM series of maximum frequency is still present and again it is not observed by the ionosonde. The heights modelled by EDAM are again at approximately 110 km throughout the day, with some observations from the ionosonde also reaching these lower altitudes during similar times.

On the 16 June 2003 (Figure 105) there is a lack of ionosonde observations in both the morning and evening sectors. The comparison however is focussed around 12:00 UT. The variability modelled by EDAM is present on this day. The frequencies converted from the EDAM modelled electron densities are double those from the ionosonde. In the bottom panel of Figure 105, the heights modelled by EDAM are mostly around 110 km throughout the day. The Chilton ionosonde does not observe all frequencies values at this altitude but there are points around 110 km and 150 km during the day which compare better with EDAM.

17 June 2003 is the day where high Kp indices were prevalent (Figure 96) and the Dst index started showing fluctuations to between -60 nT and -80 nT (Figure 97) which provide evidence for high geomagnetic activity. Figure 106 shows that the maximum frequencies of the ionosonde are mostly around 5MHz. There are still large differences between EDAM and ionosonde maximum frequencies, with the values from EDAM varying between 7 MHz and 12 MHz. EDAM heights are generally at approximately 110 km. On this day many of the heights observed by the Chilton ionosonde are at approximately 110 km, matching with EDAM. This is the strongest evidence of Sporadic E being present and evidence of EDAM correctly modelling Sporadic E during this day.

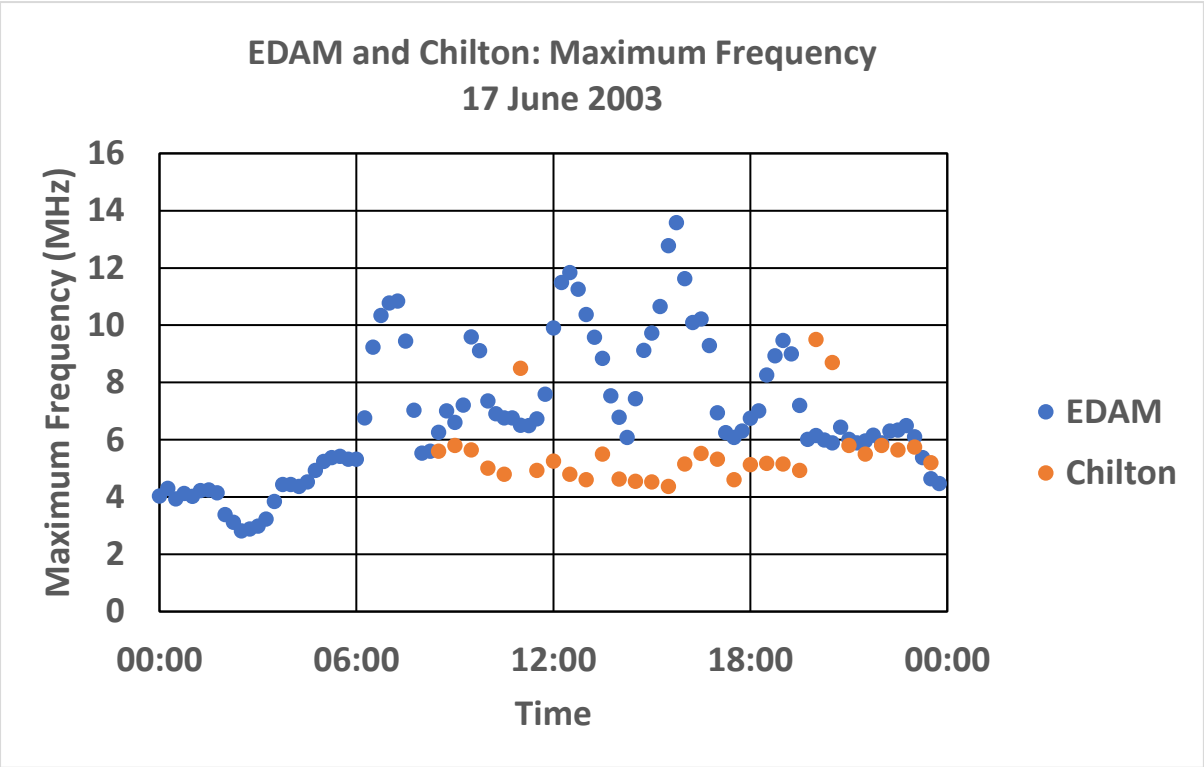

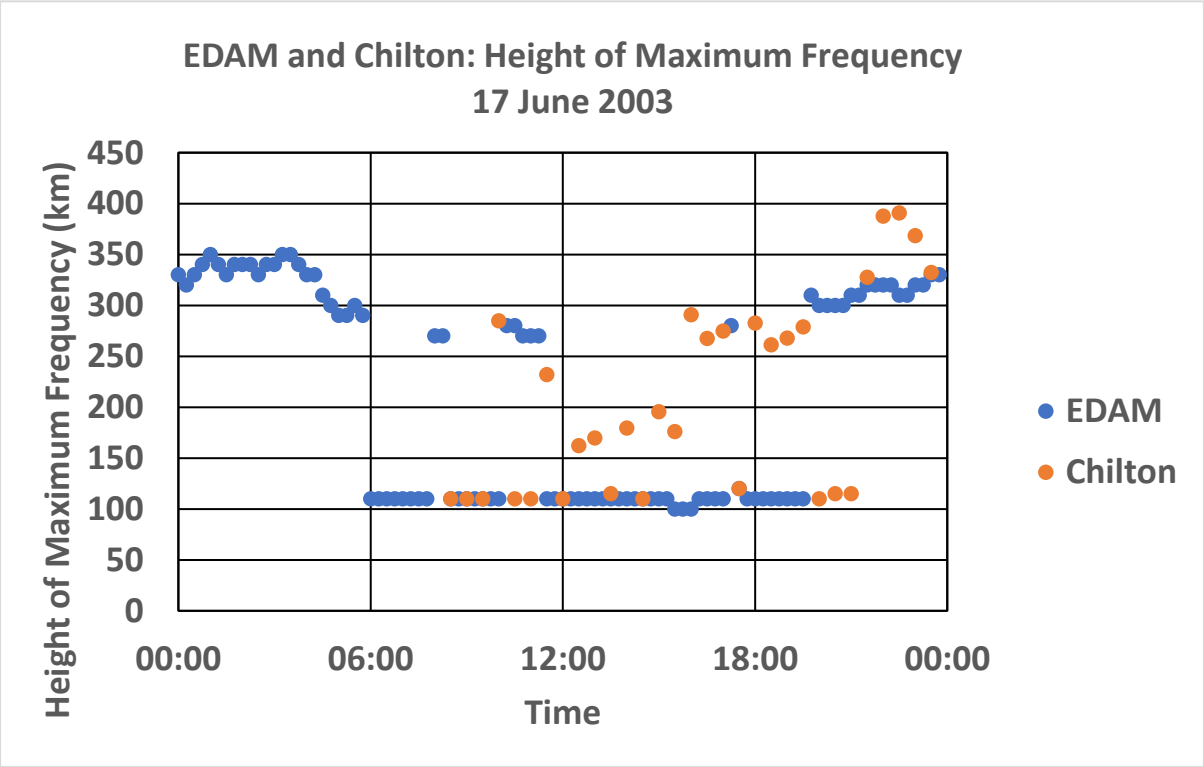

Figure 106 – Comparisons of maximum frequency (top) and height of the maximum frequency (bottom) between EDAM and Chilton ionosonde for the 17 June 2003. The maximum frequency plot is consistent with what was observed for the two previous days. There is a substantial change in the height of the maximum frequency where the Chilton ionosonde has observed a lot more heights of maximum frequency at 110 km altitude. This is the first time there is a large number of data points observed by the ionosonde at the altitude of Sporadic E.

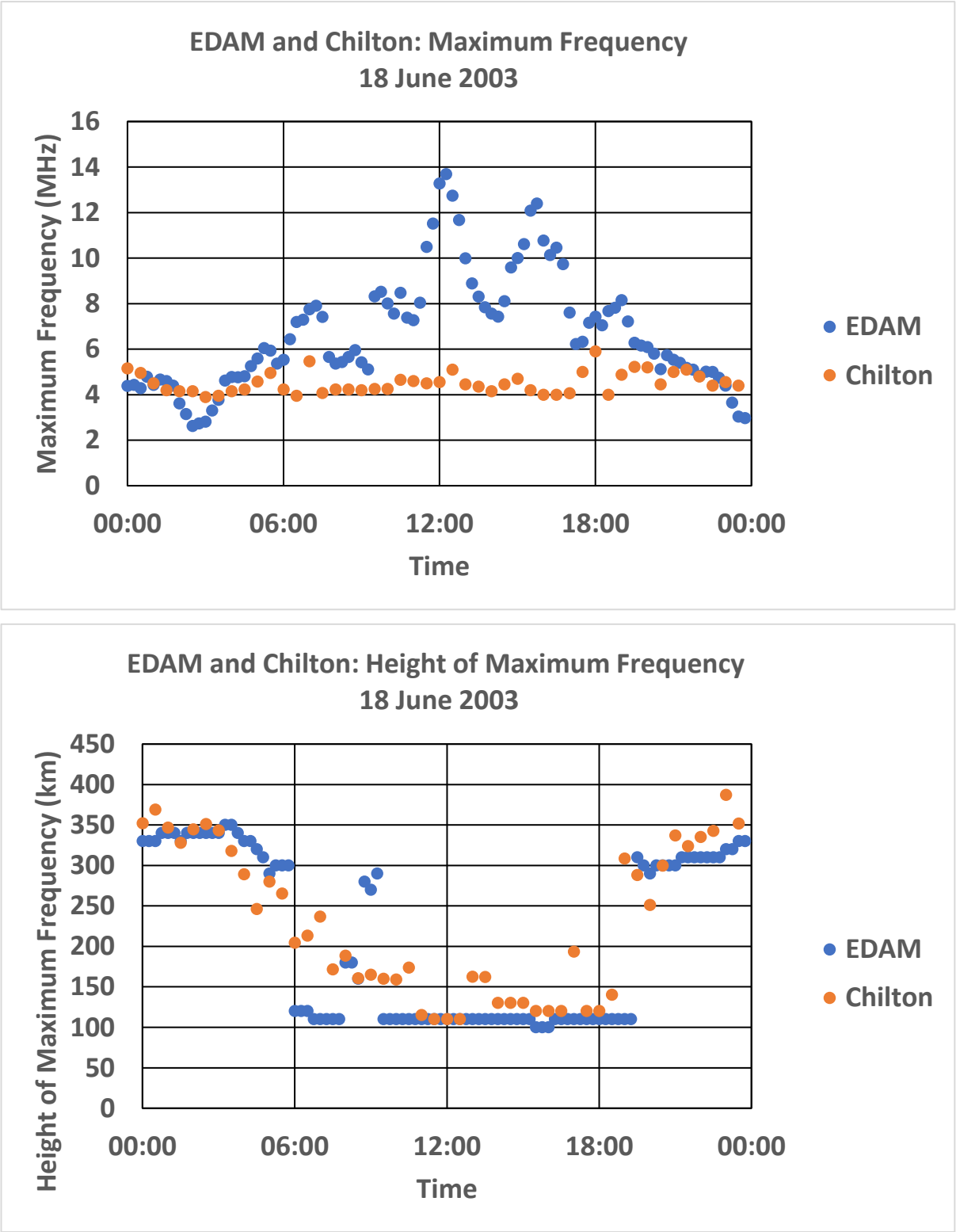

Figure 107 – Comparisons of maximum frequency (top) and height of the maximum frequency (bottom) between EDAM and Chilton ionosonde for the 18 June 2003. There is decrease in the maximum frequency observed by the Chilton ionosonde, with values now closer to 4 MHz. The variability seen in the previous days of the EDAM series is still evident. Like the previous day there are a number of observed maximum frequencies at heights of around 110 km.

Figure 107 shows the comparisons for the 18 June. This is the day when the geomagnetic activity is at its strongest between 13 and 20 June 2003 (Figures 92 and 93). The maximum frequencies shown in the EDAM series show the variability. The observed maximum frequencies at the ionosonde are slightly lower across the whole day, now at roughly 4 MHz, and are not very variable. The height of the maximum frequencies shows similarities to the previous day where the ionosonde observed most of the maximum frequencies at lower altitudes, roughly around 110 km which agrees with some of the modelled heights from EDAM.

19 June 2003 begins the period where the levels of geomagnetic activity begin to decrease. In Figure 108, the frequencies from the Chilton ionosonde show a steady increase throughout the day, from 4 MHz to 6 MHz. It is different in the EDAM series, where the zig-zag pattern is still prevalent, with maximum frequencies reaching 14 MHz. The heights of the maximum frequencies remain at about 110 km. The ionosonde observed low altitudes early on in the day, around dawn, where EDAM has not modelled these low heights. In the afternoon, there were still low altitudes observed by the ionosonde until approximately after 15:00 UT. There was an anomalous point observed by the ionosonde, around 15:00 UT, at heights around 400-450 km, which has not previously been seen in the study.

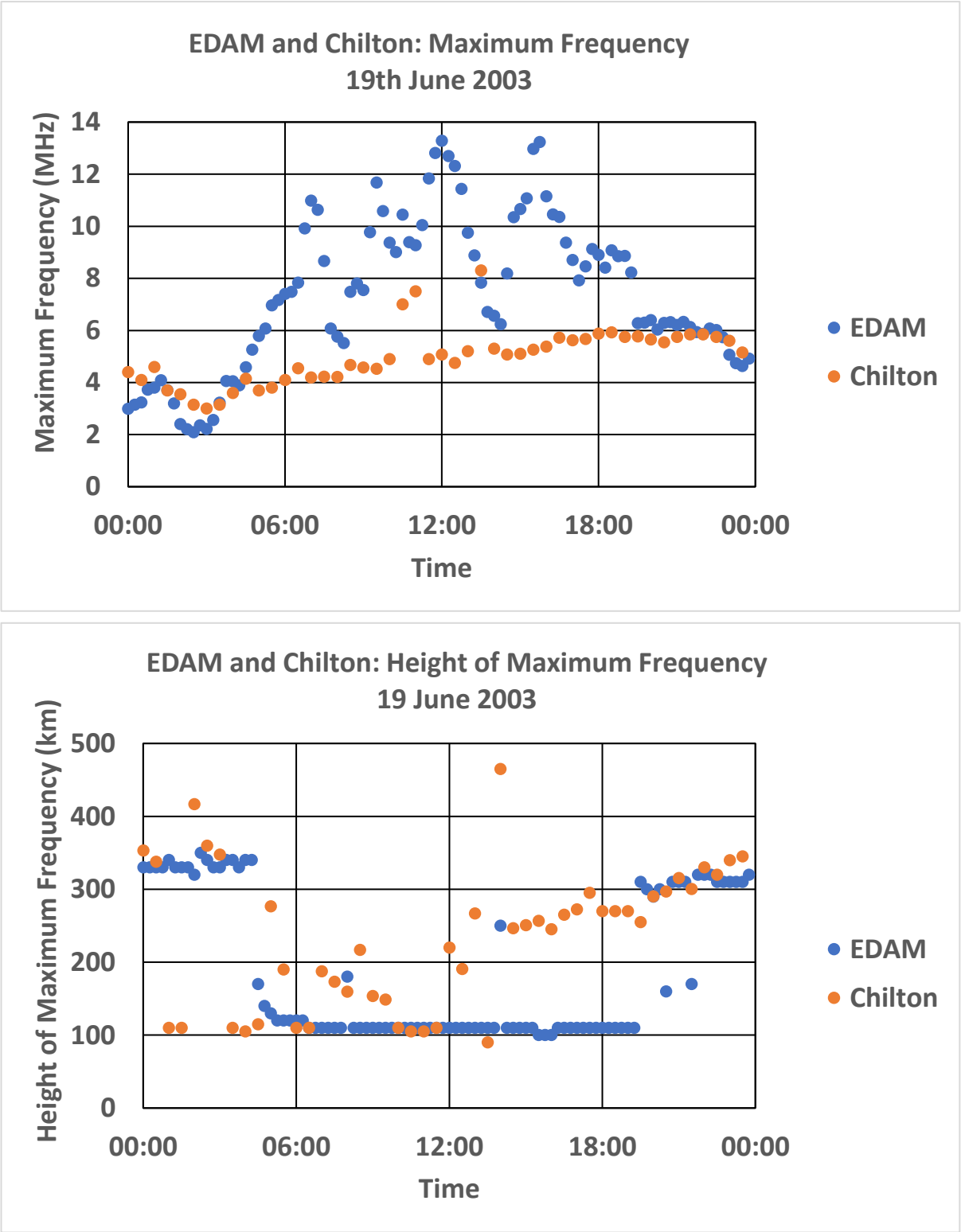

Figure 108 – Comparisons of maximum frequency (top) and height of the maximum frequency (bottom) between EDAM and Chilton ionosonde for the 19 June 2003. The maximum frequencies observed by the ionosonde show a steady increase throughout the day, from 4 MHz to 6 MHz. The height of the frequencies observed by the ionosonde were at roughly 110 km, between approximately 04:00 UT to 06:00 UT. This is earlier than previously observed, but there were heights observed at this altitude until 15:00UT. EDAM is similar to the previous day except for larger maximum frequencies.

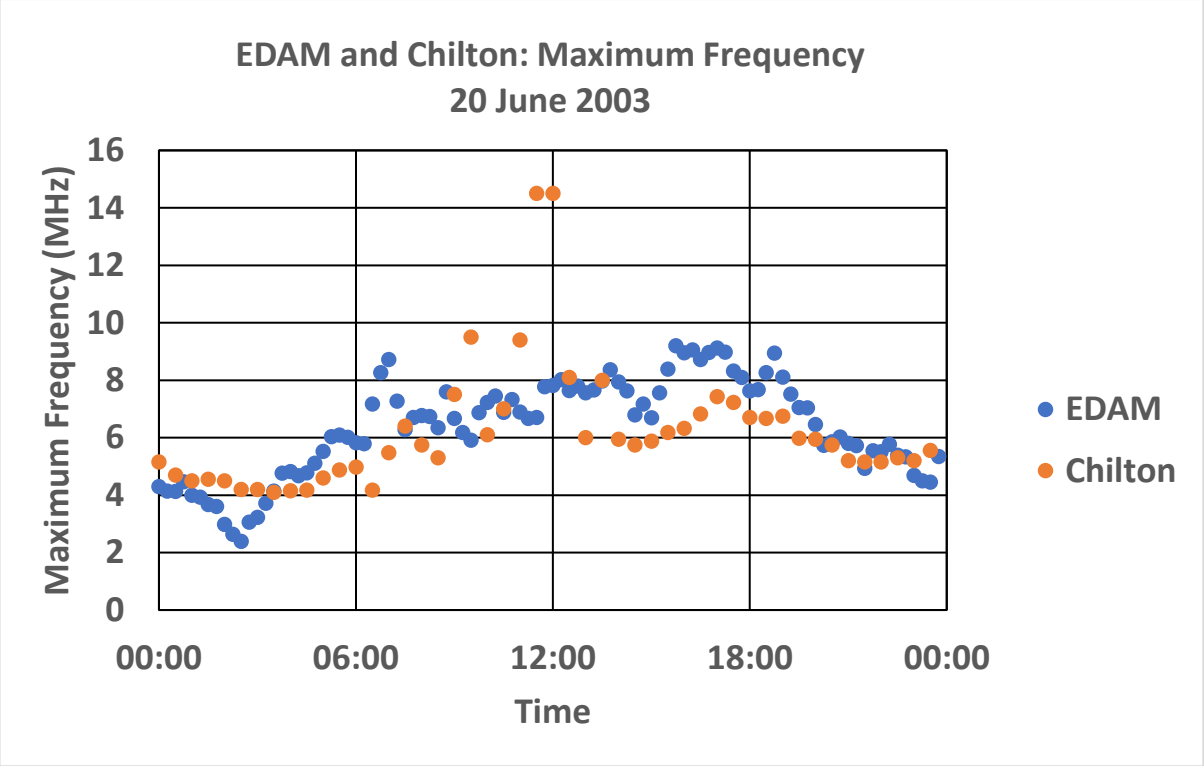

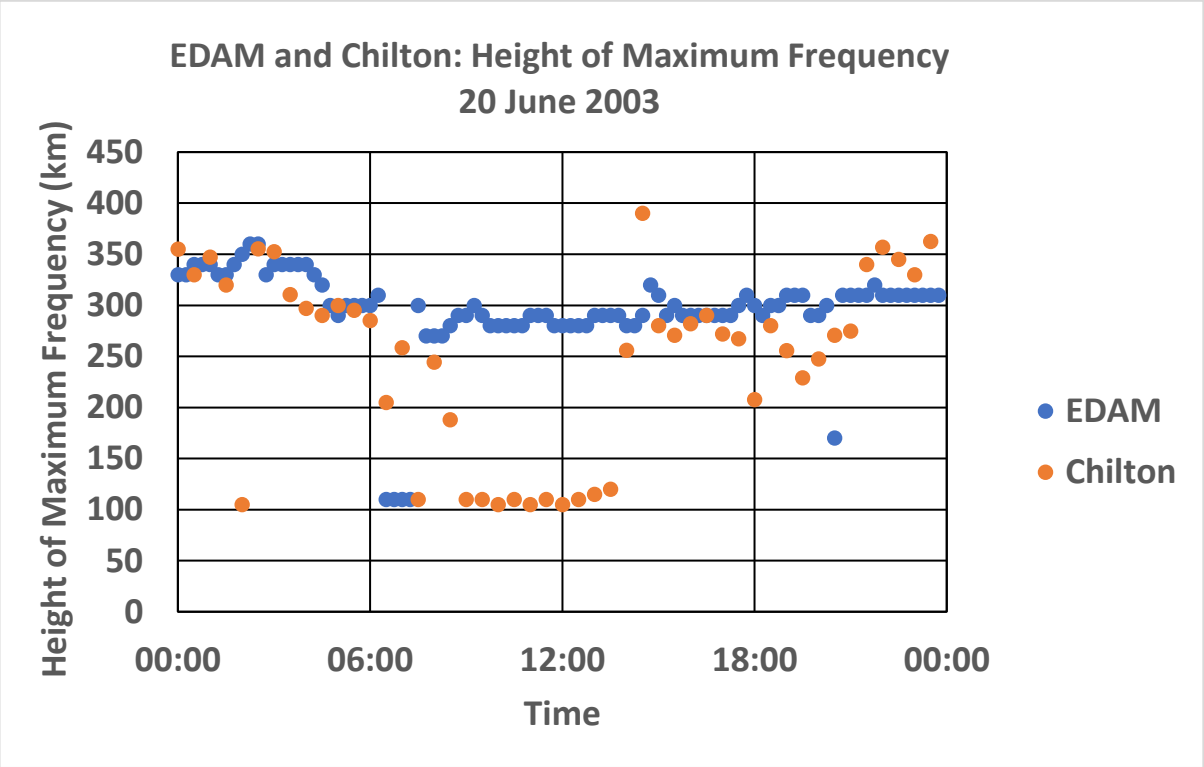

Figure 109 – Comparisons of maximum frequency (top) and height of the maximum frequency (bottom) between EDAM and Chilton ionosonde for the 20 June 2003. The maximum frequencies in the EDAM series have decreased substantially, now around 6-8 MHz, and the variability that was present in the last few days is no longer there. There is now agreement between the ionosonde observations and EDAM for most of this day in maximum frequency. There are two points, observed by the ionosonde, that are outliers at approximately 15 MHz. The heights of the maximum frequencies modelled by EDAM have increased to approximately 300 km with a few points after 06:00 UT at 110 km. This is not in agreement with the ionosonde observations with frequencies observed at approximately 110 km from 07:30 UT to 13:30 UT.

The final day of this comparison, 20 June 2003, is shown in Figure 109. The maximum frequencies converted from the EDAM electron densities have decreased in values, to between 6 MHz and 8 MHz, and compare well with the ionosonde observations throughout the day. There are two outliers in the ionosonde observations of maximum frequency around midday at values of 15 MHz, electron density values of approximately $2.8x10^{12}$ m^{-3}. There is also good agreement in the height of the maximum frequencies in the morning and evening sector. However, while EDAM has modelled heights of the maximum frequency at around 300km, the ionosonde observed evidence of Sporadic E between 07:30 UT and 13:30 UT which was not modelled by EDAM. Overall this comparison questions the ability of EDAM to correctly model Sporadic E, and if this phenomenon affects EDAM to the point it begins to underperform in modelling the ionosphere in the latitude and longitude grid, defined in Chapter 5.

8.4 Discussion

Modified Taylor Diagrams, along with plots of sTEC and comparisons with ionosonde observations, have been used in a study to investigate why EDAM underperforms during June 2003 in comparison with the truth HERS observations. The Modified Taylor Diagrams were used to identify the time sectors of underperformance, and how each of the individual satellites were performing. From these results, sTEC comparisons between EDAM, IRI and the truth data were presented for three chosen satellites that were underperforming between 13 and 20 June 2003. Geomagnetic data was presented to show the geomagnetic conditions during this time period. EDAM was overestimating sTEC values predominantly

after midday, and the presented electron density plots from EDAM showed that maximum electron density values were being modelled over the region of the HERS receiver at low altitudes of approximately 110 km. This was presented as a signature of Sporadic E. Comparisons of maximum frequency and heights of that frequency were presented between EDAM converted electron density and observed data from the Chilton ionosonde, in an attempt to investigate the possibility of Sporadic E effects.

Sporadic E morphology was described in Section 2.6.2 and is usually formed in the ionosphere at altitudes of approximately between 100 to 125 km. The thickness of the Sporadic E layer in the ionosphere has been observed to be approximately 5 to 10 km in altitude (Kantarizis, 1971; Mathews, 1998; Kagan et al., 2002). A comparison the thickness of the sporadic E layer and the path length between a satellite-receiver pair is important because a satellite orbits the Earth at approximately 20,000 km. There is significant amount of ionisation that a satellite-to-receiver signal would have passed through compared to the ionisation in the thickness of the sporadic E layer. When EDAM models the electron densities from the assimilated GPS receivers, the ionisation is spread across the defined altitude range of the grid and the detail of the phenomenon is expected to be lost within the rest of the ionisation. However, in this study EDAM may have retained the detail of the Sporadic E, with evidence presented in Figure 100, and the comparison of Figures 102-109 with the ionosonde observations. It is also of note that the higher densities modelled by EDAM at the lower altitudes do not always match the ionosonde observations.

The results in Section 8.3.3 compared with the ionosonde observations in Section 8.3.4 showed that there were no sTEC changes in the HERS observed data with evidence that Sporadic E is prevalent in the ionosphere above Chilton.

Figures 93-95 showed that EDAM was overestimating the TEC values by some 20 TECU in comparison to the measured values of the HERS receiver when Sporadic E was said to be prevalent. From the HERS receiver there appears to be little to no fluctuation in the TEC values observed between the receiver and satellite. Maeda and Heki (2015) studied the morphological characteristics of mid-latitude Sporadic E by using 2D TEC maps from the Japanese network of GPS receivers. They showed that the fluctuation in the sTEC in the presence of Sporadic E was roughly a maximum of 1 TECU with smaller variations highlighted in Figure 2 of their work, using a single satellite as an example, satellite 12. This a much smaller variation than that modelled by EDAM.

The maps of the vertical TEC anomaly in Figure 3 of Maeda and Heki (2015), show that the vertical TEC anomalies appear to be extended by 5° in longitude and approximately 1° in latitude. This is much smaller than the Sporadic E modelled by EDAM (Figure 100) where the modelled increased density is extended over 30° in longitude and 10° in latitude. This is factor of 10 increase in latitude and almost a factor of 10 increase in longitude. The study by Muafiry et al. (2018) used 3D tomography to study cases of Sporadic E, confirming that Sporadic E lies at altitudes 100 km and that the fluctuation observed in the GPS data is of a similar order, approximately 1 TECU, to the Maeda and Heki (2015) case, which is much smaller than the fluctuations modelled by EDAM.

Sporadic E is said to have the greatest impact on HF radio waves (3-30 MHz) and lower VHF radio waves (30-100 MHz), with the ionisation in the Sporadic E reflecting these signals, and potentially preventing them reaching the F region (Rice et al., 2011). These radio waves are of a much lower frequency compared to the frequencies of GPS signals (1.2 and 1.6 GHz). As stated in the Maeda and Heki (2015) study, Sporadic E has a minimal impact on the

measurements of TEC from GPS, order of 1 TECU. It is therefore not easily observed in the HERS sTEC of this study. However, it raises questions of why EDAM has modelled the fluctuations in sTEC of 20 TECU and greater, at times broadly consistent with Sporadic E.

Figures 102 to 109 showed that Sporadic E was observed during the time period of interest. While Sporadic E can reflect HF radio waves and cause disruption in the ionosphere, it is seen as a positive phenomenon for radio amateurs who exploit the feature to communicate across thousands of kilometres (Neubeck, 1996). To corroborate with the observations of the Chilton ionosonde, radio amateur cases were used to confirm that Sporadic E was observed between 13 and 20 June 2003. This was done because during this time there was limited ionosonde data in the region of the observation to help support the Chilton ionosonde.

Figure 110 displays a map of the logs and reports of radio amateurs using Sporadic E to communicate over a large distance (DK5YA, 2003). The example is a Sporadic E cloud lasting for over three and a half hours, 13:51 – 17:27 UT, on the 16 June 2003. This evidence supports the observations from Chilton ionosonde showing Sporadic E was observed during this study with the region extending over Western Europe.

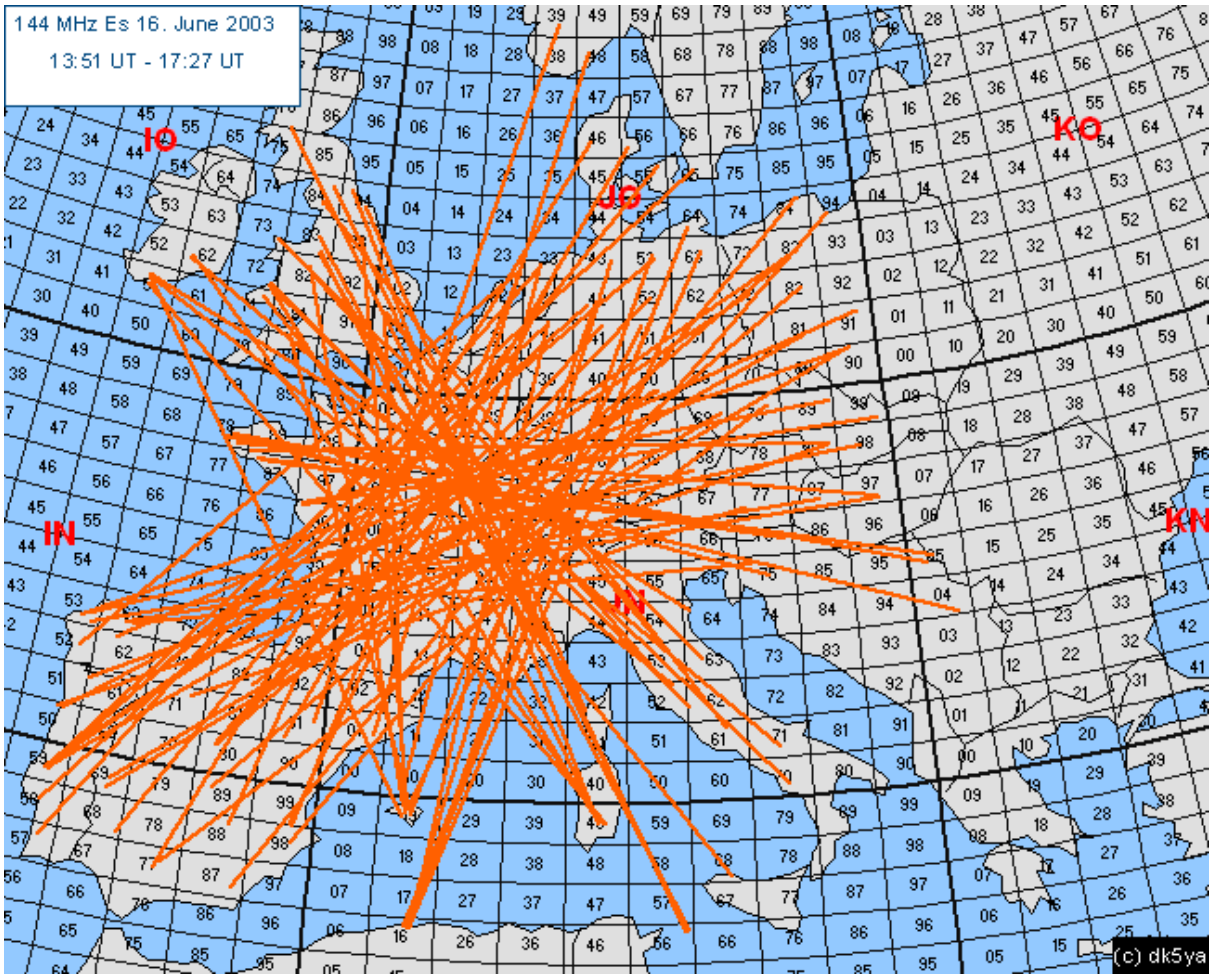

Figure 110 – A plot of radio amateur logs of communications during a Sporadic E event on 16 June 2003. This event lasted for between 13:51 UT – 17:27 UT. The feature was observed over Western Europe, mainly France. This evidence corroborates with the Chilton ionosonde observations that sporadic E was observed during this time period (DK5YA, 2003). (The records and logs have been obtained from http://www.vhfdx.de/es_summary_03_june_16.htm#DK5RQ, which was run by DK5YA between 1995 – 2017 and retains authorship of the results.)

A global survey of Sporadic E was conducted by Christina Arras (2010) which showed an occurrence map of Sporadic E between 2002 and 2008. This occurrence map was derived from CHAMP GPS Radio Occultation data and is displayed in Figure 111. In the year 2003, there was a high occurrence rate over the summer months of Sporadic E, providing additional evidence of increased probability of Sporadic E being observed in this study. Figure 111 also shows that for every year displayed there is a high occurrence rate in the summer months at

latitudes between 0°N and 60°N latitude. This shows that Sporadic E is a fairly common feature to be observed during the summer.

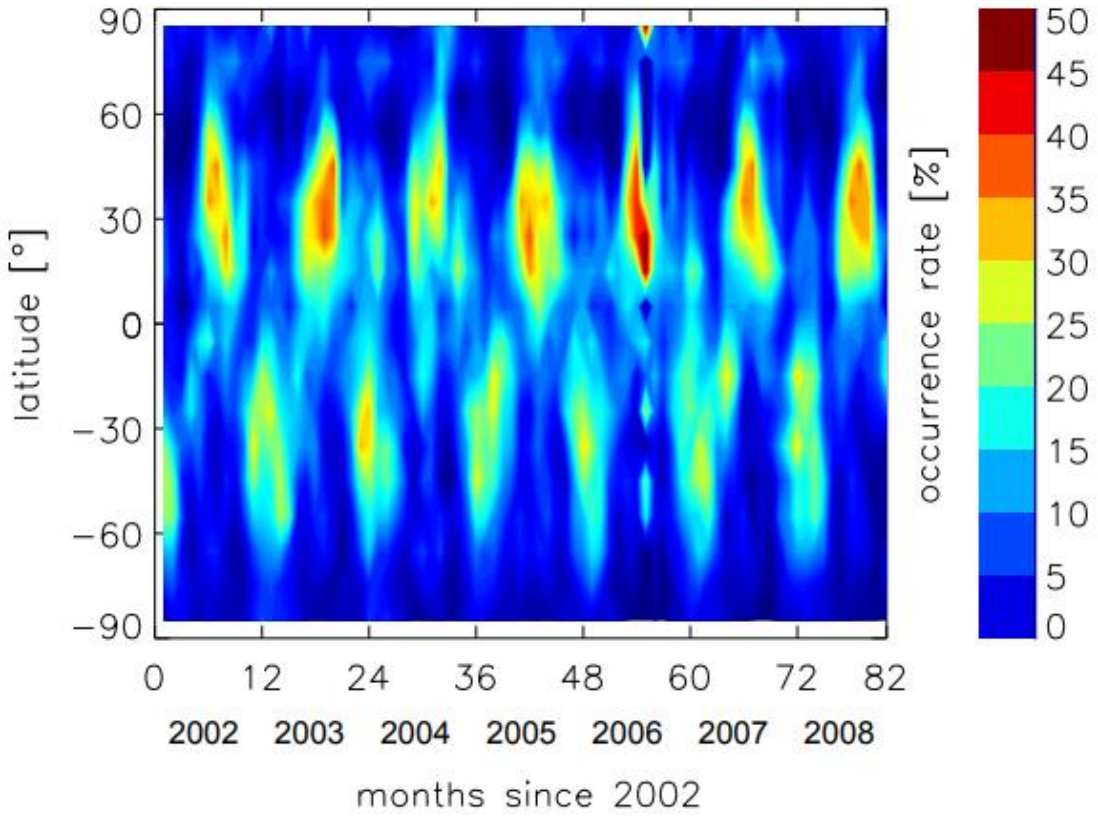

Figure 111 – Time series of Sporadic E occurrences with respect to number of months between 2002 and 2008 and latitude of occurrence. The rates have been derived from CHAMP GPS RO data. The plot has been taken from (Arras, 2010).

This study is the first time EDAM is likely to have modelled Sporadic E, even if it is overestimating its influence on the TEC in the ionosphere. The occurrence of Sporadic E has been corroborated by ionosonde data and radio amateur observations. There was difficulty comparing EDAM that has modelled Sporadic E with other models because no other ionospheric GPS based assimilative models have attempted a study to look into Sporadic E. This is down to the complexity of the phenomenon (Rice et al., 2011). There are examples of other modelling studies that include summer months. Okoh et al. (2018) assessed the NeQuick-2 and IRI-Plas 2017 models using long term and global GNSS measurements. This

study, specifically in the locations over Europe and in summer, showed that there was not as an extreme increase in TEC as observed by EDAM. The difference between the two studies is unlikely to be because of considering different years. Another comparison can be made with Chartier et al. (2011) who conducted a 12-year comparison of MIDAS and IRI-2007 modelled TEC. This study included 2003 but showed the average TEC, in TECU, of MIDAS and IRI over the 12 years. There doesn't appear to be fluctuations in the TEC values in the summer of 2003 which doesn't match the modelled values from EDAM.

The results in Chapters 5 and 7 indicated the geomagnetic activity did not affect EDAM to the degree showed in the TEC values modelled in June 2003. This by itself is therefore unlikely to be an explanation for the poor performance. It was also shown that Sporadic E cannot be the sole explanation for the poor performance due to Sporadic E having a minimal effect on the GPS frequencies, and therefore causing minimal fluctuations in TEC values. The current explanation for this poor performance may be down to a combination of all of the variability in the ionosphere during the month. June 2003 was a highly variable month in geomagnetic activity, meaning the ionosphere was always active. This month also displayed variations in the solar wind and the interplanetary magnetic field throughout the month (Figure 98). This combined with Sporadic E being present could have caused EDAM to incorrectly model this region. Future work, but outside the scope of this thesis, would be to conduct the same GPS assimilation of June 2003, but also assimilate ionosonde observations to test the performance of EDAM and to see if Sporadic E is still prevalent. This could be extended to different examples during summer time to see if the good performance seen in the current study could be duplicated.

8.5 Conclusion

This Chapter has focussed on a time period where EDAM modelled results underperformed compared to the truth data as shown by MTDs.

For July 2003, the performance of EDAM was very good compared to IRI and the truth observations, with correlation values between 0.95 and 0.99 showcasing this performance on multiple occasions in the month with very little underperformance. For June 2003 it was a different story where the correlation values were poor, with a value of less than 0.60 in correlation in the dusk sector. EDAM encountered multiple problems, particularly between 13 and 20 June 2003, in modelling sTEC data. The reasons why this was the case have been investigated and Sporadic E with variation in geomagnetic activity were given as the main causes for the fluctuations in EDAM modelled sTEC values.

The challenges shown for EDAM in this month also show the potential for improvement of the model in the future. There is potential for adapting the model to increase the capability in modelling Sporadic E. The next step would be to also use ionosonde data in the assimilation process to see if the Sporadic E could be modelled better as ionosonde data provides the altitudinal profile of the electron density. Another potential step is to use EDAM for other summer months in different years to see if this performance is repeated under the relevant geomagnetic and Sporadic E conditions.

Chapter 9

Conclusion

9.1 Conclusion

The purpose of this thesis was to validate EDAM with assimilated GPS in the European sector, a region with large scale ionospheric features. The model was used for parameterisation of the main ionospheric trough with the results compared with previous studies. It used GPS from approximately 43 receivers over the period of September 2002 to December 2002. Modified Taylor Diagrams were used to validate the performance of the model and identify when the performance was reduced. A case of SED/TOI in the Western European sector was also conducted, with the model clearly revealing the features. The results of this were presented in Chapters 5-8.

Chapter 5 showed the ability of EDAM to model the main ionospheric trough. GPS TECs along receiver-to-satellite pairs were assimilated into EDAM for the period of September to December 2002. The modelled Vertical TECs were used to obtain parameters for defining the main characteristics of the main ionospheric trough. These were then used for a statistical study during trough behaviour at times between 16:00 and 07:00 UT at a longitude of 0^{o}E. This statistical study showed the patterns that have commonly been seen in the trough behaviour during the course of the night. This was supported by evidence from Pryse et al. (2006), which was another study on the main ionospheric trough but using a different technique. The structure of the trough observed by the two techniques was very similar however, there were noticeable differences, mainly in the TEC value near the trough minimum, where the value from EDAM was some 2-3 TECU larger. This was attributed to the difference in altitude of the satellites used. The current study used GPS satellites at much higher altitudes then the NIMS satellites used by Pryse et al. (2006) and so the TEC was larger

due to the larger path lengths and the increased amount of ionisation the ray path to the receiver would traverse through.

Chapter 6 presented a SED and TOI modelled by EDAM on 30 September 2002. This feature has not been reported much in the literature in the European sector. Observations by the SuperDARN radar and data from other sources were used to confirm and understand that this was being correctly modelled. EDAM showed the feature up to 70°N. The SuperDARN data showed the plasma flow in this region and poleward which was supported by the reviewed literature. The location of the potential SED was also identified in the EDAM modelled electron densities at 58°N and 37°E, with the evolution shown throughout the day. The SED was linked to the TOI. Some evidence of the SED generation mechanism was presented in the electron density height profiles from EDAM. This was shown by the large electron density differences between the 30 September and 29 September 2002 located at altitudes in the topside ionosphere as described by Liu et al. (2016). The GPS data assimilated into EDAM modelled the maximum density value and the height of the maximum density, but caution must be taken in the results of the height of the density as shown by Elvidge et al. (2014).

Chapter 7 covered the validation of EDAM's modelling performances. The method chosen to do this validation was a statistical study between September 2002 and August 2003 using Modified Taylor Diagrams. TEC data for a receiver not included in the assimilation was used as a 'truth' source to be compared with EDAM and IRI TECs to analyse the performance of the models. The use of the Modified Taylor Diagram allowed multiple statistics to be compared on a single graph and showed the relative performance of both models compared to the truth as well as compared to each other. EDAM showed general good performance across the study for different conditions such as time of day, satellite number and geomagnetic activity. Similar

comparisons were also made using data from a 'truth' receiver at high latitude, the TRO1 receiver. The normalised biases for the TRO1 study were different to the normalised biases for the HERS study, with more positive normalised biases present for the high latitude modelled TECs. The overall performance of EDAM was strong with values for normalised standard deviation generally between 0.90 and 1.10 and correlation values between 0.90 and 1.00. However, where the study looked at months in detail, some notable poor performances were evident.

Chapter 8 looked at some of these poor performances of EDAM and why this was occurring. As a baseline a month was chosen where there was good performance in the Modified Taylor Diagram on nearly every day of the month. For this EDAM performed well compared to the truth and the correlation values were greater than 0.90. Geomagnetic conditions for the month in question with poorer performance, June 2003, were highly variable as shown in the Kp index. The time of interest for unusual poor performance was identified with a specific period in the month, 13 to 20 June. The differences in modelled sTEC and observed sTEC from HERS receiver on 14 to 19 June were 20 TECU and greater. The modelled maximum electron density at 51.70°N and 1.23°W, above the Chilton Ionosonde, expressed in terms of frequency and also the height of the maximum density was considered and compared with some parameters obtained from the Chilton ionosonde. This was to understand the high-density values at low altitudes that were being modelled by EDAM. This comparison and evidence presented from radio amateurs observations confirmed Sporadic E presence in the ionosphere, at low UK latitudes and over France, during the time period of interest. In general, Sporadic E is a common occurrence in summer (Arras, 2010), but EDAM was only severely affected in June. It was therefore suggested there must be other reasons contributing to the

underperformance of EDAM, such as the variability in the ionosphere due to the high geomagnetic activity during this period.

Taken collectively the results showcased the ability of EDAM to model large scale structures, showed the evolution with time of the features identified and yielded a statistical study of the features. The latter gave a better understanding of the features under different geomagnetic conditions and different times of the day. EDAM was shown to be an accurate model when assimilating GPS measurements but with limitations and problems when looking at the details of the statistical studies.

9.2 Future work

There is a lot room to expand on the work presented in this thesis by building upon some of the foundations made in these studies.

A much larger statistical study of the main ionospheric trough can be carried out to build on Chapter 5 with comparisons with other studies that use different techniques. The larger study could involve looking at trough behaviour over a whole solar cycle. Another route would be to use the parameterisation established by the model and create a parametrised trough in the background ionosphere model used for assimilation. This would adapt and evolve accurately with the assimilated observations.

Given the ability of EDAM to model the TOI and SED, the model now has the potential of being used in a statistical study of the features. The ideal scenario would be to bring in more data sources in the evaluation of the feature such as incoherent scatter radars. EDAM has shown

the potential of modelling the features in the European sector. It could also be used for studies in the North American sector where there is more scope to compare with previous observations of the TOI and SED. It also has the potential of being used globally. Assimilated ionosonde observations could be used to develop studies of SED and for comparison with other SED studies such as Liu et al. (2016).

Chapter 7 and 8 presented the validation of EDAM and where the modelling showed poor performance. The validation could be extended to a much longer study and using different 'truth' receivers positioned at different locations in Europe where the ionosphere structure would be different. Another way to validate EDAM would be to consider the model on the global scale and validate the performance for the equatorial, mid and high latitude ionosphere in both the northern and southern hemisphere. The most potential for future development of EDAM arises from where the poor performances in the model occurred, particularly in the evidence of Sporadic E being modelled by EDAM. The detail of this could be investigated to find other cases where Sporadic E was evident to see if EDAM can identify the structure.

For further development there is the scope of assimilating data from different observing techniques into EDAM along with GPS data. For example, ionosonde assimilation could improve the accuracy of the modelled heights of the maximum electron density and the vertical profile. More general uses of the model could be for real time monitoring of the ionosphere and for global ionospheric monitoring as well as for local regions considered in this thesis.

Appendix A – Tables of MIT Parameters

	21 and 22 UT		23 and 00 UT		01 and 02 UT	
	Lat	TEC	Lat	TEC	Lat	TEC
Eq Limit (D_E)	50.0	10.5	50.0	9.5	50.0	8.6
Eq Brkp (B_E)	52.8	8.2	53.6	7.9	53.2	7.2
Eq Hw (H_E)	57.5	6.6	56.8	7.0	56.8	6.0
Tr Min (T_M)	61.0	4.0	58.0	4.6	60.0	4.2
Pw Hw (H_P)	62.1	4.1	61.8	5.2	61.5	4.8
Pw Brkp (B_P)	64.5	4.8	63.9	6.3	63.7	5.9
Pw Max (P_{max})	68.5	11.7	67.0	9.7	66.0	9.3
Pw Limit (D_P)	70.0	10.1	70.0	9.2	70.0	8.8

Table 1a: Latitude (in degrees north) and VTEC (in TECU) of the set of parameters used to characterise the shape of the trough obtained from the EDAM model for low geomagnetic activity, Kp (0 to 2+).

	21 and 22 UT		23 and 00 UT		01 and 02 UT	
	Lat	TEC	Lat	TEC	Lat	TEC
Eq Limit (D_E)	50.0	7.2	50.0	7.0	50.0	6.7
Eq Brkp (B_E)	51.8	6.7	51.7	6.8	51.3	6.7
Eq Hw (H_E)	55.1	5.5	54.0	5.6	54.0	5.6
Tr Min (T_M)	58.0	4.4	56.0	4.2	56.0	4.4
Pw Hw (H_P)	59.5	5.2	58.9	5.4	58.1	5.6
Pw Brkp (B_P)	62.8	6.5	61.8	7.0	60.4	6.8
Pw Max (P_{max})	68.0	12.8	66.0	11.3	65.0	11.0
Pw Limit (D_P)	70.0	10.9	70.0	9.9	70.0	8.3

Table 1b: Latitude (in degrees north) and VTEC (in TECU) of the set of parameters used to characterise the shape of the trough obtained from the EDAM model for mid geomagnetic activity, Kp (3– to 4).

	21 and 22 UT		23 and 00 UT		01 and 02 UT	
	Lat	TEC	Lat	TEC	Lat	TEC
Eq Limit (D_E)	50.0	9.8	50.0	8.3	50.0	5.3
Eq Brkp (B_E)	52.7	8.9	51.3	7.5	51.4	5.5
Eq Hw (H_E)	54.3	7.4	53.9	6.1	53.5	4.6
Tr Min (T_M)	56.0	5.3	55.0	4.5	54.0	4.1
Pw Hw (H_P)	59.2	6.9	57.9	5.8	56.5	5.8
Pw Brkp (B_P)	62.9	8.5	61.1	7.2	59.1	7.3
Pw Max (P_{max})	66.0	11.7	65.0	10.0	65.0	10.1
Pw Limit (D_P)	70.0	10.2	70.0	8.6	70.0	8.2

Table 1c: Latitude (in degrees north) and VTEC (in TECU) of the set of parameters used to characterise the shape of the trough obtained from the EDAM model for high geomagnetic activity, Kp (≥ 4+).

Appendix B – Normalisation Factors

Satellite Number	Day Number							
	13	14	15	16	17	18	19	20
1	13.0413	13.8971	10.8023	8.78467	12.977	11.2171	8.20859	8.52294
2	14.6048	14.2957	13.5518	16.1863	11.017	10.3701	11.6308	14.0465
3	18.7164	21.4231	9.45868	7.95295	13.4325	13.8028	8.95562	9.29074
4	13.1724	12.5745	9.86324	9.30473	7.89341	7.05416	8.37472	10.7181
5	8.00447	19.5316	16.4792	12.6832	6.43943	6.39374	8.15364	8.40785
6	14.261	18.405	13.5271	8.18339	6.03841	7.12816	6.4823	8.74079
7	12.3424	13.2649	11.2218	11.801	6.25776	5.53805	6.85952	8.64041
8	11.7551	17.3248	10.6955	10.4825	8.41268	6.8251	8.11755	9.33394
9	10.5311	10.9568	9.52306	9.72138	7.47323	7.41202	7.24687	10.2994
10	11.7838	14.6323	14.275	10.6115	5.5664	5.75813	7.74857	9.6285
11	14.7504	15.0875	12.5689	13.854	12.2675	13.583	10.5965	11.4829
12	NA	NA	NA	NA	NA	NA	NA	NA
13	18.0322	16.3484	11.2395	8.98257	12.1446	10.945	8.98836	12.3536
14	14.1454	16.5805	7.79813	11.2613	8.53377	8.69979	7.15657	10.2292
15	16.4245	18.5556	14.4217	9.75039	11.4533	9.98798	11.2518	13.1074
16	15.2743	14.8836	10.3371	11.5648	9.42737	7.71013	9.82106	12.5404
17	12.0131	13.9597	13.8862	10.1633	8.4995	8.86288	11.1314	14.3641
18	6.03916	8.77763	10.1454	5.7611	4.79977	3.05769	6.8199	6.70419
19	NA	NA	NA	NA	NA	NA	NA	NA
20	14.5857	13.4396	12.4444	15.8408	9.00196	8.79591	9.73463	12.4421
21	14.1646	17.1825	14.8352	11.4626	9.63576	10.3742	11.8845	14.2224
22	NA	NA	NA	NA	NA	NA	NA	NA
23	8.69331	10.3034	11.3331	8.0582	5.98189	4.3423	6.85699	6.63186
24	13.5905	10.8009	11.4612	9.3495	8.22726	6.52166	8.44558	10.9091
25	18.6035	16.6922	14.9764	11.8278	13.8145	13.4613	12.8691	15.4838
26	11.9328	13.1798	10.7523	11.6185	6.29249	6.19811	8.90381	11.8443
27	10.5923	11.721	9.25653	9.94187	7.54023	5.88309	8.41897	8.26251
28	10.0632	9.18537	8.99804	8.07527	8.49778	8.85291	7.2866	12.2012
29	7.42049	13.8653	12.128	9.91971	6.27848	3.84836	6.05329	7.73477
30	12.4847	15.7159	15.1939	10.4826	5.80041	5.9491	8.08984	6.07163
31	18.4722	17.815	11.6519	8.27269	14.751	NA	8.96901	8.4763

Table 2: Normalisation Factors for all individual satellites between 13 – 20 June 2003.

Appendix C – Satellite Orbits

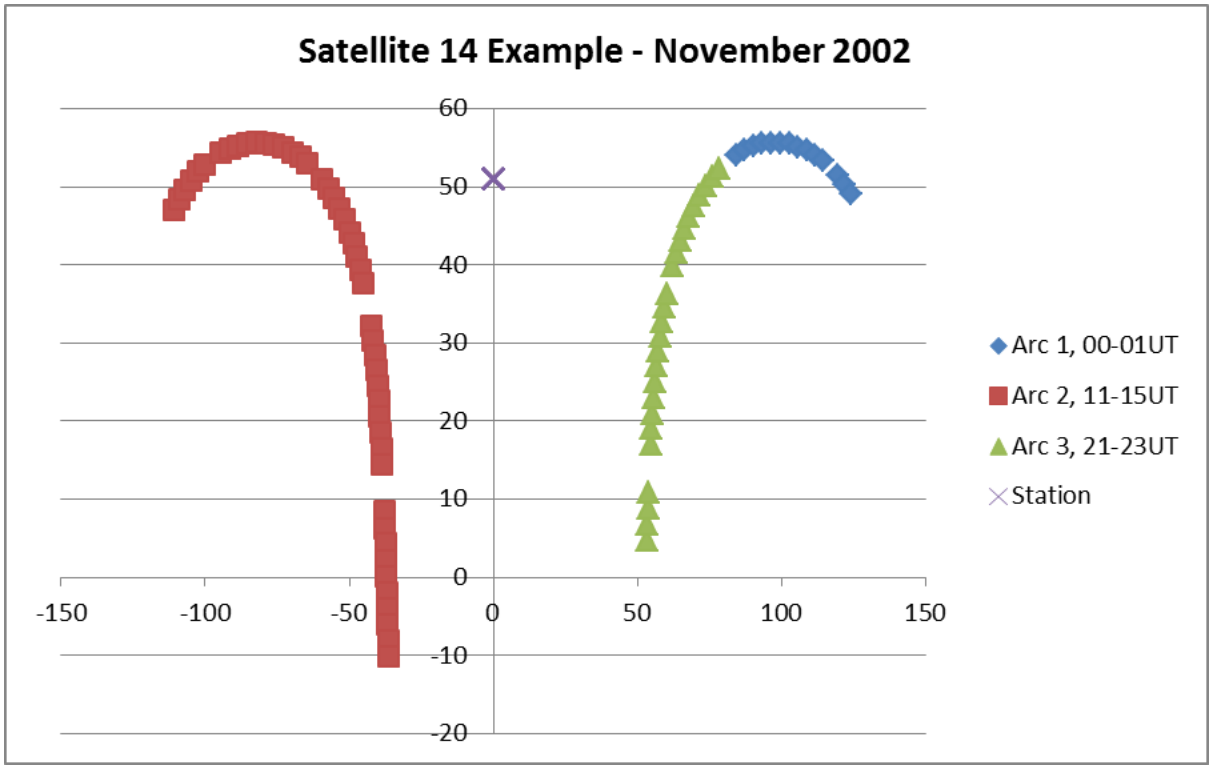

Figure 112 – An orbit example of satellite number 14 in November 2002 with HERS station referenced on the plot.

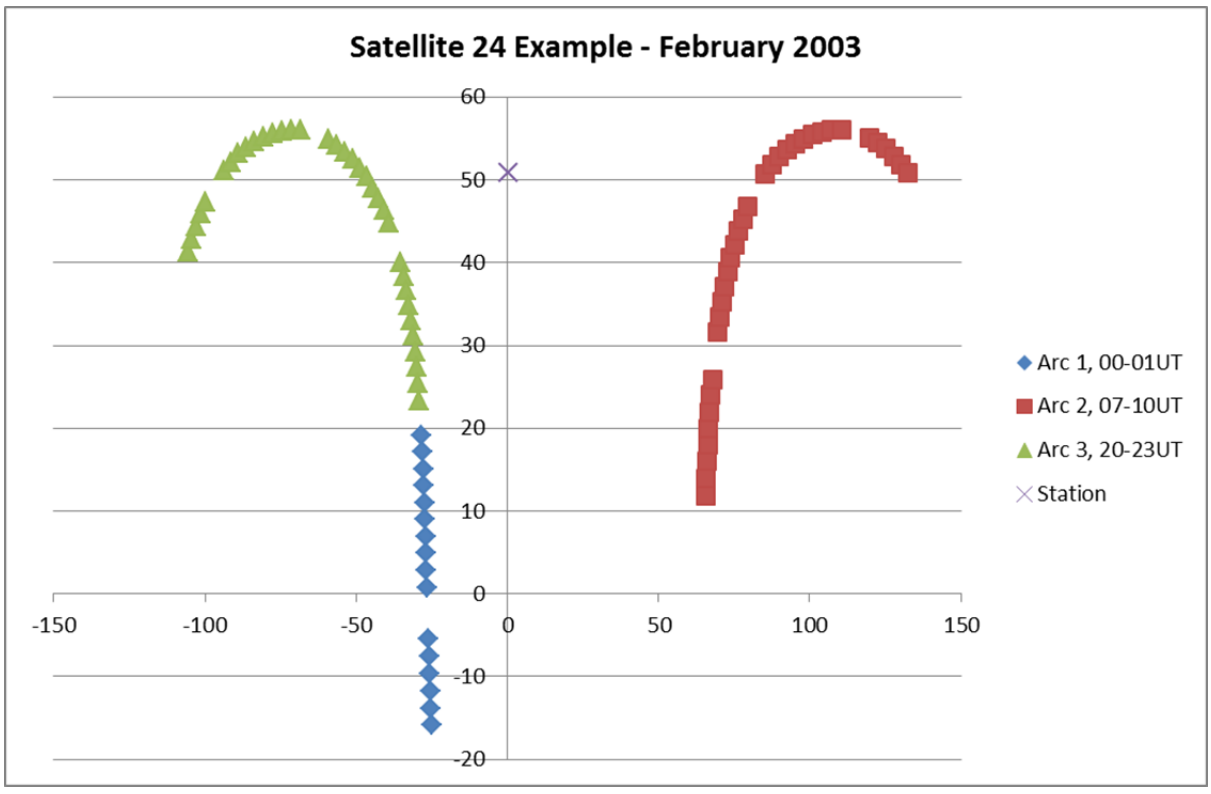

Figure 113 – An orbit example of satellite number 24 in February 2003 with HERS station referenced on the plot.

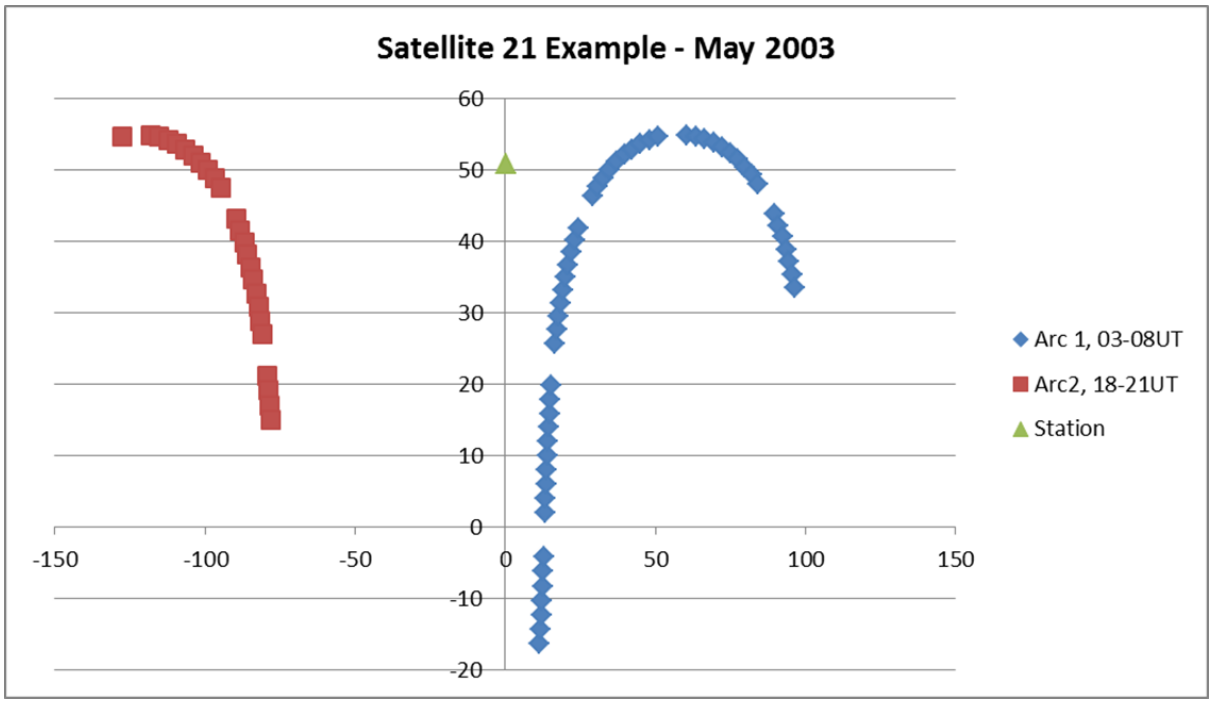

Figure 114 – An orbit example of satellite number 21 in May 2003 with HERS station referenced on the plot.

References

Akasofu, S-I., Polar and Magnetospheric Substorms, D. Reidel, Dordrecht, The Netherlands, 1968.

Andreev, M. Yu., Lukicheva, T. N., Mingalev, V. S., Model study of the effect of the main ionospheric trough on oblique HF radiowave propagation. Geomagn. Aeron., 46 (1), 94–100, 2006.

Angling, M. J., and Cannon, P. S., Assimilation of radio occultation measurements into background ionospheric models, Radio Sci., 39(RS1S08), 2004.

Angling, M. J., and Khattatov, B., Comparative study of two assimilative models of the ionosphere, Radio Sci., 41(RS5S20), 2006.

Angling, M. J., and Jackson-Booth, N. K., A short note on the assimilation of collocated and concurrent GPS and ionosonde data into the Electron Density Assimilative Model, Radio Sci., 46, RS0D13, doi:10.1029/2010RS004566, 2011.

Appleton, E. V. and Barnett, M. A. F., 'Local Reflection Of Wireless Waves From The Upper Atmosphere' Nature 115, 333-334, Doi:10.1038/115333a0, 1925.

Arras, C., Wickert, J., Beyerle, G., Heise, S., Schmidt, T. and Jacobi, C., A global climatology of ionospheric irregularities derived from GPS radio occultation. Geophys Res Lett 35:L14809. doi:10.1029/2008GL034158, 2008.

Arras, C., 'A Global Survey of Sporadic E Layers based on GPS Radio Occultations by CHAMP, GRACE and FORMOSAT-3/COSMIC, Scientific Technical Report STR10/09, GFZ Helhomltz-Zentrum Postdam, DOI: 10.2312/GFZ.b103-10097, DOI: 10.2312/GFZ.b103-100918, 2010.

Bates, H. F., Belon, A. E., and Hunsucker, R. D., Aurora and the poleward edge of the main ionospheric trough, J. Geophys. Res., 78(4), 648–658, doi:10.1029/JA078i004p00648, 1973.

Berchem, J., and Russell, C. T., The thickness of the magnetopause current layer: ISEE 1 and 2 observations, J. Geophys. Res., 87(A4), 2108–2114, doi:10.1029/JA087iA04p02108, 1982.

Bilitza, D., Reinisch, B. W., Radicella, S. M., Pulinets, S., Gulyaeva, T., and Triskova, L., Improvements of the International Reference Ionosphere model for the topside electron density profile, Radio Sci., 41, RS5S15, doi:10.1029/2005RS003370, 2006.

Bilitza, D., and Reinisch, B. W., International Reference Ionosphere 2007 improvements and new parameters, Adv. Space Res., 42(4), 599–609, doi:10.1016/j.asr.2007.07.048, 2008.

Bilitza, D., Altadill, D., Zhang, Y., Mertens, C., Truhlik, V., Richards, P., McKinnell, L.-A. and Reinisch, B., The International Reference Ionosphere 2012—A model of international collaboration, J. Space Weather Space Clim., 4, 1–12, 2014.

Birkeland, K., The Norwegian Aurora Polaris Expedition 1902–1903, Vol 1, 1st. sec, H. Aschehoug, Christiania, 1908.

Brekke, A., Physics of the Upper Polar Atmosphere, Wiley, New York, ISBN 0-471-96018-7, 1992.

Brunner, F. K., and Gu, M., An improved model for the dual frequency ionospheric correction of GPS observations, Manuscr. Geod., 16(3), 205–214, 1991.

Buonsanto, M. 'IONOSPHERIC STORMS – A REVIEW' Space Science Reviews, 88: 563. https://doi.org/10.1023/A:1005107532631, 1999.

Cavendish, H., On the Height of the Luminous Arch Which Was Seen on Feb. 23, 1784. By Henry Cavendish, Esq. F. R. S. and A. S. Philosophical Transactions of the Royal Society of London, 80, 101-105. Retrieved from http://www.jstor.org/stable/106832, 1790.

Chapman, S. and Ferraro, V. C. A., 'A new theory of magnetic storms', Terr. Magn. Atmos. Elec. 36, 77–97, 171–186, 1931.

Chappell, C. R., Conference on Magnetospheric Ionospheric Coupling, Eos Trans. AGU, 55(8), 776–795, doi:10.1029/EO055i008p00776, 1974.

Chartier, A. T., Mitchell, C. N., Jackson, D. R., A 12 year comparison of MIDAS and IRI 2007 ionospheric Total Electron Content, Advances in Space Research, Volume 49, Issue 9, Pages 1348-1355, ISSN 0273-1177, https://doi.org/10.1016/j.asr.2012.02.014, 2012.

Chisham, G., Lester, M., Milan, S. E., Freeman, M. P., Bristow, W. A., Grocott, A., McWilliams, K. A., Ruohoniemi, J. M., Yeoman, T. K., Dyson, P. L., Greenwald, R. A., Kikuchi, T., Pinnock, M., Rash, J. P. S., Sato, N., Sofko, G. J., Villain, J.-P. and Walker, A. D. M., A decade of the Super Dual Auroral Radar Network (SuperDARN): Scientific achievements, new techniques and future directions, Surveys of Geophysics, 28, 33-109, doi: 10.1007/s10712-007-9017-8, 2007.

Chiu, M., Von-Mehlem, U., Willey, C., Betenbaugh, T. M., Maynard, J. J., Krein, J. A., R. F. Conde, W. T. Gray, Hunt, Jr., J. W., Mosher, L. E., Mccullough, M. G., Panneton, P. E., Staiger, J. P. and Rodberg, E. H., ACE spacecraft, Space Sci. Rev., 86, 257, https://doi.org/10.1023/A:1005002013459, 1998.

Cho, H. R., and Yeh, K. C., Neutral Winds and the Behavior of the Ionospheric F_2Region, *Radio Sci.*, 5(6), 881–894, doi: 10.1029/RS005i006p00881, 1970.

Coster, A., Colerico, M., Foster, J.C., Ruohoniemi, J.M., Observations of the Tongue of Ionization with GPS TEC and SuperDARN. In Characterising the Ionosphere (pp. 7-1 – 7-14). Meeting Proceedings RTO-MP-IST-056, Paper 7. Neuilly-sur-Seine, France: RTO, 2006.

Coster, A. J., Colerico, M. J., Foster, J. C., Rideout, W., and Rich, F., Longitude sector comparisons of storm enhanced density, Geophys. Res. Lett., 34, L18105, doi:10.1029/2007GL030682, 2007.

Cramer, W. D., Turner, N. E., Fok, M., and Buzulukova, N. Y., Effects of different geomagnetic storm drivers on the ring current: CRCM results. Journal of Geophysical Research A: Space Physics, 118(3), 1062-1073, 2013.

Crowley, G., Critical Review of Ionospheric Patches and Blobs, 619-648, Review of Radio Science 1993-1996, edited by W. Ross Stone, URSI by Oxford University Press, 1996.

Curto, J. J., Araki, T., and Alberca, L. F., Evolution of the concept of Sudden Storm Commencements and their operative identification, Earth Planets Space, 59, i–xii, 2007.

Danskin, D. W., Koustov, A. V., Makarevitch, R. A. and Lester, M., Observations of double-peaked E region coherent spectra with the CUTLASS Finland HF radar, Radio Sci., 39, RS2006, doi:10.1029/2003RS002932, 2004.

David, M., Sojka, J. J., Schunk, R. W., and Coster, A. J., Polar cap patches and the tongue of ionization: A survey of GPS TEC maps from 2009 to 2015, Geophys. Res. Lett., 43, 2422–2428, doi:10.1002/2016GL068136, 2016.

Davis, T. N., and Sugiura, M., Auroral electrojet activity index AE and its universal time variations, J. Geophys. Res., 71(3), 785–801, doi:10.1029/JZ071i003p00785, 1966.

Deines, S. D., "Precise pseudoranges obtained from combining code and dual carrier measurements in Global Positioning System receivers", Retrospective Theses and Dissertations (1900), 2006.

Deng, Y., and Ridley, A. J., Role of vertical ion convection in the high-latitude ionospheric plasma distribution, J. Geophys. Res., 111, A09314, doi:10.1029/2006JA011637, 2006.

DK5YA – Sporadic E maps and records of radio amateur observations in 2003: Retrieved from http://www.vhfdx.de/es_summary_03_june_16.htm#DK5RQ on 14/09/2018, (2003).

Elvidge, S., Angling, M. J. and Nava B., On the use of modified Taylor diagrams to compare ionospheric assimilation models, Radio Sci., 49, 737–745, doi:10.1002/2014RS005435, 2014.

Evans, J. V., The June 1965 magnetic storm: Millstone Hill observation, J. Atmos. Terr. Phys. 3, 2, 1629-1640, 1970.

Feichter, E., and Leitinger, R., Properties of the main trough of the F region derived from Dynamic Explorer 2 data, Annals of Geophysics, 45(1), doi:10.4401/ag-3491, 2002.

Feltens, J., Angling, M., Jackson-Booth, N., Jakowski, N., Hoque, M., Hernández-Pajares, M., Aragón-Àngel, A., Orús, R., and Zandbergen, R., Comparative testing of four ionospheric models driven with GPS measurements, Radio Sci., 46, RS0D12, doi:10.1029/2010RS004584, 2011.

Foster, J. C., Storm time plasma transport at middle and high latitudes, J. Geophys. Res., 98(A2), 1675–1689, doi:10.1029/92JA02032, 1993.

Foster, J. C., and Vo, H. B., 'Average characteristics and activity dependence of the subauroral polarization stream', J. Geophys. Res., 107(A12), 1475, doi:10.1029/2002JA009409, 2002.

Foster, J. C., Coster, A. J., Erickson, P. J., Holt, J. M., Lind, F. D., Rideout, W., McCready, M., van Eyken, A., Barnes, R. J., Greenwald, R. A., and Rich F. J., 'Multiradar observations of the polar tongue of ionization', J. Geophys. Res., 110, doi:10.1029/2004JA010928, 2005.

Glassmeier, K.-H. and Tsurutani, B. T.: Carl Friedrich Gauss – General Theory of Terrestrial Magnetism – a revised translation of the German text, Hist. Geo Space. Sci., 5, 11-62, https://doi.org/10.5194/hgss-5-11-2014, 2014.

Greenwald, R. A., Baker, K. B., Hutchins, R. A. and Hanuise, C., 'An HF phased-array radar for studying small-scale structure in the high-latitude ionosphere.' Radio Sci 20:63–79, 1985.

Greenwald, R.A., Baker, K.B., Dudeney, J.R., Pinnock, M., Jones, T. B., Thomas, E. C., Villain, J. -P., Cerisier, J. -C., Senior, C., Hanuise, C., Hunsucker, R. D., Sofko, G., Koehler, J., Nielsen, E., Pellinen, R., Walker, A. D. M., Sato, N., Yamagishi, H., DARN/SuperDARN - A global view of the dynamics of high-latitude convection Space Sci Rev, 71: 761. https://doi.org/10.1007/BF00751350, 1995.

Grewal, M. S., Weill, L. R., Andrews, A. P., Global positioning systems, inertial navigation, and integration. John Wiley and Sons. ISBN 978-0-47135-032-3, 2001.

Hajj, G. A., Lee, L. C., Pi, X., Romans, L. J., Schreiner, W. S., Straus, P. R., and Wang, C., COSMIC GPS Ionospheric Sensing and Space Weather, TAO, 11(1), 235-272, 2000.

Haldoupis, C., A tutorial review on sporadic E layers. In Aeronomy of the Earth's atmosphere and ionosphere (pp. 381–394). Dordrecht: Springer. https://doi.org/10.1007/978-94-007-0326-1_29, (2011).

Hargreaves K.J., The Solar-Terrestrial Environment, Cambridge University Press, Cambridge, 1992.

He, M., Liu, L., Wan, W., and Zhao B., A study on the nighttime midlatitude ionospheric trough, J. Geophys. Res., 116, A05315, doi:10.1029/2010JA016252, 2011.

Hedin, M., Häggström, I., Pellinen-Wannberg, A., Andersson, L., Brändström, U., Gustavsson, B., Steen, Å., Westman, A., Wannberg, G., Eyken, T. V, Aso, T., Cattell, C., Carlson, C. W., and Klumpar, D., 3-D extent of the main ionospheric trough--a case study, Adv. Polar Upper Atmos. Res., 14, 157-162, 2000.

Heelis, R & B. Hanson, W & L. Burch, J., Ion convection velocity reversals in the dayside cleft. J Geophys Res. 81. 10.1029/JA081i022p03803, 1976.

Heelis, R. A., The effects of interplanetary magnetic field orientation on dayside high-latitude ionospheric convection, J. Geophys. Res., 89(A5), 2873–2880, 1984.

Heppner, J. P., and Maynard, N. C., Empirical high-latitude electric field models, J. Geophys. Res., 92, 4467, 1987.

Hochegger, G., Nava, B., Radicella, S., and Leitinger, R., A family of ionospheric models for different uses, Physics and Chemistry of the Earth, Part C: Solar, Terrestrial & Planetary Science, 25(4), 307-310, ISSN 1464-1917, http://dx.doi.org/10.1016/S1464-1917(00)00022-2, 2000.

Hofmann-Wellenhof, B., Lichtenegger, H., and Collins, J., GPS Theory and Practice, Fifth, revised edition, ISBN 3-211-83534-2 Springer-Verlag Wien New York, 2000.

Horvath, I., and Crozier, S., Software developed for obtaining GPS-derived total electron content values, Radio Sci., 42, RS2002, doi:10.1029/2006RS003452, 2007.

Hosokawa, K., Tsugawa, T., Shiokawa, K., Otsuka, Y., Nishitani, N., Ogawa, T. and Hairston, M. R., Dynamic temporal evolution of polar cap tongue of ionization during magnetic storm, J. Geophys. Res., 115, A12333, doi: 10.1029/2010JA015848, 2010.

Hundhausen, A.J., Bame, S.J., Ashbridge, J.R and Sydoriak, S.J. 'Solar wind proton properties: Vela 3 observations from July 1965 to June 1967', J. Geophys. Res., 75, 4643-4657, 1970.

Hunsucker, R. D., Radio Techniques for probing the terrestrial ionosphere, Springer-Verlag, Berlin, 1991.

Hunsucker, R. D., "Auroral and polar-cap ionospheric effects on radio propagation," in IEEE Transactions on Antennas and Propagation, vol. 40, no. 7, pp. 818-828, doi: 10.1109/8.155747, 1992.

Imber, S. M., Milan, S. E. and Lester, M., The Heppner-Maynard Boundary measured by SuperDARN as a proxy for the latitude of the auroral oval, J. Geophys. Res. Space Physics, 118, 685–697, doi:10.1029/2012JA018222, 2013.

Ishida, T., Ogawa, Y., Kadokura, A., Hiraki, Y., and Häggström, I., Seasonal variation and solar activity dependence of the quiet-time ionospheric trough, J. Geophys. Res. Space Physics, 119, 6774–6783, doi:10.1002/2014JA019996, 2014.

Jayawardena, T. S. P., Chartier, A. T., Spencer, P., and Mitchell, C. N., Imaging the topside ionosphere and plasmasphere with ionospheric tomography using COSMIC GPS TEC, J. Geophys. Res. Space Physics, 121, 817–831, doi:10.1002/2015JA021561, 2016.

Jin, Y., Jøran M. I. and Wojciech, M. J., GPS scintillation effects associated with polar cap patches and substorm auroral activity: direct comparison J. Space Weather Space Clim. 4 A23, DOI: 10.1051/swsc/2014019, 2014.

Jones, K. L., and H. Rishbeth, 'The origin of storm increases of midlatitude F-layer electron concentration', J. Atmos. Terr. Phys. 3, 3, 391-401, 1971.

Joselyn, J. A., and B. T. Tsurutani, Geomagnetic sudden impulses and storm sudden commencements: A note on terminology, Eos Trans. AGU, 71(47), 1808-1809, 1990
Kersley, L., Pryse, S. E., Walker, I. K., Heaton, J. A. T., Mitchell, C. N., Williams, M. J., and Willson, C. A., Imaging of electron density troughs by tomographic techniques, Radio Sci., 32,1607-1621, 1997.

Kagan, L. M., Bakhmet'eva, N. V., Belikovich, V. V. Tolmacheva, A. V. and Kelley, M. C., Structure and dynamics of sporadic layers of ionization in the atmospheric E region, Radio Sci., 37(6), 1106, doi:10.1029/2001RS002534, 2002.

Kalman, R. E., "A New Approach to Linear Filtering and Prediction Problems," Transaction of the ASME—Journal of Basic Engineering, pp. 35-45, 1960.

Kantarizis, E., Measurement of the thickness of a sporadic E-layer, Journal of Atmospheric and Terrestrial Physics, Volume 33, Issue 10, Pages 1651-1656, ISSN 0021-9169, https://doi.org/10.1016/0021-9169(71)90083-3, 1971.

Kersley, L., Malan, D., Pryse, S. E., Cander, L. R., Bamford, R. A., Belehaki, A., Leitinger, R., Radicella, S. M., Mitchell, C. N., and Spencer, P. S. J., Total electron content: A key parameter in propagation: measurement and use in ionospheric imaging, Ann. Geophys. 47(2-3): 1067-1091, 2004.

Klobuchar, J. A., Ionospheric effects on GPS, in Global Positioning System: Theory and Applications, vol. 1, edited by B. W. Parkinson et al., pp. 485–515, Am. Inst. of Aeronaut. and Astronaut., Washington, D. C., 1996.

Knudsen, W. C., Magnetospheric convection and the high-latitude F2 ionosphere, J. Geophys. Res., 79, 1046, 1974.

Köhnlein, W., A model of the electron and ion temperatures in the ionosphere, Planetary and Space Science, Volume 34, Issue 7, Pages 609-630, ISSN 0032-0633, https://doi.org/10.1016/0032-0633(86)90039-5. 1986,

Krankowski, A., Shagimuratov, I. I., Ephishov, I. I., Krypiak-Gregorczyk, A., and Yakimova, G., The occurrence of the mid-latitude ionospheric trough in GPS-TEC measurements, Adv. Space Res., 43(11), 1721-1731, ISSN 0273-1177, 2009.

Kumar, S., Performance of IRI-2012 model during a deep solar minimum and a maximum year over global equatorial regions, J. Geophys. Res. Space Physics, 121, 5664–5674, doi:10.1002/2015JA022269, 2016.

Le, H., Yang, N., Liu, L., Chen, Y. and Zhang H., The latitudinal structure of nighttime ionospheric TEC and its empirical orthogonal functions model over North American sector, J. Geophys. Res. Space Physics, 122, 963–977, doi:10.1002/2016JA023361, 2017.

Lee, I. T., Wang, W., Liu, J. Y., Chen, C. Y., and Lin, C. H., The ionospheric midlatitude trough observed by FORMOSAT-3/COSMIC during solar minimum, J. Geophys. Res., 116, A06311, doi:10.1029/2010JA015544, 2011.

Lester, M. and Cowley, S.W.H., The solar-terrestrial interaction and its importance for space weather, Advances in Space Research, Volume 26, Issue 1, Pages 79-88, ISSN 0273-1177, https://doi.org/10.1016/S0273-1177(99)01029-7, 2000.

Lester, M., Chapman, P. J., Cowley, S. W. H., Crooks, S. J., Davies, J. A., Hamadyk, P., McWilliams, K. A., Milan, S. E., Parsons, M. J., Payne, D. B., Thomas, E. C., Thornhill, J. D., Wade, N. M., Yeoman, T. K., and Barnes, R. J.: Stereo CUTLASS - A new capability for the SuperDARN HF radars, Ann. Geophys., 22, 459-473, https://doi.org/10.5194/angeo-22-459-2004, 2004.

Liu, J., Wang, W., Burns, A., Solomon, S. C., Zhang, S., Zhang, Y., and Huang, C., Relative importance of horizontal and vertical transports to the formation of ionospheric storm-enhanced density and polar tongue of ionization, J. Geophys. Res. Space Physics, 121, 8121–8133, doi:10.1002/2016JA022882, 2016.

Loewe, C. A., and Prölss, G. W., Classification and mean behavior of magnetic storms, J. Geophys. Res., 102(A7), 14209–14213, doi:10.1029/96JA04020, 1997.

Lunt, N., Kersley, L., Bishop, G. J., and Mazzella Jr., A. J., The contribution of the protonosphere to GPS total electron content: Experimental measurements, Radio Sci., 34(5), 1273–1280, doi:10.1029/1999RS900016, 1999.

Lyons, L.R, Formation of auroral arcs via magnetosphere-ionosphere coupling, Rev. Geophys, 30, 93, 1992.

Maeda, J. & Heki, K., 'Morphology and dynamics of daytime mid-latitude sporadic-E patches revealed by GPS total electron content observations in Japan', Earth Planet Sp, 67: 89. https://doi.org/10.1186/s40623-015-0257-4, 2015.

Mathews, J. D., Sulzer, M. P. and Perillat, P. (1997) Aspects of layer electrodynamics revealed by high-resolution ISR observations of the 80-270 km ionosphere. Geophysical Research Letters 24, 1411-1414.

Mathews, J. D., Sporadic E: Current views and recent progress, J. Atmos. Sol. Terr. Phys., 60, 413 – 435, 1998.

Marrison, W., "The Evolution of the Quartz Crystal Clock". *Bell System Technical Journal*. AT&T. **27**: 510–588. doi:10.1002/j.1538-7305.1948.tb01343.x, 1948.

McComas, D. J., Bame, S. J., Barker, P., Feldman, W. C., Phillips, J. L., Riley, P. and Griffee, J. W., Solar Wind Electron Proton Alpha Monitor (SWEPAM) for the Advanced Composition Explorer, Space Sci. Rev., 86, 561, 1998.
Mitchell, C. N., Cannon, P., S., and Spencer, P. S. J., Multi-Instrument Data Analysis System (MIDAS) Imaging of the Ionosphere, Report for the United States Air Force European Office of Aerospace Research and Development, 2002.

Mitchell, C. N., and Spencer, P. S. J., A three-dimensional time-dependent algorithm for ionospheric imaging using GPS, Ann. Geophys., 46(4), 687–696, doi:10.4401/ag-4373, 2003.

Moffet, R. J. and Quegan, S.: The Mid-Latitude trough in the Electron Concentration of the Ionospheric F-Layer: A Review of Observations and Modelling, J. Atmos. Terr. Phys., 45, 315–343, https://doi.org/10.1016/S0021-9169(83)80038-5, 1983.

Muafiry, I. N, Heki, K. and Maeda, J., '3D tomography of midlatitude sporadic-E in Japan from GNSS-TEC data', Earth Planets Space 70:45. https://doi.org/10.1186/s40623-018-0815-7, 2018.

Muldrew, D. B., F-layer ionization troughs deduced from Alouette data, J. Geophys. Res., 70(11), 2635–2650, doi:10.1029/JZ070i011p02635, 1965.

Nose M., Iyemori T., Sugiura M. and Kamei T., World Data Center for Geomagnetism, Kyoto - Geomagnetic Dst index, DOI:10.17593/14515-74000, 2015.

Neubeck, K. E. (1996), Using the combined resources of amateur radio observations and ionosonde data in the study of temperate zone sporadic-E, J. Atmos. Terr. Phys., 58, 1355–1365, doi:10.1016/0021-9169(95)00170-0.

Okoh, D., Onwuneme, S., Seemala, G., Jin, S., Rabiu, B., Nava, B., Uwamahoro, J., Assessment of the NeQuick-2 and IRI-Plas 2017 models using global and long-term GNSS measurements, Journal of Atmospheric and Solar-Terrestrial Physics, Volume 170, Pages 1-10, ISSN 1364-6826, https://doi.org/10.1016/j.jastp.2018.02.006, 2018.

Park, J., Ehrlich, R., Lühr, H. and Ritter, P., Plasma irregularities in the high-latitude ionospheric F-region and their diamagnetic signatures as observed by CHAMP, J. Geophys. Res., 117, A10322, doi: 10.1029/2012JA018166, 2012.

Parker, E. N., Dynamics of the interplanetary gas and magnetic fields, Astrophys. J. 128, 664-676 (1958a) .

Parker, E. N., Sudden expansion of the corona following a large solar flare and the attendant magnetic field and cosmic-ray effects, Astrophys. J. 133, 1014-1033 (1961a) .

Parker, E. N., Sudden expansion of the corona following a large solar flare and the attendant magnetic field and cosmic-ray effects, Astrophys. J. 133, 1014-1033 (1961b).

Parker, J. A. D., Pryse, S. E., Jackson-Booth, N., and Buckland, R. A.: Modelling the main ionospheric trough using the Electron Density Assimilative Model (EDAM) with assimilated GPS TEC, Ann. Geophys., 36, 125-138, https://doi.org/10.5194/angeo-36-125-2018, 2018.

Pryse, S. E., Kersley, L., Rice, D. L., Russell, C. D., and Walker, I. K., Tomographic imaging of the ionospheric mid-latitude trough, Ann. Geophys., 11,144-149, 1993.

Pryse, S.E., Kersley, L., Walker, I. K., Blobs and irregularities in the auroral ionosphere, Journal of Atmospheric and Terrestrial Physics, Volume 58, Issues 1–4, Pages 205-215, ISSN 0021-9169, https://doi.org/10.1016/0021-9169(95)00030-5, 1996.

Pryse, S. E., Dewis, K. L., Balthazor, R. L., Middleton, H. R. and Denton, M. H., The dayside high-latitude trough under quiet geomagnetic conditions: Radio tomography and the CTIP model, Ann. Geophys., 23, 1199-1206, 2005.

Pryse, S. E., Kersley, L., Malan, D., and Bishop, G. J.: Parameterization of the main ionospheric trough in the European sector, Radio Sci., 41, RS5S14, https://doi.org/10.1029/2005RS003364, 2006.

Raymund, T. D., Pryse, S. E., Kersley, L., and Heaton, J. A. T., Tomographic reconstruction of ionospheric electron density with European incoherent scatter radar verification, Radio Sci., 28(5), 811–817, doi:10.1029/93RS01102, 1993.

Redmon, R. J., Denig, W. F., Kilcommons, L. M. and Knipp, D. J., New DMSP database of precipitating auroral electrons and ions, J. Geophys. Res. Space Physics, 122, 9056–9067, doi: 10.1002/2016JA023339, 2017.

Rice, J., Mathematical Statistics and Data Analysis. Belmont, CA: Brooks/Cole Cengage Learning. p. 138. ISBN 978-0534-39942-9, 2007.

Rice, D. D., Sojka, J. J., Eccles, J. V., Raitt, J. W., Brady, J. J., and Hunsucker R. D., First results of mapping sporadic E with a passive observing network, Space Weather, 9, doi: 10.1029/2011SW000678, 2011.

Rishbeth, H., The effect of winds on the ionospheric F2-peak, Journal of Atmospheric and Terrestrial Physics, vol. 29, no. 3, pp. 225-238, 10.1016/0021-9169(67)90192-4, 1967JATP...29..225R, 1967.

Rodger, A. S., Moffett, R. J., and Quegan, S., The role of ion drift in the formation of ionization troughs in the mid- and high-latitude ionosphere – a review, J. Atmos. Terr. Phys., 54 (1), 1–30, 1992.

Rodgers, C. D., Inverse methods for atmospheric sounding: theory and practice, World Scientific Publishing, Singapore, 2000.

Rostoker, G., Akasofu, S.-I., Foster, J., Greenwald, R., Kamide, Y., Kawasaki, K., Lui, A., McPherron, R., and Russell C., Magnetospheric substorms—definition and signatures, J. Geophys. Res., 85(A4), 1663–1668, doi: 10.1029/JA085iA04p01663, 1980.

Ruohoniemi, J. M., and Baker, K. B., Large-scale imaging of high-latitude convection with Super Dual Auroral Radar Network HF radar observations, J. Geophys. Res., 103, 20,797, doi:10.1029/98JA01288, 1998.

Russell, C. T., Zhou, X. W., Chi, P. J., Kawano, H., Moore, T. E., Peterson, W. K., Cladis, J. B., and Singer, H. J., Sudden compression of the outer magnetosphere associated with an ionospheric mass ejection, First published: 1 August 1999, Full publication history, DOI: 10.1029/1999GL900455

Rycroft, M. J., and Burnell, S. J., Statistical analysis of movements of the ionospheric trough and the plasmapause, J. Geophys. Res., 75(28), 5600–5604, doi:10.1029/JA075i028p05600, 1970.

Sato, T., Morphology of ionospheric F2 disturbances in the polar regions, A linkage between polar patches and plasmaspheric drainage plumes, Rep. Ionos. Res. Space Res. Jpn., 131, 91, 1959.

Schreiner, W. S., Sokolovskiy, S. V., Rocken, C. and Hunt, D. C., Analysis and validation of GPS/MET radio occultation data in the ionosphere, Radio Sci., 34(4), 949–966, doi:10.1029/1999RS900034, 1999.

Schunk, R. W. and Nagy, A. F., Ionospheres: Physics, Plasma Physics, and Chemistry, Second Edition, ISBN: 978-0-521-87706-0, Cambridge University Press, 2000.

Spiro, R. W., Heelis, R. A., and Hanson, W. B., Ion convection and the formation of the mid-latitude F region ionization trough, J. Geophys. Res., 83(A9), 4255–4264, doi:10.1029/JA083iA09p04255, 1978.

Spiker, J. J., 'GPS signal structure and theoretical performance. In Parkinson B. W., Spiker, J. J, Global positioning system: theory and applications.' American institute of Aeronautics and Astronautics, Washington DC, vol1: 57-119.

Solomon, S. C., Qian, L., & Mannucci, A. J., Ionospheric electron content during solar cycle 23. Journal of Geophysical Research: Space Physics, 123,5223–5231. https://doi.org/10.1029/2018JA025464, 2018.

Sugiura, M., and Chapman, S., The Average Morphology of Geomagnetic Storms With Sudden Commencement, Abhandl. Akad. Wiss. Göttingen, Math.-Phys. Kl., Sonderheft 4, Göttingen, 1960.

Taylor, K. E., Summarizing multiple aspects of model performance in a single diagram, J. Geophys. Res., 106(D7), 7183–7192, doi:10.1029/2000JD900719, 2001.

Titheridge, J. E., Ionogram analysis with the generalized program POLAN, World Data Center A for Solar-Terrestrial Physics Report UAG-93, 1985.

Thomas, E. G., Baker, J. B. H., Ruohoniemi, J. M., Clausen, L. B. N., Coster, A. J., Foster, J. C. and Erickson, P. J., Direct observations of the role of convection electric field in the formation of a polar tongue of ionization from storm enhanced density, J. Geophys. Res. Space Physics, 118, 1180–1189, doi:10.1002/jgra.50116, 2013.

Tsurutani, B. T., Gonzalez, W. D., Tang, F. Akasofu, S. I., and Smith, E. J., Origin of interplanetary southward magnetic field responsible for major magnetic storms near solar maximum (1978–1979), J. Geophys. Res., 93, 8519–8531, 1988.

VanZandt, T. E., Clark, W. L. and Warnock, J. M., Magnetic Apex Coordinates: A Magnetic Coordinate System for the Ionospheric F2 Layer, J. Geophys. Res., 77, 1972.

Venkatesh, K., Fagundes, P. R., Seemala, G. K., de Jesus, R., de Abreu, A. J. and Pillat, V. G., On the performance of the IRI-2012 and NeQuick2 models during the increasing phase of the unusual 24th solar cycle in the Brazilian equatorial and low-latitude sectors, J. Geophys. Res. Space Physics, 119, 5087–5105, doi: 10.1002/2014JA019960, 2014.

Villain, J.-P., Greenwald, R. A., Baker, K. B. and Ruohoniemi, J. M., HF radar observation of E region plasma irregularities produced by oblique electron streaming, J. Geophys. Res., 92, 12,327, 1987.

Voiculescu, M., Nygrén, T., Aikio, A., and Kuula, R., An olden but golden EISCAT observation of a quiet-time ionospheric trough, J. Geophys. Res., 115, A10315, doi:10.1029/2010JA015557, 2010.

Werner, S., and Prölss, G. W., The position of the ionospheric trough as a function of local time and magnetic activity, Adv. Space Res., 20, 1717–1722, doi:10.1016/S0273-1177(97)00578-4, 1997.

Whalen, J. A., Daytime F Layer Trough Observed on a Macroscopic Scale, J. Geophys. Res., 92, 2571-2576, 1987.

Whalen, J. A., The daytime F layer trough and its relation to ionospheric-magnetospheric convection, J. Geophys. Res., 94, 17169–17184, 1989.

Wu, D. L., Ao, C. O., Hajj, G. A., de la Torre Juarez, M. and Mannucci, A. J., Sporadic E morphology from GPS-CHAMP radio occultation, J. Geophys. Res., 110, A01306, doi: 10.1029/2004JA010701, 2005.

Yang, N., Le, H., and Liu, L., Statistical analysis of ionospheric mid-latitude trough over the Northern Hemisphere derived from GPS total electron content data, Earth, Planets and Space, 201567:196 DOI: 10.1186/s40623-015-0365-1, 2015.

Yeh, K. C., and Raymund, T. D., Limitations of ionospheric imaging by tomography, Radio Sci., 26(6), 1361–1380, doi:10.1029/91RS01873, 1991.

Yizengaw, E., and Moldwin, M. B., The altitude extension of the mid-latitude trough and its correlation with plasmapause position, Geophys. Res. Lett., 32, L09105, doi:10.1029/2005GL022854, 2005.

Yuan, Z.-G., Deng, X.-H. and Wang, J.-F., DMSP/GPS observations of intense ion upflow in the midnight polar ionosphere associated with the SED plume during a super geomagnetic storm, Geophys. Res. Lett., 35, L19110, doi: 10.1029/2008GL035462, 2008.

Zou, S., Moldwin, M. B., Coster, A., Lyons, L. R, and Nicolls, M. J., GPS TEC observations of dynamics of the mid-latitude trough during substorms, Geophys. Res. Lett., 38, L14109, doi:10.1029/2011GL048178, 2011.